

ABSTRACT

This final report summarizes the results obtained on Grant AFOSR-91-025. The overall objective of this basic research program was the quantitative investigation of the fundamental phenomena relevant to aero-thermodynamic distortion induced structural dynamic blade responses in multistage gas turbine engines and the study of the fundamental unsteady aerodynamics and heat transfer phenomena inherent in turbines. The technical approach involved unique benchmark experiments and also analyses. In particular, the flow physics of multistage blade row interactions were investigated, with unique unsteady aerodynamic data obtained and analyses developed to understand, quantify, and discriminate the fundamental flow phenomena as well as to direct the modeling of advanced analyses.

Accession For	
NTIS	CRA&I
DTIC	TAE
Unannounced	
Justification	
By	
Distribution /	
Availability	
Dist	Availability or Special
A-1	

AEOSR-TR- 94 0338

Approved for public release;
distribution unlimited.

DTIC QUALITY INSPECTED 2

94-16976



10/88

94 6 6 050

TABLE OF CONTENTS

ABSTRACT

I. INTRODUCTION	1
II. PUBLICATIONS	1
APPENDIX I. Oscillating Cascade Unsteady Aerodynamics Including Separated Flow Effects	3
APPENDIX II. Rotor Blade Unsteady Aerodynamic Gust Response to Inlet Guide Vane Wakes	
APPENDIX III. Forcing Function Generation Fluid Dynamic Effects on Compressor Blade Gust Response	
APPENDIX IV. Compressor Blade Row Unsteady Aerodynamic Response to Attached and Separated Flow Forcing Functions	
APPENDIX V. Single Passage Euler Analysis of Oscillating Cascade Unsteady Aerodynamics for Arbitrary Interblade Phase Angle	
APPENDIX VI. Acoustic Resonance Flow Conditions on Wake Generated Rotor Blade Gust Response	
APPENDIX VII. Compressor Unsteady Aerodynamic Response to Rotating Stall and Surge Excitations	

I. INTRODUCTION

This is the final report on Grant AFOSR-91-025, a research program directed at the quantitative investigation of the fundamental unsteady aerodynamic phenomena driving forced response in turbomachine blade rows and the study of the fundamental unsteady aerodynamics and heat transfer phenomena inherent in turbines. The technical approach involved unique benchmark experiments and also analyses. In particular, the flow physics of multistage blade row interactions were investigated, with unique unsteady aerodynamic data obtained and analyses developed to understand, quantify, and discriminate the fundamental flow phenomena as well as to direct the modeling of advanced analyses.

The research results obtained are contained in both the publications and the graduate student theses. The technical publications are summarized in the following, with the detailed results and publications presented in the appendices.

II. PUBLICATIONS

Eley, J.A. and Fleeter, S., "Oscillating Cascade Unsteady Aerodynamics Including Separated Flow Effects," *Computational Mechanics*, Vol. 8, No. 6, pp. 383-398, 1991.

Manwaring, S.R., and Fleeter, S., "Rotor Blade Unsteady Aerodynamic Gust Response to Inlet Guide Vane Wakes," *ASME Journal of Turbomachinery*, Vol. 115, No. 1, January 1993, pp. 197-206.

Kim, K and Fleeter, S., "Forcing Function Generation Fluid Dynamic Effects on Compressor Blade Gust Response," *AIAA Journal of Propulsion and Power*, Vol. 10, Number 2, March-April 1994, pp. 204-216.

Manwaring, S. R. and Fleeter, S., "Reduced Frequency Effects on Gust Response Unsteady Aerodynamics in Turbomachines," *IUTAM 6th International Symposium on Unsteady Aerodynamics and Aeroelasticity of Turbomachines and Propellers*, The University of Notre Dame, September 1991.

Kim, K and Fleeter, S., "Compressor Blade Row Unsteady Aerodynamic Response to Attached and Separated Flow Forcing Functions," *AIAA Paper 92-0147* January 1992 (also *International Journal of Turbo & Jet Engines*, in press).

Wolff, J.M. and Fleeter, S., "Single Passage Euler Analysis of Oscillating Cascade Unsteady Aerodynamics for Arbitrary Interblade Phase Angle," *AIAA Paper 93-0389*, January 1993 (also *AIAA Journal for Propulsion and Power*, in press).

Manwaring, S.R. and Fleeter, S., "Acoustic Resonance Flow Conditions on Wake Generated Rotor Blade Gust Response," *ASME Paper 93-187*, May 1993..

Kim, K. and Fleeter, S., "Compressor Unsteady Aerodynamic Response to Rotating Stall and Surge Excitations," *AIAA Paper 93-2087*, June 1993 (also *AIAA Journal for Propulsion and Power*, in press).

APPENDIX I

Oscillating Cascade Unsteady Aerodynamics Including Separated Flow Effects

Computational Mechanics, Vol. 8, No. 6, pp. 383-398, 1991

Oscillating cascade unsteady aerodynamics including separated flow effects

J. A. Eley and S. Fleeter

School of Mechanical Engineering, Purdue University, West Lafayette, Indiana 47907, USA

Abstract. A mathematical model is developed to predict the effect of flow separation on the unsteady aerodynamic lift and moment acting on a two-dimensional flat plate cascade which is harmonically oscillating in a subsonic flow field. The unsteady flow is considered to be a small perturbation to the uniform steady flow, with the steady flow assumed to separate at a specified fixed position on the airfoil suction surface. This formulation does not require the difference in the upwash velocity across the airfoil in the separated flow region to be determined before calculating the unsteady pressure difference across the chordline of the airfoils, thereby eliminating the assumption that the upwash difference is zero at the trailing edge when the steady flow is separated. Results obtained demonstrate that although flow separation decreases bending mode stability, it does not result in bending mode flutter. However, flow separation can result in torsion mode flutter, with this instability being a function of the location of both the separation point and the elastic axis.

List of symbols

d	nondimensional distance D/C
h	nondimensional distance H/C
k	reduced frequency, $\omega C/U_\infty$
p	perturbation pressure
u	perturbation velocity in the x direction
v	perturbation velocity in the y direction
x	nondimensional chordwise Cartesian coordinate, X/C
x_s	nondimensional separation point location measured from the leading edge
y	nondimensional normal Cartesian coordinate, Y/C
y_b	bending mode nondimensional displacement
C	airfoil chord
C_L	unsteady lift coefficient
C_M	unsteady moment coefficient
C_p	pressure difference coefficient, $\Delta p/\rho_\infty U_\infty^2$
D	distance between leading edges of adjacent airfoils as measured in the x direction
H	distance between mean positions of adjacent airfoils as measured in the Y direction
M_∞	Mach number at $x = \pm \infty$
P	fluid static pressure
P_∞	fluid static pressure at $x = \pm \infty$
S	spacing between adjacent airfoils
α	airfoil angular displacement for torsional oscillations
β	$(1 - M_\infty^2)^{1/2}$
γ	cavitation number
θ	cascade stagger angle
ν	Fourier transform variable
σ	cascade interblade phase angle
ϕ	velocity potential
ω	circular frequency

Subscripts

b	bending mode oscillation
α	torsional mode oscillation
$+$	upper surface
$-$	lower surface

Superscripts

ATT	attached flow
COR	correction
SEP	separated flow
*	Fourier transform
(-)	complex amplitude

1 Introduction

The continuing demand for more efficient axial flow compressors for gas turbine engines is being achieved by higher rotational speeds, thinner airfoils, higher pressure ratios per stage, and increased operating temperatures. As a result, the possibility of an aerodynamic blade row instability is an important design consideration. Namely, under certain conditions, a blade row operating in a completely uniform flow field can enter into a self-excited oscillation known as flutter. The motion is sustained by the extraction of energy from the uniform flow during each vibratory cycle, with the flutter frequency generally corresponding to one of the lower blade or coupled blade-disk natural frequencies.

To predict the aerodynamic stability of a rotor, a typical airfoil section approach is utilized. The three-dimensional flow field through the rotor is approximated by two-dimensional strips along the blade span. For each strip, the structural dynamic properties and the unsteady aerodynamic loading due to harmonic airfoil oscillations must be determined. Finite element techniques enable the structural and vibrational characteristics to be accurately predicted. However, accurate predictions of the flutter characteristics of the blade row cannot be made due to inadequacies in current state-of-the-art oscillating cascade models.

Unsteady aerodynamic models are typically restricted to thin airfoil theory, with the unsteady disturbances generated by the oscillating airfoils assumed to be small compared to the mean steady potential flow field. In addition, the airfoils are considered to be flat plates at zero incidence. Thus, the unsteady aerodynamics become uncoupled from the steady flow, leading to a model wherein the flow is linearized about a uniform and parallel flow. Kernel function methods can then often be utilized to determine analytical solutions for the unsteady aerodynamic lift and moment acting on the oscillating airfoils.

When the mean flow does not separate from the airfoil, i.e., unstalled flutter, a number of such unsteady aerodynamic models have been developed. For example, Whitehead (1960) developed a model for incompressible flow through an infinite cascade of oscillating flow plate airfoils by constructing a vorticity distribution on each airfoil which satisfied the boundary conditions. Fleeter (1973) extended this model to include compressible flow by using Fourier transform theory and the linearized small perturbation potential flow equation. Smith (1972) developed an analogous subsonic model by replacing the airfoils by a series of continuous singularity distributions. For both subsonic and supersonic inlet flow Mach numbers, Ni (1979) developed a corresponding kernel function analysis.

The particular problem of interest herein is subsonic stall flutter. It is the oldest, most common type of flutter and is generally attributed to separated flow on the suction surface of the airfoils caused by operating beyond some critical mean flow incidence angle at subsonic Mach numbers. Bending, torsion, and coupled vibrational modes have been documented when this type of flutter is encountered at part speed in a high speed fan and at or near the design speed in a low or high pressure compressor.

Only a very few unsteady aerodynamic models appropriate for stall flutter prediction have been developed. In these, the flow is considered to separate at a specified position on the airfoil suction surface, with this separation point fixed throughout the airfoil oscillation cycle. Also, the pressure in the separated flow region and the wake is assumed to be constant. Woods (1957) developed a model for incompressible potential flow past an isolated airfoil. An incompressible flow oscillating cascade unsteady aerodynamic model for turbomachine applications was formulated by Sisto (1967). Perumal and Sisto (1975) developed a model for incompressible flow through an infinite cascade of oscillating airfoils using conformal mapping and the acceleration potential.

More recently, Chi (1980, 1985) used Fourier transform theory and the linearized small perturbation potential flow equation to develop an oscillating airfoil and airfoil cascade model for subsonic compressible flow. This solution consists of an attached flow unsteady aerodynamic solution and a correction to account for the effects of the flow separation. This correction is determined by solving two integral equations: one for the difference in the upwash velocity across the airfoil in the separated flow region, and a second for the correction of the unsteady pressure difference across the airfoil chordline due to the separated flow. However, Chi assumes that the Kutta condition applies to the separated flow region, i.e., the upwash difference becomes zero at the airfoil trailing edge even though the flow is separated.

In this paper, an unsteady aerodynamic cascade analysis which is appropriate for the design prediction of subsonic stall flutter in turbomachines is developed. In particular, this model will predict the effect of flow separation on the unsteady lift and moment acting on a two-dimensional flat plate airfoil cascade which is harmonically oscillating in a subsonic flow field. The unsteady flow field is considered to be a small perturbation to the uniform steady flow, with the steady flow assumed to separate at a specified fixed position on the suction surface of the airfoils. In this formulation, the difference in the upwash velocity across the airfoil in the separated flow region is not required to be determined before calculating the correction of the unsteady pressure difference across the chordline of the airfoils, thereby eliminating the assumption that the upwash difference is zero at the trailing edge when the steady flow is separated.

2 Unsteady aerodynamic model

This model considers the inviscid flow past an oscillating airfoil cascade. The fluid is assumed to be a thermally and calorically perfect gas, with the subsonic flow inviscid and irrotational. The far upstream flow is uniform with velocity U_∞ and approaches the cascade at zero mean incidence angle. The steady flow is assumed to separate from a specified fixed position on the suction surfaces of the airfoils, with the constant pressure separated flow region confined to a thin slit extending to downstream infinity, Fig. 1. The unsteady aerodynamics of interest are generated by small amplitude translational or torsional oscillations of the airfoil cascade, with a constant interblade phase angle.

The linearized partial differential equation for the unsteady velocity potential, ϕ , is given in Eq. (1), with the linearized unsteady Bernoulli equation specified in Eq. (2).

$$\frac{\partial^2 \phi}{\partial X^2} + \frac{\partial^2 \phi}{\partial Y^2} - \frac{1}{a_\infty^2} \left(\frac{\partial^2 \phi}{\partial t^2} + 2U_\infty \frac{\partial^2 \phi}{\partial X \partial t} + U_\infty^2 \frac{\partial^2 \phi}{\partial X^2} \right) = 0, \quad p = -\rho_\infty \left(\frac{\partial \phi}{\partial t} + U_\infty \frac{\partial \phi}{\partial X} \right). \quad (1.2)$$

Equations (1) and (2) are first used to derive the unsteady pressure difference across the airfoil for attached flow, and then to derive a correction for the flow separation using the condition that the pressure is constant in the separated flow region. As this is a linear analysis, the unsteady pressure

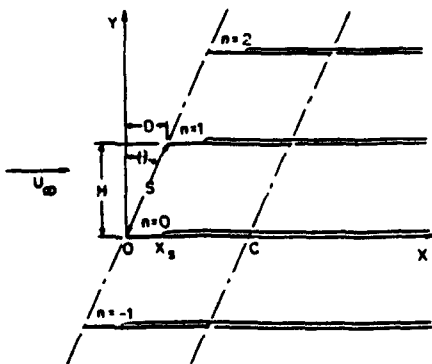


Fig. 1. Cascade and flow field configuration

and the resulting unsteady aerodynamic lift and moment acting on the airfoils are expressed as a sum of the fully attached flow solution and a correction due to the flow separation.

For the portion of the airfoil where the flow is attached, the velocity component normal to the airfoil surface, the upwash velocity, must be equal to the airfoil surface velocity. This boundary condition, Eq. (3a), is satisfied at the airfoil mean position. However, in the separated flow region, the velocity component normal to the airfoil surface is not equal to the surface velocity, and therefore is unknown. This perturbation velocity must be determined using the condition that the pressure is constant in the separated flow region, with the cavitation number defined in Eq. (3b) and the separated flow region boundary condition given in Eq. (4).

$$v = \frac{dY_b}{dt} + U_{\infty}(X - X_{se}) \frac{d\alpha}{dt} + U_{\infty} \alpha \quad \text{at } Y = 0^{\pm}, \quad 0 \leq X \leq X_s, \quad \gamma(t) = -\frac{\rho}{\frac{1}{2}\rho_{\infty} U_{\infty}^2} X > X_s, \quad (3a, b)$$

$$p = -\frac{1}{2}\rho_{\infty} U_{\infty}^2 \gamma(t) \quad \text{at } Y = 0^+, \quad X > X_s, \quad (4)$$

where X_s specifies the separation chordwise position.

Nondimensionalizing the spatial dimensions with respect to the airfoil chord, C , assuming harmonic time dependence for the airfoil motion and the flow variables at a frequency ω and substituting these quantities into Eqs. (1,2) and (3), results in the following for the perturbation velocity potential, the perturbation pressure, and the attached and separated flow unsteady boundary conditions.

$$\beta^2 \frac{\partial^2 \bar{\phi}}{\partial x^2} + \frac{\partial^2 \bar{\phi}}{\partial y^2} - 2ikM_{\infty}^2 \frac{\partial \bar{\phi}}{\partial x} + k^2 M_{\infty}^2 \bar{\phi} = 0, \quad \bar{p} = -\frac{\rho_{\infty} U_{\infty}}{C} \left(ik + \frac{\partial}{\partial x} \right) \bar{\phi} \quad (5,6)$$

$$\bar{v} = U_{\infty} \{ \bar{q} + \bar{\alpha}(1 + ik(x - x_{se})) \} \quad \text{at } y = 0^{\pm}, \quad 0 \leq x \leq x_s, \quad \bar{p} = -\frac{1}{2}\rho_{\infty} U_{\infty}^2 \bar{\gamma} \quad \text{at } y = 0^+, \quad x > x_s, \quad (7,8)$$

where

$$M_{\infty} = \frac{U_{\infty}}{a_{\infty}}; \quad \beta^2 = 1 - M_{\infty}^2; \quad k = \frac{\omega C}{U_{\infty}} \quad \text{and} \quad \bar{q} = ik\bar{y}_b.$$

Once Eq. (5) is solved, Eq. (6) is used to compute the unsteady pressure difference across the airfoil. This is then integrated to obtain the unsteady aerodynamic lift and moment acting on the airfoil.

3 Fourier transforms

Equation (5) for the perturbation velocity potential is reduced to an ordinary differential equation by use of Fourier transforms, with the Fourier transform pair defined in Eq. (9).

$$FT[g(x)] = g^*(v) = \int_{-\infty}^{+\infty} g(x) \exp(-ivx) dx \quad \text{and} \quad g(x) = \frac{1}{2\pi} \int_{-\infty}^{+\infty} g^*(v) \exp(ivx) dv. \quad (9)$$

Applying the Fourier transform technique and assuming that all flow perturbations remain bounded in the far field leads to the following ordinary differential equations for the transformed perturbation velocity potential and pressure.

$$\frac{d^2 \bar{\phi}^*}{dy^2} + \mu^2 \bar{\phi}^* = 0, \quad \bar{p}^*(v, y) = -\frac{i\rho_{\infty} U_{\infty}}{C} \{k + v\} \bar{\phi}^*(v, y) \quad (10,11)$$

where $\mu^2 = -\beta^2 v^2 + 2kM_{\infty}^2 v + k^2 M_{\infty}^2$.

The general solution to Eq. (10) for the perturbation velocity potential is given in Eq. (12).

$$\bar{\phi}^* = A_1 \sin(\mu y) + A_2 \cos(\mu y) \quad (12)$$

The constants A_1 and A_2 are evaluated from the normal velocity boundary conditions on two adjacent airfoils. The time dependent perturbations at $(x+d, y+h)$ are taken to lead the same perturbations at (x, y) by the constant interblade phase angle σ .

The transformed boundary conditions on the upper surface of the zeroth airfoil and the lower surface of the first airfoil of Fig. 1 are given in Eqs. (13).

$$\left. \frac{\partial \bar{\phi}^*}{\partial y} \right|_{y=0^+} = C \bar{v}^*(v)|_{y=0^+} = C \bar{v}_+^*, \quad \left. \frac{\partial \bar{\phi}^*}{\partial y} \right|_{y=h^-} = C \exp(i(\sigma - vd)) \bar{v}^*(v)|_{y=h^-} = C \exp(i(\sigma - vd)) \bar{v}_-^*. \quad (13a, b)$$

Equations (13) are used to solve for the constants A_1 and A_2 in Eq. (12) in terms of \bar{v}_+^* and \bar{v}_-^* . Recall that for attached flow, both \bar{v}_+^* and \bar{v}_-^* are known. However, in the separated flow region, \bar{v}_+^* is unknown. The resulting solution for $\bar{\phi}^*$ is given in Eq. (14).

$$\bar{\phi}^*(v, y) = \frac{C \bar{v}_+^* \sin(\mu y)}{\mu} + \frac{C(\bar{v}_-^* \cos(\mu h) - \bar{v}_-^* \exp(-i(vd - \sigma)) \cos(\mu y))}{\mu \sin(\mu h)}. \quad (14)$$

This expression for $\bar{\phi}^*$ is used in the unsteady pressure equation, Eq. (11), with the following definitions useful

$$\bar{p}_+^* \equiv \bar{p}^*|_{y=0^+}, \quad \bar{p}_-^* \equiv \bar{p}^*|_{y=0^-}, \quad \bar{\phi}_+^* \equiv \bar{\phi}^*|_{y=0^+}, \quad \bar{\phi}_-^* \equiv \bar{\phi}^*|_{y=0^-}. \quad (15a, b)$$

Evaluating Eq. (11) at $y=0^+$ and 0^- and then using Eq. (14), the unsteady pressure on the upper and lower surfaces of the zeroth airfoil is determined

$$\frac{\bar{p}_+^*}{\rho_\infty U_\infty^2} = A^* \frac{\bar{v}_+^*}{U_\infty} - B^* \frac{\bar{v}_-^*}{U_\infty}, \quad \frac{\bar{p}_-^*}{\rho_\infty U_\infty^2} = C^* \frac{\bar{v}_+^*}{U_\infty} - A^* \frac{\bar{v}_-^*}{U_\infty}, \quad (16a, b)$$

where

$$A^* = \frac{(k+v) \cos(\mu h)}{i\mu \sin(\mu h)} = \frac{(k+v) \cot(\mu h)}{i\mu},$$

$$B^* = \frac{(k+v) \exp(-i(vd - \sigma))}{i\mu \sin(\mu h)} \quad \text{and} \quad C^* = \frac{(k+v) \exp(i(vd - \sigma))}{i\mu \sin(\mu h)}.$$

Equation (16) is used to obtain independent equations for the upwash difference coefficient and the unsteady pressure difference correction coefficient. First Eq. (20) is rewritten as follows:

$$\frac{\bar{p}^{*AVE}}{\rho_\infty U_\infty^2} + \frac{1}{2} \frac{\Delta \bar{p}^*}{\rho_\infty U_\infty^2} = (A^* - B^*) \frac{\bar{v}^{*AVE}}{U_\infty} + \frac{1}{2} (A^* + B^*) \frac{\Delta \bar{v}^*}{U_\infty},$$

$$\frac{\bar{p}^{*AVE}}{\rho_\infty U_\infty^2} - \frac{1}{2} \frac{\Delta \bar{p}^*}{\rho_\infty U_\infty^2} = (A^* - C^*) \frac{\bar{v}^{*AVE}}{U_\infty} + \frac{1}{2} (A^* + C^*) \frac{\Delta \bar{v}^*}{U_\infty}. \quad (17a, b)$$

Subtracting Eq. (17b) from Eq. (17a) and manipulating the results leads to Eq. (18)

$$\frac{\bar{v}^{*AVE}}{U_\infty} = K^* \frac{\Delta \bar{p}^*}{\rho_\infty U_\infty^2} + L^* \frac{\Delta \bar{v}^*}{U_\infty}, \quad (18)$$

where

$$K^* = \frac{1}{2A^* - B^* - C^*} \quad \text{and} \quad L^* = \frac{(C^* - B^*)}{2(2A^* - B^* - C^*)}.$$

Equation (17a) is then multiplied by $(A^* - C^*)$ and Eq. (17b) by $(A^* - B^*)$, with the resulting equations added. This gives the following

$$\frac{\bar{p}^{*AVE}}{\rho_\infty U_\infty^2} = L^* \frac{\Delta \bar{p}^*}{\rho_\infty U_\infty^2} + M^* \frac{\Delta \bar{v}^*}{U_\infty}, \quad \text{where} \quad M^* = \frac{A^{*2} - B^* C^*}{2A^* - B^* - C^*}. \quad (19)$$

Chi (1980, 1985) performs the Fourier inversion of Eqs. (18) and (19) and further manipulates the result to obtain integral equations for $\frac{\Delta \bar{v}(x)}{U_\infty}$ and $\frac{\Delta \bar{p}^{COR}(x)}{\rho_\infty U_\infty^2}$.

However, by further manipulating Eqs. (18) and (19), independent equations may be derived for the upwash difference coefficient and the unsteady pressure difference correction coefficient. First, substitute

$$\frac{\bar{v}^{*AVE}}{U_\infty} = \frac{\bar{v}_-^*}{U_\infty} + \frac{1}{2} \frac{\Delta \bar{v}^*}{U_\infty} \quad \text{and} \quad \frac{\Delta \bar{p}^*}{\rho_\infty U_\infty^2} = \frac{\Delta \bar{p}^{*ATT}}{\rho_\infty U_\infty^2} + \frac{\Delta \bar{p}^{*COR}}{\rho_\infty U_\infty^2}$$

into Eq. (18). The result is:

$$\frac{\bar{v}_-^*}{U_\infty} + \frac{1}{2} \frac{\Delta \bar{v}^*}{U_\infty} = K^* \frac{\Delta \bar{p}^{*ATT}}{\rho_\infty U_\infty^2} + K^* \frac{\Delta \bar{p}^{*COR}}{\rho_\infty U_\infty^2} + L^* \frac{\Delta \bar{v}^*}{U_\infty} \quad (20)$$

In the attached flow region of the airfoil, Eq. (21) is valid, with the only unknown being the attached flow unsteady pressure difference

$$\frac{\bar{v}_-^*}{U_\infty} = K^* \frac{\Delta \bar{p}^{*ATT}}{\rho_\infty U_\infty^2} \quad (21)$$

An equation for the separated flow unsteady pressure difference correction coefficient is obtained by subtracting Eq. (21) from Eq. (20)

$$\frac{\Delta \bar{p}^{*COR}}{\rho_\infty U_\infty^2} = (A^* - C^*) \frac{\Delta \bar{v}^*}{U_\infty} \quad (22)$$

In this equation, both the unsteady pressure difference correction coefficient and the upwash difference coefficient are unknown. Therefore, another equation is needed.

Rewriting Eq. (19) yields the following

$$\frac{\bar{p}_+^*}{\rho_\infty U_\infty^2} - \left(L^* + \frac{1}{2} \right) \frac{\Delta \bar{p}^{*ATT}}{\rho_\infty U_\infty^2} = \left(L^* + \frac{1}{2} \right) \frac{\Delta \bar{p}^{*COR}}{\rho_\infty U_\infty^2} + M^* \frac{\Delta \bar{v}^*}{U_\infty} \quad (23)$$

Equation (22) is solved for $\Delta \bar{v}^*/U_\infty$ which is then substituted into Eq. (23). The resulting equation leads to the following independent equation for the unsteady pressure difference correction coefficient

$$K^* \frac{\Delta \bar{p}^{*COR}}{\rho_\infty U_\infty^2} = \left(T^* - \frac{1}{2} \hat{K}_c^* \right) \frac{\Delta \bar{p}^{*ATT}}{\rho_\infty U_\infty^2} + (\hat{K}_c^* - Q^*) \frac{\bar{p}_+^*}{\rho_\infty U_\infty^2} \quad (24)$$

where

$$T^* = \frac{L^{*2}}{A^*}; \quad Q^* = \frac{L^*}{A^*}; \quad \text{and} \quad K_c^* = \frac{1}{2A^*}$$

An equation for $\Delta \bar{v}^*/U_\infty$ is obtained by substituting Eq. (22) into Eq. (19)

$$\frac{\Delta \bar{v}^*}{U_\infty} = -(Q^* + \hat{K}_c^*) \frac{\Delta \bar{p}^{*ATT}}{\rho_\infty U_\infty^2} + 2\hat{K}_c^* \frac{\bar{p}_+^*}{\rho_\infty U_\infty^2} \quad (25)$$

The Fourier inversion may now be performed for both the attached flow solution, Eq. (21), and the separated flow correction, Eqs. (24) and (25).

The Fourier inversion for the attached flow, Eq. (21), noting that $\frac{\Delta \bar{p}^{*ATT}(\zeta)}{\rho_\infty U_\infty^2} = 0$ off of the airfoil, is given in Eq. (26),

$$\frac{\bar{v}_-(x)}{U_\infty} = \int_0^1 K(x-\zeta) \frac{\Delta \bar{p}^{*ATT}(\zeta)}{\rho_\infty U_\infty^2} d\zeta; \quad \text{where} \quad K(\eta) = \frac{1}{2\pi} \int_{-\infty}^{+\infty} K^* \exp(i\eta v) dv \quad (26)$$

Note that this is the same attached flow equation as obtained by Smith (1972) when differences in notation are taken into account.

The Fourier inversion of the separated flow equation is:

$$\int_{LL}^{+\infty} K(x-\zeta) \frac{\Delta\bar{p}^{COR}(\zeta)}{\rho_{\infty} U_{\infty}^2} d\zeta = \int_{LL}^{+\infty} \left\{ T(x-\zeta) - \frac{1}{2} \hat{K}_c(x-\zeta) \right\} \frac{\Delta\bar{p}^{ATT}(\zeta)}{\rho_{\infty} U_{\infty}^2} d\zeta + \int_{LL}^{+\infty} \left\{ \hat{K}_c(x-\zeta) - Q(x-\zeta) \right\} \frac{\bar{p}_+(\zeta)}{\rho_{\infty} U_{\infty}^2} d\zeta, \quad (27)$$

where

$$T(\eta) = \frac{1}{2\pi} \int_{-\infty}^{+\infty} T^* \exp(i\nu\eta) d\nu, \quad Q(\eta) = \frac{1}{2\pi} \int_{-\infty}^{+\infty} Q^* \exp(i\nu\eta) d\nu, \quad \hat{K}_c(\eta) = \frac{1}{2\pi} \int_{-\infty}^{+\infty} \hat{K}_c^* \exp(i\nu\eta) d\nu.$$

LL = Lower Limit (to be determined) and $T(\eta)$, $Q(\eta)$ and $\hat{K}_c(\eta)$ are evaluated in the Appendices.

The inverse transform of the upwash differences, Eq. (25), is

$$\frac{\Delta\bar{p}(x)}{U_{\infty}} = - \int_{x_s}^1 \left\{ Q(x-\zeta) + \hat{K}_c(x-\zeta) \right\} \frac{\Delta\bar{p}^{ATT}(\zeta)}{\rho_{\infty} U_{\infty}^2} d\zeta - R(x), \quad (28)$$

where $R(x) = \int_{x_s}^{+\infty} \hat{K}_c(x-\zeta) \bar{p}_+ d\zeta$ and is presented in the appendix.

The cascade unsteady pressure difference correction equation becomes

$$\int_{x_s}^{+\infty} K(x-\zeta) \frac{\Delta\bar{p}^{COR}(\zeta)}{\rho_{\infty} U_{\infty}^2} d\zeta = \int_{x_s}^1 \left\{ T(x-\zeta) - \frac{1}{2} \hat{K}_c(x-\zeta) \right\} \frac{\Delta\bar{p}^{ATT}(\zeta)}{\rho_{\infty} U_{\infty}^2} d\zeta - \frac{1}{2} \int_{x_s}^{\infty} \left\{ \hat{K}_c(x-\zeta) - Q(x-\zeta) \right\} \bar{p}_+ d\zeta. \quad (29)$$

The upper limits of $+\infty$ are undesirable since $\Delta\bar{p}^{COR}(\zeta)/\rho_{\infty} U_{\infty}^2$ will be obtained by collocation. To eliminate this problem, this equation is rewritten by breaking the first and third integrals into integrals from $\zeta = x_s$ to $\zeta = 1$ and from $\zeta = 1$ to $\zeta = +\infty$

$$\int_{x_s}^1 K(x-\zeta) \frac{\Delta\bar{p}^{COR}(\zeta)}{\rho_{\infty} U_{\infty}^2} d\zeta + \int_1^{+\infty} K(x-\zeta) \frac{\Delta\bar{p}^{COR}(\zeta)}{\rho_{\infty} U_{\infty}^2} d\zeta = \int_{x_s}^1 \left\{ T(x-\zeta) - \frac{1}{2} \hat{K}_c(x-\zeta) \right\} \frac{\Delta\bar{p}^{ATT}(\zeta)}{\rho_{\infty} U_{\infty}^2} d\zeta - \frac{1}{2} \int_{x_s}^1 \left\{ \hat{K}_c(x-\zeta) - Q(x-\zeta) \right\} \bar{p}_+ d\zeta - \frac{1}{2} \int_1^{\infty} \left\{ \hat{K}_c(x-\zeta) - Q(x-\zeta) \right\} \bar{p}_+ d\zeta. \quad (30)$$

As $x_s \rightarrow 1$, the integrals with upper limit of 1 become zero. Then

$$\int_1^{+\infty} K(x-\zeta) \frac{\Delta\bar{p}^{COR}(\zeta)}{\rho_{\infty} U_{\infty}^2} d\zeta = - \frac{1}{2} \int_1^{+\infty} \left\{ \hat{K}_c(x-\zeta) - Q(x-\zeta) \right\} \bar{p}_+ d\zeta.$$

Since both of these integrals are independent of x_s , they must be equal for all x_s . Subtracting these from Eq. (30), the final cascade separated flow unsteady pressure difference correction equation is obtained

$$W(x) = \int_{x_s}^1 K(x-\zeta) \frac{\Delta\bar{p}^{COR}(\zeta)}{\rho_{\infty} U_{\infty}^2} d\zeta, \quad (31)$$

where

$$W(x) = \int_{x_s}^1 \left\{ T(x-\zeta) - \frac{1}{2} \hat{K}_c(x-\zeta) \right\} \frac{\Delta\bar{p}^{ATT}(\zeta)}{\rho_{\infty} U_{\infty}^2} d\zeta - \frac{1}{2} \int_{x_s}^1 \left\{ \hat{K}_c(x-\zeta) - Q(x-\zeta) \right\} \bar{p}_+ d\zeta.$$

Once the attached flow solution is determined from Eq. (26) and the cavitation number specified, Eq. (31) is solved by collocation to obtain the separated flow unsteady pressure difference correction coefficient.

4 Unsteady aerodynamic lift and moment coefficients

The unsteady lift coefficient, positive in the $+y$ direction, is defined as

$$\bar{C}_L = \frac{\bar{L}}{\rho_{\infty} U_{\infty}^2 C} = - \int_0^1 \frac{\Delta \bar{p}(\zeta)}{\rho_{\infty} U_{\infty}^2} d\zeta. \quad (35)$$

Substituting Eq. (36) into Eq. (35) and noting that the unsteady pressure difference correction is zero upstream of the separation point, leads to Eq. (37):

$$\frac{\Delta \bar{p}(\zeta)}{\rho_{\infty} U_{\infty}^2} = \frac{\Delta \bar{p}^{ATT}(\zeta)}{\rho_{\infty} U_{\infty}^2} + \frac{\Delta \bar{p}^{COR}(\zeta)}{\rho_{\infty} U_{\infty}^2} \quad (36)$$

$$\bar{C}_L^{SEP} = \bar{C}_L^{ATT} + \bar{C}_L^{COR}, \quad \text{where} \quad \bar{C}_L^{ATT} = - \int_0^1 \frac{\Delta \bar{p}^{ATT}(\zeta)}{\rho_{\infty} U_{\infty}^2} d\zeta \quad \text{and} \quad \bar{C}_L^{COR} = - \int_{x_s}^1 \frac{\Delta \bar{p}^{COR}(\zeta)}{\rho_{\infty} U_{\infty}^2} d\zeta. \quad (37)$$

The unsteady moment coefficient, positive counterclockwise about an elastic axis at the leading edge, is defined as

$$\bar{C}_M = \frac{\bar{M}}{\rho_{\infty} U_{\infty}^2 C^2} = - \int_0^1 \zeta \frac{\Delta \bar{p}(\zeta)}{\rho_{\infty} U_{\infty}^2} d\zeta. \quad (38)$$

Substituting Eq. (36) into Eq. (38) yields:

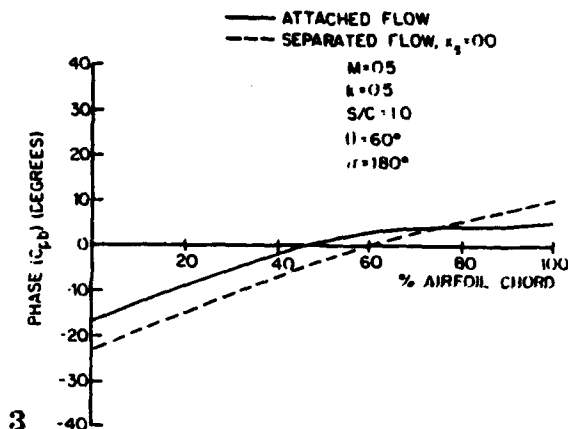
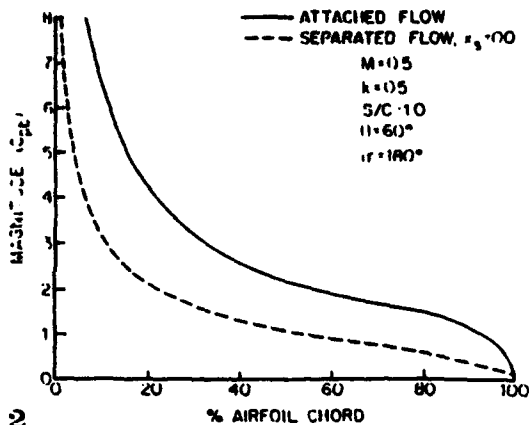
$$\bar{C}_M^{SEP} = \bar{C}_M^{ATT} + \bar{C}_M^{COR}, \quad \text{where} \quad \bar{C}_M^{ATT} = - \int_0^1 \zeta \frac{\Delta \bar{p}^{ATT}(\zeta)}{\rho_{\infty} U_{\infty}^2} d\zeta \quad \text{and} \quad \bar{C}_M^{COR} = - \int_{x_s}^1 \zeta \frac{\Delta \bar{p}^{COR}(\zeta)}{\rho_{\infty} U_{\infty}^2} d\zeta. \quad (39)$$

5 Results

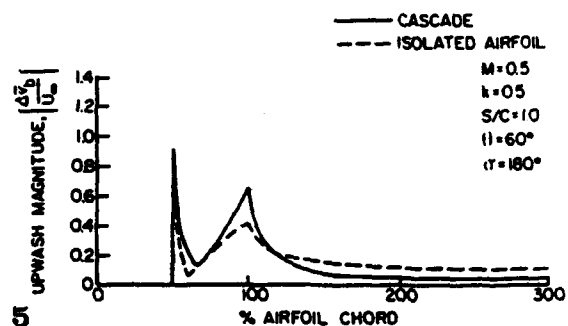
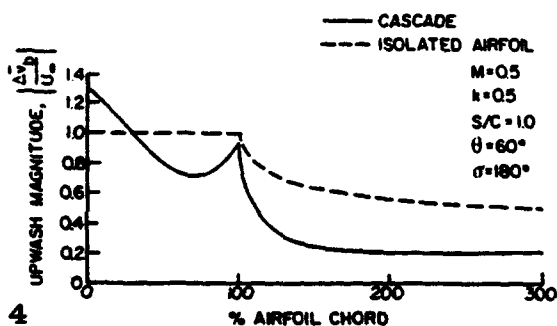
The mathematical model developed herein is utilized to demonstrate the effects of flow separation on the unsteady aerodynamics of an harmonically oscillating flat plate cascade in a subsonic flow field. The attached flow part of the model predictions are obtained from the Smith code (1987). It predicts the unsteady pressure difference coefficient and the cascade translation and torsion mode unsteady aerodynamic lift and moment coefficients. The separated flow part of the model uses the attached flow results to analyze the separated flow unsteady pressure difference correction coefficient, the unsteady aerodynamic lift and moment correction coefficients, and the upwash difference coefficient for a specified separation point location and cavitation number. Note that for the results presented herein, a zero cavitation number is considered. The separated flow unsteady aerodynamic lift and moment coefficients are then added to the attached flow values to obtain the separated flow coefficients.

The effect of flow separation on the magnitude and phase of the cascade bending mode unsteady pressure difference coefficient is shown in Figs. 2 and 3. A leading edge flow separation point decreases the magnitude of C_{pb} by a factor of approximately two. Also, the attached and separated flow phase angles of C_{pb} are not equal.

Figure 4 shows the magnitude of the bending mode upwash difference coefficient with leading edge flow separation for an isolated airfoil and an airfoil cascade. Recall that the upwash difference coefficient is zero for attached flow. Note that the upwash difference coefficient is not zero downstream of the trailing edge for either the isolated airfoil or the cascade, as was assumed by Chi (1980, 1985). The fact that a nonzero constant value is approached downstream of the trailing



Figs. 2 and 3. 2 Magnitude of bending mode unsteady pressure difference coefficient for attached flow and leading edge separation. 3 Phase angle of bending mode unsteady pressure difference coefficient for attached flow and leading edge separation



Figs. 4 and 5. Magnitude of bending mode upwash difference coefficient 4 for leading edge flow separation; 5 for midchord flow separation

edge is consistent with the assumption that the separation wake extends to downstream infinity. Midchord flow separation, Fig. 5, tends to produce a more rapidly changing upwash difference coefficient magnitude than does leading edge separation. Again, the upwash difference coefficient does not become zero downstream of the trailing edge. Also, the separated flow upwash difference magnitude for both the isolated airfoil and the cascade exhibit a sharp dip near 60% chord. Both the real and imaginary parts of the upwash difference coefficient are smooth in the region of 60% airfoil chord, with this dip being caused by the real part of the coefficient passing through zero at this point.

The effects of leading edge flow separation on the bending mode suction surface upwash velocity distribution are shown in Figs. 6 and 7 for an isolated airfoil and an airfoil cascade. The attached flow results are the same for both the isolated airfoil and the cascade since both upwash velocities are equal to the airfoil surface velocity. The cascading effects are shown by the differences between the isolated airfoil and cascade separated flow upwash distributions. In Fig. 7 the separated flow curve for the isolated airfoil is identical to the attached flow curve.

To demonstrate the effects of flow separation on bending mode stability, the complex unsteady lift coefficients are calculated using ten collocation points for a cascade with solidity of one and a stagger angle of 60 degrees. In particular, Figs. 8 through 13 show the attached flow, midchord flow separation, and leading edge flow separation complex bending mode lift coefficients for inlet Mach numbers of 0.0 and 0.5, with interblade phase angle and reduced frequency as parameters. It should be noted that the Mach 0.5 unsteady lift coefficients change rapidly near the acoustic resonance conditions. Thus a smaller range of interblade phase angle values is considered for Mach

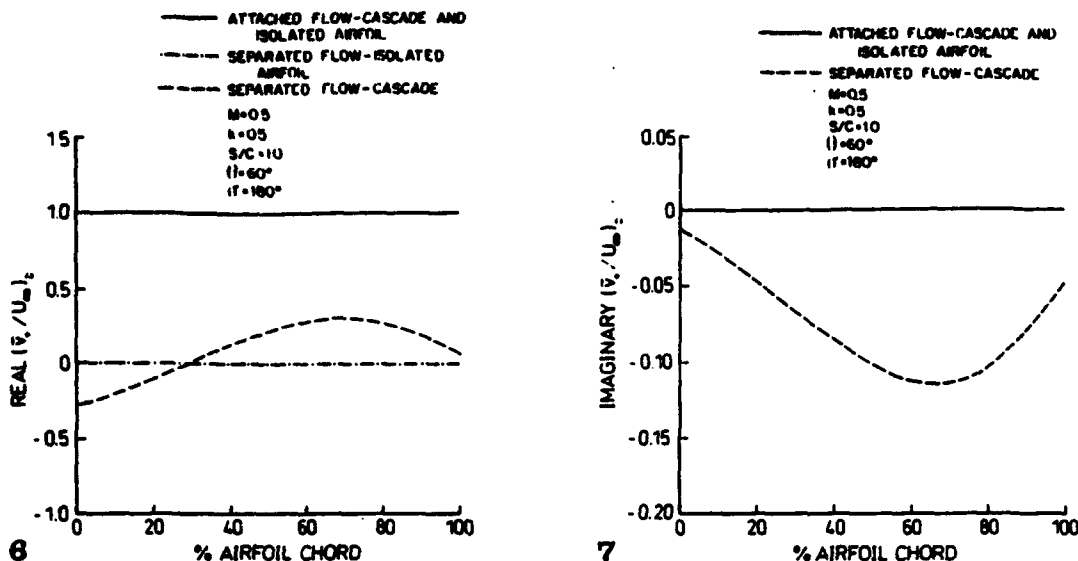


Fig. 6 and 7. 6 Real part of bending mode suction surface upwash velocity for attached flow and leading edge separation. 7 Imaginary part of bending mode suction surface upwash velocity for attached flow and leading edge separation

0.5 than for Mach 0.0 to avoid these resonances. Also, a positive value of the real part of \bar{C}_{Lz} indicates a bending mode instability when there is no mechanical damping.

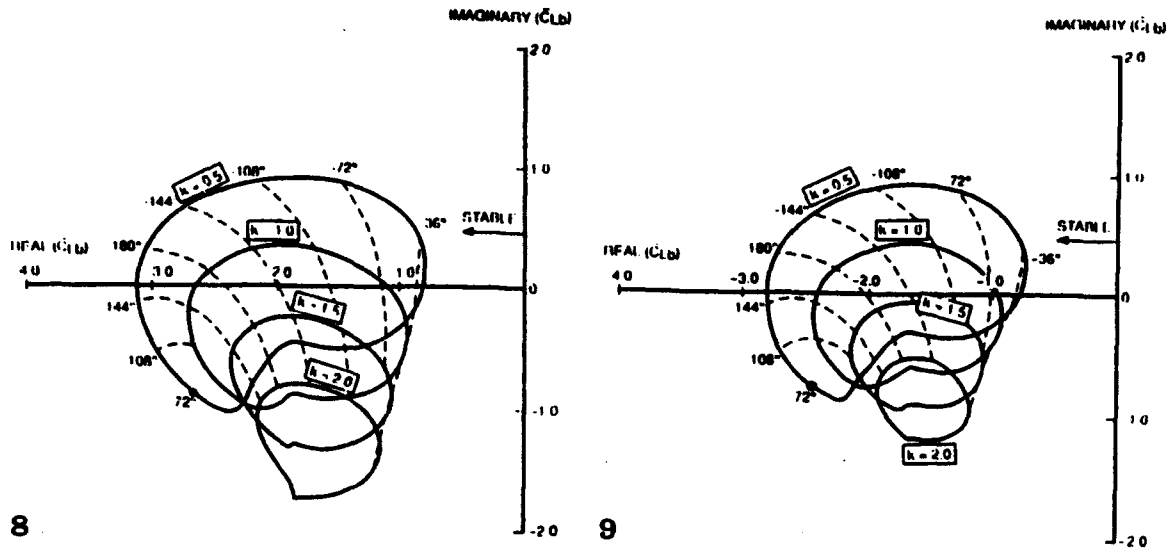
With attached flow, the cascade is stable for all interblade phase angles and reduced frequencies for both values of the inlet Mach number. As the region of flow separation increases, i.e., as the separation point moves from the midchord to the leading edge, the unsteady lift coefficient reduced frequency contours decrease in size and shift to the right, although remaining in the stable range. Thus, flow separation, although not resulting in bending mode flutter, does decrease the bending mode stability of the cascade.

For the case of torsional flutter, stability is determined from the imaginary part of the unsteady moment coefficient. In particular, for zero mechanical damping, a torsion mode instability exists whenever $\text{Imaginary } (\bar{C}_{Mz}) \geq 0.0$, with the flutter reduced frequency defined as the value at which $\text{Imaginary } (\bar{C}_{Mz}) = 0.0$. To demonstrate the effects of flow separation on torsion mode stability, a baseline cascade with a solidity of one and a stagger angle of 60 degrees is considered.

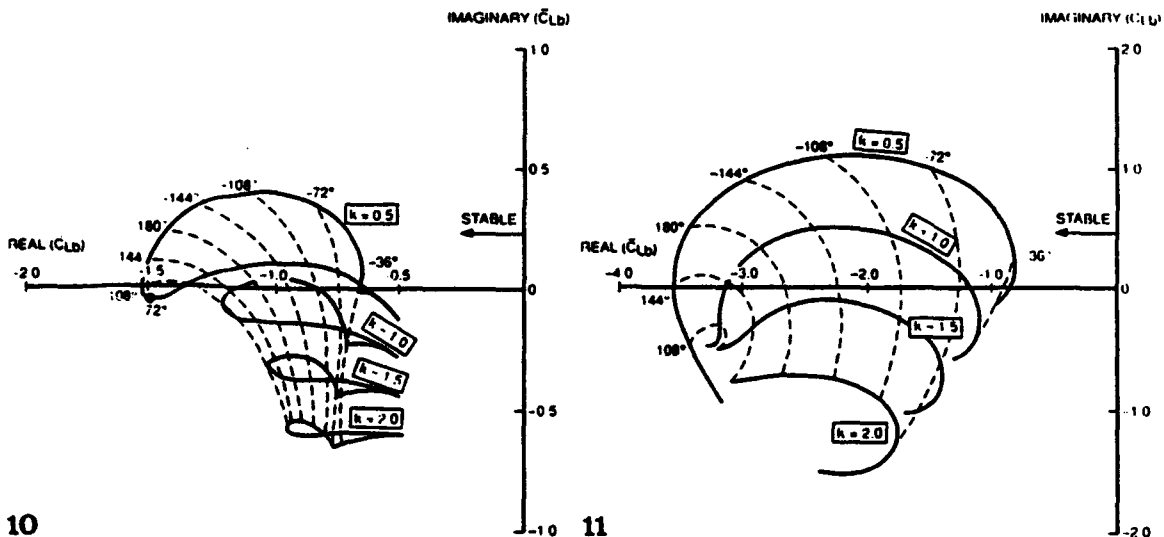
The baseline cascade with attached flow is unstable for certain interblade phase angle values and elastic axis locations. The flutter boundary interblade phase angle, i.e., the interblade phase angle which yields the largest range of reduced frequencies for which flutter is possible is shown as a function of elastic axis location in Fig. 14 for inlet Mach numbers of 0.0, 0.3, and 0.8. Utilizing these interblade phase angle values, Fig. 15 shows the attached flow flutter boundaries of the baseline cascade in the form of reduced frequency for flutter as a function of elastic axis location, with Mach number as a parameter. Each curve represents the neutral stability boundary, with the airfoils being unstable at reduced frequencies below the curve and stable for reduced frequencies above the curve. Note that a decreasing flutter reduced frequency corresponds to an increasing value of U_∞ for which flutter is just possible. Increasing the Mach number is seen to enhance the cascade stability, indicated by the decreased unstable reduced frequency range.

The effects of flow separation on torsional flutter are demonstrated by determining the flutter boundaries of the baseline cascade with attached flow and with flow separation at midchord, 10% chord, and at the leading edge. These results, generated by varying the reduced frequency and utilizing the previously determined attached flow flutter boundary interblade phase angle values, are presented in the form of torsional flutter boundary versus elastic axis location for inlet Mach numbers of 0.0, 0.3, and 0.8, with separation point location as a parameter, Figs. 16 through 18.

Torsion mode stability is seen to be a function of the location of both the separation point and the elastic axis. Midchord flow separation produces a larger range of frequencies for which flutter



Figs. 8 and 9. Bending mode unsteady lift coefficient 8 for attached flow; 9 for midchord flow separation. ($S/C = 1.0$, $\theta = 60$ degrees, and $M = 0.0$)

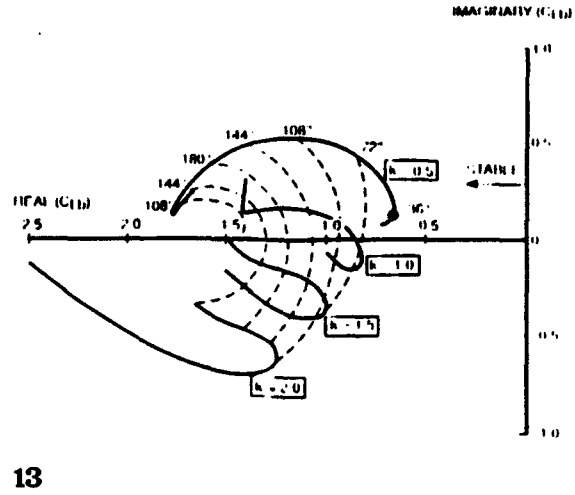
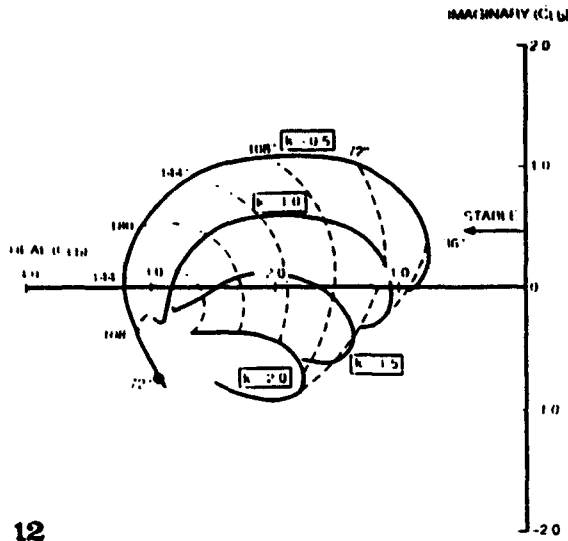


Figs. 10 and 11. Bending mode unsteady lift coefficient 10 for leading edge flow separation ($S/C = 1.0$, $\theta = 60$ degrees, and $M = 0.0$); 11 for attached flow ($S/C = 1.0$, $\theta = 60$ degrees, and $M = 0.5$)

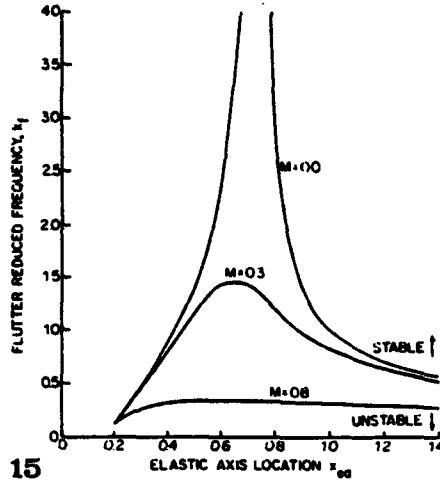
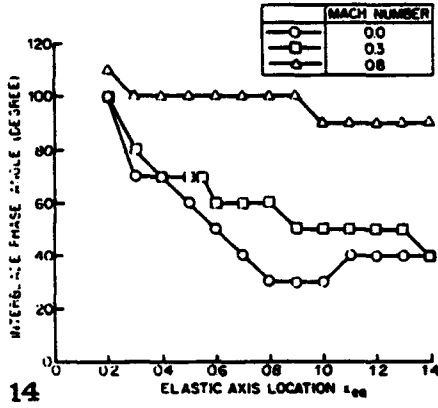
may occur than does attached flow for elastic axis locations in the range of 20% to about 65% chord for all Mach numbers. This indicates decreased cascade stability for these elastic axis locations. For elastic axis locations aft of about 65% chord, midchord flow separation tends to have a stabilizing effect for all Mach numbers.

Flow separation at 10% airfoil chord has a destabilizing effect for elastic axis locations from 20% to about 40% chord, and a stabilizing effect for elastic axis locations greater than about 40% chord.

Leading edge flow separation has a stabilizing effect for all elastic axis locations. It should be noted that a considerable part of the torsional unsteady moment coefficient value is derived from the singular nature of the unsteady pressure distribution in the airfoil leading edge region. For the cases of flow separation of 10% and 50% chord, the unsteady pressure distribution is unaffected



Figs. 12 and 13. Bending mode unsteady lift coefficient 12 for midchord flow separation, 13 for leading edge separation. ($S/C = 1.0$, $\theta = 60$ degrees, and $M = 0.5$)

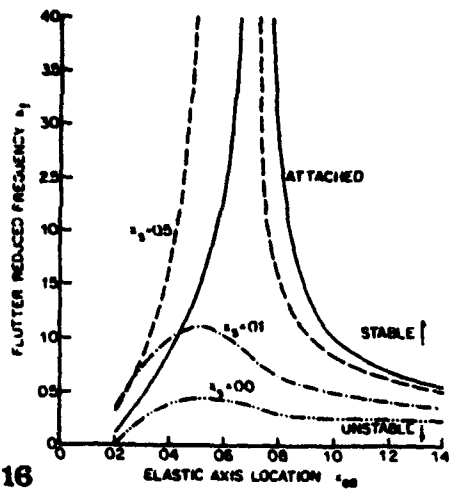


Figs. 14 and 15. 14 Interblade phase angles for torsional flutter boundary, 15 torsional flutter boundary for attached flow. ($S/C = 1.0$ and $\theta = 60$ degrees)

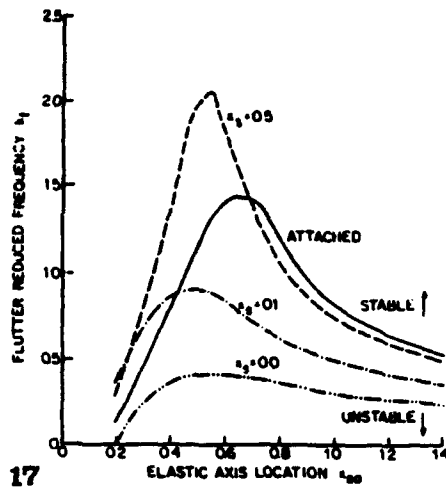
by the flow separation in the region near the leading edge, whereas for leading edge flow separation the entire unsteady pressure distribution is affected.

As for the attached flow flutter boundaries, increasing the Mach number enhances the separated flow cascade stability, indicated by the decreased unstable reduced frequency range.

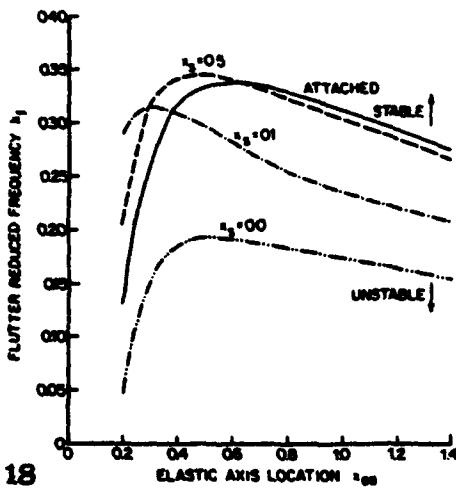
It is generally expected that flow separation would decrease the torsion mode cascade stability. As previously stated, the results obtained from the separated flow analysis developed herein indicate that the stability is a function of both the separation point and the elastic axis. However, it should be noted that this analysis is based on quite restrictive assumptions. A zero mean incidence angle is considered, thereby eliminating the nonlinear features of the attached and separated flow fields. Also, the separation point location is fixed throughout the cycle of airfoil oscillation. In reality, the flow may separate and reattach during each cycle of airfoil motion



16

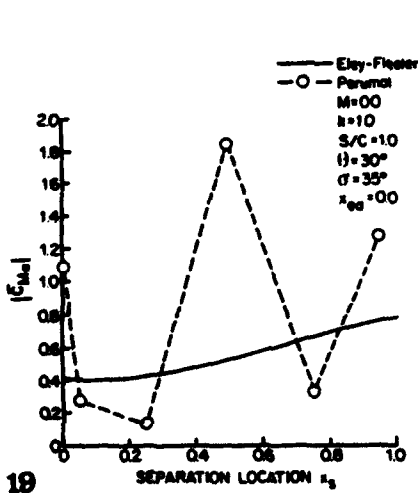


17

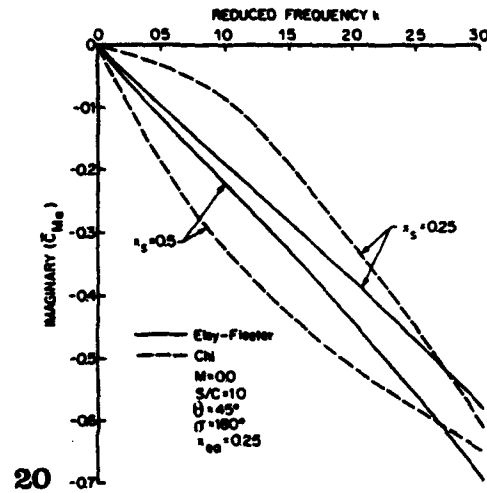


18

Figs. 16-18. Torsional flutter boundary for separated flow. ($S/C = 1.0$, $\theta = 60$ degrees, and $M = 0.0$; 17 $M = 0.3$; 18 $M = 0.8$)



19



20

Figs. 19 and 20. 19 Torsion mode unsteady moment coefficient magnitude, comparison to Perumat. 20 Imaginary torsional mode unsteady moment coefficient, comparison to Chi

creating hysteresis effects in the torsional unsteady moment coefficient. Finally, the separation region may be large and partially block the flow passage, thereby affecting the flow field upstream of the separation point. If these restrictions were removed from the model, it might be found that flow separation tends to always decrease cascade stability.

Finally, comparisons of the results obtained with the model developed herein and those developed by Perumal (1975) and Chi (1980, 1985) are considered for an airfoil cascade executing harmonic torsion mode oscillations in an incompressible flow. The comparison with the Perumal model predictions of the magnitude of the unsteady moment coefficient versus separation point location are shown in Fig. 19. The analysis developed herein predicts a smoothly varying moment coefficient with separation point location, as expected based on the model assumptions. In contrast, the Perumal model yields widely varying and probably unrealistic results. Fig. 20 shows a comparison of the results obtained with the model developed herein and that of Chi with flow separation at 25% and 50% airfoil chord. The Chi model predicts larger changes in the imaginary part of the moment coefficient as the separation point location is moved from 25% to 50% airfoil chord than does the present analysis.

6 Summary and conclusions

A mathematical model was developed to predict the effect of flow separation on the unsteady aerodynamic lift and moment acting on two-dimensional flat plate airfoils and cascades which are harmonically oscillating in a subsonic flow field. The unsteady flow was considered to be a small perturbation to the uniform steady flow, with the steady flow assumed to separate at a specified fixed position on the suction surface of the airfoils. In this formulation, the difference in the upwash velocity across the airfoil in the separated flow region was not required to be determined before calculating the unsteady pressure difference across the chordline of the airfoils, thereby eliminating the assumption that the upwash difference is zero at the trailing edge when the steady flow is separated.

This model was then used to investigate the effect of flow separation on bending and torsion mode cascade stability. In the bending mode, the effects of airfoil leading edge and midchord flow separation on the unsteady aerodynamic lift coefficient for several reduced frequency and interblade phase angle values were considered for inlet Mach numbers of 0.0 and 0.5. In the torsion mode, the effects of airfoil leading edge, 10% and 50% chord flow separation on the cascade flutter boundary as a function of the elastic axis location were considered for inlet Mach numbers of 0.0, 0.3, and 0.8. These results demonstrated that although flow separation does decrease the bending mode stability, it does not result in flutter. In the torsion mode, however, flow separation can lead to flutter, with the cascade torsional stability being a function of both the location of the separation point and the elastic axis.

Acknowledgements

This research was sponsored, in part, by the Air Force Office of Scientific Research.

Appendix A

The functions $T(x)$, $Q(x)$ and $\hat{K}_c(x)$ are evaluated by the residue theorem of complex variables. These functions are given in Eqs. (A1) through (A3).

$$T(x) = \frac{\exp\left\{\frac{ikM^2 x}{\beta^2}\right\}}{4h} \left\{ \frac{(1 + \operatorname{sgn}(x))}{2} \Omega(x) + \operatorname{sgn}(x) \sum_{m=1}^{\infty} \Psi_m(x) + \operatorname{sgn}(x) \sum_{n=0, \pm 1, \pm 2, \dots} \Gamma_n(x) \right\} \quad (\text{A1})$$

$$Q(x) = -\frac{i \exp\left\{\frac{ikM_\infty^2 x}{\beta^2}\right\}}{2h} \left\{ \frac{(1 + \operatorname{sgn}(x))}{2} \Omega(x) + \operatorname{sgn}(x) \sum_{m=1}^{\infty} \Psi_m(x) + \operatorname{sgn}(x) \sum_{n=0, \pm 1, \pm 2, \dots} \Gamma_n(x) \right\} \quad (\text{A2})$$

$$\hat{K}_c(x) = -\frac{\exp\left\{\frac{ikM_\infty^2 x}{\beta^2}\right\}}{2h} \left\{ \frac{1 + \operatorname{sgn}(x)}{2} \Omega(x) + \operatorname{sgn}(x) \sum_{m=1}^{\infty} \Psi_m(x) \right\} \quad (\text{A3})$$

where

$$\Omega(x) = -\frac{hk \tanh(hk) \sin^2(z_0 d - \delta) e^{i z_0 x}}{\{\cosh(hk) - \cos(z_0 d - \delta)\}^2}, \quad \Psi_m(x) = \frac{(\mu_m h)^2 \tan^2(z_m d - \delta) e^{i z_m x}}{h^2 \beta^2 z_m \left(z_m + \frac{k}{\beta^2}\right)}$$

$$\Gamma_n(x) = \frac{\{(i\bar{\mu}_n h x + \Theta_n) \tan(\bar{\mu}_n h) + (2d + \Theta_n) \bar{\mu}_n h\} e^{i z_n x}}{(d - \Theta_n)^2 \left(\bar{z}_n + \frac{k}{\beta^2}\right)} - \frac{\bar{\mu}_n h g(\bar{z}_n) e^{i z_n x}}{(d - \Theta_n)^2 \left(\bar{z}_n + \frac{k}{\beta^2}\right)^2}$$

$$g(\bar{z}_n) = \left\{ \left(\bar{z}_n + \frac{k}{\beta^2}\right) \left((d^2 - \Theta_n^2) - \Lambda_n \tan(\bar{\mu}_n h) - \Theta_n (d - \Theta_n) \tan^2(\bar{\mu}_n h) \right) + (d - \Theta_n) \tan(\bar{\mu}_n h) \right\}$$

$$z_0 = -\frac{k}{\beta^2}, \quad \delta = \sigma - \frac{kM_\infty^2 d}{\beta^2}, \quad \mu_m h = \frac{(2m-1)\pi}{2}, \quad m=1, 2, 3, \dots, \quad z_m = \frac{i \operatorname{sgn}(x) P_m}{\beta h}, \quad m=1, 2, 3, \dots$$

$$P_m = \left\{ \left(\frac{(2m-1)\pi}{2} \right)^2 - \left(\frac{kM_\infty h}{\beta} \right)^2 \right\}^{1/2}, \quad \Theta_n = \frac{d\mu h}{dz} \Big|_{z=i_n}, \quad \Lambda_n = \frac{d^2\mu h}{dz^2} \Big|_{z=i_n}, \quad \bar{\mu}_n h = \bar{z}_n d + (2n\pi - \sigma),$$

$$n=0, \pm 1, \pm 2, \dots$$

Note that:

$$\hat{K}_c^* = \frac{1}{2A^*} \quad \text{and} \quad K^* = \frac{1}{2A^* - B^* - C^*} = \frac{1}{2A^* - (B^* + C^*)}$$

For zero stagger angle and ninety degree interblade phase angle: $(B^* + C^*) = 0$ so that $K^* = \hat{K}_c^*$. The function $\hat{K}_c(x)$ is found to give identical values, to six digits right of the decimal point, to Smith's function $K(x)$ evaluated at the special case just described.

Appendix B

The function $R(x)$ is obtained by evaluating Eq. (B1) by analytical integration, Eq. (B2).

$$R(x) = \int_{x_0}^{+\infty} \hat{K}_c(x - \zeta) \bar{y} d\zeta. \quad (\text{B1})$$

$$R(x) = \bar{y} \left[\sum_{m=1}^{\infty} \left\{ \frac{f_m}{a_m} + \frac{g_m}{b_m} (e^{\delta_m(x-x_0)} - 1) \right\} + \frac{i \tanh(hk)}{2} \{ e^{-ik(x-x_0)} - 1 \} \right], \quad (\text{B2})$$

where

$$f_m = -\frac{(\mu_m h)^2}{2h P_m \left(P_m + \frac{ikh}{\beta} \right)}$$

$$a_m = \left(\frac{P_m}{\beta h} + \frac{ikM_{\infty}^2}{\beta^2} \right), \quad y_m = -\frac{(\mu_m h)^2}{2hP_m \left(P_m - \frac{ihk}{\beta} \right)}, \quad h_m = \left(-\frac{P_m}{\beta h} + \frac{ikM_{\infty}^2}{\beta^2} \right),$$

$$P_m = \left\{ \left(\frac{(2m-1)\pi}{2} \right)^2 - \left(\frac{kM_{\infty} h}{\beta} \right)^2 \right\}^{1/2}; \quad \mu_m h = \frac{(2m-1)\pi}{2}, \quad m = 1, 2, 3, \dots$$

References

- Chi, M. R. (1980): Unsteady Aerodynamics in Stalled Cascade and Stall Flutter Prediction. ASME Paper 80-C2/Aero-1
- Chi, M. R. (1985): Separated Flow Unsteady Aerodynamic Theory. *J. Aircraft* 22/11, 956-964
- Fletcher, S. (1973): Fluctuating Lift and Moment Coefficients for Cascaded Airfoils in a Nonuniform Compressible Flow. *J. Aircraft* 10/2, 93-98
- Ni, R. H. (1979): A Rational Analysis of Periodic Flow Perturbation in Supersonic Two-Dimensional Cascade. ASME J. Eng. for Power. 101/3, 431-439
- Perumal, P. V. K. (1975): Thin Airfoil in Eddy Array and Part-Stalled Oscillating Cascade. Ph.D. Thesis, Stevens Inst. of Technol.
- Sisto, F. (1967): Linearized Theory of Nonstationary Cascades at Fully Stalled or Supercavitated Conditions. *ZAMM*, 47, 531-541
- Smith, S. N. (1972): Discrete Frequency Sound Generation in Axial Flow Turbomachines. ARCR & M 3709
- Whitehead, D. S. (1960): Force and Moment Coefficients for Vibrating Airfoils in Cascade. ARCR & M 3254
- Whitehead, D. S. (1987): Classical Two-Dimensional Methods. AGARD Manual in Aeroelasticity in Axial Flow Turbomachines. AGARD AG 298
- Woods, L. C. (1957): Aerodynamic Forces on an Oscillating Airfoil Fitted With a Spoiler. *Proc. Roy. Soc. London. Series A*, 239, 328-337

APPENDIX II

Rotor Blade Unsteady Aerodynamic Gust Response to Inlet Guide Vane Wakes

***ASME Journal of Turbomachinery*, Vol. 115, No. 1, January 1993, pp. 197-206**

Rotor Blade Unsteady Aerodynamic Gust Response to Inlet Guide Vane Wakes

S. R. Manwaring¹

S. Fleeter

Thermal Sciences and Propulsion Center,
School of Mechanical Engineering,
Purdue University,
West Lafayette, IN 47907

A series of experiments is performed in an extensively instrumented axial flow research compressor to investigate the fundamental flow physics of wake-generated periodic rotor blade row unsteady aerodynamics at realistic values of the reduced frequency. Unique unsteady data are obtained that describe the fundamental unsteady aerodynamic gust interaction phenomena on the first-stage rotor blades of a research axial flow compressor generated by the wakes from the inlet guide vanes. In these experiments, the effects of steady blade aerodynamic loading and the aerodynamic forcing function, including both the transverse and chordwise gust components, and the amplitude of the gusts, are investigated and quantified.

Introduction

Periodic aerodynamic excitations generate unsteady aerodynamic forces and moments on turbomachinery blading. At the resonance conditions where the aerodynamic excitation frequency matches a blade natural frequency, catastrophic vibrational responses of the blading may occur. In the design process, Campbell diagrams are utilized to predict the occurrence of the resonant conditions in the operating range of the blade row. Unfortunately, accurate predictions of the amplitude of the blade vibration at these resonances cannot currently be made due to the inability of mathematical models to predict the unsteady aerodynamics accurately, i.e., the aerodynamic forcing function to the blade row and the resulting unsteady aerodynamics acting on the blading. As a result, empirical correlations are currently used to indicate the blade row response to an excitation, with varying degrees of success.

On a first principles basis, forced response unsteady aerodynamics are analyzed by first defining the forcing function in terms of harmonics. The periodic response of an airfoil row to each harmonic is then assumed to be comprised of two components. One is due to the harmonic components of the unsteady aerodynamic forcing function being swept past the nonresponding airfoil row, termed the streamwise and transverse gust responses. The second, the self-induced unsteady aerodynamics, arises when a vibrational response of the airfoil row is generated.

The gust and motion-induced unsteady aerodynamic models involve many physical and numerical assumptions. Therefore, experimental modeling of the fundamental distortion and wake-generated blade row periodic unsteady aerodynamic response,

including both the forcing function and the resulting blade row unsteady aerodynamics, is needed for validation and enhancement of theoretical and numerical models.

Unsteady aerodynamic gust experiments of direct interest to turbomachines have been performed in low-speed research compressors. Fleeter et al. (1978, 1980) investigated the effects of airfoil camber and rotor-stator axial spacing on the unsteady aerodynamics of a stator vane row of a single-stage low-speed research compressor. Capece et al. (1986) and Capece and Fleeter (1987) performed measurements in a three-stage low-speed research compressor to investigate the effect of steady airfoil loading and detailed aerodynamic forcing function waveshape on the unsteady aerodynamic response of a stator vane row. Gallus et al. (1980) performed measurements at the midspan of a low camber vane of a single-stage axial flow compressor. The unsteady lift coefficients corresponding to the first five harmonics of rotor blade wake passing were measured with five transducers embedded in each vane surface.

Gust experiments performed in rotor blade rows include the following. With regard to inlet flow distortions, O'Brien et al. (1980) utilized six dynamic pressure transducers embedded on each rotor blade surface to measure the unsteady aerodynamic response to a distorted inlet flow field. However, the periodic rotor blade row inlet flow field was not measured and, thus, the unsteady aerodynamic gust forcing function was not quantified. Hardin et al. (1987) measured low reduced frequency oscillating airfoil aerodynamics on the rotor of a single-stage compressor and also stated that they performed similar distortion experiments, although the results were not presented.

Manwaring and Fleeter (1989, 1991) experimentally investigated the unsteady aerodynamic rotor blade row gust response generated by low reduced frequency inlet distortions and wake type disturbances. The major advantage of rotor-based unsteady gust experiments over stationary blade row experiments is that the unsteady aerodynamic forcing function is located in the stationary reference frame. This enables a

¹Current address: Engineer, Aerodynamics Research Laboratory, General Electric Aircraft Engines, Cincinnati, OH.

Contributed by the International Gas Turbine Institute and presented at the 36th International Gas Turbine and Aeroengine Congress and Exposition, Orlando, Florida, June 3-6, 1991. Manuscript received at ASME Headquarters February 20, 1991. Paper No. 91-GT-129. Associate Technical Editor: L. A. Riekert.

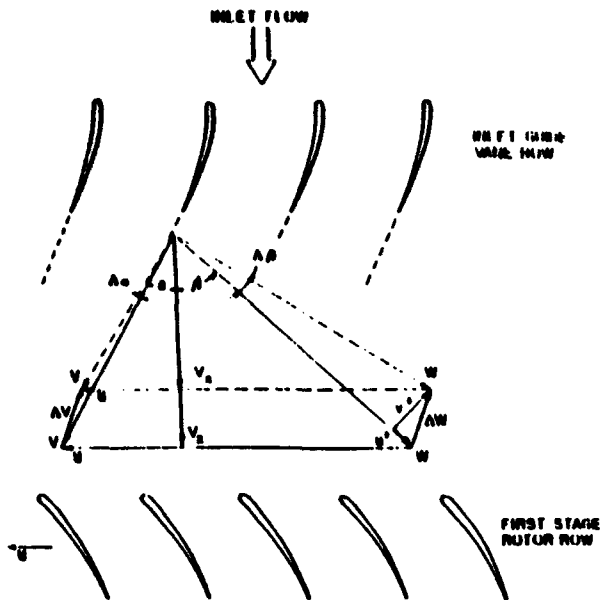


Fig. 1 Schematic of IGV wake-generated transverse and streamwise unsteady velocities, u^* and v^*

wide range of forcing function to be more easily generated, without large detrimental effects on compressor overall performance.

In this paper, the rotor blade row fundamental unsteady aerodynamic flow physics generated by period wakes are investigated at realistic values of the reduced frequency. In particular, the effects of the detailed unsteady aerodynamic forcing function, including both the transverse and chordwise gust components and the gust amplitude, as well as steady aerodynamic loading on the unsteady aerodynamic gust response of the first-stage rotor blade row, are investigated. This is accomplished by means of a series of experiments performed in an extensively instrumented axial flow research compressor. Unique unsteady aerodynamic data are obtained that describe both the detailed unsteady aerodynamic forcing function generated by the wakes from the IGVs and the resulting first-stage rotor blade row unsteady aerodynamic gust response.

In these experiments, the primary data obtained define the midspan chordwise distributions of both the steady and unsteady pressure on the rotor blade surfaces, with the aerodynamic forcing function generated in the stationary reference frame. These forcing functions are measured with a rotating cross hot-wire probe, with these data then analyzed to determine the streamwise and transverse velocity components, u^* and v^* , shown in Fig. 1. The resulting unsteady aerodynamic gust generated rotor blade surface unsteady pressure chordwise distributions are measured with embedded ultraminiature high-response dynamic pressure transducers. The blade surface

Table 1 Overall airfoil and compressor characteristics

	ROTOR	STATOR	IGV
Airfoil type	C4	C4	C4
Number of Airfoils	43	31	36
Chord, C (mm)	30	30	30
Solidity, C/S	1.14	1.09	0.96
Camber, θ	28.0	27.7	36.9
Stagger Angle, γ	36.0	36.0	21.0
Inlet Metal Angle, β_1	50.0	30.0	0.0
Aspect Ratio	2.0	2.0	2.0
Thickness/Chord (%)	10.0	10.0	10.0
Flow Rate (kg/s)	2.03		
Design Axial Velocity (m/s)	24.4		
Design Rotational Speed (RPM)	2250		
Number of Stages	1		
Design Stage Pressure Ratio	1.0		
Inlet Tip Diameter (mm)	420		
Hub/Tip Radius Ratio	0.714		
Stage Efficiency (%)	85		

steady pressure chordwise distributions are measured with blade surface static taps ported to a rotor-based Scanivalve system.

Research Compressor

The Purdue Axial Flow Research Compressor models the fundamental turbomachinery unsteady aerodynamic multi-stage interaction phenomena, which include the incidence angle, the velocity and pressure variations, the aerodynamic forcing function waveforms, the reduced frequency, and the unsteady blade row interactions. The compressor is driven by a 15 hp dc-electric motor at a speed of 2250 rpm. Each identical stage contains 43 rotor blades and 31 stator vanes having a British C4 airfoil profile, with the first-stage rotor inlet flow field established by a variable setting inlet guide vane (IGV) row of 36 airfoils. The overall compressor and airfoil characteristics are defined in Table 1.

The compressor aerodynamic performance is determined utilizing a 48 port Scanivalve system, thermocouples, and a venturi orifice to measure the required pressures, temperatures, and flow rate, respectively. The Scanivalve transducer is calibrated each time data are acquired, thus automatically compensating for zero and span shifts of the transducer output. A 95 percent confidence interval, root-mean-square error analysis of 20 samples is performed for each steady data measurement.

Instrumentation

Both steady and unsteady rotor blade row data are required. These are acquired with the rotor-based instrumentation system schematically depicted in Fig. 2. The steady data quantify

Nomenclature

b = rotor blade semichord	\bar{i} = rotor blade mean incidence angle	\hat{v}^* = transverse gust first harmonic component
\bar{C}_l = rotor blade steady loading = $\int_0^c (\bar{C}_{p, \text{pressure}} - \bar{C}_{p, \text{suction}}) dx$	k = reduced frequency = $\omega b / \bar{V}_x$	V_x = mean axial velocity
\bar{C}_p = rotor blade steady pressure coefficient	p = digitized ensemble-averaged unsteady pressure	ΔV = absolute velocity vector difference from mean value
C_p = rotor blade unsteady pressure coefficient	P_s = rotor blade surface steady pressure	ΔW = total unsteady velocity
$C_{\Delta p}$ = rotor blade unsteady pressure difference coefficient	\hat{p} = first harmonic complex unsteady pressure	$\bar{\beta}$ = relative mean flow angle
	\hat{u}^* = streamwise gust first harmonic component	$\Delta \beta$ = relative flow angle difference from mean value
		ω = forcing function frequency, rad

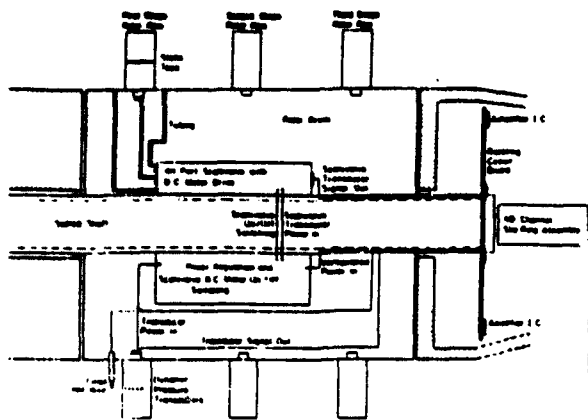


Fig. 2 Rotor-based instrumentation

the rotor row mean inlet flow field and the resulting rotor blade midspan steady loading distribution. The unsteady data define the periodic aerodynamic forcing function and the resulting midspan blade surface periodic unsteady pressure distributions.

The inlet flow field, both steady and unsteady, is measured with a rotating cross hot-wire probe. Disturbances in the stationary frame of reference, i.e., the IGV wakes, are the unsteady aerodynamic forcing functions to the first-stage rotor row. The rotor periodic unsteady inlet flow field generated by these disturbances is measured with a cross hot-wire mounted in the rotor frame of reference. The probe is axially mounted 30 percent of rotor chord upstream of the rotor leading edge plane. A potential flow field analysis determined this axial location to be such that leading edge potential effects are negligible for all steady loading levels. The probe is angularly aligned to obtain rotor relative velocity and flow angle data. The cross hot-wire probe was calibrated and linearized for velocities from 18.3 m/s to 53.4 m/s and ± 35 deg angular variation, with the accuracy of the velocity magnitude and flow angle were determined to be 4 percent and ± 1.0 deg, respectively. Centrifugal loading effects on the rotating hot-wire sensor resistances and, thus, the responses, were found to be negligible.

The detailed steady aerodynamic loading on the rotor blade surfaces is measured with a chordwise distribution of 20 midspan static pressure taps, 10 on each surface. The static pressure at the rotor exit plane, measured with a rotor drum static tap, is used as the blade surface static pressure reference. These static pressure measurements are made using a rotor-based 48 port constant speed drive Scanivalve system located in the rotor drum.

The measurement of the midspan rotor blade surface unsteady pressures is accomplished with 20 ultraminiature, high-response transducers embedded in the rotor blades at the same chordwise locations as the static pressure taps. To minimize the possibility of flow disturbances associated with the inability of the transducer diaphragm to maintain the surface curvature of the blade exactly, a reverse mounting technique is utilized. The pressure surface of one blade and the suction surface of the adjacent blade are instrumented, with transducers embedded in the nonmeasurement surface and connected to the measurement surface by a static tap. The embedded dynamic transducers are both statically and dynamically calibrated. The static calibrations show good linearity and no discernible hysteresis. The dynamic calibrations demonstrate that the frequency responses, in terms of gain attenuation and phase shift, are not affected by the reverse mounting technique. The accuracy of the unsteady pressure measurements, determined from the calibrations, is ± 4 percent.

The rotor-based static pressure Scanivalve transducer, ro-

tating cross hot-wire probe, and 20 blade surface dynamic pressure transducers are interfaced to the stationary frame-of-reference through a 40 channel slip ring assembly. On-board signal conditioning of the transducer output signals is performed to maintain a good signal-to-noise ratio through the slip rings. The remaining 17 channels of the slip-ring assembly are used to provide excitation to the transducers and on/off switching to the Scanivalve d-c motor.

Data Acquisition and Analysis

Steady Data. The rotor blade surface static pressure data, measured with the rotor-based Scanivalve system, are defined by a root-mean-square error analysis of 20 samples with a 95 percent confidence interval. The reference for these midspan blade pressure measurements is the static pressure at the exit of the rotor measured in the rotor drum. Thus, the blade surface and the reference static pressures are measured at different radii. Hence, a correction for the resulting difference in the radial acceleration is applied in calculating the blade surface static pressure coefficient:

$$\bar{C}_p = \frac{\bar{P}_s - \bar{P}_{\text{exit}}}{1/2\rho U_t^2} \quad (1)$$

where U_t is the rotor blade tip speed.

Periodic Data. The periodic data of interest are the harmonic components of the aerodynamic forcing function to the first-stage rotor blade row together with the resulting rotor blade surface unsteady pressures and unsteady pressure differences. These are determined by defining a digitized ensemble-averaged periodic unsteady aerodynamic data set consisting of the rotating cross hot-wire probe and blade surface dynamic pressure transducer signals at each steady operating point. In particular, these time-variant signals are digitized with a high-speed A-D system at a rate of 100 kHz and then ensemble averaged.

The key to this averaging technique is the ability to sample data at a preset time, accomplished by an optical encoder mounted on the rotor shaft. The microsecond range step voltage signal from the encoder is the data initiation time reference and triggers the high-speed A-D multiplexer system. To reduce significantly the random fluctuations superimposed on the periodic signals of interest, 200 averages are used. A Fast Fourier Transform (FFT) algorithm is then applied to these ensemble-averaged signals to determine the harmonic components of the unsteady aerodynamic forcing function and the resulting rotor blade surface harmonic unsteady pressures and pressure differences.

The unsteady inlet flow field to the rotor row is measured with the rotating cross hot-wire probe, which quantifies the relative velocity and flow angle. The velocity triangle relations depicted in Fig. 1 are then used to determine the unsteady inlet flow field to the rotor, in particular, the streamwise and transverse velocity components, u^+ and v^+ , respectively. These are then Fourier decomposed to determine the first harmonic of the streamwise and transverse velocity components, termed the streamwise and transverse gust components, \hat{u}^+ and \hat{v}^+ .

The various unsteady aerodynamic gust mathematical models reference the gust-generated airfoil aerodynamic response to a transverse gust at the leading edge of the airfoil. However, in the experiments described herein, the time-variant data are referenced to the initiation of the data acquisition shaft trigger pulse. Thus, for consistency with the models, the periodic data are further analyzed and referenced to a transverse gust at the leading edge of the first stage rotor blade. This is accomplished by assuming that: (1) the aerodynamic forcing function remains fixed in the stationary reference frame; and (2) the forcing function does not decay from the rotating hot-wire probe axial location to the rotor row leading edge plane.

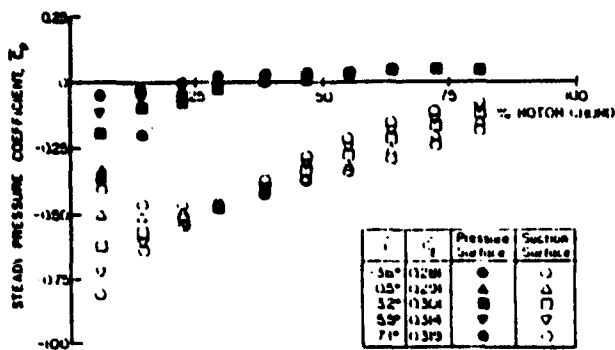


Fig. 3 Steady pressure chordwise distributions for five steady loading levels

The rotor blade surface unsteady pressure data, measured with the embedded high response pressure transducers, are analyzed to determine the harmonics of the chordwise distribution of the unsteady pressure coefficient, C_p , and the unsteady pressure difference coefficient, $C_{\Delta p}$. These are defined in Eq. (2) and are specified from the Fourier coefficients of the digitized ensemble-averaged dynamic pressure transducer signals.

$$C_p = \frac{\bar{p}}{\rho \bar{V}_x^2 \left(\frac{\hat{v}^+}{\bar{V}_x} \right) \bar{\beta}} \quad (2a)$$

$$C_{\Delta p} = C_{p, \text{pressure}} - C_{p, \text{suction}} \quad (2b)$$

where \hat{v}^+ is the first harmonic transverse gust component, \bar{V}_x is the mean axial velocity, and $\bar{\beta}$ is the relative mean flow angle in rad.

The final forms of the gust-generated rotor blade row unsteady aerodynamic data define the chordwise distribution of the harmonic complex unsteady pressure and pressure difference coefficients. Also included as a reference are predictions from the transverse gust analysis of Smith (1971). This model analyzes the unsteady aerodynamics generated on a flat plate airfoil cascade at zero incidence by a transverse gust convected with an inviscid, subsonic, compressible flow.

Results

A series of experiments are performed to investigate and quantify the effects on the unsteady aerodynamic gust response of the first-stage rotor blade row due to the detailed variation of the unsteady aerodynamic forcing function generated by the IGV wakes. Forcing function effects include both the transverse and chordwise gust components, defined by the ratio of the amplitudes of the first harmonic streamwise-to-transverse gust components, $|\hat{u}^+/\hat{v}^+|$, and the gust amplitude, defined by the ratio of the first harmonic transverse gust magnitude to mean axial velocity, $|\hat{v}^+/\bar{V}_x|$. The ratio of the streamwise-to-transverse gust amplitude, $|\hat{u}^+/\hat{v}^+|$, was varied by changing the IGV setting angle. The level of steady aerodynamic loading, characterized by the mean incidence angle, was varied as a parameter. The variation in the rotor blade steady loading was obtained by holding the rotor speed constant and varying the mass flow rate and, thus, the mean flow incidence angle to the rotor blade row.

Periodic Aerodynamic Forcing Function. Four distinct 36-per-revolution aerodynamic forcing functions to the first-stage rotor blade row are generated, characterized by nominal first harmonic streamwise-to-transverse gust amplitude ratios of 0.29, 0.37, 0.45, and 0.55. The unsteady aerodynamic gust generated from the IGV wake first harmonic have nominal reduced frequency values between 5 and 6. The Fourier decomposition of these IGV wake aerodynamic forcing functions to

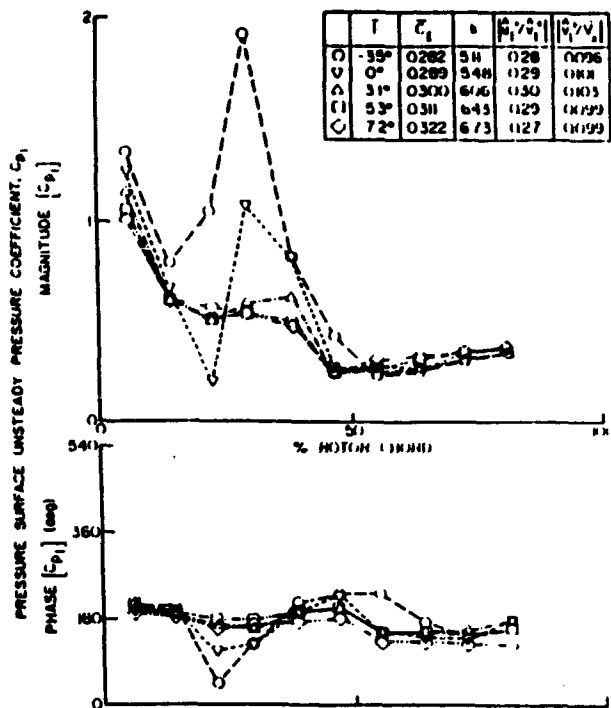


Fig. 4 Steady loading effect on blade pressure surface unsteady response for a nominal first harmonic $|\hat{u}^+/\hat{v}^+|$ of 0.29

the first-stage rotor row shows a dominant 36-per-rev excitation fundamental harmonic with smaller higher harmonics. As the gust amplitude ratio increases, the transverse harmonic gust amplitudes become smaller while the streamwise harmonic gust amplitudes becomes larger with respect to the mean axial velocity.

Blade Surface Steady Pressures. The effect of steady aerodynamic loading as characterized by the mean incidence angle on the rotor blade surface steady pressure coefficient is shown in Fig. 3. The level of steady loading only affects the steady pressure distribution on the pressure surface over the front 40 percent of the chord. On the suction surface, the steady loading variation has a large effect on the steady pressure distribution over the entire suction surface. Also, these data give no indication of suction surface flow separation. It should be noted that these surface steady pressure distributions are not affected by the characteristics of the periodic unsteady aerodynamic forcing function.

Rotor Row Periodic Aerodynamic Response. The periodic aerodynamic responses of the first-stage rotor blade row to the IGV wake first harmonic forcing function are presented in the format of the chordwise distribution of the complex unsteady pressure coefficient on the individual rotor blade surfaces as well as the corresponding complex unsteady pressure difference coefficient generated by the 36-per-rev IGV wake first harmonic forcing function, with the steady loading level as a parameter.

Pressure Surface Unsteady Pressure. The effect of steady aerodynamic loading level on the IGV wake-generated first harmonic complex unsteady pressure distribution on the rotor blade pressure surface is shown in Figs. 4, 5, 6, and 7 for nominal streamwise-to-transverse gust amplitude ratios of 0.29, 0.37, 0.45, and 0.55, respectively. The first harmonic gust amplitude, characterized by $|\hat{v}^+/\bar{V}_x|$ values of approximately 0.1, is small compared to the mean axial velocity.

For each gust amplitude ratio value, the form of the dimensionless unsteady pressure coefficient specified in Eq. (2)

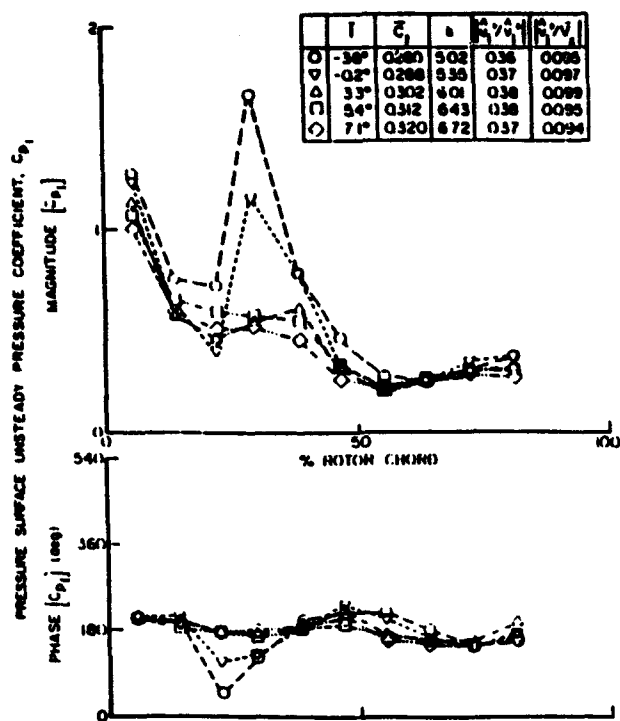


Fig. 5 Steady loading effect on blade pressure surface unsteady response for a nominal first harmonic $|\dot{d}^*/\theta^*|$ of 0.37

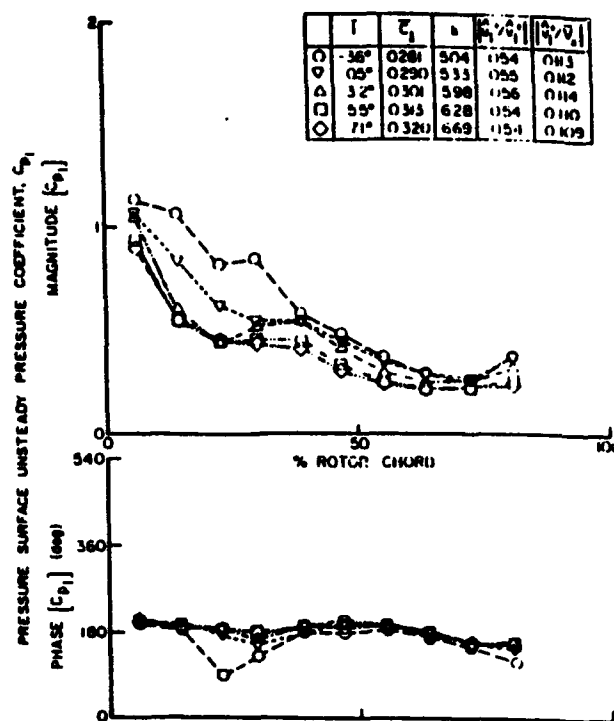


Fig. 7 Steady loading effect on blade pressure surface unsteady response for a nominal first harmonic $|\dot{d}^*/\theta^*|$ of 0.55

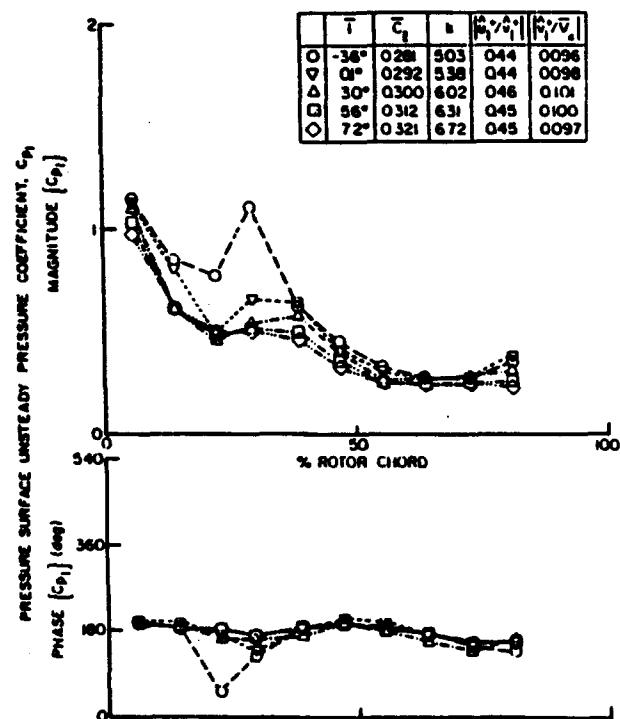


Fig. 8 Steady loading effect on blade pressure surface unsteady response for a nominal first harmonic $|\dot{d}^*/\theta^*|$ of 0.45

results in a compression of the unsteady pressure magnitude data over the entire pressure surface for all gust amplitude ratios and all but the two lowest steady loading levels. For these two loading cases, large variations are found in the magnitude data in the neighborhood of the quarter chord, with these variations decreasing with increasing gust amplitude ratio. This corresponds to the previously noted effects of steady

loading on the rotor blade surface steady pressure wherein loading primarily influences the front part of the pressure surface. Namely, the steady pressure coefficient value for the rotor drum hub steady pressure coefficient upstream of the rotor row is approximately -0.24 , thereby indicating that the mean flow field accelerates around the pressure surface leading edge before decelerating (diffusing) for the two lowest mean incidence angles, i.e., the steady pressure coefficient decreases and then increases.

The level of steady loading has only a minimal effect on the pressure surface unsteady pressure phase, the exception being the two lowest steady loading levels in the front chord region. Also as $|\dot{d}^*/\theta^*|$ increases, the decrease in phase in the 25 percent chord region becomes less for the two low steady loading levels, while the three highest steady loading levels in the front chord region and all steady loading levels in the aft chord region remain relatively unaffected by the gust amplitude ratio.

Suction Surface Unsteady Pressures. The effect of steady aerodynamic loading on the IGV wake-generated first harmonic complex unsteady pressure on the rotor blade suction surface is shown in Figs. 8, 9, 10, and 11 for the four nominal gust amplitude ratio values.

The unsteady pressure coefficient magnitude on the entire suction surface is a strong function of the level of steady aerodynamic loading. This corresponds to the previously presented suction surface steady pressure data variation with mean incidence angle. For all gust amplitude ratios, the front-to-midchord region data show a decreasing-increasing magnitude trend with chord, with the minimum magnitude chordwise location moving forward with increasing steady loading. This minimum corresponds to the minimum in the steady pressure chordwise distribution, Fig. 5, wherein the chordwise location of the change from accelerating to decelerating mean flow moves forward with increasing mean incidence. Thus, similar to the pressure surface unsteady response in the front chord region at negative mean incidence angle, the unsteady gust interacts with the accelerating mean flow field around the

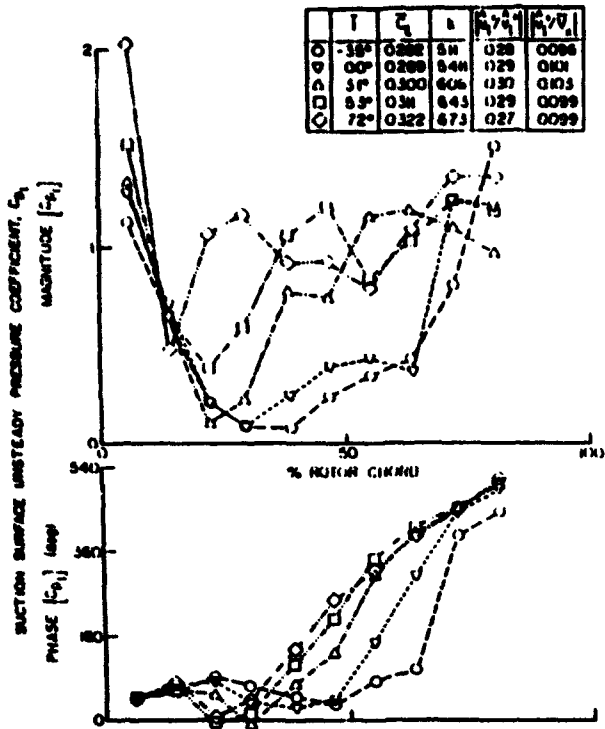


Fig. 8 Steady loading effect on blade suction surface unsteady response for a nominal first harmonic $|\delta^*/\theta^*|$ of 0.29

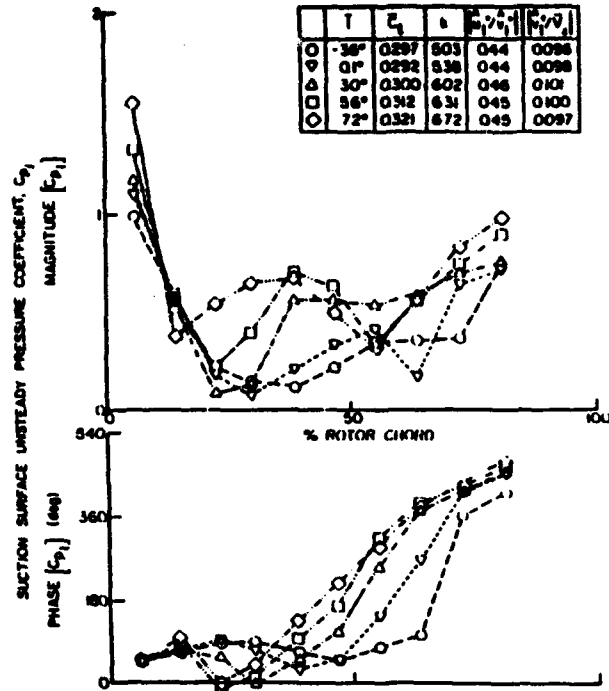


Fig. 10 Steady loading effect on blade suction surface unsteady response for a nominal first harmonic $|\delta^*/\theta^*|$ of 0.45

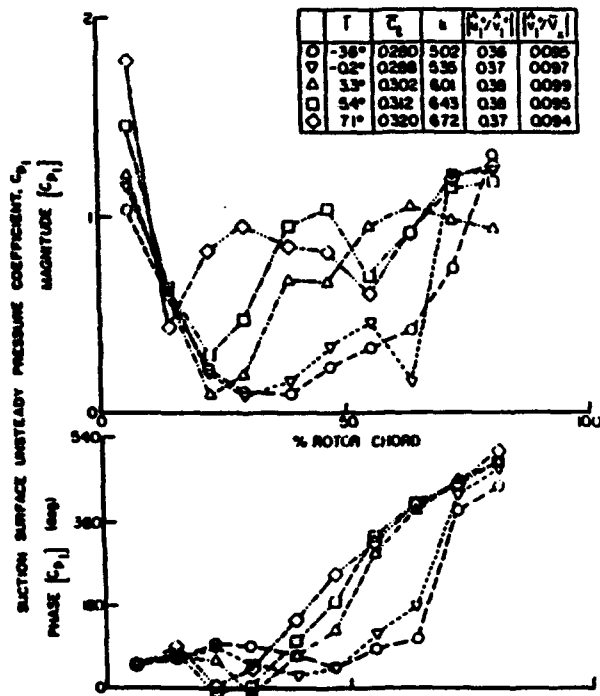


Fig. 9 Steady loading effect on blade suction surface unsteady response for a nominal first harmonic $|\delta^*/\theta^*|$ of 0.37

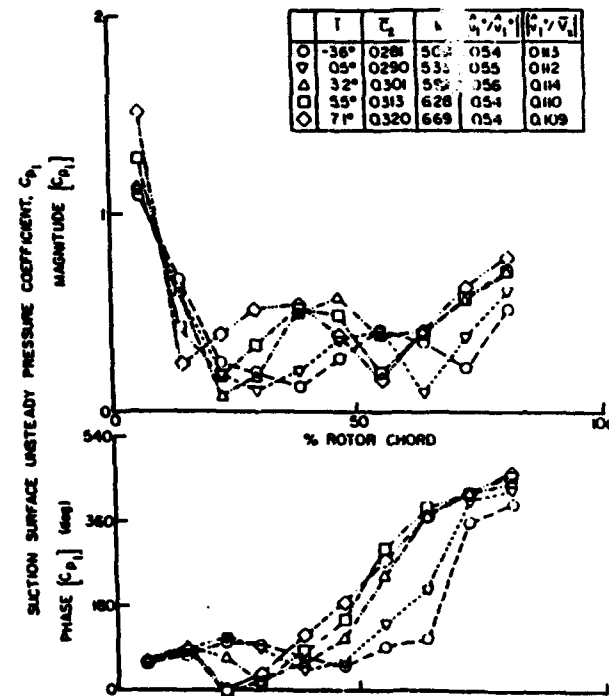


Fig. 11 Steady loading effect on blade suction surface unsteady response for a nominal first harmonic $|\delta^*/\theta^*|$ of 0.55

suction surface in the front chord region. In the mid-to-aft chord region, the gust amplitude ratio alters the effect of steady loading on the chordwise distributions of the unsteady pressure response. Namely, for the large gust amplitude ratios, a decreasing-increasing unsteady pressure magnitude trend with chord occurs, with the minimum moving forward with in-

creasing steady loading. As $|\delta^*/\theta^*|$ decreases, this increasing-decreasing magnitude trend with chord becomes smoother and the data increase dramatically in magnitude in the aft half chord. Thus, for this higher camber suction surface, the mean flow field interacts with the unsteady gust over the entire blade surface, with the gust amplitude ratio affecting the response over the aft half of the surface.

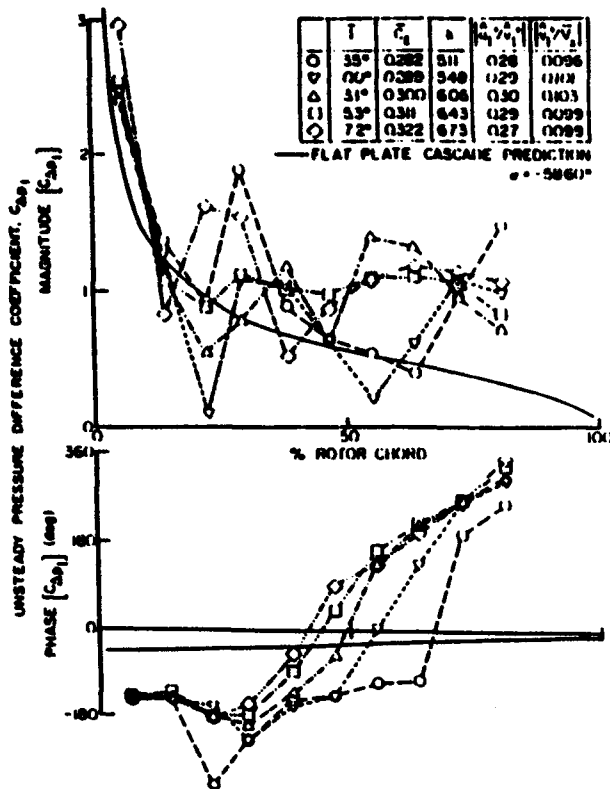


Fig. 12 Steady loading effect on blade unsteady pressure difference response for a nominal first harmonic $|\theta^*|$ of 0.29

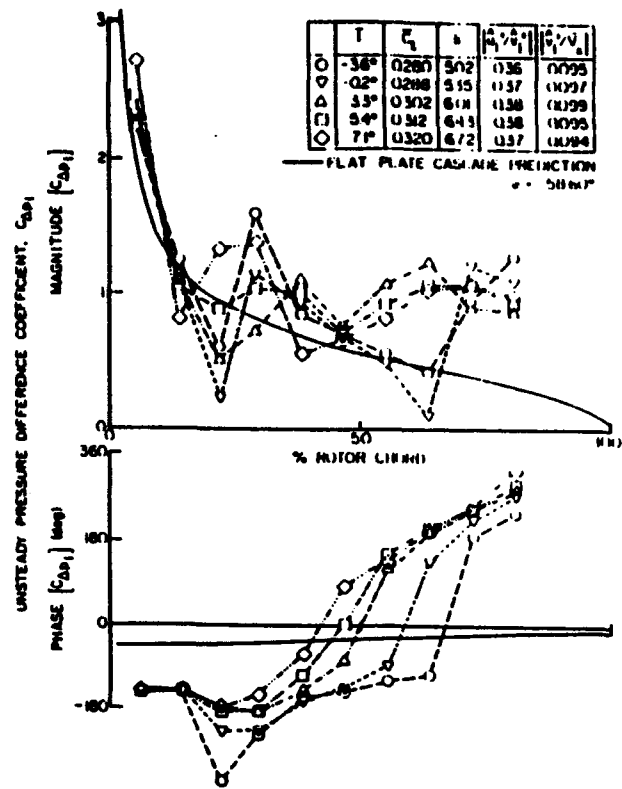


Fig. 13 Steady loading effect on blade unsteady pressure difference response for a nominal first harmonic $|\theta^*|$ of 0.37

Nearest to the leading edge, the magnitude data increase with increasing steady loading level. As noted previously, this steady loading trend is attributed to the IGV wake first harmonic gust interacting with the mean accelerating flow field around the blade leading edge. Hathaway et al. (1987) have experimentally demonstrated the interaction of a rotor wake with a downstream stator row. They found that from approximately -20 to 10 percent of the downstream stator chord, the rotor wake-generated unsteady velocity magnitude increases, with the increase becoming larger as steady loading increases. This indicates that the wake-generated gust magnitude increases due to the interaction with the accelerating mean flow field around the blade leading edge.

With regard to the phase of the unsteady pressure, the streamwise-to-transverse gust amplitude ratio has minimal effect, with steady loading primarily affecting the phase on the aft three quarters of the chord. As the mean incidence angle is increased from the low loading level, the chordwise variation of the phase data on the aft part of the surface becomes linear, with the extent of this linear distribution increasing with increasing mean incidence. This linear chordwise distribution indicates the existence of a wave phenomenon, with a convective velocity equal to the mean axial velocity through the blade row (20.5 m/s). This mean axial velocity wave phenomenon has been experimentally detected by other authors (Fleeter et al., 1980; Hodson, 1985) but is yet to be physically explained.

Summarizing these blade surface steady loading and gust amplitude ratio effects, for the low camber pressure surface in the chordwise region where the mean flow field does not accelerate, i.e., the mid-to-aft chord region for all steady loading levels and the front chord region for the three high steady loading levels, the data compress for all gust amplitude ratios, indicating that steady loading as characterized by the mean flow incidence is a key mechanism for the low camber unsteady aerodynamic wake response. However, in an accelerating mean

flow field, i.e., the front chord region for the two low steady loading levels, mean flow field interactions with the unsteady gust are also important. As the gust amplitude ratio increases, this interaction lessens. On the higher camber suction surface, the interaction between the mean flow field and the unsteady gust affects the unsteady aerodynamic response over the entire blade surface for all steady loading levels and streamwise-to-transverse gust amplitude ratios. Also, the gust amplitude ratio has a large effect on these interactions over the aft half of the blade surface.

Unsteady Pressure Differences. The steady loading effect on the first harmonic of the complex unsteady pressure difference across the rotor blade camberline is shown in Figs. 12, 13, 14, and 15 for the nominal streamwise-to-transverse gust amplitude ratios of 0.29, 0.37, 0.45, and 0.55, respectively. Also presented as a reference are the flat plate cascade, inviscid, transverse gust predictions of Smith (1971) and Whitehead (1987).

The effects of steady loading on the previously presented individual pressure and suction surface magnitude and phase data are still apparent, with the suction surface effects being dominant. For example, analogous to the high gust amplitude steady loading trends on the suction surface for the high gust amplitude ratio, the unsteady pressure difference magnitude data show two decreased magnitude regions, one in the front chord region and the other in the mid-to-aft chord region, with the chordwise location of the magnitude minima moving forward with increased steady loading. Also, the chordwise location where the rapid increase in value of the phase data begins to occur moves forward with increasing steady loading similar to the suction surface, whereas for the low steady loading level, the phase decreases sharply at 25 percent rotor chord per the pressure surface trends. Similar to the steady loading trends in the suction surface aft chord region, as the gust amplitude ratio decreases, the magnitude data increase.

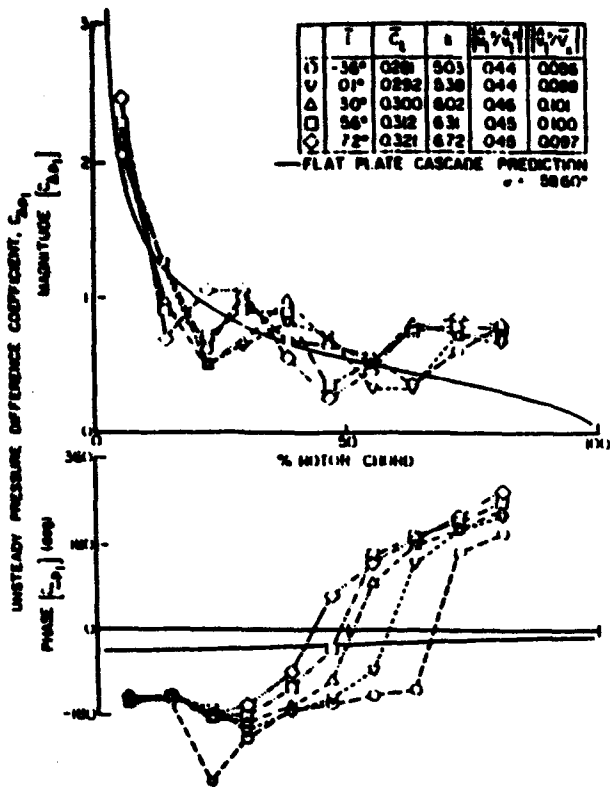


Fig. 14 Steady loading effect on blade unsteady pressure difference response for a nominal first harmonic $|\delta^*/V_\infty|$ of 0.45

These steady loading effects cause the chordwise distribution of the unsteady pressure difference magnitude and phase data to differ greatly from the flat plate cascade predictions, with the magnitude data not just decreasing with increasing chord and the phase data not remaining nearly constant with chord per the predictions. The lowest steady loading level, which most closely approximates the prediction model no loading condition, shows fair comparison with the magnitude data, except in chord regions where strong gust interactions with the steady flow field occur, i.e., the pressure surface interaction at 25 percent chord and the suction surface interaction in the aft chord. The prediction differs from the phase data by approximately 90 deg over the entire blade except, once again, in the 25 percent and aft chord region.

Effect of Gust Amplitude. The previous results considered the periodic aerodynamic response of the first-stage rotor blade row to relatively small amplitude IGV wake first harmonic gusts, with the ratio of the transverse gust to mean axial velocity on the order of 0.1. The effect of larger amplitude gusts, $|\delta^*/V_\infty|$ on the order of 0.3, on the blade surface unsteady pressure response, including the effect of steady loading, are presented in Figs. 16 and 17, where the effect of operation at the five nominal steady loading levels is also included. In particular, these figures present the chordwise distribution of the complex unsteady pressure coefficient on the pressure and suction surfaces generated by large amplitude 36-per-rev IGV wake first harmonic forcing functions.

The effect of the larger amplitude gusts on the pressure surface unsteady pressure response is demonstrated by comparing the high-amplitude gust generated response with that resulting from the low-amplitude gust of the same nominal streamwise-to-transverse gust amplitude ratio value, Figs. 5 and 16. Nearly identical unsteady pressure magnitude and phase responses are shown for both gust amplitudes except in the 25

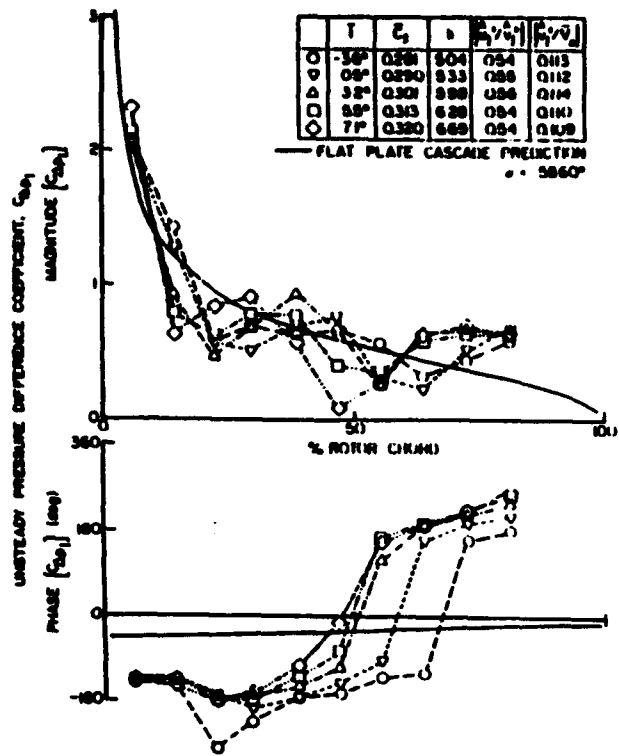


Fig. 15 Steady loading effect on blade unsteady pressure difference response for a nominal first harmonic $|\delta^*/V_\infty|$ of 0.55

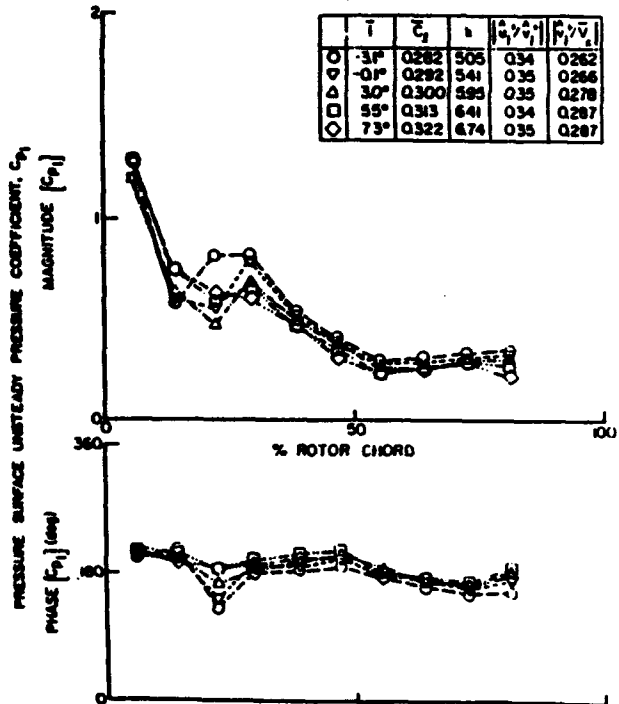


Fig. 16 Steady loading effect on blade pressure surface response for large-amplitude gusts

percent chord region for the lowest two mean flow incidence angles. In this front chord region at negative mean flow incidence, the interaction of the accelerating mean flow field and the unsteady gust is weaker for the larger amplitude

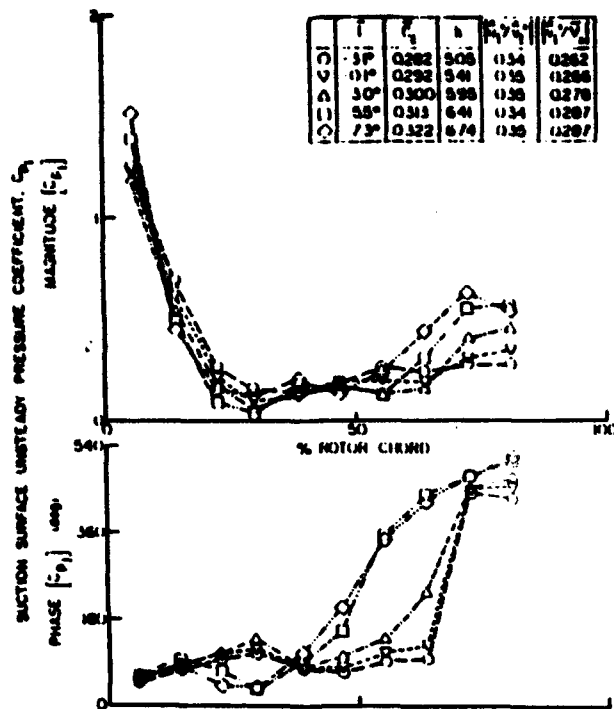


Fig. 17 Steady loading effect on blade suction surface response for large-amplitude gusts

gust, as evidenced by the decrease in the magnitude and phase variation.

The effect of large-amplitude gusts on the suction surface unsteady pressure response is seen by comparing the high and low-amplitude gust-generated response for equivalent gust amplitude ratio values, Figs. 9 and 17. The phase data are unaffected by the gust amplitude, with the steady loading effect on the phase chordwise distributions being nearly equivalent. However, the magnitude data are greatly affected by the gust amplitude, particularly over the aft three quarters of the surface. The high-amplitude gust magnitude data are greatly decreased compared to the low-amplitude gust magnitude data, with the steady loading effect being greatly reduced. Thus, similar to the pressure surface front chord region at negative mean flow incidence, the interaction of high-amplitude gusts with the mean flow is weaker than the interaction of low-amplitude gusts with the mean flow.

Summary and Conclusions

The rotor blade row fundamental unsteady aerodynamic flow physics generated by periodic wakes were investigated at realistic values of the reduced frequency. In particular, the effects of the detailed unsteady aerodynamic forcing function, including both the transverse and chordwise first harmonic gust components and the gust amplitude, as well as steady aerodynamic loading on the unsteady aerodynamic gust response of the first-stage rotor blade row, were investigated and quantified. This was accomplished by means of a series of experiments performed in an extensively instrumented axial flow research compressor.

The rotor blade surface steady loading distributions were quantified with surface static pressure taps and a rotor-based Scanivalve system. The aerodynamic forcing function to the rotor blade row was determined with a rotating cross hot-wire probe, with the aerodynamic gust-generated rotor blade surface unsteady pressure chordwise distributions measured with embedded ultraminiature high-response dynamic pressure transducers.

The detailed IGV wake-generated unsteady aerodynamic results of these experiments are summarized in the following.

Forcing Function

- The IGV wake forcing function shows a dominant 36-per-rev, with smaller higher harmonic content.

Blade Surface Steady Pressures

- Steady loading affects the steady pressure distribution on the front portion of the blade pressure surface and over the entire suction surface.
- The unsteady gust amplitude ratio and magnitude have negligible effect on the steady pressure distribution.

Pressure Surface Response

- The unsteady pressure phase data are nearly independent of the steady loading level and the gust amplitude ratio except in the front chord region at negative mean flow incidence.
- The selected unsteady pressure nondimensionalization compresses the magnitude data with regard to mean flow incidence angle for each gust component amplitude ratio except in the front chord region for negative mean flow incidence.
- Increasing the gust amplitude ratio results in weaker interactions between the mean and unsteady flow fields in the front chord region at negative mean flow incidence.
- Large-amplitude gusts reduce this interaction between the unsteady gust and the accelerating mean flow field.
- The magnitude of the unsteady pressure response on the blade pressure surface, i.e., the low camber surface, is thus primarily affected by the level of steady loading as characterized by the mean flow incidence angle except in the accelerating mean flow field of the front chord region at negative mean flow incidence.

Suction Surface Response

- The unsteady pressure phase data are nearly independent of the gust component amplitude ratio, with increased mean incidence, resulting in a linear chordwise distribution, which corresponds to a wave phenomenon convected at the mean axial velocity of the flow through the rotor blade row.
- The selected unsteady pressure nondimensionalization does not compress the magnitude data with regard to mean flow incidence angles.
- The mid-to-aft chord magnitude data are a strong function of the gust amplitude ratio, with the increase in magnitude with increasing steady loading becoming smaller with increasing gust amplitude ratio.
- Large-amplitude gusts reduce these mean flow field interactions with the unsteady gust, similar to the pressure surface.
- The magnitude of the unsteady pressure response on the blade suction surface, i.e., the higher camber surface, is thus affected by both the steady flow field interactions and the gust amplitude ratio.

Unsteady Pressure Difference Response

- The unsteady pressure difference data reflect the effects of loading on the pressure and suction surface unsteady data, with the suction surface effects being dominant.
- These steady loading effects cause the chordwise distribution of the magnitude and phase data to differ greatly from the flat plate cascade predictions.
- The lowest steady loading level data were correlated with flat plate cascade predictions, with the unsteady aerodynamic response correlation being fair.

Acknowledgments

Research sponsored by the Air Force Office of Scientific Research (AFSC) under Contract No. F49620-88-C-0022. The United States Government is authorized to reproduce and dis-

tribute reprints for governmental purposes notwithstanding any copyright notation hereon.

References

- Capocci, V. R., and Fleeter, S., 1987, "Unsteady Aerodynamic Interactions in a Multi-stage Compressor," *ASME JOURNAL OF TURBOMACHINERY*, Vol. 109, pp. 420-428.
- Capocci, V. R., Maunwaring, S. R., and Fleeter, S., 1986, "Unsteady Blade Row Interactions in a Multi-stage Compressor," *AIAA Journal of Propulsion*, Vol. 2, No. 2, pp. 168-174.
- Fleeter, S., Bennett, W. A., and Jay, R. L., 1980, "The Time-Variant Aerodynamic Response of a Stator Row Including the Effects of Airfoil Camber," *ASME Journal of Engineering for Power*, Vol. 102, pp. 334-343.
- Fleeter, S., Jay, R. L., and Bennett, W. A., 1978, "Rotor Wake Generated Unsteady Aerodynamic Response of a Compressor Stator," *ASME Journal of Engineering for Power*, Vol. 100, pp. 664-675.
- Giallus, H. E., Lambertz, J., and Walkman, Th., 1980, "Blade-Row Interaction in an Axial-Flow Subsonic Compressor Stage," *ASME Journal of Engineering for Power*, Vol. 102, pp. 169-177.
- Hardin, I. W., Carta, F. O., and Verdon, J. M., "Unsteady Aerodynamic Measurements on a Rotating Compressor Blade Row at Low Mach Number," *ASME JOURNAL OF TURBOMACHINERY*, Vol. 109, No. 4, pp. 499-507.
- Hathaway, M. D., Suder, K. L., Okiishi, T. H., Strazisar, A. J., and Adamczyk, J., 1987, "Measurements of the Unsteady Flow Field Within the Stator Row of a Transonic Axial-Flow Fan. II—Results and Discussion," *ASME Paper No. 87-GT-227*.
- Hodson, H. P., 1985, "Measurements of Wake-Generated Unsteadiness in the Rotor Passages of Axial Flow Turbines," *ASME Journal of Engineering for Gas Turbines and Power*, Vol. 107, pp. 467-476.
- Maunwaring, S. R., and Fleeter, S., 1990, "Inlet Distortion Generated Periodic Aerodynamic Rotor Response," *ASME JOURNAL OF TURBOMACHINERY*, Vol. 112, No. 2, pp. 298-307.
- Maunwaring, S. R., and Fleeter, S., 1991, "Forcing Function Effects on Rotor Periodic Aerodynamic Response," *ASME JOURNAL OF TURBOMACHINERY*, Vol. 113, pp. 312-319.
- O'Brien, W. F., Collins, W. R., and Sexton, M. R., 1980, "Unsteady Pressure Measurements and Data Analysis Techniques in Axial-Flow Compressors," *Measurement Methods in Rotating Components of Turbomachinery*, ASME, pp. 195-210.
- Smith, S. N., 1971, "Discrete Frequency Sound Generation in Axial Flow Turbomachines," *ARC R&M 3709*.
- Suder, K. L., Hathaway, M. D., Okiishi, T. H., Strazisar, A. J., and Adamczyk, J., 1987, "Measurements of the Unsteady Flow Field Within the Stator Row of a Transonic Axial-Flow Fan. I—Measurement and Analysis Technique," *ASME Paper No. 87-GT-226*.
- Whitehead, D. S., 1987, "Classical Two-Dimensional Methods," *AGARD Manual on Aeroelasticity in Axial Flow Turbomachines, Vol. 1: Unsteady Turbomachinery Aerodynamics*, AGARDograph No. 298, pp. 3-1-3-30.

APPENDIX III

Forcing Function Generation Fluid Dynamic Effects on Compressor Blade Gust Response

AIAA Journal of Propulsion and Power, Vol. 10, Number 2, March-April 1994,
pp. 204-216.

Forcing Function Generator Fluid Dynamic Effects on Compressor Blade Gust Response

Kuk H. Kim* and Sanford Fleetert
Purdue University, West Lafayette, Indiana 47907

To investigate the fundamental flow forcing function phenomena generating different blade row gust responses, in particular attached and separated flow forcing functions, a series of experiments are performed in an extensively instrumented axial flow research compressor. In these experiments, the gust ratio magnitude is controlled without affecting the forcing function fluid dynamics, i.e., attached or separated flow, thereby enabling a controlled study of the effect of steady loading. Periodic 2-F unsteady aerodynamic forcing functions to the first stage rotor are generated by fundamentally equivalent honeycomb sections and flat plate airfoils, with unsteady linear theory gust requirements considered. Then the resulting rotor blade row gust response is measured over a range of steady loading levels and the gust response data correlated with the appropriate linear theory predictions. These experiments show that the forcing function generator fluid dynamics is significant with regard to the resulting unsteady aerodynamic gust response. Also demonstrated is the decreased correlation of the gust response data with linear theory predictions as the steady loading is increased.

Nomenclature

$C_{p,m}$	= pressure surface complex unsteady pressure coefficient
$C_{p,s}$	= suction surface complex unsteady pressure coefficient
$\hat{C}_{p,i}$	= steady pressure coefficient at i th chord position
$\hat{C}_{p,p}$	= pressure surface steady pressure coefficient
$\hat{C}_{p,s}$	= suction surface steady pressure coefficient
\hat{C}_l	= steady lift coefficient
i	= rotor relative flow incidence angle
I	= mean rotor relative flow incidence angle
k_1	= streamwise wave number, reduced frequency
k_2	= transverse wave number
\bar{p}_{exit}	= static pressure at rotor exit
p_i	= first harmonic of Fourier decomposed pressure
U	= flow velocity or wheel speed
u	= streamwise gust component
u'	= first harmonic streamwise gust component
u'/v'	= streamwise to transverse gust ratio
\bar{V}_x	= mean axial velocity
v	= transverse gust component
v'	= first harmonic transverse gust component
\bar{W}	= mean rotor relative velocity
w	= instantaneous rotor relative velocity
x_1	= first chordwise position for blade surface steady pressure measurement
x_2	= last chordwise position for blade surface steady pressure measurement
α	= absolute flow angle
$\bar{\alpha}$	= mean absolute flow angle
β	= rotor relative flow angle

$\bar{\beta}$	= mean rotor relative flow angle
$\Delta C_p, C_{\Delta p}$	= complex unsteady pressure difference coefficient
$\Delta \hat{C}_p$	= steady pressure difference coefficient

Introduction

THE spatial flow nonuniformities generated by inlet guide vanes, stator vanes, and struts are periodic temporal variations to downstream rotor blades. These spatial flow nonuniformities in the stationary frame of reference are sources of periodic excitation to the rotor blades. When the frequency of these periodic flow nonuniformities coincides with a blade natural frequency, fatigue failure of the rotor blade may result, thereby compromising engine durability.

The prediction of the flow-induced vibratory response of a blade row first requires a definition of the unsteady aerodynamic forcing function in terms of its harmonics, with each harmonic independently considered. Thus, even though forcing functions may be generated by a wide variety of fundamentally different sources, the forcing functions are assumed to be equivalent if their harmonics are the same. The unsteady aerodynamic response of the blade row to each forcing function harmonic is then assumed to be comprised of two components: the disturbance being swept past the nonresponding airfoils, termed the gust unsteady aerodynamic and the airfoil vibratory response to this disturbance, referred to as the motion-induced unsteady aerodynamics or the aerodynamic damping.

Early treatments of unsteady flow due to periodic gusts were developed in the linear approximation wherein the mean flow is assumed to be uniform. In this approximation, the steady and unsteady flowfields are completely uncoupled from one another, with the upstream generated periodic gust aerodynamic forcing functions convected with the uniform mean flow. Semianalytical unsteady aerodynamic analyses based on this linear model have been developed for cascades in subsonic and supersonic flows.¹⁻⁴ Such models are currently being extended to consider unsteady flows linearized about a non-uniform mean flow, with the gust interacting with the mean flow.⁵⁻⁷

A number of experiments have been directed at the verification of such mathematical models and the determination of their applicability and limitations. As a generalization, it appears that if the assumptions inherent in these analyses are modeled, then the experiments provide data which are in

Presented as Paper 93-0157 at the 31st Aerospace Sciences Meeting, Reno, NV, Jan. 11-14, 1993; received April 19, 1993; revision received Aug. 24, 1993; accepted for publication Sept. 9, 1993. Copyright © 1993 by K. H. Kim and S. Fleetert. Published by the American Institute of Aeronautics and Astronautics, Inc., with permission.

AFRAIPT Trainee, School of Mechanical Engineering.

*Professor, School of Mechanical Engineering.

Table 1 Overall airfoil and compressor characteristics

	IGV	Rotor	Stator
Airfoil type	C4	C4	C4
Number of airfoils	36	43	31
Chord, C , mm	30	30	30
Solidity, C/S	0.96	1.14	0.822
Camber, η	36.9	28.0	27.7
Stagger angle, α	21.0	36.0	-36.0
Inlet metal angle, β_1	0.0	50.0	30.0
Aspect ratio	2.0	2.0	2.0
Thickness/chord, %	10.0	10.0	10.0
Axial spacing (% C)	IGV/R = 0.63	R/S = 0.55S/R = 0.38	—
Reynolds number $\times 10^{-6}$ (based on chord)	5.0	6.3	6.3
Flow rate, kg/s	—	2.03	—
Design axial velocity, m/s	—	24.4	—
Design rotational speed, rpm	—	2250	—
Number of stages	—	3	—
Design stage pressure ratio	—	1.0	—
Inlet tip diameter, mm	—	420	—
Hub/tip radius ratio	—	0.714	—
Stage efficiency, %	—	85	—

agreement with the predictions. However, if actual compressor operating conditions, i.e., finite camber, steady loading, and nonzero incidence angle, are experimentally modeled, then the data-prediction correlations are not nearly as good.

Of particular interest herein are the experiments performed by Manwaring and Fleeter,⁸ which investigated the unsteady aerodynamic response of a rotor blade row to two classically equivalent forcing functions, as defined by linear theory. Their data first revealed the dependency of the unsteady aerodynamic response to a particular forcing function.

Later, Kim and Fleeter⁹ identified the importance of the gust generator fluid dynamics on the resulting blade row response. Their data attributed the differences in the gust response of the 2 per rotor revolution or 2-E inlet distortion and flat plate wakes of Manwaring and Fleeter⁸ to the fluid dynamics of the gust generators. Namely, the inlet distortion gust was generated by an attached flow gust, while the flat plate gust was due to a separated flow gust. However, in these experiments, a controlled study of the effect of steady loading could not be performed because of the particular forcing function generators, i.e., the gust ratio magnitude, u^*/v^* , could not be controlled without affecting the forcing function fluid dynamics.

In this article, the fundamental forcing function phenomena fluid dynamics generating different blade row gust responses are investigated in a controlled manner, including the important effects associated with the forcing function gust magnitude. This is accomplished by means of a series of experiments directed at the investigation of unsteady aerodynamic blade row response to gusts generated by attached and separated flow fluid dynamics from nonairfoil shape gust generators. With these gust generators, the gust ratio magnitude can be controlled without affecting the forcing function fluid dynamics, i.e., attached or separated flow, thereby enabling a controlled study of the effect of steady loading.

Periodic 2 per rotor revolution or 2-E unsteady aerodynamic forcing functions to the first-stage rotor row of the extensively instrumented Purdue Axial Flow Research Compressor are generated by two honeycomb sections and flat plates installed in the compressor inlet. These forcing functions are measured with a rotating cross hot-wire, with the resulting blade row unsteady aerodynamic gust response measured with dynamic pressure transducers embedded in the blade for steady loading levels ranging from -3 to 6 deg. Furthermore, unsteady linear theory gust requirements are considered, with appropriate gust response data correlated

with predictions from the subsonic unsteady aerodynamic flat plate cascade analysis of Smith.¹⁰

Research Compressor

The Purdue Axial Flow Research Compressor models the fundamental turbomachinery unsteady aerodynamic multi-stage interaction phenomena, which include the incidence angle, the velocity and pressure variations, the aerodynamic forcing function waveforms, the reduced frequency, and the unsteady blade row interactions. The compressor is driven by a 15 hp dc electric motor at a speed of 2250 rpm. Each identical stage contains 43 rotor blades and 31 stator vanes having a British C4 airfoil profile, with the first stage rotor inlet flowfield established by an inlet guide vane (IGV) row of 36 airfoils. The 2-E unsteady aerodynamic forcing functions are generated by two honeycomb sections and flat plates installed 180-deg apart in the compressor inlet. The overall compressor and airfoil characteristics are defined in Table 1.

The compressor aerodynamic performance is determined utilizing a 48-port Scanivalve system, thermocouples, and a venturi orifice to measure the required pressures, temperatures, and flow rate, respectively. The Scanivalve transducer is calibrated each time data are acquired, thus automatically compensating for zero and span shifts of the transducer output. A 95% confidence interval, rms error analysis of 20 samples is performed for each steady data measurement.

Instrumentation

Both steady and unsteady rotor blade row data are obtained. The steady data quantify the rotor row mean inlet flowfield and the resulting rotor blade midspan steady loading distribution. The unsteady data define the periodic aerodynamic forcing function and the resulting midspan blade surface periodic unsteady pressure distributions.

The inlet flowfield, both steady and unsteady, is measured with a rotating cross hot-wire probe. The inlet flowfield of the first-stage rotor row is measured in the rotating frame of reference by mounting the hot wire on the rotor drum 18.8% chord upstream and 65% blade spacing from a rotor blade, depicted in Fig. 1. The hot wire is oriented for maximum sensitivity, achieved when the 0-deg flow incidence corresponds to the position at which the flow angle is 45 deg to both wires. The hotwire is calibrated for velocities from 21.3 to 62.5 m/s and ± 40 -deg flow angle variations. The uncertainties in the velocity and the flow angle measurements were determined to be 5% and ± 0.5 deg. Centrifugal loading ef-

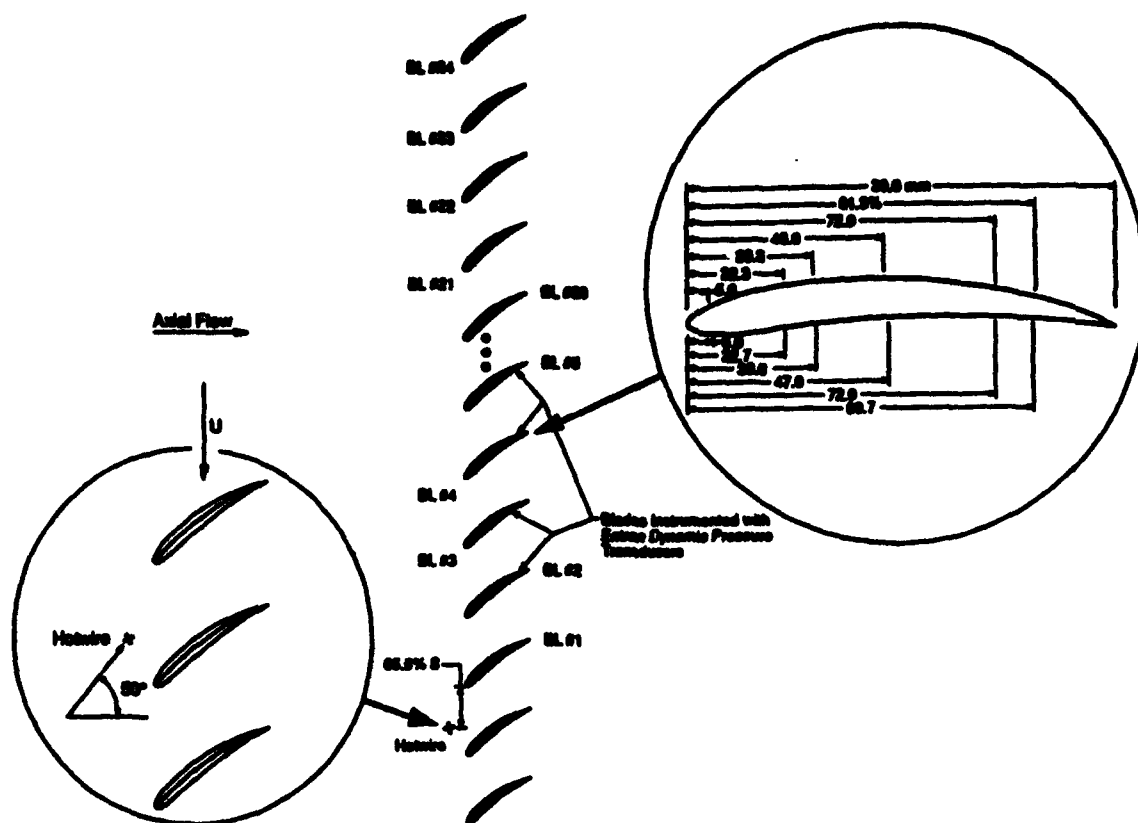


Fig. 1 Rotor instrumentation.

fects on the rotating hot-wire sensor resistances and thus the responses were found to be negligible.

The detailed steady aerodynamic loading on the rotor blade surfaces is measured with a chordwise distribution of 20 mid-span static pressure taps, 10 on each surface. The static pressure at the rotor exit plane, measured with a rotor drum static tap, is used as the blade surface static pressure reference. These static pressure measurements are made using a rotor based, 48-port constant speed drive Scanivalve system located in the rotor drum.

The measurement of the midspan rotor blade surface unsteady pressures is accomplished with 20 ultraminiature, high-response transducers embedded in the rotor blades at the same chordwise locations as the static pressure taps. To minimize the possibility of flow disturbances associated with the inability of the transducer diaphragm to exactly maintain the surface curvature of the blade, a reverse mounting technique is utilized. The pressure surface of one blade and the suction surface of the adjacent blade are instrumented, with transducers embedded in the nonmeasurement surface and connected to the measurement surface by a static tap. The embedded dynamic transducers are both statically and dynamically calibrated. The static calibrations show good linearity and no discernible hysteresis. The dynamic calibrations demonstrate that the frequency response, in terms of gain attenuation and phase shift, are not affected by the reverse mounting technique. The maximum error in gain and phase angle were determined to be 0.60 dB and 1.5 deg, respectively.

The rotor-based static pressure Scanivalve transducer, rotating cross hot-wire probe and 20 blade surface dynamic pressure transducers are interfaced to the stationary frame-of-reference through a 40-channel slip-ring assembly. On-board signal conditioning of the transducer output signals is performed to maintain a good signal-to-noise ratio through the slip rings. The remaining 17 channels of the slip-ring assembly are used to provide excitation to the transducers and on/off switching to the Scanivalve dc motor.

Data Acquisition and Analysis

Steady Pressure Data

The rotor blade surface static pressure data are defined by an rms error analysis of 20 samples with a 95% confidence interval. The airfoil surface static pressures are presented in terms of a nondimensional steady pressure coefficient, with the steady lift coefficient calculated by integrating the differential steady pressure coefficient across the rotor blade chord:

$$C_{p,i} = \frac{p_i - p_{\text{ref}}}{\rho W^2} \quad (1)$$

Since the blade surface and the reference static pressures are measured at different radii, a correction is applied to the exit steady pressure to account for centrifugal effects.¹⁴ The uncertainty in the steady pressure coefficient was estimated to be $\pm 5.6\%$.

Periodic Data

The periodic data of interest are the harmonic components of the aerodynamic forcing function to the first stage rotor blade row, together with the resulting rotor blade surface unsteady pressures and unsteady pressure differences. These are determined by defining a digitized ensemble-averaged periodic unsteady aerodynamic data set consisting of the rotating cross hot-wire probe and blade surface dynamic pressure transducer signals at each steady operating point. In particular, these time-variant signals are digitized with a high-speed analog-digital (A-D) system at a rate of 20 kHz and then ensemble averaged.

The key to this averaging technique is the ability to sample data at a preset time, accomplished by an optical encoder mounted on the rotor shaft. The microsecond range step voltage signal from the encoder is the data initiation time reference and triggers the high-speed A-D multiplexer system. To significantly reduce the random fluctuations superimposed on

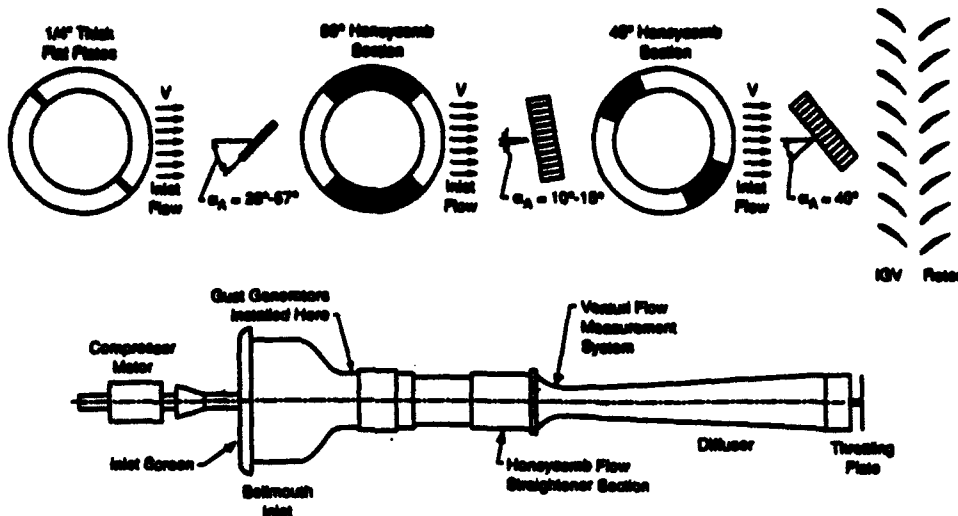


Fig. 2 Facility and gust generators.

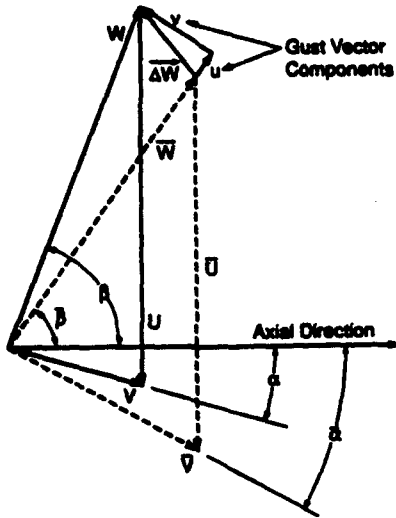


Fig. 3 Decomposition of rotor inlet velocity: —, instantaneous velocity triangle; ----, mean velocity triangle.

the periodic signals of interest. 200 averages are used. A fast Fourier transform (FFT) algorithm is then applied to these ensemble-averaged signals to determine the harmonic components of the unsteady aerodynamic forcing function and the resulting rotor blade surface harmonic unsteady pressures and pressure differences. Since ensemble averaging adequately separates the major frequency components, no windowing functions are applied to the data during FFT.

Forcing Function

The 2-E unsteady aerodynamic forcing functions are generated by two honeycomb sections and flat plates installed 180 deg apart in the compressor inlet, as illustrated in Fig. 2. These forcing functions are broadly categorized as attached flow and separated flow. The forcing function to the first-stage rotor, the unsteady rotor inlet flowfield, is measured with the rotating cross hot-wire probe which quantifies the relative velocity and flow angle. To the rotor, the flow from the upstream honeycombs or flat plates appear as deficits in the rotor relative inlet velocity W and fluctuations in the rotor relative inlet flow angle. Therefore, the total flow consists of freestream and wake regions, with the instantaneous value of W increased in the wake region and decreased in the freestream. The total rotor inlet relative velocity gust ΔW is the vector difference between the instantaneous and mean relative velocity W . It has two components, u and v , parallel and

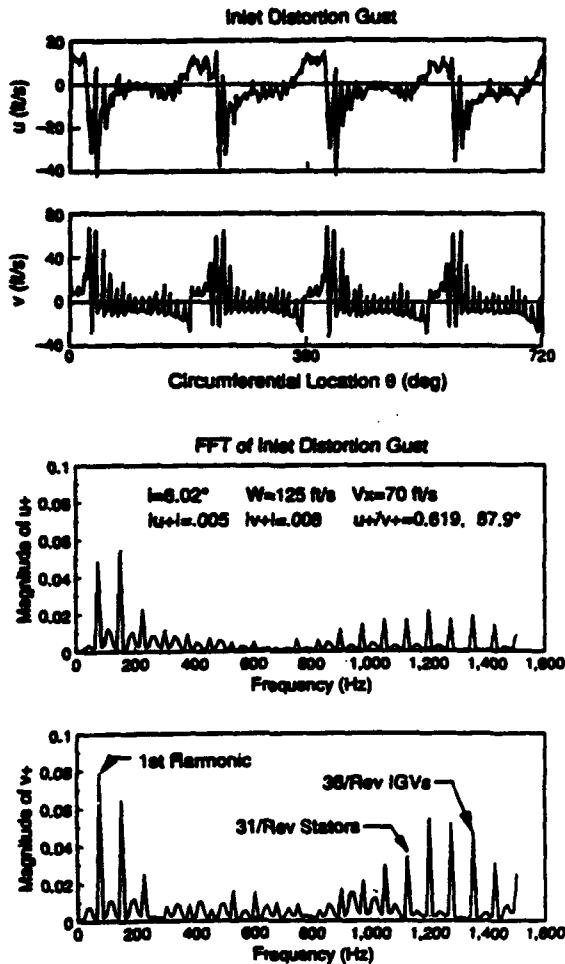


Fig. 4 Forcing function and streamwise and normal gust component FFT.

normal to the mean flow direction. The gust and its components are depicted in the velocity diagram of Fig. 3.

The fundamental frequency of interest is the 2-E forcing function frequency. Thus, an harmonic analysis is utilized in the data analysis, accomplished by taking the FFT of both the time variant rotor inlet flowfield and the resulting unsteady aerodynamic response of the first-stage rotor row, with only the components at the fundamental frequency or its harmonics analyzed. Figure 4 shows the streamwise and trans-

verse gust components and their FFT, with the u and v harmonics denoted by u' and v' , and nondimensionalized by the mean rotor relative velocity. This Fourier transformed inlet flow, defined by u' and v' , is the unsteady aerodynamic forcing function to the downstream rotor row.

Unsteady Pressure Data

The rotor blade pressure and suction surface unsteady pressure data are analyzed to determine the harmonics of the chordwise distribution of the unsteady pressure coefficient:

$$C_{p,u} = \frac{p'_u}{\rho W^2 v'} \quad (2)$$

The unsteady differential pressure coefficient is determined by subtracting the unsteady pressure coefficient on the suction surface from that on the pressure surface. The uncertainty in the unsteady pressure coefficient was estimated to be $\pm 6.7\%$. The resulting unsteady lift is calculated by integrating the unsteady differential pressure coefficient over the chord. Then the measured and predicted unsteady lift values are correlated by means of the unsteady lift ratio, with both the theoretical and experimental differential pressure coefficients integrated between the first and last chordwise positions of the experimental data:

$$L_{unsteady} = \frac{C_{l,exp}}{C_{l,theory}} = \frac{\frac{1}{c} \int_{x_1}^{x_2} \Delta C_{p,exp} dx}{\frac{1}{c} \int_{x_1}^{x_2} \Delta C_{p,theory} dx} \quad (3)$$

Note that if the experimental data are in exact agreement with the unsteady linear theory prediction, the unsteady lift ratio $L_{unsteady}$ will have a magnitude of 1.0 and a phase angle of 0 deg.

Results

A series of experiments are performed in the Purdue Axial Flow Research Compressor to investigate in a controlled manner the fundamental forcing function fluid dynamics generating different blade row gust responses effects, i.e., attached or separated flow, as well as steady loading effects on the resulting gust response of the first-stage rotor row. Attached flow forcing functions are generated by 90-deg honeycomb sections at 5–15-deg angle of attack (AOA), with separated flow forcing functions resulting from flat plates at 28–57-deg AOA, and 45-deg honeycomb sections at 40-deg AOA. With these gust generators, the gust ratio magnitude could be controlled without affecting the forcing function fluid dynamics, i.e., attached or separated flow, thereby enabling a controlled study of the effect of steady loading.

For each forcing function flow, four steady loading conditions, as characterized by the rotor relative mean flow incidence angles are studied: $i = -3, 0, 3,$ and 6 deg. The magnitude and phase of u'/v' as a function of loading for the 90- and 45-deg honeycombs and flat plates are shown in Fig. 5. At each steady loading, the magnitude of u'/v' is held relatively constant at 0.80 for the 90-deg honeycombs and the flat plates and at 0.62 for the 45-deg honeycomb. However, the resulting phase of u'/v' varies from 83 to 69 deg for the 90-deg honeycomb, from 96 to 88 deg for the 45-deg honeycomb, and from 59 to 63 deg with the flat plates.

Surface Steady Pressure Distributions

The chordwise rotor blade surface steady pressure distributions for the three forcing function flow types are presented in Fig. 6 for the low and high rotor steady loading levels, $i = -3$ and 6 deg. These data are compared with predictions from an incompressible, inviscid small camber airfoil cascade

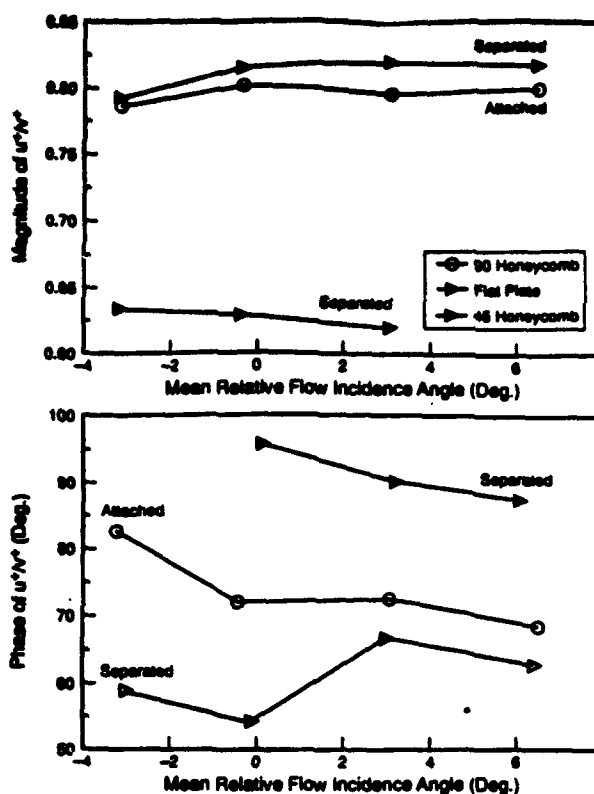


Fig. 5 Honeycomb and flat plate forcing functions.

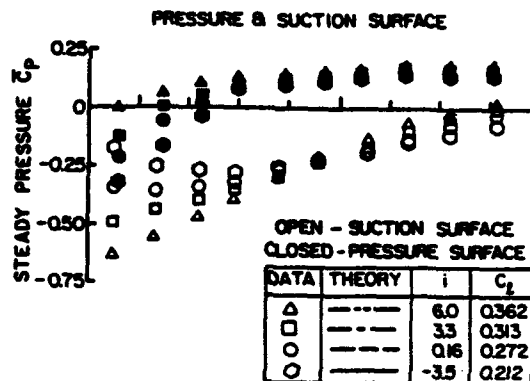


Fig. 6 Loading effect on rotor blade surface steady pressures.

analysis. The rotor blade surface steady pressure distribution is a function of the steady loading level, but independent of the forcing function.

In the pressure surface leading-edge region, the steady pressure coefficient increases with loading. It then increases until approximately 30% chord where it becomes constant, independent of the loading. In contrast, steady loading affects the suction surface over the entire chord, with the suction surface steady pressure coefficient a strong function of the steady

loading level. Note that there is no evidence of suction surface steady flow separation. With regard to the differential steady pressure coefficient, the leading-edge value is negative at negative values of the relative mean flow incidence, approximately zero at (l-deg incidence, increasing with increased loading. These data exhibit relatively good correlation with the predictions. The steady pressure data is accomplished by the mean rotor relative velocity measured with the rotor blades adjacent to the hot wire removed to determine the value of the mean rotor relative velocity W .

Honeycomb and Flat Plate Attached and Separated Flow Generated Forcing Functions

Figure 7 shows the Fourier decomposition of the 90-deg honeycomb attached flow forcing function. The dominant u' magnitude occurs at the fundamental frequency with the higher harmonic magnitudes decreased. The v' spectrum also has a dominant v' magnitude at the fundamental frequency, with the higher harmonic magnitudes decreasing rapidly.

The Fourier decomposition of the flat plate generated separated flow forcing function spectrum is presented in Fig. 7. In contrast to the attached flow forcing function, the fundamental frequency u' magnitude does not dominate and the higher harmonics are an integral part of the entire spectrum.

Similarly, no particular harmonic of v' dominates, and the magnitudes of all harmonics are large. In addition, there is a minimum v' harmonic.

The second separated flow forcing function is generated by the 45-deg honeycomb sections. The Fourier decomposition of this separated flow forcing function exhibits some differences as compared to the separated flow forcing functions generated by the flat plates (Fig. 7). The first two harmonics of u' dominate the spectrum, with the second harmonic being larger than the first, but the higher harmonics are of lower magnitude than the flat plate forcing function. The first three harmonics of v' and the harmonics near 1200 Hz are dominant in the v' spectrum, thereby producing a minimum v' harmonic, analogous to the flat plate separated forcing function.

These differences in the forcing function spectrum between the attached flow 90-deg honeycomb and the separated flow flat plates and 45-deg honeycomb are similar to the differences that resulted from changing the gust generating airfoil AOA from 5 to 20 deg," i.e., the magnitudes of the higher harmonics increase with flow separation relative to the fundamental frequency value leading to a more impulsive forcing function when the flow generating the gust is separated. These results indicate that attached and separated flow forcing functions have key characteristics that do not depend on the particular

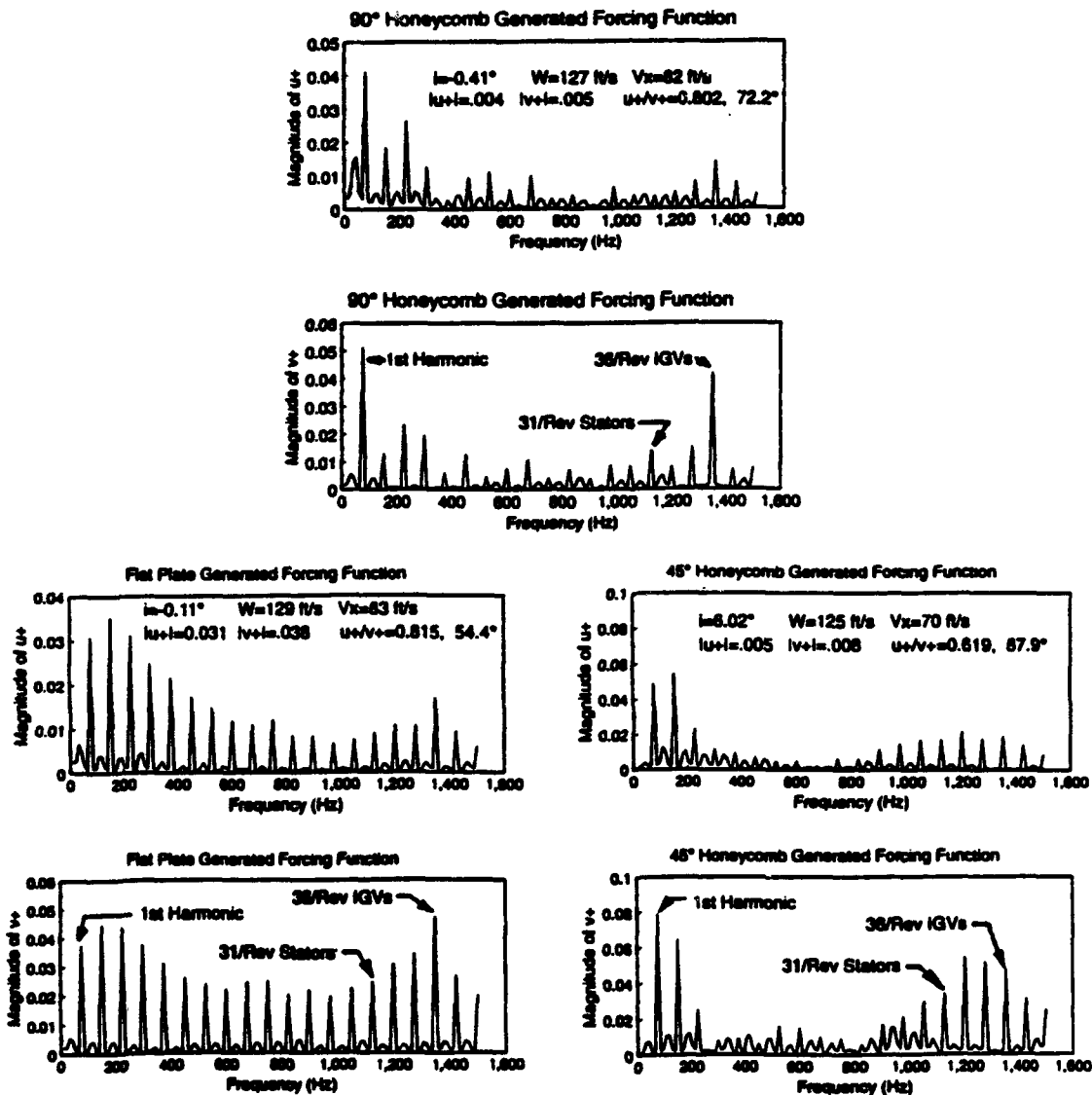


Fig. 7 FFT of forcing functions.

forcing function generator. Thus, the concept of attached and separated flow forcing functions is applicable to any gust generators exhibiting these key characteristics.

Forcing Function Generator Fluid Dynamic Effects on Gust Response

Pressure Surface

Figure 8 shows the pressure surface gust response from the 90-deg honeycomb attached flow generated forcing function. The magnitude data smoothly decrease with chord, becoming constant at approximately 20% chord, and have a small dependence on steady loading. The phase data are independent of steady loading and increase smoothly from the leading edge, becoming constant at approximately 40% chord.

The chordwise trends in the magnitude response data resulting from the flat plate and the 45-deg honeycomb separated flow generated forcing functions (Figs. 9 and 10) are generally the same as that of the 90-deg honeycomb attached flow generated response. However, the magnitude data from the flat plate separated flow generated forcing function are a stronger function of steady loading over the entire chord, with the 45-deg honeycomb separated flow generated response magnitude data independent of steady loading over the front 30% chord, then becoming a weak function of steady loading. In addition, the level of the magnitude data from the flat plate is smaller than that resulting from the attached flow 90-deg honeycombs and the separated flow 45-deg honeycombs, with the magnitude data levels generated by the honeycombs approximately the same.

The pressure surface phase response data are unchanged as the forcing function generator is altered from the 90-deg honeycombs with attached flow to the flat plates with separated flow and the 45-deg honeycombs with separated flow. In comparison to the pressure surface response data resulting from the NACA airfoil generated attached and separated flow forcing functions reported by Kim and Fleeter,⁹ the 90-deg honeycomb attached flow response differs significantly. However, the flat plate and 45-deg honeycomb separated flow forcing function generated responses agree in trend with those of the airfoil generated separated flow forcing function. These results reveal that the pressure surface gust response resulting from the attached flow generated forcing functions is sensitive to the particular forcing function generator, but that the pressure surface gust response resulting from separated flow generated forcing functions is less sensitive to the particular wake generator.

Suction Surface

Altering the attached flow forcing function from that generated by the 90-deg honeycombs to the separated flow forcing functions generated by the flat plates and the 45-deg honeycombs has a significant effect on the resulting suction surface gust response (Figs. 11-13). With the attached flow generated forcing function, the gust response magnitude rapidly decreases in the leading-edge region, becoming somewhat constant between 20-40% chord, then decreasing to a minimum near 50% chord. Aft of 55% chord, there is a large increase followed by a sudden decrease. Also, these magnitude data are a function of steady loading near the leading edge and aft of 55% chord.

As the forcing function generator flowfield is changed to separated flow, the resulting chordwise trends in the suction surface gust response from both the flat plate and the 45-deg honeycomb are similar to the attached flow forcing function generated gust magnitude response. However, the chordwise distribution of the magnitude data become smoother with the magnitude data decreasing more rapidly in the leading-edge region. Also, the flat plate separated flow forcing function generated gust magnitude data at the leading edge show little effect from steady loading changes. Rather, these magnitude data are strongly influenced by steady loading between 10%

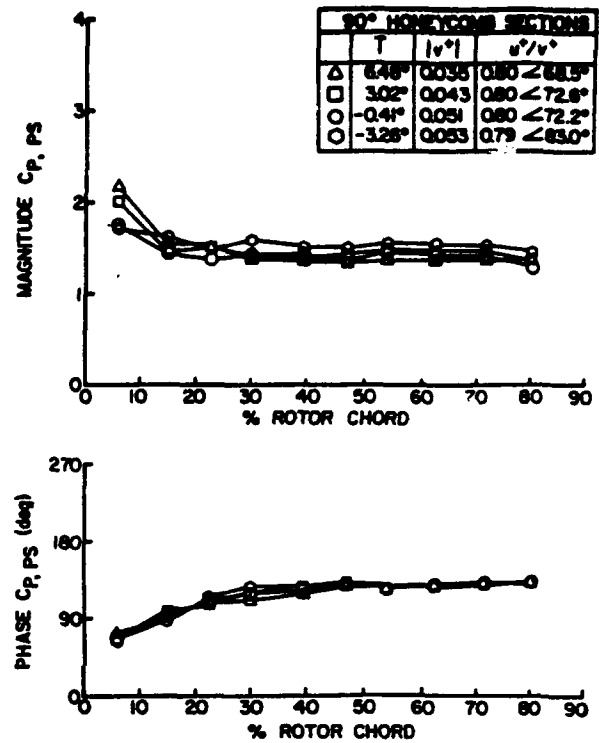


Fig. 8 Pressure surface 90-deg honeycomb attached flow generated gust response.

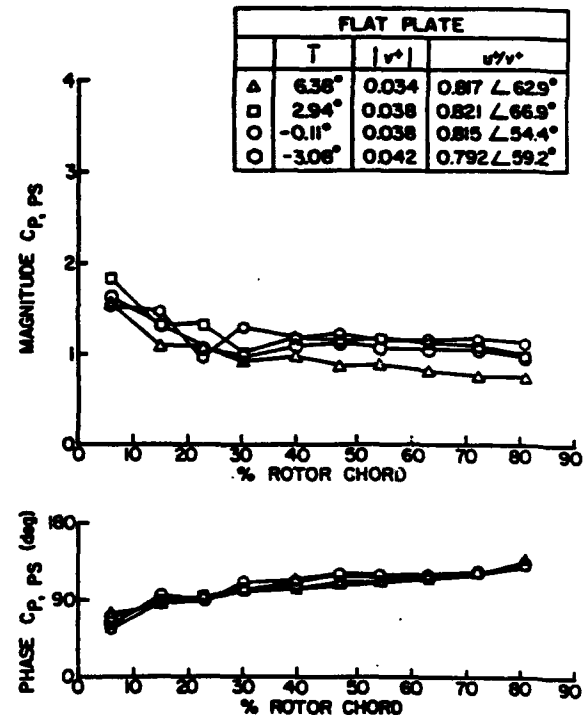


Fig. 9 Pressure surface flat plate separated flow generated gust response.

chord and the trailing edge. The gust magnitude data generated by the separated flow 45-deg honeycomb have similar trends over the front 40% chord, but become less dependent on steady loading aft of 40% chord.

With regard to the suction surface phase response data, the 90-deg honeycomb generated gust phase response is independent of steady loading over the front 20% chord and decreases gradually with chord, becoming a function of steady

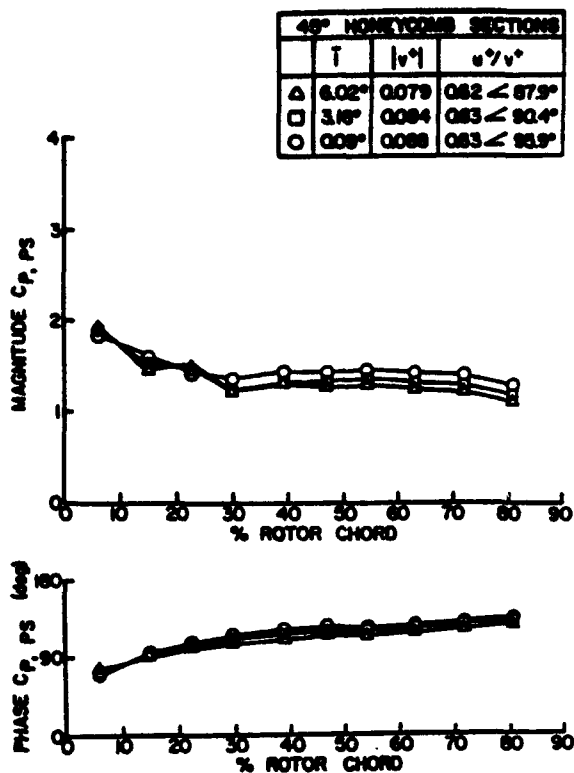


Fig. 10 Pressure surface 45-deg honeycomb separated flow generated gust response.

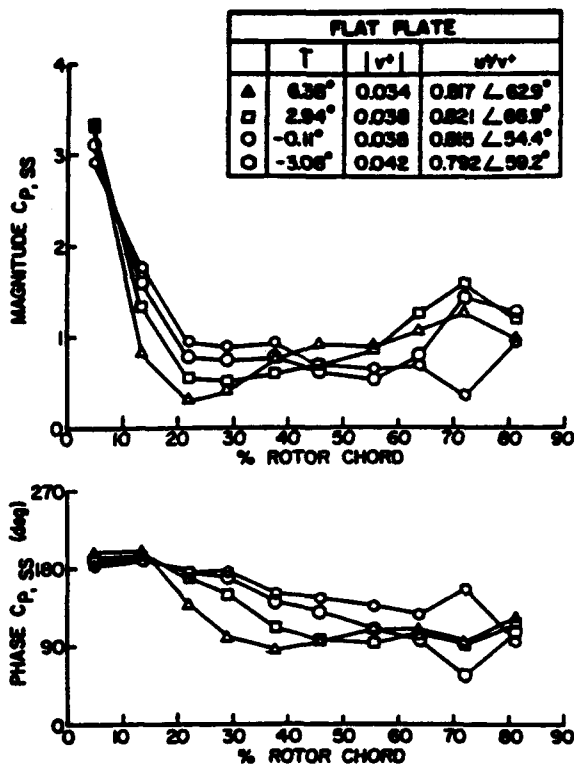


Fig. 12 Section surface flat plate separated flow generated gust response.

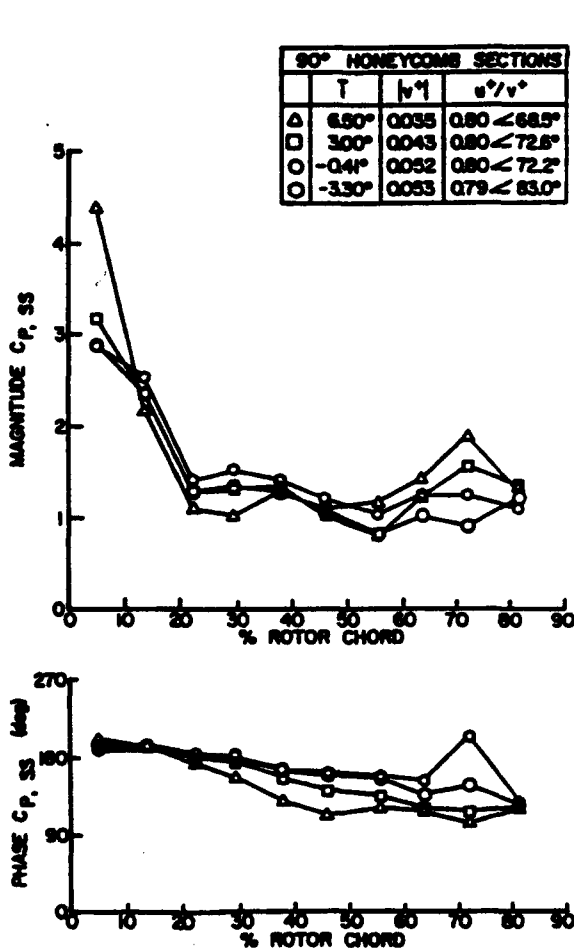


Fig. 11 Section surface 90-deg honeycomb attached flow generated gust response.

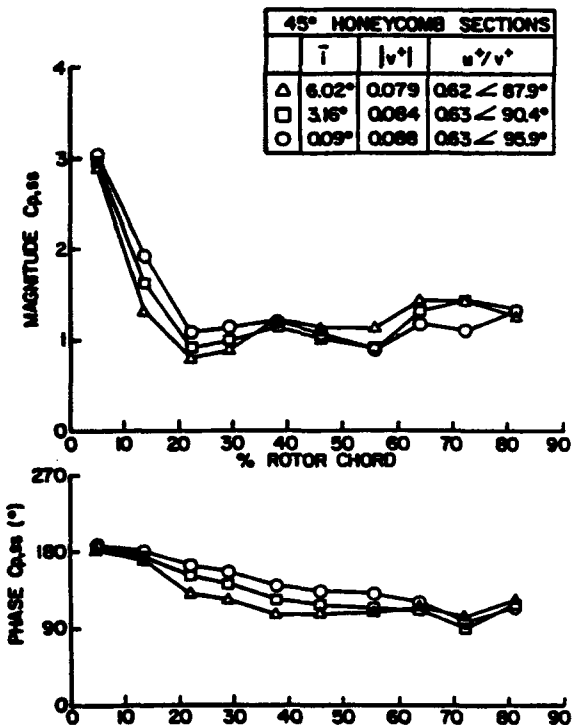


Fig. 13 Section surface 45-deg honeycomb separated flow generated gust response.

loading at approximately 20% chord for flow incidence angles of 3 and 6 deg. There is also a rapid increase and decrease in the gust phase response at 65% chord for the -3-deg flow incidence. The suction surface gust phase response from the flat plate and the 45-deg honeycomb forcing functions are very similar to that generated by the 90-deg honeycomb attached flow, but the steady loading dependence occurs at all levels (Figs. 12 and 13). These gust phase responses differ

from those resulting from the airfoil generated separated flow in that the chordwise position at which the large phase decrease starts moves forward.

As compared to the attached and separated flow generated suction surface responses of Kim and Fleeter,⁹ the chordwise trends in the suction surface response are similar for the magnitude data, but different for the phase data. Thus, the suction surface gust response magnitude appears to be less sensitive to the particular forcing function generator than the pressure surface gust response for both attached and separated flow forcing functions.

Unsteady Pressure Difference

As expected, based on the individual airfoil surface data, changes in the gust generator flowfield has a significant effect on the unsteady pressure difference. Figures 14-16 show the pressure difference gust response resulting from the 90-deg honeycomb attached flow forcing function, flat plate separated flow forcing function, and the 45-deg honeycomb separated flow forcing function. The pressure difference magnitude data decrease with chord, with the decrease in the leading-edge region being more rapid as the flow becomes separated and with increased steady loading. This results in good agreement between the attached flow 90-deg honeycomb generated pressure difference magnitude data and the linear theory prediction, with the agreement decreasing for the separated flow forcing function generated responses due to the flat plates and the 45-deg honeycombs.

The resulting gust pressure difference phase from the 90-deg honeycomb attached flow forcing function is independent of chord over the front 40% chord, becoming a strong function of steady loading, increasing in value with loading and chordwise position. The phase data are in poor agreement with theory, with the sudden increase in phase in the aft chord region not predicted by theory. When the forcing function flowfield is changed to separated flow, significant changes occur. Note that the gust phase responses due to the flat plate and 45-deg honeycomb separated flow forcing functions are nearly identical (Figs. 14 and 15). Unlike the attached flow generated response, the phase response increases with chord and steady loading over most of the chord. However, the

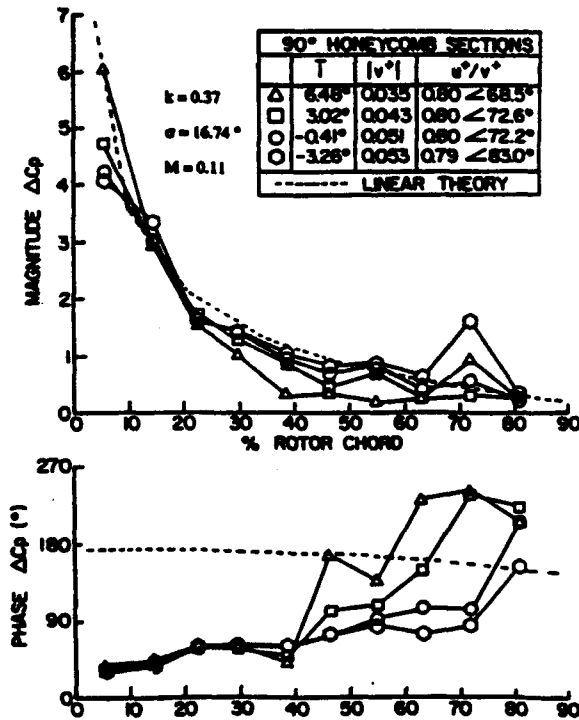


Fig. 14 Pressure difference 90-deg honeycomb attached flow generated gust response.

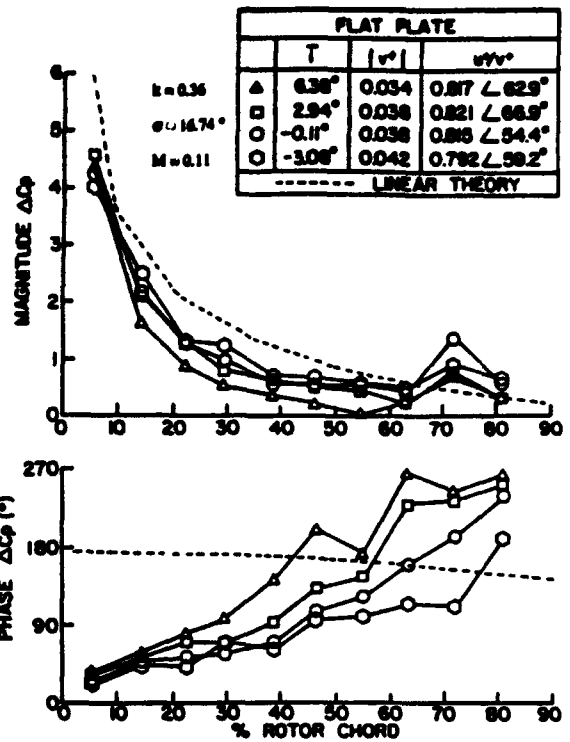


Fig. 15 Pressure difference flat plate separated flow generated gust response.

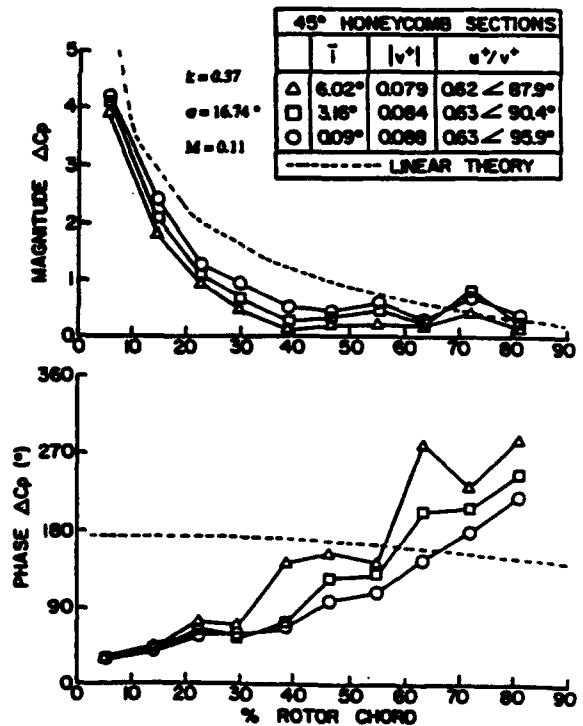


Fig. 16 Pressure difference 45-deg honeycomb separated flow generated gust response.

pressure difference phase data from the separated flow forcing functions are also in poor agreement with the linear theory predictions for both separated flow forcing functions.

These results, combined with those of the NACA airfoil generated responses, show that the unsteady pressure difference resulting from different gust generators with attached flow have similar magnitude trends, but not necessarily phase data trends. For separated flow generated forcing func-

tions of different gust generators, the responses have similar trends in both magnitude and phase. These differences in the pressure difference gust response among different gust generators are similar to those seen on the suction surface. This suggests that the suction surface gust response is dominant over the pressure surface gust response. Also, in general, the pressure and suction surface and the pressure difference responses resulting from attached flow forcing functions are more sensitive to the gust generator than the corresponding gust responses generated by separated forcing functions.

Unsteady Lift Correlation with Linear Theory

The deviation of the differential pressure coefficient data from the linear theory prediction is quantified through the unsteady lift coefficient ratio L_{corr} . Figure 17 shows the variation of L_{corr} with the mean flow incidence angle. The NACA 0024 airfoil generated data of Kim and Fleeter⁹ are also shown in these figures for comparison. In regard to the magnitude correlation, the 90-deg honeycomb attached flow generated forcing function correlates much better than the separated flow generated forcing functions—the flat plates and the 45-deg honeycombs.

These data further support the influence of forcing function flow separation on decreased correlation with linear theory, discovered by Kim and Fleeter.⁹ Furthermore, the effect of decreased magnitude correlation with steady loading is clearly evident in the nearly linear way in which the 90-deg honeycomb, flat plate, and the 45-deg honeycomb forcing function generated data correlation decreases with steady loading. These results are possible with the honeycombs and flat plates because the magnitude of the gust ratio, u^*/v^* could be controlled, which was not possible with the NACA 0024 airfoils. The pressure difference phase correlation with linear theory is unaffected by the forcing function fluid dynamics, i.e., attached or separated flow.

Forcing Function Fundamental Parameters

To begin to understand the fundamental differences between the response data generated by the attached and sep-

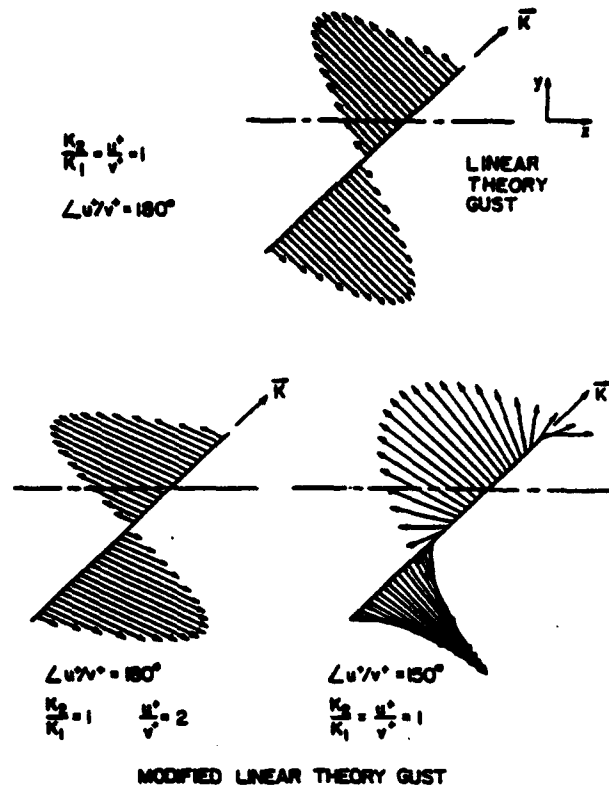


Fig. 18 Linear theory gust.

arated flow and the correlation of these data with linear theory, the validity of the unsteady linear theory model for these flows is considered. In particular, as considered by Henderson and Fleeter,^{11,12} linear theory requires that 1) the vortical gust vector components u^* and v^* are 180 deg out of phase; 2) the magnitude of u^*/v^* is equal to the ratio k_2/k_1 , determined from the steady flow velocity triangle; 3) the vortical gust vector is perpendicular to the direction of gust convection; and 4) the vortical gust vectors are parallel to one another. Note the presence of these features in the linear theory vortical gust, shown in Figure 18. When assumptions 1 and 2 are valid, the gust automatically satisfies assumptions 3 and 4. However, if these assumptions are not satisfied, the character of the vortical gust changes in the manner shown in Fig. 18. When the phase angle requirement is violated, the gust vectors become nonperpendicular to the direction of gust convection, whereas when the wave number to gust magnitude equivalency is violated, the gust vectors become nonparallel.

The importance of the gust ratio phase angle with regard to the applicability of linear theory to turbomachine blade rows is illustrated by the consideration of the first linear theory assumption: the streamwise and transverse vortical gust components, u^* and v^* , are 180 deg out of phase. This assumption is violated independent of whether the forcing function gusts are generated by separated or attached flows. For all of the experiments, the phase of u^*/v^* was generally near 70 deg. The significance of the gust ratio phase parameter for the pressure difference phase data-theory correlation is evident in Fig. 19, which shows L_{corr} as a function of the gust ratio phase. Note that the honeycomb and flat plate generated phase data, along with the 5-deg AOA 6-deg incidence NACA 0024 airfoil generated phase data with a gust ratio phase equal to 54 deg, correlate significantly better than the other NACA 0024 airfoil generated phase data, having gust ratio phase angles less than 32 deg. Hence, the violation of the 180-deg phase requirement is an important factor in the correlation of the pressure difference phase data with linear vortical gust theory.

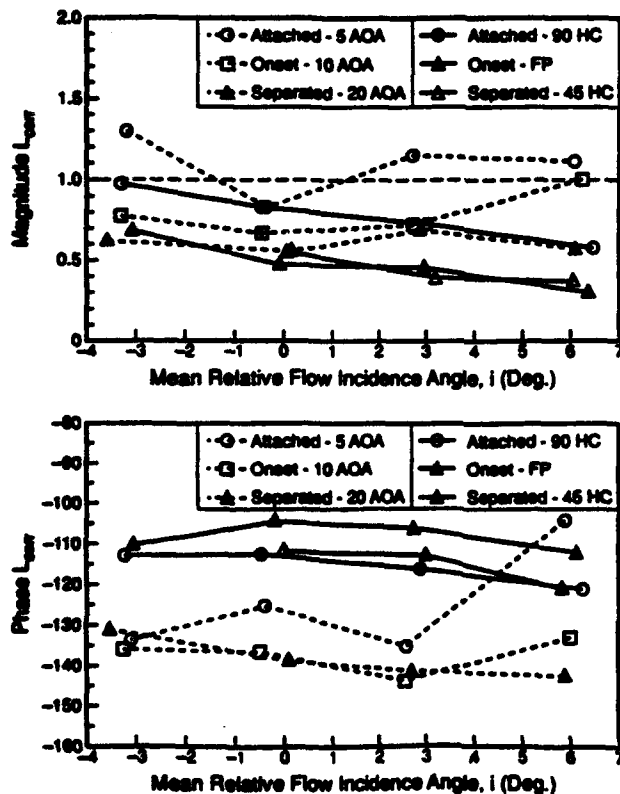


Fig. 17 Unsteady lift ratio correlation.

Table 2 Unsteady $|u^*/v^*|$ and steady flow k_2/k_1 values

Steady loading, Γ		-3 deg	0 deg	3 deg	6 deg
Forcing functions					
Attached flow (90-deg honeycombs)	$ u^*/v^* $	0.787	0.802	0.797	0.800
	k_2/k_1	0.288	0.230	0.201	0.150
	% Difference	173%	249%	297%	433%
Separated flow (flat plates)	$ u^*/v^* $	0.792	0.815	0.821	0.817
	k_2/k_1	0.300	0.250	0.124	0.104
	% Difference	168%	226%	562%	686%
Separated flow (45-deg honeycombs)	$ u^*/v^* $	—	0.634	0.628	0.620
	k_2/k_1	—	0.232	0.176	0.121
	% Difference	—	173%	257%	412%

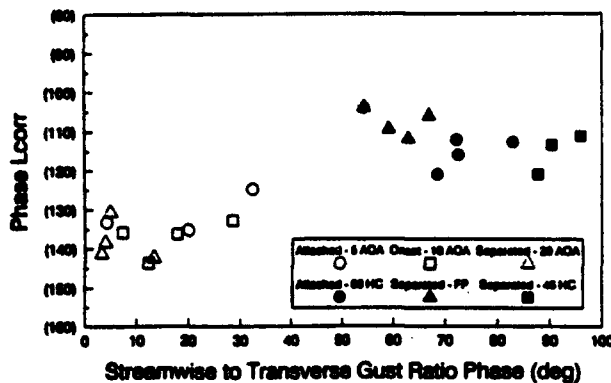


Fig. 19 Unsteady lift ratio variation with gust component ratio.

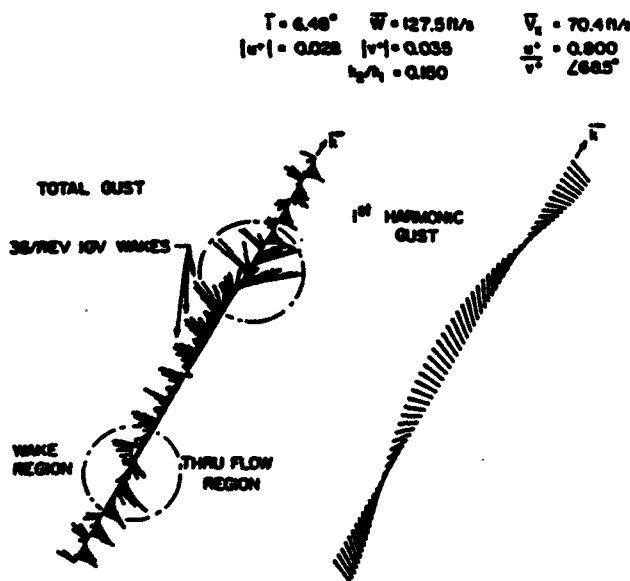


Fig. 20 90-deg honeycomb attached flow generated unsteady aerodynamic gust.

Linear theory also requires the magnitude of the vortical gust component ratio u^*/v^* be equal to the ratio k_2/k_1 , the wave number ratio calculated from the steady velocity data. This assumption is grossly violated as evident in Table 2. There is not a single case for which the two values agree. In fact, the unsteady u^*/v^* values are 2-5 times greater than that of the steady k_2/k_1 values.

The effect of violating the above assumptions on the unsteady aerodynamic gust may be reflected in the interesting trend apparent in the first harmonic gust vectors. These gust vectors represent the spatial distribution of the forcing function aerodynamic gust vector, ΔW , in the direction of gust

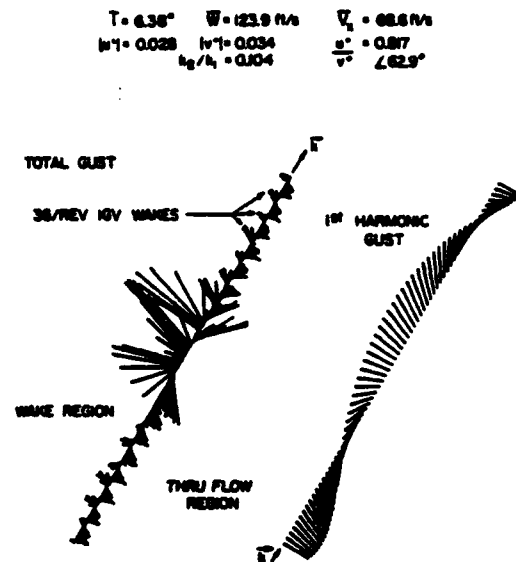


Fig. 21 Flat plate separated flow generated unsteady aerodynamic gust.

convection. This spatial distribution of the gust vector is constructed by plotting the temporal variations in ΔW spatially in the direction of gust convection, with the magnitude and direction with respect to k maintained. The maximum magnitude of the first harmonic gust vectors from the 90-deg honeycomb attached flow (Fig. 20), the flat plate separated flow (Fig. 21), and the 45-deg honeycomb separated flow (Fig. 22) are all in the midwake and midthrough flow regions. Thus, the gust vectors form a shape that is somewhat sinusoidal. In particular, note the symmetry of the 45-deg honeycomb first harmonic gust vectors with the largest gust ratio phase angle of 87.9 deg (Fig. 22). Kim and Fleeter⁶ had discovered that the gust shapes were skewed-sinusoidal when the gust phase angles were near zero. Thus, the first harmonic gust vectors are influenced significantly by the gust ratio phase angle, independent of the forcing function fluid dynamics. This supports the findings of Kim and Fleeter that the gust ratio phase angles closer to 180 deg produce wakes that resemble more the linear theory gust.

The prevalence of the sinusoid shape for these three gust vectors, despite the different levels of discrepancy between the magnitude of u^*/v^* and k_2/k_1 , support the findings of Kim and Fleeter⁶ that the gust ratio phase angle is the dominant factor in the gust shape determination than the matching of u^*/v^* magnitude to k_2/k_1 .

The violation of the first two assumptions leads to the violation of the last two assumptions, resulting in gust vectors which are neither parallel to one another nor perpendicular to the direction of wake convection. The assumptions of perpendicularity between the vortical gust vectors and the di-

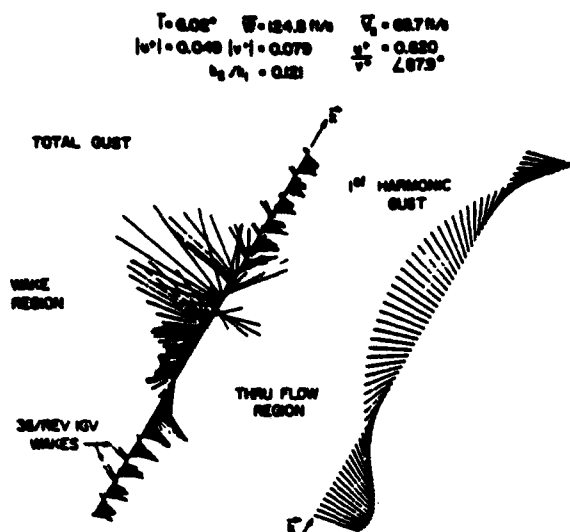


Fig. 22 45-deg honeycomb separated flow generated unsteady aerodynamic gust.

rection of the vortical gust convection k are clearly inappropriate, as demonstrated in Figs. 18–20 which show the honeycomb and flat plate generated total and first harmonic gust vectors that are convected over the rotor blade. Note that few, if any, of the vectors in the total gust are perpendicular to the direction of convection. In fact, what is evident is a fanning out trend of the vectors in the wake region that increases with increased forcing function flow separation. Note, in all these cases, the 36/rev IGV wakes are embedded within the larger 2/rev NACA airfoil wake in the total gust. The 2/rev total gust vectors from the 90-deg honeycomb attached flow differ from those of the 5-deg AOA airfoil with attached flow, with the 2/rev gust vectors of the honeycombs crossing only in the edges of the wake region, shown as circled regions in Fig. 20, but fan in the wake region. However, this fanning may be due to the IGV wakes since the total gust magnitudes of the IGV are of the same order of magnitude as the honeycomb total gust magnitude. The total gust vectors from the separated flow plate and 45-deg honeycomb (Figs. 21 and 22) continuously fan over the entire wake region. In summary, the total gust vectors are not perpendicular to the direction of gust convection, nor are they parallel to one another. For most wake generators, regardless of type, the gust vectors start being crossed with attached flow and fan with increased separation, with the fanning being particularly wide for more separated flows. These results indicate that the total forcing function gust vectors are largely affected by the forcing function fluid dynamics, in contrast to the first harmonic gust vectors.

Therefore, the consideration of some essential assumptions inherent in the unsteady linear vortical gust theory indicate that these assumptions are not appropriate for turbomachine blade rows and cannot be applied. The poor data-theory correlation of the resulting blade row unsteady aerodynamic response suggests an intimate relationship between the characteristics of the gust vector and the degree of correlation of the compressor blade row unsteady aerodynamic gust response data with linear theory. Current models do not incorporate the specific details of the gust such as the gust ratio phase angle. Instead, since certain characteristics are inherent in the current linear theory model, any deviation from these characteristics would contribute to an error in the prediction value of the unsteady aerodynamics. Hence, advancements in the gust modeling technique to include parameters, such as the gust ratio phase angle, the gust ratio magnitude, and potential effects are critical to improving the ability to predict blade unsteady pressure response.

Summary and Conclusions

A series of experiments were performed to investigate the fundamental forcing function phenomena fluid dynamics generating different blade row gust responses in a controlled manner, including the important effects associated with the forcing function gust magnitude. This was accomplished through the investigation of unsteady aerodynamic blade row response to gusts generated by attached and separated flow fluid dynamics from nonairfoil shape gust generators. With these gust generators, the gust ratio magnitude can be controlled without affecting the forcing function fluid dynamics, i.e., attached or separated flow, thereby enabling a controlled study of the effect of steady loading.

These experiments clearly show that the forcing function generator fluid dynamics is significant with regard to the resulting unsteady aerodynamic gust response of a downstream airfoil row, while enabling a controlled study of the effect of steady loading for the first time. The applicability of the concept of attached and separated flow forcing functions and the resulting unsteady aerodynamic response is broadened over previous data⁷ to include nonairfoil shape gust generators. It was shown that although differences in the individual surface responses occur, gust generator flowfields can be broadly categorized into attached or separated flow forcing functions, with the resulting gust response correlation with linear theory models predictable. In particular, the attached flow and separated flows generate large and important differences in forcing function characteristics and the resulting unsteady aerodynamic blade row gust response, such that the correlation with linear theory decreases with increased forcing function flow separation. Steady loading is found to linearly decrease the unsteady aerodynamic pressure difference data-theory correlation.

The forcing function fluid dynamics was analyzed in terms of the requirements inherent in the linear theory vortical gust modeling. This showed that the forcing function violation of the 180-deg phase requirement between the streamwise and transverse gust components contributed to the poor data-theory phase correlation, and that the addition of the values of $|u'/v'|$ and k_2/k , not being equal leads to unsteady gust vectors which are neither parallel to one another nor perpendicular to the direction of wake convection, as also inherent in linear theory vortical gust models. Thus, the degree of correlation of the rotor blade unsteady gust response data with linear theory is closely related to the characteristics of the forcing function gust generating the response.

Acknowledgment

Research was sponsored by the Air Force Office of Scientific Research (AFSC) under Contract F49620-88-C-0022.

References

- Whitehead, D. S., "Classical Two-Dimensional Methods," *AGARDograph No. 298, AGARD Manual on Aeroelasticity in Axial Flow Turbomachines, Volume 1: Unsteady Turbomachinery Aerodynamics*, pp. 3.1–3.30.
- Fleeter, S., "The Fluctuation Lift and Moment Coefficients for Cascaded Airfoils in a Nonuniform Compressible Flow," *Journal of Aircraft*, Vol. 10, No. 2, 1973, pp. 93–98.
- Adamczyk, J. J., and Goldstein, M. E., "Unsteady Flow in a Supersonic Cascade with Subsonic Leading Edge Locs," *AIAA Journal*, Vol. 16, No. 12, 1978, pp. 1248–1254.
- Verdon, J. M., and Usab, W. J., "Application of a Linearized Unsteady Aerodynamic Analysis to Standard Cascade Configurations," *American Society of Mechanical Engineers Paper 90-GT-11*, June 1990.
- Verdon, J. M., and Hall, K. C., "Development of a Linearized Unsteady Aerodynamic Analysis for Cascade Gust Response Predictions," *NASA Rept. 4308*, July 1990.
- Scott, J. S., and Atassi, H. M., "Numerical Solutions of the Linearized Euler Equations for Unsteady Vortical Flows Around Lifting Airfoils," *AIAA Paper 90-0694*, Jan. 1990.

Fang, J., "Compressible Flows with Vortical Disturbances Around Cascades of Airfoils," Ph.D. Dissertation, Univ. of Notre Dame, Notre Dame, IN, April 1991.

Manwaring, S. R., and Fleeter, S., "Forcing Function Effects on Rotor Periodic Aerodynamic Response," *Journal of Turbomachinery*, Vol. 113, No. 2, 1991, pp. 312-319.

Kim, K. H., and Fleeter, S., "Compressor Blade Row Unsteady Aerodynamic Response to Attached and Separated Flow Forcing Functions," AIAA Paper 92-0147, Jun. 1992.

Smith, S. N., "Discrete Frequency Sound Generation in Axial

Flow Turbomachines," Aeronautical Research Council R&M 3709, Great Britain, UK, March 1972.

Henderson, G. H., and Fleeter, S., "Forcing Function Effects on Unsteady Aerodynamic Gust Response: Part I Forcing Functions," American Society of Mechanical Engineers Paper 92-GT-174, June 1992.

Henderson, G. H., and Fleeter, S., "Forcing Function Effects on Unsteady Aerodynamic Gust Response: Part II Low Solidity Airfoil Row Response," American Society of Mechanical Engineers Paper 92-GT-175, June 1992.

APPENDIX IV**Compressor Blade Row Unsteady Aerodynamic Response to Attached and Separated Flow****Forcing Functions**

AIAA Paper 92-0147 January 1992
(also International Journal of Turbo & Jet Engines, in press)

COMPRESSOR BLADE ROW UNSTEADY AERODYNAMIC RESPONSE TO ATTACHED AND SEPARATED FLOW FORCING FUNCTIONS

Kuk H. Kim and Sanford Fleeter
School of Mechanical Engineering
Purdue University
West Lafayette, Indiana 47907

Abstract

A series of experiments are performed to investigate the fundamental flow forcing function phenomena generating different blade row gust responses, in particular attached and separated flow forcing functions. Furthermore, unsteady linear theory gust requirements are considered. Two NACA 0024 airfoils are installed in an extensively instrumented axial flow compressor inlet to generate the periodic 2-E unsteady aerodynamic forcing functions to the first stage rotor. These forcing functions are measured with a rotating cross hot-wire, with the resulting rotor blade row unsteady aerodynamic gust response measured with dynamic pressure transducers embedded in the rotor blade over a range of steady loading levels. The rotor blade gust response unsteady aerodynamic data are then correlated with appropriate predictions. These experiments revealed the new result that the forcing function generator fluid dynamics is significant with regard to the resulting unsteady aerodynamic gust response of the downstream airfoil row. Namely, the degree of correlation of the rotor blade unsteady gust response data with linear theory is closely related to the characteristics of the forcing function gust generating the response.

Nomenclature

\bar{C}_l	steady lift coefficient
$C_{p,ps}$	pressure surface complex unsteady pressure coefficient
$C_{p,ss}$	suction surface complex unsteady pressure coefficient
$\Delta C_p, C_{\Delta p}$	complex unsteady pressure difference coefficient
\bar{C}_{pi}	steady pressure coefficient at i^{th} chord position
$\bar{C}_{p,p}$	pressure surface steady pressure coefficient
$\bar{C}_{p,s}$	suction surface steady pressure coefficient
$\Delta \bar{C}_p$	steady pressure difference coefficient
i	rotor relative flow incidence angle
\bar{i}	mean rotor relative flow incidence angle
p_1	1 st harmonic of Fourier decomposed pressure
P_{exit}	static pressure at rotor exit
u	streamwise gust component
u^+	1 st harmonic streamwise gust component
U	flow velocity or wheel speed
v	transverse gust component
v^+	1 st harmonic transverse gust component
\bar{V}_x	mean axial velocity
w	instantaneous rotor relative velocity
\bar{W}	mean rotor relative velocity
α	absolute flow angle
$\bar{\alpha}$	mean absolute flow angle
β	rotor relative flow angle
$\bar{\beta}$	mean rotor relative flow angle

Introduction

The spatial flow nonuniformities generated by inlet guide vanes, stator vanes and struts are periodic temporal variations to downstream rotor blades. These spatial flow nonuniformities in the stationary frame of reference are sources of periodic excitation to the rotor blades. When the frequency of these periodic flow nonuniformities coincides with a blade natural frequency, fatigue failure of the rotor blade may result, thereby compromising the durability of the engine.

The prediction of the flow induced vibratory response of a blade row first requires a definition of the unsteady aerodynamic forcing function in terms of its harmonics, with each harmonic independently considered. Thus, even though forcing functions may be generated by a wide variety of fundamentally different sources, the forcing functions are assumed to be equivalent if their harmonics are the same. The unsteady aerodynamic response of the blade row to each forcing function harmonic is then assumed to be comprised of two components: the disturbance being swept past the nonresponding airfoils, termed the gust unsteady aerodynamic and the airfoil vibratory response to this disturbance, referred to as the motion-induced unsteady aerodynamics or the aerodynamic damping.

Early treatments of unsteady flow due to periodic gusts were developed in the linear approximation wherein the mean flow is assumed to be uniform. In this approximation, the steady and unsteady flow fields are completely uncoupled from one another, with the upstream generated periodic gust aerodynamic forcing functions convected with the uniform mean flow. Semi-analytical unsteady aerodynamic analyses based on this linear model have been developed for cascades in subsonic and supersonic flows [1,2,3,4]. Such models are currently being extended to consider unsteady flows linearized about a nonuniform mean flow, with the gust interacting with the mean flow [5,6,7].

A number of experiments have been directed at the verification of such mathematical models and the determination of their applicability and limitations. As a generalization, it appears that if the assumptions inherent in these analyses are modeled, then the experiments provide data which are in agreement with the predictions. However, if actual compressor operating conditions, i.e., finite camber, steady loading and nonzero incidence angle, are experimentally modeled, then the data-prediction correlation is not nearly as good.

Of particular interest herein are the experiments which investigated the unsteady aerodynamic response of a research compressor rotor performed by Manwaring and Fleeter [8]. The first harmonic gust response of the 1st stage rotor generated by two equivalent 2-per-revolution (2-E) unsteady forcing functions were measured: (1) an inlet flow distortion and (2) the wakes behind flat plate airfoils. The inlet distortion and wake first harmonic unsteady aerodynamic forcing functions were fundamentally equivalent, having the same gust characteristics including the ratio of the streamwise-to-normal gust components u^+/v^+ and reduced frequency values.

The first harmonic gust response of the 1st stage rotor generated by these two different but equivalent forcing functions is presented in Figure 1. Clearly, the first harmonic gust response unsteady aerodynamics, shown in the form of the

chordwise variation of the complex unsteady pressure difference across the rotor blade chord, are dependent on the particular forcing function. However, because the two first harmonic forcing functions are equivalent in terms of classical unsteady aerodynamic theory, these results can not be predicted.

In this paper, this interesting result is further investigated. The fundamental flow forcing function phenomena generating different blade row gust responses are investigated, in particular attached and separated flow forcing functions. Furthermore, unsteady linear theory gust requirements are considered. This is accomplished through a series of experiments performed in the extensively instrumented Purdue Axial Flow Research Compressor. Two NACA 0024 airfoils are installed in the compressor inlet to generate the periodic 2-E unsteady aerodynamic forcing functions to the first stage rotor. These forcing functions are measured with a rotating cross hot-wire, with the resulting rotor blade row unsteady aerodynamic gust response measured with dynamic pressure transducers embedded in the rotor blade over a range of steady loading levels. Appropriate rotor blade gust response unsteady aerodynamic data are then correlated with predictions from the subsonic unsteady aerodynamic flat plate cascade analysis of Smith [9].

Research Compressor

The Purdue Axial Flow Research Compressor models the fundamental turbomachinery unsteady aerodynamic multistage interaction phenomena which include the incidence angle, the velocity and pressure variations, the aerodynamic forcing function waveforms, the reduced frequency, and the unsteady blade row interactions. The compressor is driven by a 15 HP DC electric motor at a speed of 2,250 RPM. Each identical stage contains 43 rotor blades and 31 stator vanes having a British C4 airfoil profile, with the first stage rotor inlet flow field established by an inlet guide vane (IGV) row of 36 airfoils. The 2-E unsteady aerodynamic forcing functions are generated by two NACA 0024 profile airfoils installed 180° apart in the compressor inlet. The overall compressor and airfoil characteristics are defined in Table 1.

The compressor aerodynamic performance is determined utilizing a 48 port Scanivalve system, thermocouples, and a venturi orifice to measure the required pressures, temperatures and flow rate, respectively. The Scanivalve transducer is calibrated each time data are acquired, thus automatically compensating for zero and span shifts of the transducer output. A 95% confidence interval, root-mean-square error analysis of 20 samples is performed for each steady data measurement.

Instrumentation

Both steady and unsteady rotor blade row data are obtained. The steady data quantify the rotor row mean inlet flowfield and the resulting rotor blade midspan steady loading distribution. The unsteady data define the periodic aerodynamic forcing function and the resulting midspan blade surface periodic unsteady pressure distributions.

The inlet flow field, both steady and unsteady, is measured with a rotating cross hot-wire probe. The inlet flow field of the 1st stage rotor row is measured in the rotating frame of reference by mounting the hotwire on the rotor drum 18.8% chord upstream and 65% blade spacing from a rotor blade. The hotwire is oriented for maximum sensitivity, achieved when the 0° flow incidence corresponds to the position at which the flow angle is 45° to both wires. The hotwire is calibrated for velocities from 21.3 m/s to 62.5 m/s and ±40° flow angle variations. The uncertainties in the velocity and the flow angle measurements were determined to be 5% and ± 0.5°. Centrifugal loading effects on the rotating hot-wire sensor resistances and thus the responses were found to be negligible.

The detailed steady aerodynamic loading on the rotor blade surfaces is measured with a chordwise distribution of 20 midspan static pressure taps, 10 on each surface. The static pressure at the rotor exit plane, measured with a rotor drum static tap, is used as the blade surface static pressure reference. These static pressure measurements are made using a rotor based 48 port constant speed drive Scanivalve system located in the rotor drum.

The measurement of the midspan rotor blade surface unsteady pressures is accomplished with 20 ultra-miniature, high response transducers embedded in the rotor blades at the same chordwise locations as the static pressure taps. To minimize the possibility of flow disturbances associated with the inability of the transducer diaphragm to exactly maintain the surface curvature of the blade, a reverse mounting technique is utilized. The pressure surface of one blade and the suction surface of the adjacent blade are instrumented, with transducers embedded in the nonmeasurement surface and connected to the measurement surface by a static tap. The embedded dynamic transducers are both statically and dynamically calibrated. The static calibrations show good linearity and no discernible hysteresis. The dynamic calibrations demonstrate that the frequency response, in terms of gain attenuation and phase shift, are not affected by the reverse mounting technique. The maximum error in gain and phase angle were determined to be 0.60 dB and 1.5° respectively.

The rotor-based static pressure Scanivalve transducer, rotating cross hot-wire probe and 20 blade surface dynamic pressure transducers are interfaced to the stationary frame-of-reference through a 40 channel slip ring assembly. On-board signal conditioning of the transducer output signals is performed to maintain a good signal-to-noise ratio through the slip rings. The remaining 17 channels of the slip-ring assembly are used to provide excitation to the transducers and on/off switching to the Scanivalve DC motor.

Data Acquisition and Analysis

Steady Pressure Data

The rotor blade surface static pressure data are defined by a root-mean-square error analysis of 20 samples with a 95% confidence interval. The airfoil surface static pressures are presented in terms of a nondimensional steady pressure coefficient, with the steady lift coefficient calculated by integrating the differential steady pressure coefficient across the rotor blade chord.

$$\bar{C}_{p,i} = \frac{\bar{P}_i - \bar{P}_{\text{exit}}}{\rho W^2} \quad (1)$$

Since the blade surface and the reference static pressures are measured at different radii, a correction is applied to the exit steady pressure to account for centrifugal effects [8].

Periodic Data

The periodic data of interest are the harmonic components of the aerodynamic forcing function to the first stage rotor blade row together with the resulting rotor blade surface unsteady pressures and unsteady pressure differences. These are determined by defining a digitized ensemble averaged periodic unsteady aerodynamic data set consisting of the rotating cross hot-wire probe and blade surface dynamic pressure transducer signals at each steady operating point. In particular, these time-variant signals are digitized with a high speed A-D system at a rate of 20 kHz and then ensemble averaged.

The key to this averaging technique is the ability to sample data at a preset time, accomplished by an optical encoder mounted on the rotor shaft. The microsecond range step voltage signal from the encoder is the data initiation time reference and

triggers the high speed A-D multiplexer system. To significantly reduce the random fluctuations superimposed on the periodic signals of interest, 200 averages are used. A Fast Fourier Transform (FFT) algorithm is then applied to these ensemble averaged signals to determine the harmonic components of the unsteady aerodynamic forcing function and the resulting rotor blade surface harmonic unsteady pressures and pressure differences.

Forcing Function

The 2-E unsteady aerodynamic forcing functions are generated by two NACA 0024 profile airfoils installed 180° apart in the compressor inlet. Forcing functions broadly categorized as attached flow, onset of separated flow, and fully separated flow, are generated by varying the angle of attack (AOA) of the two NACA 0024 profile airfoils from 5° to 10° to 20°. The point of separation of 10° is based on wind tunnel tests. Note that since the airfoils are set at a fixed angle of attack, the values of the resulting streamwise-transverse gust ratio depend on the compressor steady loading level.

The forcing function to the 1st stage rotor, the unsteady rotor inlet flow field, is measured with the rotating cross hot-wire probe which quantifies the relative velocity and flow angle. To the rotor, the flow from the upstream NACA 0024 airfoils appear as deficits in the rotor relative inlet velocity W and fluctuations in the rotor relative inlet flow angle β . Thus, the total flow consists of freestream and wake regions, with the instantaneous value of W increased in the wake region and decreased in the freestream. The total rotor inlet relative velocity gust ΔW is the vector difference between the instantaneous and mean relative velocity \bar{W} . It has two components, u and v , parallel and normal to the mean flow direction. The gust and its components are depicted in the velocity diagram of Figure 2.

The fundamental frequency of interest is the 2-E forcing function frequency. Thus, an harmonic analysis is utilized in the data analysis, accomplished by taking the Fast Fourier Transforms (FFT) of both the time variant rotor inlet flow field and the resulting unsteady aerodynamic response of the 1st stage rotor row, with only the components at the fundamental frequency or its harmonics analyzed. Figure 3 shows the streamwise and transverse gust components and their FFT, with the u and v harmonics denoted by u^+ and v^+ and nondimensionalized by the mean rotor relative velocity. This Fourier transformed inlet flow, defined by u^+ and v^+ , is the unsteady aerodynamic forcing function to the downstream rotor row.

Unsteady Pressure Data

The rotor blade pressure and suction surface unsteady pressure data are analyzed to determine the harmonics of the chordwise distribution of the unsteady pressure coefficient.

$$C_{p,i} = \frac{p_i^*}{\rho \bar{W}^2 v^*} \quad (2)$$

The unsteady differential pressure coefficient is determined by subtracting the unsteady pressure coefficient on the suction surface from that on the pressure surface, with the resulting unsteady lift calculated by integrating the unsteady differential pressure coefficient over the chord. The measured and predicted unsteady lift values are correlated by means of the unsteady lift ratio, with both the theoretical and experimental differential pressure coefficients integrated between the first and last chordwise positions of the experimental data.

$$L_{\text{corr}} = \frac{C_{l, \text{exp}}}{C_{l, \text{theory}}} = \frac{\frac{1}{c} \int_0^c \Delta C_{p, \text{exp}} dx}{\frac{1}{c} \int_0^c \Delta C_{p, \text{theory}} dx} \quad (3)$$

Note that if the experimental data are in exact agreement with the unsteady linear theory prediction, the unsteady lift ratio will have a magnitude of 1.0 and a phase angle of 0°.

Results

A series of experiments are performed in the Purdue Axial Flow Research Compressor to investigate the effect of inlet flow forcing function type, i.e., generated by an attached flow, onset of separated flow, or a fully separated flow, and rotor steady loading on the gust response of the first stage rotor blade. For each forcing function flow type, four steady loading conditions as characterized by the rotor relative mean flow incidence angles are studied, $i = -3^\circ, 0^\circ, 3^\circ,$ and 6° .

Surface Steady Pressure Distributions

The chordwise rotor blade surface steady pressure distributions for the three forcing function flow types are presented in Figure 4 for the low and high steady rotor steady loading levels, $i = -3^\circ$ and 6° . These data are compared with predictions from an incompressible, inviscid small camber airfoil cascade analysis [10]. The rotor blade surface steady pressure distribution is a function of the steady loading level but independent of the forcing function.

In the pressure surface leading edge region, the steady pressure coefficient increases with loading. It then increases until approximately 30% chord where it becomes constant, independent of the loading. In contrast, steady loading affects the suction surface over the entire chord, with the suction surface steady pressure coefficient a strong function of the steady loading level. Note that there is no evidence of suction surface steady flow separation. With regard to the differential steady pressure coefficient, the leading edge value is negative at negative values of the relative mean flow incidence, approximately zero at 0° incidence, increasing with increased loading. These data exhibit relatively good correlation with the predictions, accomplished by utilizing the mean rotor relative velocity measured with the rotor blades adjacent to the hotwire removed to determine the value of the mean rotor relative velocity \bar{W} for the nondimensionalization of the steady pressure coefficient.

Attached & Separated Flow Generated Forcing Functions

The Fourier decomposition of the attached flow forcing function generated by the 5° AOA NACA 0024 airfoils is presented in Figure 5. The dominant u^+ amplitude occurs at the 2/rev fundamental frequency, with the higher order harmonic amplitudes generally smaller and decreasing with increased frequency. The Fourier decomposed v^+ amplitudes of the attached inlet flow forcing function are approximately equal and small for all frequencies. Note that not all of the u^+ and v^+ harmonics are of the same magnitude nor are they distinct. Also the characteristics of the u^+ spectrum resemble that of a harmonic forcing function having a high fundamental frequency component with lower amplitude higher harmonics.

The Fourier decomposition of the 10° AOA NACA 0024 airfoil data representing the onset of separated flow generated forcing function is also shown in Figure 5. The primary difference between this result and the previous attached flow forcing function is that the higher harmonic amplitudes of both u^+ and v^+ are increased relative to the fundamental frequency value and are larger in value. These differences result in the

forcing function starting to resemble an impulse function. Note that a pure sine function has only the fundamental harmonic whereas a pure impulse function has an infinite number of harmonics with the magnitudes of lower harmonics having the same order of magnitude as the fundamental harmonic. Analogous to the attached flow generated forcing functions, the u^+ dominant amplitude occurs at the fundamental frequency, with the higher harmonic magnitudes decreasing with increased frequency. Also, there is no dominant v^+ amplitude, with the higher harmonic amplitudes either approximately equal or larger than the fundamental frequency value. Note that all of the harmonics of u^+ and v^+ are relatively large.

The Fourier decomposition of the fully separated inlet flow forcing function generated by the 20° AOA NACA 0024 airfoils is also shown in Figure 5. Although the magnitude of u^+ at the fundamental frequency is large, it no longer dominates the u^+ spectrum. The higher harmonic amplitudes are much larger relative to the fundamental frequency value than those of the attached and the onset of separated flow forcing functions, i.e., higher harmonics are a significant part of the complete forcing function. However, the higher harmonic amplitudes continue to decrease with increased frequency, as per the attached and onset of separated flow generated forcing functions. The behavior of v^+ is similar to that of the forcing function generated by an onset of separated inlet flow. No particular harmonic of v^+ dominates the forcing function. However, unlike the behavior of the v^+ forcing function generated by a flow at the onset of separation, the forcing function generated by the fully separated flow has a frequency at which a minimum v^+ occurs. Thus, the separated flow forcing function more closely resembles an impulse function due to these increases in the higher harmonic amplitudes.

Forcing Function Generator Fluid Dynamic Effects on Gust Response

Pressure Surface

Figures 6, 7 and 8 show the change in the pressure surface gust response when the flow field generating the forcing function is changed from an attached flow to a flow at the onset of separation to a fully separated flow, accomplished by changing the NACA 0024 airfoil AOA from 5° to 10° to 20°. Altering the forcing function generator from an attached flow to a separated flow has a noticeable effect on the pressure surface gust response. With the attached flow generated forcing function, the magnitude and phase of the pressure surface gust response are clearly a function of the steady loading level, Figure 6. As the AOA increases to 10° and then to 20°, the pressure surface response becomes much less dependent on the steady loading level. At 10° AOA, there is a smooth decrease in the unsteady pressure magnitude with chord which becomes independent of the loading in the midchord region, Figure 7. The phase response shows an increasing trend with chord, with loading still having an influence. At 20° AOA, the magnitude still smoothly decreases with chord, Figure 8. However, the level of the magnitude response is increased as compared to the corresponding 5° and 10° AOA data. Also, the 20° AOA phase response is now independent of the loading level, with a smooth phase increase with chord.

Suction Surface

Figures 9, 10 and 11 show the suction surface gust response resulting from the different forcing function generator flow fields. Altering the forcing function generating flow field from an attached flow to a flow at the onset of separation to a separated flow also has an effect on the suction surface gust response. With the attached flow forcing function, the response magnitude decreases sharply in the leading edge region, attaining a relative minimum value near 25% chord and then increasing

slightly before decreasing to an absolute minimum near 65% chord. In the trailing edge region, there is a relatively large increase and a subsequent decrease. Also, these magnitude data are a function of the steady loading level, particularly in the airfoil leading and trailing edge regions. As the AOA is increased to 10° and then to 20°, the overall trends of these magnitude response data are unchanged. However, the chordwise distribution of the magnitude data becomes smoother, i.e., the magnitude data decrease more rapidly in the leading edge region, attaining a somewhat constant level in the 25% to 50% chord region, then decreasing to a minimum near 60% chord. The rapid increase and decrease in the magnitude near the trailing edge is still evident, with it being smallest at 10° AOA.

The suction surface gust response phase of the airfoil is also a function of the forcing function generator flow field. At 5° AOA attached flow, the unsteady pressure phase response is constant with chord at the highest steady loading of 6° mean flow incidence. As the loading is changed from this level, there is a large phase decrease in the aft chord region, with the phase remaining constant over the front of the airfoil. Also, the phase is a function of the steady loading level. Increasing the forcing function generator AOA to 10° and to 20° has a clear effect on the phase response. Namely, in the front chord region, the phase response becomes independent of loading. Also, the large phase change near the trailing edge is suppressed as the AOA is increased. Instead, the phase decreases from the leading to trailing edge more gradually as the AOA is increased and the flow generating the forcing function flow changes to a separated flow field.

Unsteady Pressure Difference

As expected based on the individual airfoil surface data, altering the forcing function generator from an attached flow to one at the onset of separation to a separated flow has a significant effect on the pressure difference gust response, Figures 12, 13 and 14. The pressure difference magnitude data generally decrease with chord, with the decrease in the leading edge region becoming larger as the forcing function generator flow field changes to one at the onset of separation and then to a separated flow. Note that this general trend is in agreement with the linear theory prediction. However, the degree of correlation with the linear theory prediction is dependent on the forcing function generator fluid dynamics. Namely, at an AOA of 5°, the pressure difference magnitude data are typically increased in value as compared to the prediction, Figure 12. Increasing the forcing function generator AOA to 10° and 20° results in these magnitude data decreasing in value with respect to the prediction, being slightly decreased at 10° and further decreased at 20°, Figures 13 and 14. Thus, the interesting but unexplained result of Manwaring and Fleeter [8] can now be attributed to the attached and separated flow nature of the forcing functions utilized in their experiments. Namely, the inlet distortion forcing function was generated by an attached flow forcing function. In contrast, the airfoil wake forcing function was generated by a flat plate at an angle of attack, thereby resulting in a separated flow generated forcing function.

The more detailed effect of the forcing function generator fluid dynamics on the differential pressure response magnitude data includes the nonsmooth variation with chord in the midchord region and in the trailing edge region at 5° AOA. Increasing the AOA to 10° and to 20° results in a smoothing of the midchord region data and a decrease in the magnitude of the variation of the data in the trailing edge region. This trailing edge data variation is due to a potential effect from the downstream stator vane row.

With regard to the unsteady pressure difference response phase angle, at 5° AOA the phase is constant but is a function of the steady loading level over the front half of the chord. Aft of midchord, there is a large jump in the phase. Increasing the AOA to 10° and then to 20° results in the front chord region

unsteady pressure phase data becoming independent of the steady loading level and also causes the location of the large phase jump to move forward. Note that the phase correlation with the linear theory prediction is poor everywhere, with the large phase increases not predicted.

Unsteady Lift Correlation with Linear Theory

The level of deviation of the unsteady differential pressure data from the linear theory prediction is quantified through the unsteady lift coefficient ratio L_{corr} . Figure 15 shows the variation of L_{corr} as a function of the mean relative flow incidence angle. In general, the attached flow generated forcing function at 5° AOA correlates reasonably well with linear theory, with the degree of correlation decreasing as the AOA increases to 10° and 20°. With regard to the phase of L_{corr} , the attached flow generated forcing function again exhibits the best correlation with theory. However, all of the forcing function phase correlations are poor.

Forcing Function Fundamental Parameters

To begin to understand the significant effect of altering the forcing function generator fluid dynamics on the unsteady gust response of the downstream rotor blade row, it is noted that the forcing functions at 5°, 10° and 20° AOA are not equivalent in terms of the fundamental forcing function parameters. In particular, the magnitude and phase of the first harmonic gust component ratio, u^+/v^+ , are different.

Figure 16 shows the magnitude and phase of the first harmonic gust ratio, u^+/v^+ , as a function of the steady loading level, with the AOA as a parameter. The gust characteristics, in particular the magnitude and phase of u^+/v^+ , are clearly a function of the fluid dynamics of the forcing function generator. Namely, as the forcing function generator fluid dynamics changes from an attached flow to a flow at the onset of separation to a separated flow, both the magnitude and the phase of u^+/v^+ typically decrease, with this decrease a function of the steady loading level.

The effect of the forcing function gust characteristics, in particular, the phase of u^+/v^+ , on the rotor blade gust generated unsteady pressure response is demonstrated in Figure 17 which shows the variation of the L_{corr} as a function of the phase of u^+/v^+ , with the AOA as a parameter. Although the gust ratio phase has no clear effect on the magnitude of the lift correlation, it has a noticeable effect on the phase of L_{corr} , with the phase data-theory correlation improving, i.e., approaching 0°, with increasing gust ratio phase.

To begin to understand the fundamental difference between the response data generated by the attached flow, the flow at the onset of separation, and the fully separated flow and the correlation of these data with linear theory, the validity of the unsteady linear theory model for these flows is considered. In particular, as considered by Henderson and Fleeter [11, 12], linear theory requires that: (1) the gust vector components u^+ and v^+ are 180° out of phase; (2) the magnitude of u^+/v^+ is equal to the ratio k_2/k_1 , determined from the steady flow free stream and wake region velocity triangles; (3) the gust vector is perpendicular to the direction of gust convection; and (4) the gust vectors are parallel to one another. Note that satisfying only the first two conditions automatically satisfies the last two conditions.

The importance of the gust ratio phase angle is illustrated by the requirement that the streamwise and transverse gust components u^+ and v^+ are 180° out of phase. This assumption is violated independent of whether the forcing function gusts are generated by separated or attached flows. The phase of u^+/v^+ is generally near zero for fully separated flow but larger for onset of separation or attached flows, with an increase in the phase of

the gust ratio u^+/v^+ resulting in better phase correlation. Hence the violation of the 180° phase requirement is a contributing factor to the poor correlation of these phase data with the theory.

From linear theory, the magnitude of the gust component ratio $|u^+/v^+|$ from the unsteady forcing function velocity data must also be equal to the ratio k_2/k_1 , the wave number ratio calculated from the steady free stream and wake region inlet velocity triangles. This requirement is grossly violated, as evident in Table 2. There is not a single case for which the two values agree. In fact, the unsteady $|u^+/v^+|$ values are 2 to 20 times greater than that of the steady k_2/k_1 values.

The effect of violating the above assumptions on the unsteady aerodynamic gust is reflected in the interesting trend apparent in the first harmonic gust vectors. Note that the gust vector represents the spatial distribution of the forcing function

aerodynamic gust vector ΔW in the direction of gust convection. This spatial distribution of the gust vector is constructed by

plotting the temporal variations in ΔW spatially in the direction of gust convection, with the magnitude and direction with respect to k maintained. In other words, the gust vectors which are vectorially determined from successive points in time are plotted in the direction of gust convection determined from the steady flow data. The maximum magnitude of the first harmonic gust vectors from the 5° AOA airfoil attached flow, Figure 18, is approximately in the mid-wake and mid-free stream regions. Thus, the gust vectors form a shape that is somewhat sinusoidal. However, the first harmonic gust vectors from the 10° AOA airfoils at the onset of separated flow, Figure 19, and the 20° AOA airfoils with separated flow, Figure 20, have the first harmonic gust vector of maximum magnitude near one of the wake-free stream boundaries. Thus these gust vectors form a skewed-sinusoid. The common factor in this shape of the first harmonic gust is the gust ratio phase angle, $\angle u^+/v^+$. The 5° AOA attached flow forcing function has a gust ratio phase angle of 54.4° while the other forcing functions have gust ratio phase angles of 27.3° and 14.9°. Note that this effect of gust ratio phase angle on the shape of the first harmonic gust is similar to the changes in the shape of the linear theory gust caused by the modification of u^+/v^+ magnitude or the phase of u^+/v^+ [11]. At low gust ratio phase angles, Figures 19 and 20, the gust vectors are nearly parallel to one another but are skewed in shape because the value of u^+/v^+ differs significantly from k_2/k_1 . However, at high gust ratio phase angles, the gust shape stays sinusoidal, perhaps suggesting that the gust ratio phase angle is the dominant factor in the gust shape determination than the matching of u^+/v^+ magnitude to k_2/k_1 . Clearly, the first harmonic gust vectors are influenced significantly by the gust ratio phase angle and the degree of equivalence between k_2/k_1 and the magnitude of u^+/v^+ , independent of the forcing function fluid dynamics. In contrast, the total forcing function gust vectors are largely affected by the forcing function fluid dynamics, as will be discussed.

The violation of the first two linear theory gust conditions leads to the violation of the last two, resulting in gust vectors which are neither parallel to one another nor perpendicular to the direction of wake convection. The assumptions of perpendicularity between the gust vectors and the direction gust convection k are clearly inappropriate, as demonstrated in Figures 18, 19 and 20 which also show the NACA 0024 airfoil generated total gust vectors. Note that few, if any, of the vectors in the total gust are perpendicular to the direction of convection. In fact, what is evident is a fanning out trend of the vectors in the wake region that increases with increased forcing function flow separation. Also, the 36/rev IGV wakes are embedded within the larger 2/rev NACA airfoil wakes in the total gust.

The violation of the last condition that the gust vectors are parallel to one another is also evident in these figures. With an attached inlet flow, the 2/rev total gust vectors cross one another in the wake region. This crossing of the vectors is present in all gusts produced by the NACA 0024 airfoil generated attached flow. For an inlet flow generated at the onset of separation, the 2/rev total gust vectors do not cross one another as much as they did for the attached inlet flow. In fact, on one side of the wake, the 2/rev total gust vectors start to fan or spread apart from one another. With a separated inlet flow, this fanning of the total gust vector is even more pronounced. The total gust vector in the wake region fans continuously from one side to another with no intersections.

Thus, the consideration of some essential assumptions inherent in the unsteady linear theory indicates that these assumptions are not appropriate for turbomachine blade rows and cannot be applied. The poor data-theory correlation of the resulting blade row unsteady aerodynamic response suggests an intimate relationship between the characteristics of the gust vector and the degree of correlation of the compressor blade row unsteady aerodynamic gust response data with linear theory.

Summary & Conclusions

A series of experiments were performed to investigate the fundamental flow forcing function phenomena generating different blade row gust responses, in particular attached and separated flow forcing functions generated with NACA 0024 airfoils.

These experiments revealed the new result that the forcing function generator fluid dynamics is significant with regard to the resulting unsteady aerodynamic gust response of a downstream airfoil row. Namely, attached flow, onset-of-separated flow and separated flow forcing function generators result in large and important differences in the resulting unsteady aerodynamic gust response of the downstream airfoil row and the correlation of these data with linear theory predictions. Steady rotor blade loading also significantly affected this data-theory correlation. These differences in the detailed forcing function fluid dynamics explain the significant differences in Manwaring and Fleeter's [8] fundamentally equivalent 2-E inlet distortion and wake generated gust response data. Namely, their inlet distortion forcing function was generated by an attached flow whereas the flat plate wake forcing function was generated by a separated flow. Hence the differences in the resulting rotor blade row gust unsteady aerodynamic response.

The forcing function fluid dynamics was analyzed in terms of the requirements inherent in the linear theory gust modeling. This showed that the forcing function violation of the 180° phase requirement between the streamwise and transverse gust components contributed to the poor data-theory phase correlation and that the addition of the values of lu^+/v^+ and k_2/k_1 not being equal leads to unsteady gust vectors which are neither parallel to one another nor perpendicular to the direction of wake convection, as also inherent in linear theory gust models. Thus, the degree of correlation of the rotor blade unsteady gust response data with linear theory is closely related to the characteristics of the forcing function gust generating the response.

Acknowledgments

Research sponsored by the Air Force Office of Scientific Research (AFSC) under Contract F49620-88-C-0022. The United States Government is authorized to reproduce and distribute reprints for governmental purposes notwithstanding any copyright notation hereon.

References

1. Whitehead, D.S., "Classical Two-Dimensional Methods," *AGARDograph No. 298, AGARD Manual on Aeroelasticity in Axial Flow Turbomachines, Volume 1: Unsteady Turbomachinery Aerodynamics*, pp.3.1-3.30.
2. Fleeter, S., "The Fluctuation Lift and Moment Coefficients for Cascaded Airfoils in a Nonuniform Compressible Flow," *AIAA Journal of Aircraft*, Vol. 10, No. 2, February 1973, pp. 93-98.
3. Adamczyk, J.J. and Goldstein, M.E., "Unsteady Flow in a Supersonic Cascade with Subsonic Leading Edge Locus," *AIAA Journal*, Vol. 16, No. 12, 1978, pp. 1248-1254.
4. Verdon, J.M. and Usab, W.J., "Application of a Linearized Unsteady Aerodynamic Analysis to Standard Cascade Configurations," *ASME Paper 90-GT-11*, June 1990.
5. Verdon, J.M. and Hall, K.C., "Development of a Linearized Unsteady Aerodynamic Analysis for Cascade Gust Response Predictions," *NASA Report 4308*, July 1990.
6. Scott, J.S. and Atassi, H.M., "Numerical Solutions of the Linearized Euler Equations for Unsteady Vortical Flows Around Lifting Airfoils," *AIAA Paper 90-*, 1990
7. Fang, J., "Compressible Flows With Vortical Disturbances Around Cascades of Airfoils," *Ph.D. Thesis, University of Notre Dame*, April 1991
8. Manwaring, S.R. and Fleeter, S., "Forcing Function Effects on Rotor Periodic Aerodynamic Response," *ASME Journal of Turbomachinery*, Vol. 113, No. 2, April 1991, pp. 312-319.
9. Smith, S.N. "Discrete Frequency Sound Generation in Axial Flow Turbomachines," *Aeronautical Research Council R&M 3709*, Great Britain, March 1972.
10. Henderson, G.H. and Fleeter, S., "The Response of a Low Solidity Symmetric Airfoil Cascade to Compressor Wake and Linear Theory Gusts," *IUTAM 6th International Symposium on Unsteady Aerodynamics and Aeroelasticity of Turbomachines and Propellers*, The University of Notre Dame, September 1991.
11. Henderson, G.H. and Fleeter, S., "Forcing Function Effects on Unsteady Aerodynamic Gust Response: Part I Forcing Functions" *ASME Gas Turbine Conference*, June 1992.
12. Henderson, G.H. and Fleeter, S., "Forcing Function Effects on Unsteady Aerodynamic Gust Response: Part II Low Solidity Airfoil Row Response" *ASME Gas Turbine Conference*, June 1992.

Table 1. Overall airfoil and compressor characteristics

	ROTOR	STATOR	IGV
Airfoil type	C4	C4	C4
Number of Airfoils	43	31	36
Chord, C (mm)	30	30	30
Solidity, C/S	1.14	1.09	0.96
Camber, θ	28.0	27.7	36.9
Stagger Angle, γ	36.0	-36.0	21.0
Inlet Metal Angle, β_1	50.0	30.0	0.0
Aspect Ratio	2.0	2.0	2.0
Thickness/Chord (%)	10.0	10.0	10.0
Reynolds Number $\times 10^{-5}$ (based on chord)	6.3	6.3	5.0
Flow Rate (kg/s)		2.03	
Design Axial Velocity (m/s)		24.4	
Design Rotational Speed (RPM)		2250	
Number of Stages		3	
Design Stage Pressure Ratio		1.0	
Inlet Tip Diameter (mm)		420	
Hub/Tip Radius Ratio		0.714	
Stage Efficiency (%)		85	

Table 2. Unsteady lu^+/v^* and steady flow k_2/k_1 values

Steady Loading		-3°	0°	3°	6°
Forcing Functions					
Attached Flow (5° AOA)	lu^+/v^*	2.04	2.37	2.69	2.37
	k_2/k_1	0.281	0.237	0.182	0.128
	% Difference	626 %	900 %	1,378 %	1,752 %
Onset of Separation (10° AOA)	lu^+/v^*	1.15	1.63	1.64	2.13
	k_2/k_1	0.279	0.226	0.185	0.140
	Difference	312 %	621 %	786 %	1,421 %
Separated Flow (20° AOA)	lu^+/v^*	0.783	1.14	1.55	1.07
	k_2/k_1	0.300	0.234	0.177	0.132
	Difference	161 %	387 %	776 %	711 %

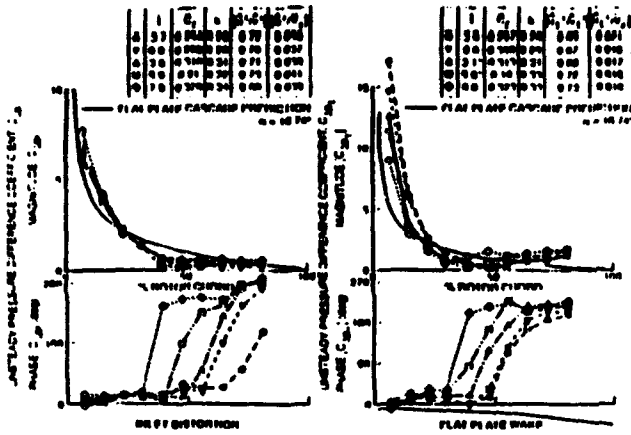


Figure 1. Inlet distortion and wake generated gust response [8]

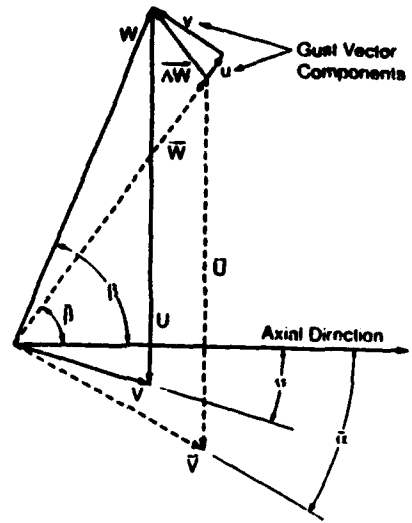


Figure 2. Decomposition of rotor inlet velocity

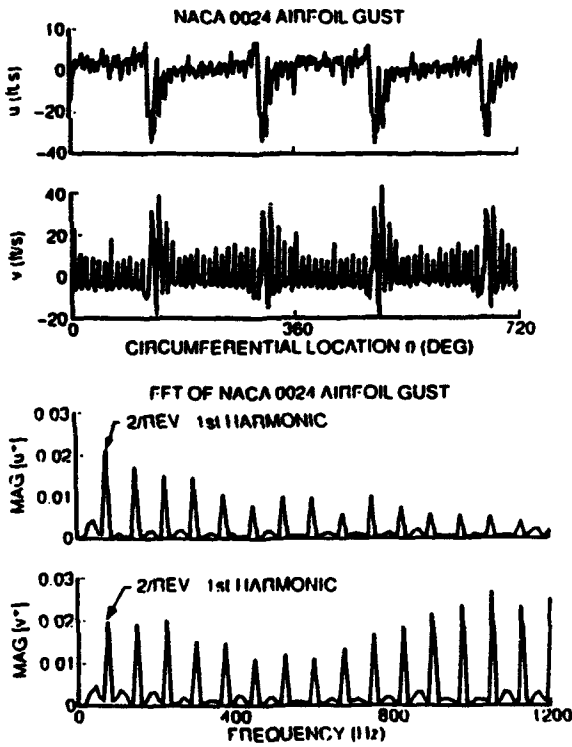


Figure 3. Forcing function and streamwise and normal gust component FFT

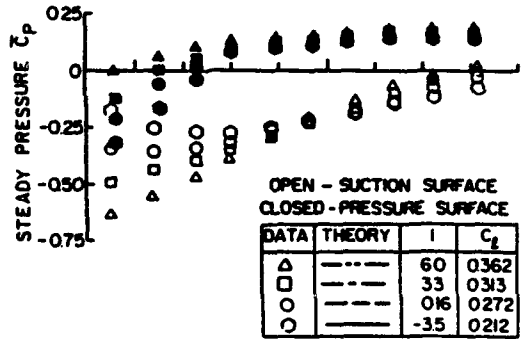


Figure 4. Loading effect on rotor blade surface steady pressures

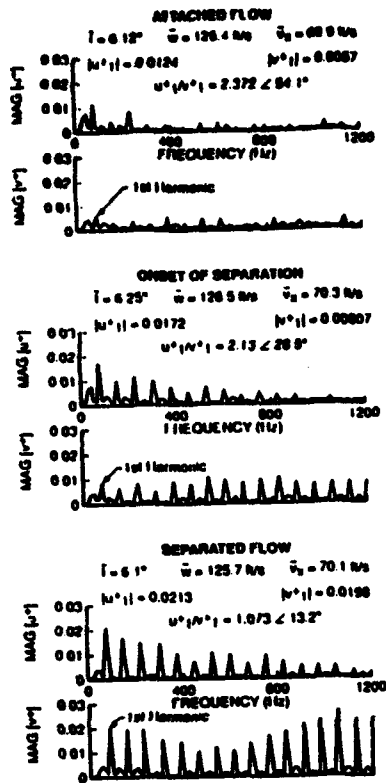


Figure 5. FFT of forcing functions

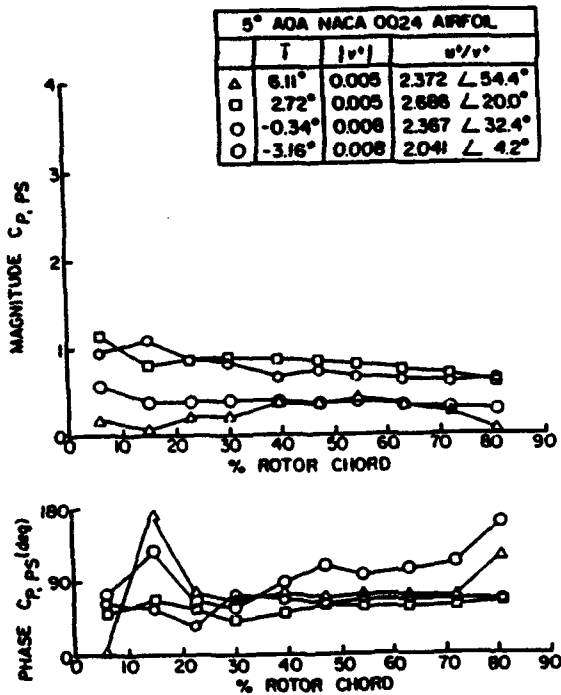


Figure 6. Pressure surface attached flow generated gust response

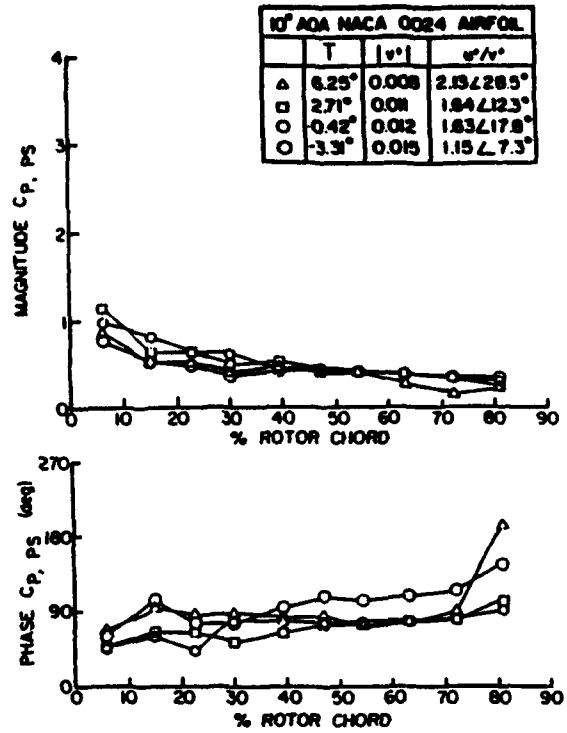


Figure 7. Pressure surface onsets of separated flow generated gust response

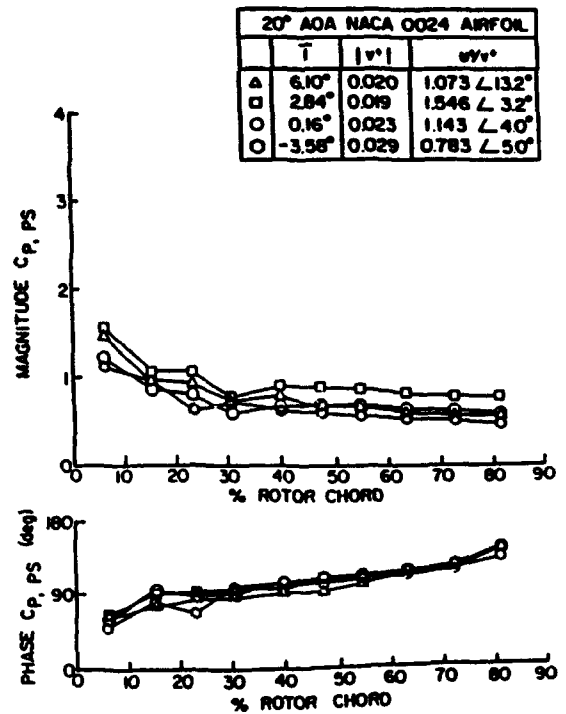


Figure 8. Pressure surface separated flow generated gust response

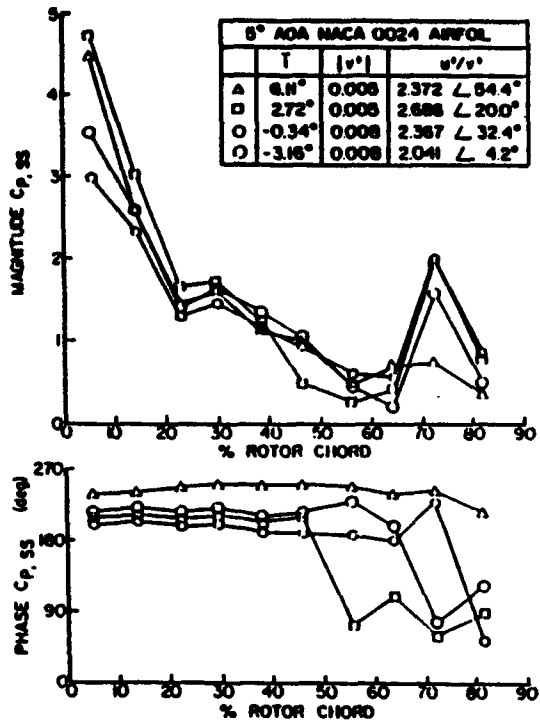


Figure 9. Suction surface attached flow generated gust response

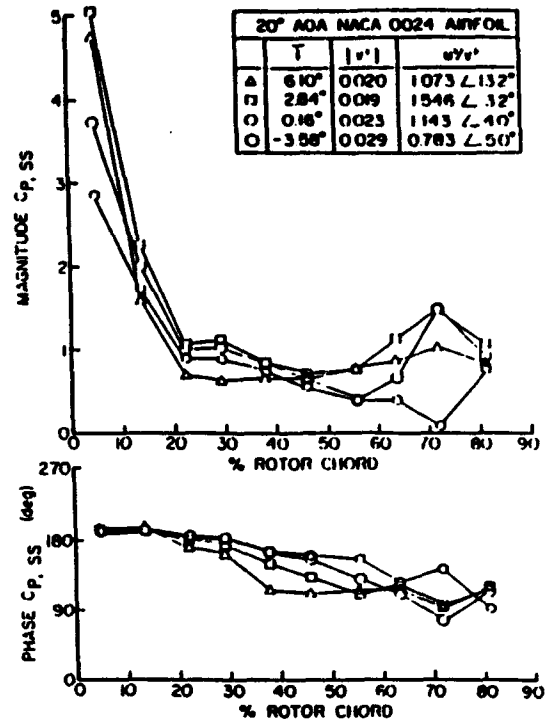


Figure 11. Suction surface separated flow generated gust response

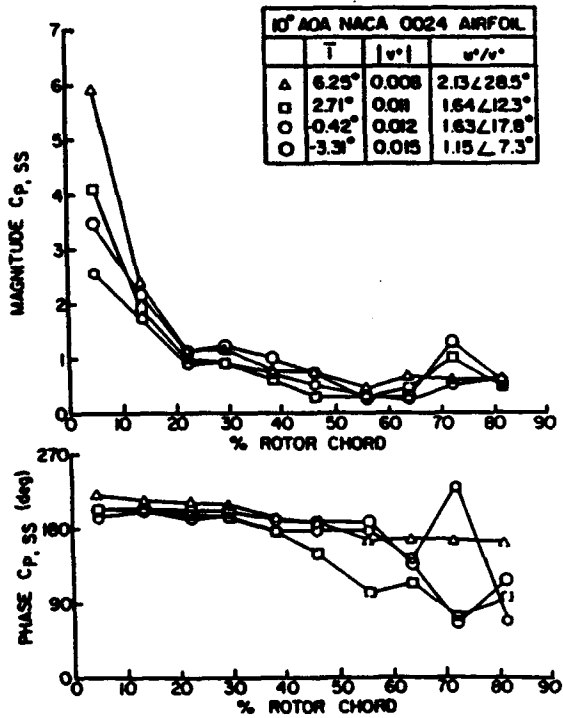


Figure 10. Suction surface onset of separated flow generated gust response

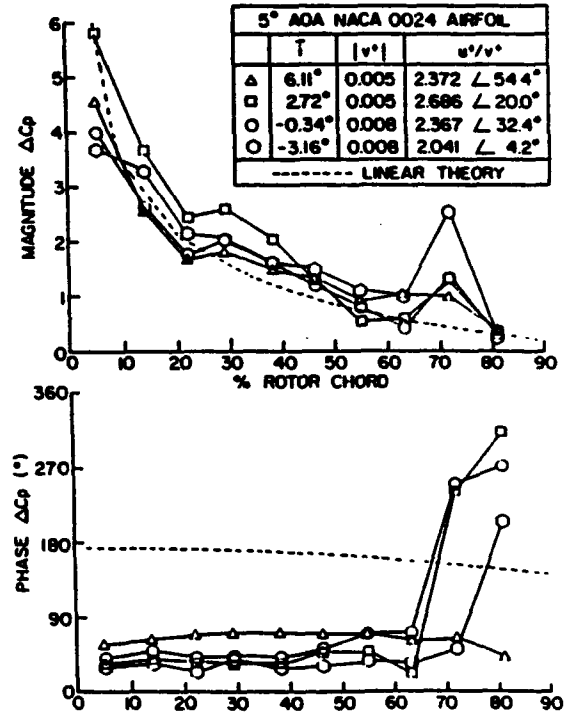


Figure 12. Pressure difference attached flow generated gust response

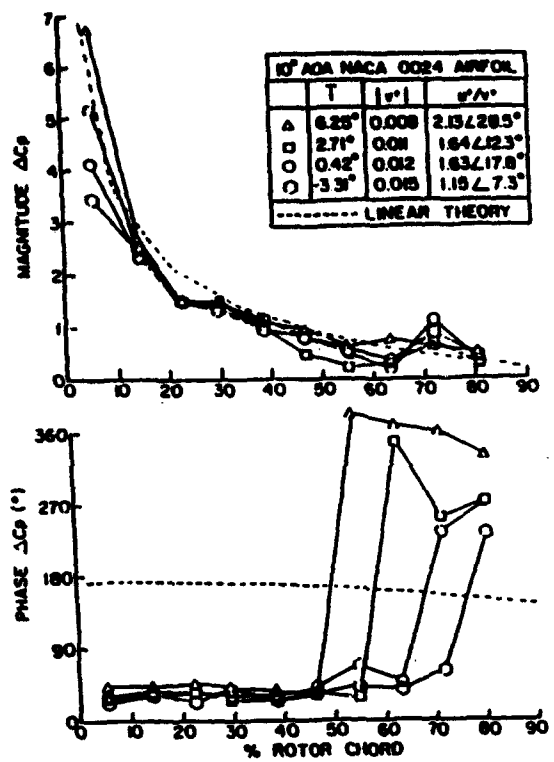


Figure 13. Pressure difference onset of separated flow generated gust response

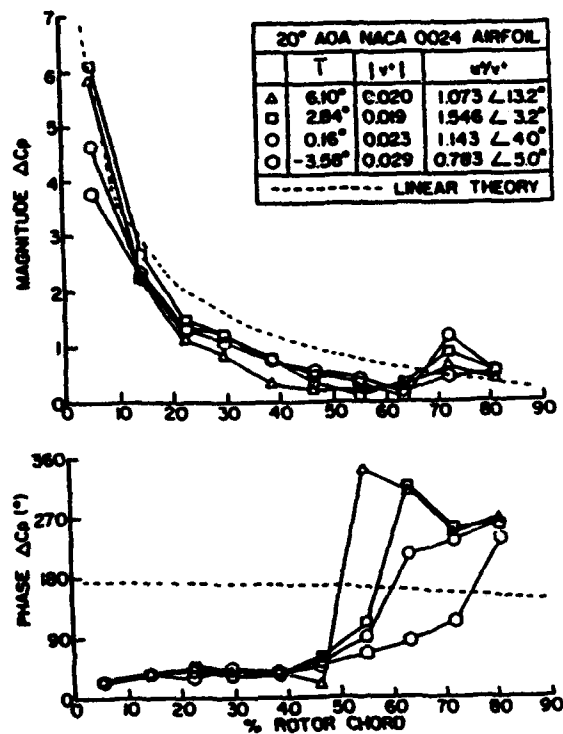


Figure 14. Pressure difference separated flow generated gust response

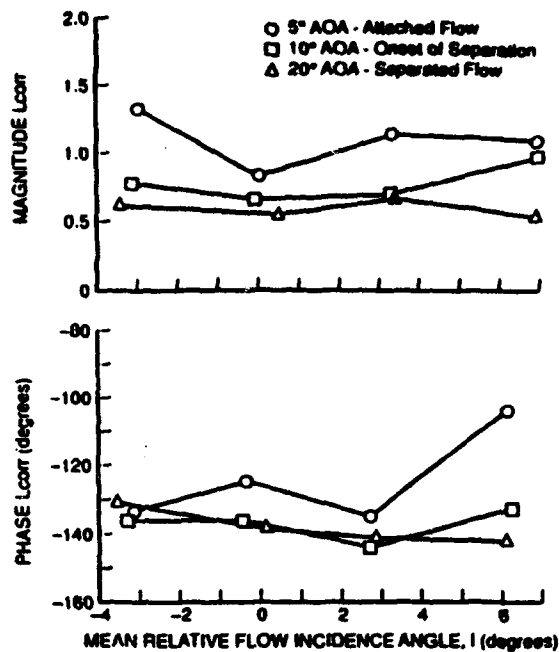


Figure 15. Unsteady lift ratio correlation

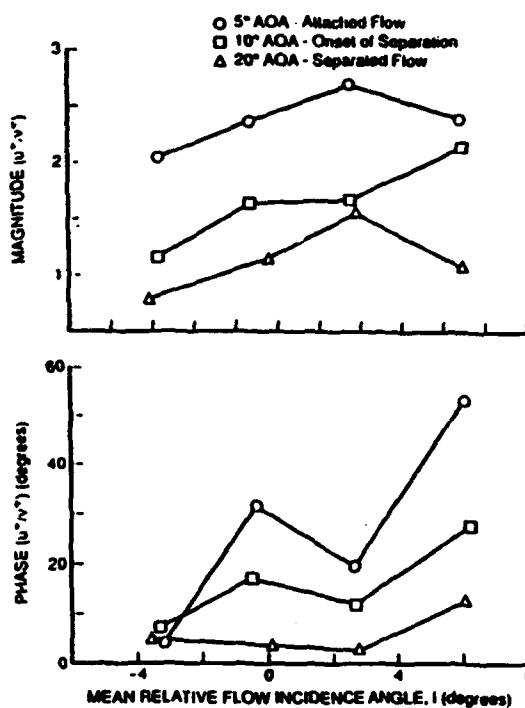


Figure 16. Gust component ratio variation with incidence angle

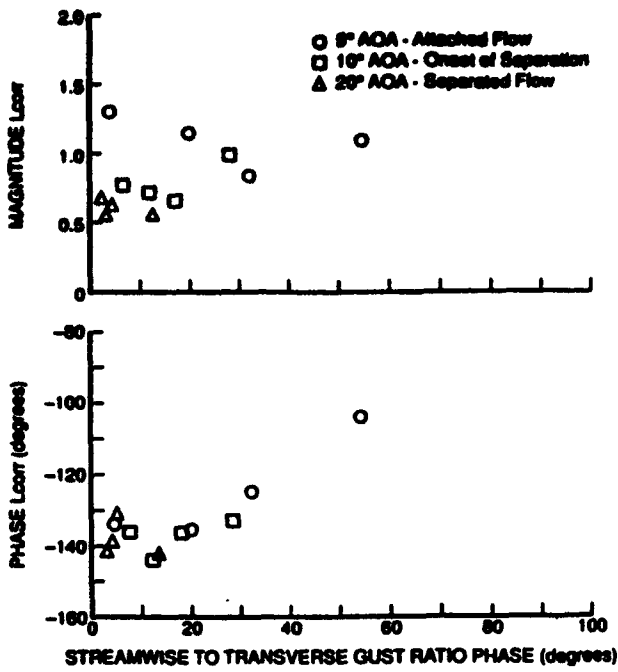


Figure 17. Unsteady lift ratio variation with gust component ratio

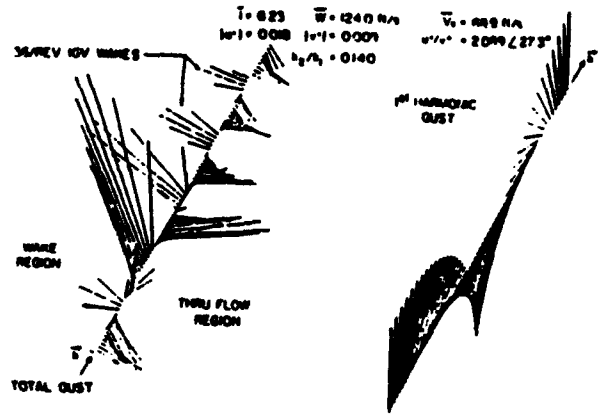


Figure 19. Onset of separated flow generated unsteady aerodynamic gust

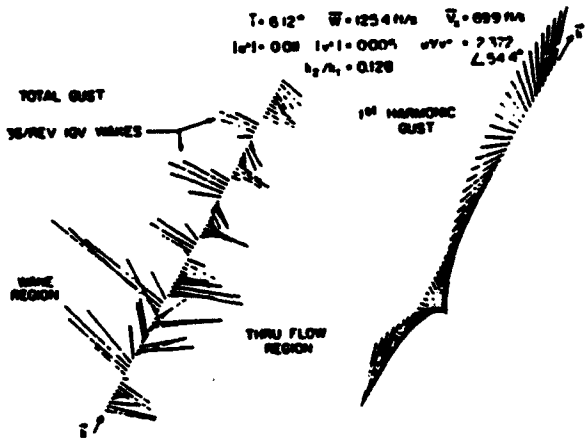


Figure 18. Attached flow generated unsteady aerodynamic gust

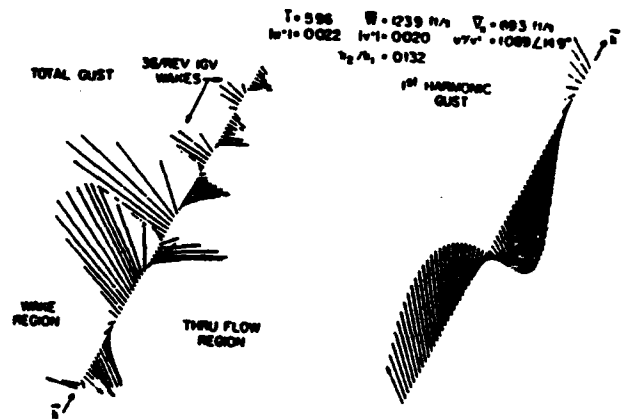


Figure 20. Separated flow generated unsteady aerodynamic gust

APPENDIX V

**Single Passage Euler Analysis of Oscillating Cascade Unsteady Aerodynamics for
Arbitrary Interblade Phase Angle**

*AIAA Paper 93-0389, January 1993
(also AIAA Journal for Propulsion and Power, in press).*

SINGLE PASSAGE EULER ANALYSIS OF OSCILLATING CASCADE UNSTEADY AERODYNAMICS FOR ARBITRARY INTERBLADE PHASE ANGLE

James M. Wolff* and Sanford Fleeter[†]
School of Mechanical Engineering
Purdue University
West Lafayette, Indiana 47907

Abstract

The unsteady flow field through an harmonically oscillating cascade of airfoils is investigated using a time-marching Euler code implemented on a deforming C-grid. Various methods of calculating the boundary conditions are considered, with special attention paid to the unsteady periodic boundary conditions and reducing computer resource requirements. The Euler code is then used to predict the unsteady aerodynamics for both translational and torsional cascade oscillations for several cascade flow geometries. A flat plate cascade is used to verify the flow solver with linear theory predictions. A typical compressor rotor configuration is used to introduce nonlinear effects. The effect of a strong normal shock with varied amplitudes of oscillation demonstrates the nonlinear behavior of the periodic boundary conditions and helps to define the limiting conditions for linearized analyses.

Nomenclature

Symbol	Description
A, B, K	flux Jacobians
C	airfoil chord
C_M	unsteady moment coefficient, $m(C^2 \rho_1 V_1^2)$
C_p	pressure coefficient, $-(p-p_1)/(\frac{1}{2} \rho_1 V_1^2)$
ΔC_p	pressure difference coefficient, $(p_2 - p_1)/(\frac{1}{2} \rho_1 V_1^2 x_1)$
F, G	flux vectors
h_1	amplitude of translational motion based on chord
J	metric Jacobian
k	reduced frequency, $(\omega C/2V_1)$
l, r	left and right eigenvectors, respectively
$L_j(m, n)$	Lilienthal function
m	moment
M	free-stream Mach number
p	static pressure
P_0	total pressure
Q	dependent variable vector
R	residual
S	cascade spacing
t, τ	time
T, T ⁻¹	eigenvector matrices
V	total velocity
u, v	velocities in the x and y directions
x_{el}	elastic axis location
x, y	spatial coordinates
α	incidence angle (degrees)
α_1	amplitude of oscillation for torsion (degrees)
γ	ratio of specific heats

ρ	fluid density
σ	interblade phase angle (degrees)
ξ, η	curvilinear coordinate directions
ω	angular frequency
ζ	cascade stagger angle (degree)
Subscripts	
0	steady solution
1, 2	inlet/exit conditions
L, U	upper/lower periodic boundary condition
Superscript	
0	time average value
n	time level index

Introduction

Unsteady aerodynamic phenomena continue to produce serious aeroelastic problems in the development of new turbomachinery. To minimize this development problem, accurate unsteady aerodynamic cascade models are required. Such models are generally time linearized, with the validity of these linearized models for subsonic flows well established for low aerodynamic loading.^{1,2} However these linearized flow models may not be valid for many situations. For example, nonlinear effects are quite likely to be associated with larger amplitudes of blade oscillation as well as unsteady transonic flows induced by oscillating blades at small amplitudes.

To analyze nonlinear flow fields, unsteady Euler codes are being developed. Finite difference schemes^{3,4,5,6} are being used to solve the Euler equations for oscillating cascades by time-marching methods. However, they require much more computer time and storage than do linearized codes. For cascade studies, an important aspect of this additional computational expense is associated with the passage periodic boundary conditions which specify a constant interblade phase angle between adjacent oscillating airfoils. Several methods have been proposed to specify the periodic boundary condition, a-b and c-d in Figure 1.

The simplest method is to "stack" airfoil grids and pass information between adjacent grids. This is accomplished by expanding the grids so they overlap along the periodic boundaries, Figure 1. Each passage calculation is marched at a different time corresponding to the interblade phase angle, with the solution at the periodic boundaries then determined as part of the interior solution. With the airfoils oscillating at a fixed nonzero interblade phase angle, the minimum number of airfoils, N_a , which satisfies the periodicity requirement is

$$N_a |\sigma| = 360^\circ \quad (1)$$

A 90 degree interblade phase angle analysis thus requires modeling 4 airfoils and 4 flow passages. Although numerically exact, this method requires additional computational time for nonzero interblade phase angle calculations, with some interblade phase angles practically impossible to analyze.

* AFRAPT Trainee, Student Member AIAA

[†] Professor, Associate Fellow AIAA

Single blade passage techniques, with the periodic boundary conditions phase shifted for non-zero interblade phase angle values, minimize the computational requirements by eliminating this flow passage stacking. The direct store method, first proposed by Eides and Almer,⁷ requires that all the dependent variables on the periodic boundaries be stored for a period of airfoil oscillation. At every time step, parameters at the boundaries are updated by averaging the data obtained from the current time-marching solution and those stored according to the given interblade phase angle. At the same time the stored parameters are updated. The periodic boundary condition is satisfied when the time marching process converges to a periodic solution. The primary disadvantage of this method is the large computer storage required, especially at low cascade oscillation frequency values.

To avoid the large computer time or memory requirements of the above noted methods, He⁸ assumed a Fourier series expansion at the periodic boundaries and then lagged the boundary conditions by the interblade phase angle. In this method, the Fourier coefficients of the response at the periodic boundaries are stored and continually updated. This is more efficient in computer memory usage than that of the direct store method which stores the entire time history at the periodic boundary. Thus, this method shows tremendous promise for conserving computer resources.

In this paper, the unsteady periodic boundary conditions for unsteady Euler models are investigated, including a variation of the Fourier series lagged boundary condition originally proposed by He. The two-dimensional unsteady Euler equations are solved using a time-marching, flux-difference splitting scheme implemented on a C-grid which is allowed to deform with the airfoil motion, either torsional or translational. Predictions for both flat plate and loaded airfoil cascades are then presented, with the oscillation amplitude, cascade geometry and interblade phase angles varied.

Mathematical Model

Euler Equations

The inviscid flow field is described by the Euler equations. The non-dimensional two-dimensional, time-dependent, conservation law form of these equations in general curvilinear coordinates is

$$\frac{\partial Q}{\partial t} + \frac{\partial F}{\partial \xi} + \frac{\partial G}{\partial \eta} = 0 \quad (2)$$

where the curvilinear coordinates are defined, Figure 1, as

$$\xi = \xi(x, y, t) \quad (3a)$$

$$\eta = \eta(x, y, t) \quad (3b)$$

and the vector of the dependent variables Q and the vectors F and G are given by

$$Q = \begin{bmatrix} \rho \\ \rho u \\ \rho v \\ e \end{bmatrix}, F = \begin{bmatrix} \rho U \\ \rho U + \frac{\partial F}{\partial \xi} P \\ \rho V + \frac{\partial G}{\partial \eta} P \\ U(\rho+p) - \frac{\partial P}{\partial \xi} \end{bmatrix}, G = \begin{bmatrix} \rho V \\ \rho V + \frac{\partial F}{\partial \xi} P \\ \rho U + \frac{\partial G}{\partial \eta} P \\ V(\rho+p) - \frac{\partial P}{\partial \eta} \end{bmatrix} \quad (4)$$

The contravariant velocities U and V are defined in terms of the Cartesian velocity components u and v as

$$U = \frac{\partial \xi}{\partial x} u + \frac{\partial \xi}{\partial y} v + \frac{\partial \xi}{\partial t} \quad (5a)$$

$$V = \frac{\partial \eta}{\partial x} u + \frac{\partial \eta}{\partial y} v + \frac{\partial \eta}{\partial t} \quad (5b)$$

and the total energy, e , for a perfect gas is

$$e = \frac{p}{(\gamma-1)} + \frac{1}{2} \rho (u^2 + v^2) \quad (6)$$

Implicit Finite Volume Scheme

The inviscid computations are performed using an implicit finite volume scheme.^{9,10} In the finite volume discretization, the computational domain is divided into a number of small contiguous control volumes or cells. The partial differential equations describing the conservation laws, Equation 2, are then integrated over these volumes to obtain expressions for the physical laws in each grid cell. The balance of a physical quantity such as mass, momentum, or energy is maintained in a control volume through the flux of that physical quantity across the cell surfaces. Consequently, the conservative property of the resulting difference equation is guaranteed with a finite volume approach.

The discretized integral form of the Euler equations is obtained by integrating Equation 2 over a computational volume with the center denoted as (i,j) and changing the resulting volume integral to a surface integral using the divergence theorem. The result is

$$\frac{\partial Q}{\partial t} + \frac{\delta_x F}{\Delta \xi} + \frac{\delta_y G}{\Delta \eta} = 0 \quad (7)$$

where the central difference operators

$$\delta_m(\cdot) = (\cdot)_{m+\frac{1}{2}} - (\cdot)_{m-\frac{1}{2}}, \quad m=i,j \quad (8)$$

imply that the flux vectors are evaluated at the surfaces of a cell.

Since the dependent variables are evaluated at the cell centers, the flux vectors are determined by extrapolation from either side of a cell surface. A biased extrapolation is utilized because of the fundamental property of the hyperbolic partial differential equations, i.e., the existence of a limited domain of dependence. Information propagates in specific characteristic directions which dictate the extrapolation trends required for the determination of the flux vectors at the cell faces (upwinding). The Euler equations represented by Equation 2 have five characteristic velocities associated with each flux vector. The eigenvalues of the flux Jacobian matrices $[A] = \partial F / \partial Q$ and $[B] = \partial G / \partial Q$ are the characteristic velocities in the ξ and η directions. The flux vectors F and G can be split into subvectors, flux vector splitting, each corresponding to a distinct eigenvalue of the related flux Jacobian matrix.¹⁰

$$K = \frac{\partial K}{\partial q} = T_k \Lambda_k T_k^{-1} = K^+ + K^- \quad (9)$$

where

$$K^\pm = A^\pm, k=\xi \text{ and } K^\pm = B^\pm, k=\eta \quad (10)$$

Separate extrapolations are made for determination of the flux subvectors according to the signs of the associated characteristic velocities.

The dissipation aspect of this scheme is improved by a flux-difference split method for the residual based on the solution of approximate Riemann problems with Roe averaging at the cell faces. With the determination of the eigensystem for the flux vectors using Roe averaging and the knowledge that the interface

differential is proportional to the right eigenvectors, a first order flux at the interface $i+\frac{1}{2}$ is obtained.

$$f_{i+\frac{1}{2}} = f_i + \sum^- \lambda^j \alpha_j \tau^j = f_{i+1} - \sum^+ \lambda^j \alpha_j \tau^j \quad (11)$$

where f is the flux vector, τ^j is a right eigenvector, α_j is the difference jump across the j^{th} wave, and λ^j is an eigenvalue.

To obtain higher order spatial accuracy, a corrective flux is then added to Equation 11:

$$f_{i+\frac{1}{2}} = f_{i+\frac{1}{2}} + \frac{(1+\phi)}{4} [df_{i+\frac{1}{2}}^- - df_{i+\frac{1}{2}}^+] + \frac{(1-\phi)}{4} [df_{i+\frac{1}{2}}^- - df_{i+\frac{1}{2}}^+] \quad (12)$$

with $\phi = 1/3$ giving a third order spatial scheme.

To control dispersive errors characteristic of higher order schemes, a total variation diminishing scheme is used to limit the interface flux. This results in the following corrective flux definitions.¹⁰

$$df_{i+\frac{1}{2}}^- = \sum^+ L_j(1,-1) r_{i+\frac{1}{2}}^j \quad (13a)$$

$$df_{i+\frac{1}{2}}^+ = \sum^+ L_j(-1,1) r_{i+\frac{1}{2}}^j \quad (13b)$$

$$df_{i+\frac{1}{2}}^- = \sum^- L_j(1,3) r_{i+\frac{1}{2}}^j \quad (13c)$$

$$df_{i+\frac{1}{2}}^+ = \sum^- L_j(3,1) r_{i+\frac{1}{2}}^j \quad (13d)$$

with the limiter, L , given by

$$L_j(m,n) = \text{minmod} \left(\alpha_{i+\frac{1}{2}}^j, \beta \sigma_{i+\frac{1}{2}}^j \right) \quad (14)$$

where the minmod function is defined as

$\text{minmod}(x,y) = \text{sign}(x) \max\{0, \min\{|x|, y \text{ sign}(x)\}\}$ (15)
with the "compression" parameter β equal to 4 and σ , a parameter proportional to the interface characteristic variable jump defined by

$$\sigma_{i+\frac{1}{2}}^j = \lambda_{i+\frac{1}{2}}^j \frac{1}{\tau_{i+\frac{1}{2}}^j} dq_{i+\frac{1}{2}}^j \quad (16)$$

Excellent results^{9,10} have been obtained by evaluating the residual term with the above flux-difference split method and the left hand side operator with the flux vector split scheme, which is approximately factored into the product of two operators. The resulting two step implicit algorithm is given as

$$\left[I + \frac{2\Delta\tau}{3J^{n+1}} (\delta_1 A^+ + \delta_2 B^+) \right] \Delta q^n = \frac{1}{J^{n+1}} \left(-\frac{2}{3} \Delta\tau R^n + g_d \right) \quad (17a)$$

$$\left[I + \frac{2\Delta\tau}{3J^{n+1}} (\delta_1 A^- + \delta_2 B^-) \right] \Delta q = \Delta q^n \quad (17b)$$

$$q^{n+1} = q^n + \Delta q \quad (17c)$$

with the residual term, R^n , defined as

$$R^n = -(\delta_1 F + \delta_2 G) \quad (18)$$

The "geometric conservation law", which prevents spurious source terms due to the motion of the grid, is satisfied in Equation 17a by the following relationship

$$g_d = \frac{1}{3} [J^n \Delta q^{n-1} + \Delta J^{n-1} (q^n - \Delta q^{n-1})] - q^n \Delta J^n \quad (19)$$

with ΔJ^n given by

$$\Delta J^n = J^{n+1} - J^n = \frac{1}{3} \Delta J^{n-1} - \frac{2}{3} \Delta\tau [\delta_1 \tilde{u}_x + \delta_2 \tilde{u}_y]^{n+1} \quad (20)$$

This results in a flow solver that is third-order accurate spatially

and second-order accurate in time.^{9,10}

Computational Grid

In this paper, the Euler numerical solution is implemented on an airfoil cascade geometry, Figure 1, by a computational C-grid. In particular, the numerical solution is obtained utilizing the deforming grid technique of References 5 and 13 for zero and non-zero interblade phase angles.

The outer boundary of the C-grid is defined by the user in the grid generation program GRAPE.^{11,12} The outer boundary remains fixed in space, with a deforming grid technique used to locate the position of the airfoil. The grid lines connecting the inner and outer boundaries deform with the airfoil motion. Figure 2 shows three airfoil grids for analysis of a 90 degree interblade phase angle value. Note that the airfoil motion is exaggerated in this figure. The amount of deformation is a function of the distance from the airfoil surface. The grid deformation is defined as

$$\Delta x_{ij} = W_{ij} (\Delta x_{ij}) \quad (21a)$$

$$\Delta y_{ij} = W_{ij} (\Delta y_{ij}) \quad (21b)$$

where Δx_{ij} and Δy_{ij} are the spatial differences that would exist between successive time steps if the entire grid were moved as a rigid body, the weighting function, W , is:

$$W_{ij} = W(\xi, \eta) = \left| \frac{d(\xi, \eta)}{d(\xi, \eta_{\max})} - 1 \right| \quad (22)$$

where s is the arc length of a grid line from the airfoil surface ($\eta=1$) to some grid point along $\xi=\text{constant}$, and η_{\max} is the outer boundary grid line as shown in Figure 1.

From Equations 21 and 22, the nodes at the inner boundary ($s=0$) give $W_{ij}=1$, which means that the airfoil surface follows the rigid body motion of the blade. Conversely, the outer boundary nodes give $W_{ij}=0$, and the node positions remain fixed at the initial specified locations. The interior nodes shear in space relative to the initial grid as W_{ij} varies between 0 and 1. The node velocities are found by dividing the grid deformation by the time step value.

Boundary conditions

Solid Surface

The solid surface boundary conditions, f-g in Figure 1, implement zero pressure gradient conditions.¹⁴ These zero pressure gradient boundary conditions are sufficient as long as the grid near the surface is adequately resolved. The flow variables are averaged across the interface aft of the airfoil solid surface to the exit, e-f and g-h in Figure 1.

Steady Inlet and Exit

Characteristic variable boundary conditions (CVBC) are used for proper transmission of information into and out of the steady computational domain.¹⁴ The CVBC's are consistent with the concept of upwinding in which the signs of the characteristic velocities determine the appropriate propagation directions.¹⁴ A summary of their derivation is given in the following.

The Euler equations written in their non-conservative form are

$$\frac{\partial q}{\partial \tau} + a \frac{\partial q}{\partial \xi} + b \frac{\partial q}{\partial \eta} = 0 \quad (23)$$

with the matrices a and b determined through an eigenvalue analysis.

The inlet conditions, b-c in Figure 1, are obtained by multiplying Equation 23 by P_{η}^{-1} and neglecting the derivatives in the normal inlet ξ direction to give

$$P_1^T \frac{\partial \mathbf{q}}{\partial \eta} + P_1^T P_1 \Lambda_\eta P_1^T \frac{\partial \mathbf{q}}{\partial \eta} = 0 \quad (24)$$

where Λ_η is a diagonal matrix containing the eigenvalues, λ_η ; and P_1 and P_1^T are the left and right eigenvectors, respectively.

The characteristic vector is defined as

$$W_\eta = P_1^T \mathbf{q} \quad (25)$$

P_1 is such that the elements of the characteristic vector become

$$w_\eta^1 = \frac{1}{|\nabla \eta|} \left[\eta_x \left(\rho - \frac{P}{c^2} \right) \right] \quad (26a)$$

$$w_\eta^2 = \frac{1}{|\nabla \eta|} \left[\eta_y \left(\rho - \frac{P}{c^2} \right) \right] \quad (26b)$$

$$w_\eta^3 = \frac{1}{\sqrt{2} |\nabla \eta|} \left[\frac{P \nabla \eta}{\rho_1 c_1} + (\eta_x u + \eta_y v) \right] \quad (26c)$$

$$w_\eta^4 = \frac{1}{\sqrt{2} |\nabla \eta|} \left[\frac{P \nabla \eta}{\rho_1 c_1} - (\eta_x u + \eta_y v) \right] \quad (26d)$$

The corresponding eigenvalues are

$$\lambda_\eta^1, \lambda_\eta^2 = \eta_x + \eta_x u + \eta_y v \quad (27a,b)$$

$$\lambda_\eta^3 = (\eta_x u + \eta_y v) + c |\nabla \eta| \quad (27c)$$

$$\lambda_\eta^4 = (\eta_x u + \eta_y v) - c |\nabla \eta| \quad (27d)$$

The implementation of the characteristic variable boundary conditions requires specifying whether the boundary is an inlet or an exit boundary. Usually, this is done by computing the sign of λ to determine the directions of the characteristics. For cascades, however, the direction of the flow and the characteristics are known, with the flow-grid orientation determining the sign of the eigenvalues. If the flow is in the same direction as the increasing computational coordinate the sign of the first eigenvalue is positive. Otherwise, the flow-grid orientation is opposed giving a negative sign for the first eigenvalue. The subscript "a" denotes approaching the boundary, "b" refers to on the boundary, and "T" leaving the boundary. For a subsonic inlet, with flow direction opposite the grid direction, the characteristics approaching the boundary are set equal to the characteristics on the boundary using Equation 26.

$$\left[\eta_x \left(\rho - \frac{P}{c^2} \right) \right]_a = \left[\eta_x \left(\rho - \frac{P}{c^2} \right) \right]_b \quad (28a)$$

$$\left[\eta_y \left(\rho - \frac{P}{c^2} \right) \right]_a = \left[\eta_y \left(\rho - \frac{P}{c^2} \right) \right]_b \quad (28b)$$

$$\left\{ \begin{array}{l} \frac{P \nabla \eta}{\rho_1 c_1} + \text{sign}(\lambda_\eta^1) (\eta_x u + \eta_y v) \\ \frac{P \nabla \eta}{\rho_1 c_1} + \text{sign}(\lambda_\eta^2) (\eta_x u + \eta_y v) \end{array} \right\}_a = \left\{ \begin{array}{l} \frac{P \nabla \eta}{\rho_1 c_1} + \text{sign}(\lambda_\eta^1) (\eta_x u + \eta_y v) \\ \frac{P \nabla \eta}{\rho_1 c_1} + \text{sign}(\lambda_\eta^2) (\eta_x u + \eta_y v) \end{array} \right\}_b \quad (28c)$$

$$\left\{ \begin{array}{l} \frac{P \nabla \eta}{\rho_1 c_1} - \text{sign}(\lambda_\eta^3) (\eta_x u + \eta_y v) \\ \frac{P \nabla \eta}{\rho_1 c_1} - \text{sign}(\lambda_\eta^4) (\eta_x u + \eta_y v) \end{array} \right\}_a = \left\{ \begin{array}{l} \frac{P \nabla \eta}{\rho_1 c_1} - \text{sign}(\lambda_\eta^3) (\eta_x u + \eta_y v) \\ \frac{P \nabla \eta}{\rho_1 c_1} - \text{sign}(\lambda_\eta^4) (\eta_x u + \eta_y v) \end{array} \right\}_b \quad (28d)$$

The metrics at points "a" and "T" are assumed to be the same as those at point "b". Combining Equations 28 (c,d) gives Equation 29a, with the remaining flow variables at the inlet boundary found by simultaneous solution of Equations 28 (a-d).

$$P_b = \frac{1}{2} (P_a + P_T - \rho_1 c_1 [\eta_x (u_a - u_T) + \eta_y (v_a - v_T)]) \quad (29a)$$

$$\rho_b = \rho_a + \frac{P_b - P_a}{c^2} \quad (29b)$$

$$u_b = u_a - \eta_x \frac{P_b - P_a}{\rho_1 c_1} \quad (29c)$$

$$v_b = v_a - \eta_y \frac{P_b - P_a}{\rho_1 c_1} \quad (29d)$$

With the non-conservative flow variables found, the conservative dependent variables in Equation 4 can be easily computed at the inlet boundary.

The dependent flow variables at the exit boundaries, a-h and d-e in Figure 1, are obtained by a similar method with special attention to the flow-grid orientation effect on the sign of the first eigenvalue (i.e., d-e $\lambda_\xi^1 > 0$ and a-h $\lambda_\xi^1 < 0$). Equation 23 is multiplied by P_ξ^T and the derivatives in the normal exit η direction are neglected, therefore substitution is made of ξ for η in Equations 25 thru 28.

The characteristics on the exit boundary are set equal to the characteristics leaving the boundary. In this case, the incoming characteristic is the upstream running pressure wave and therefore the pressure is set equal to the pressure leaving. For internal steady flows, this is usually specified by the user. The non-conservative flow variables become

$$P_b = P_T \quad (30a)$$

$$\rho_b = \rho_a + \frac{P_b - P_a}{c^2} \quad (30b)$$

$$u_b = u_a + \text{sign}(\lambda_\xi^1) \xi_x \frac{P_a - P_b}{\rho_2 c_2} \quad (30c)$$

$$v_b = v_a + \text{sign}(\lambda_\xi^1) \xi_y \frac{P_a - P_b}{\rho_2 c_2} \quad (30d)$$

With the non-conservative flow variables found, the conservative dependent variables in Equation 4 can be easily computed at the exit boundary.

Note that these characteristic variable boundary conditions are only valid for steady cascade flows because the exit boundary is assumed to have uniform static pressure.

Unsteady Inlet and Exit

Approximate non-reflecting unsteady inlet and exit boundary conditions are developed by assuming that linear theory can be applied. Giles¹⁵ derived "non-reflecting" boundary conditions for a general turbomachinery Euler solver. First the steady flow is solved using the previously presented CVBC's. The linearized Euler equations are then solved at the inlet and exit boundary to determine the perturbation flow variables in terms of the characteristic variables. This allows time variations of static pressure at the exit and reduces reflections from the boundaries. A brief outline of this method is given below.

The linearized, two-dimensional Euler equations are written in terms of primitive small-perturbation variables as

$$\frac{\partial Q'}{\partial t} + A \frac{\partial Q'}{\partial x} + B \frac{\partial Q'}{\partial y} = 0 \quad (31)$$

where

$$Q' = (\delta p, \delta u, \delta v, \delta p)^T \quad (32)$$

$$A = \begin{bmatrix} u & \rho & 0 & 0 \\ 0 & u & 0 & \frac{1}{\rho} \\ 0 & 0 & u & 0 \\ 0 & \gamma P & 0 & u \end{bmatrix}, \quad B = \begin{bmatrix} v & 0 & \rho & 0 \\ 0 & v & 0 & 0 \\ 0 & 0 & v & \frac{1}{\rho} \\ 0 & 0 & \gamma P & v \end{bmatrix} \quad (33)$$

The elements of the vector Q' represent perturbations from uniform flow conditions, with the matrices A and B evaluated using these same conditions. The analysis is greatly simplified if the unsteady perturbations and the steady variables in A and B are nondimensionalized using the steady density and speed of sound. With this choice of nondimensionalization, the final forms of the matrices A and B are

$$A = \begin{bmatrix} M_x & 1 & 0 & 0 \\ 0 & M_x & 0 & 1 \\ 0 & 0 & M_x & 0 \\ 0 & 1 & 0 & M_x \end{bmatrix} \quad (34a)$$

$$B = \begin{bmatrix} M_y & 0 & 1 & 0 \\ 0 & M_y & 0 & 0 \\ 0 & 0 & M_y & 1 \\ 0 & 0 & 1 & M_y \end{bmatrix} \quad (34b)$$

where M_x and M_y are the Mach numbers in the x and y directions.

A set of eigenvectors representing an entropy wave, a vorticity wave and upstream/downstream running pressure waves are determined by Fourier analysis of these equations. Using these eigenvectors and assuming locally one-dimensional flow at the boundary, the characteristic variables for unsteady flows are written in terms of the perturbation variables as

$$\begin{bmatrix} C_1 \\ C_2 \\ C_3 \\ C_4 \end{bmatrix} = \begin{bmatrix} -1 & 0 & 0 & 0 \\ 0 & 0 & 1 & 0 \\ 0 & 1 & 0 & 1 \\ 0 & -1 & 0 & 1 \end{bmatrix} \begin{bmatrix} \delta p \\ \delta u \\ \delta v \\ \delta P \end{bmatrix} \quad (35)$$

For a subsonic inlet, the amplitudes of the incoming unsteady characteristics (C_1, C_2, C_3) are set to zero and the outgoing characteristic (C_4) is computed using Equation 35. For subsonic exit, $C_4 = 0$ and the remaining characteristics are computed. Once the characteristics are known, the perturbation variables are found using an inverse transform

$$\begin{bmatrix} \delta p \\ \delta u \\ \delta v \\ \delta P \end{bmatrix} = \begin{bmatrix} -1 & 0 & \frac{1}{2} & \frac{1}{2} \\ 0 & 0 & \frac{1}{2} & -\frac{1}{2} \\ 0 & 1 & 0 & 0 \\ 0 & 0 & \frac{1}{2} & \frac{1}{2} \end{bmatrix} \begin{bmatrix} C_1 \\ C_2 \\ C_3 \\ C_4 \end{bmatrix} \quad (36)$$

The primitive flow variables are found using the following relationships.

$$\rho = \rho_0 + \delta \rho \quad (37a)$$

$$u = u_0 + \delta u \quad (37b)$$

$$v = v_0 + \delta v \quad (37c)$$

$$P = P_0 + \delta P \quad (37d)$$

where ρ_0, u_0, v_0 and P_0 specify the steady solution.

With the non-conservative flow variables found, the conservative dependent variables in Equation 4 are easily computed at the inlet and exit boundary.

Fourier Periodic

To minimize the large computer time or memory requirements associated with implementing the periodic boundary conditions for non-zero interblade phase angle values, the flow variables at the periodic boundaries are approximately expressed as a Fourier series.⁸ This is accomplished by expanding the computational grid one node at the upper and lower periodic boundaries, Figure 1. At one node interior of the upper and lower periodic boundaries, the timewise integration for the Fourier coefficients are performed on the conservative variables ($f(x,t)$) ($\rho(x,t), p(x,t),$ etc.) at the lower and upper boundaries.

Lower Boundary:

$$A_L^n(x) = \frac{\Delta t}{\pi} \sum_{i=1}^{N_p} f_{L,i}(x,t) \sin(n\omega t) \Delta t \quad (38a)$$

$$B_L^n(x) = \frac{\Delta t}{\pi} \sum_{i=1}^{N_p} f_{L,i}(x,t) \cos(n\omega t) \Delta t \quad (38b)$$

Upper Boundary:

$$A_U^n(x) = \frac{\Delta t}{\pi} \sum_{i=1}^{N_p} f_{U,i}(x,t) \sin(n\omega t) \Delta t \quad (38c)$$

$$B_U^n(x) = \frac{\Delta t}{\pi} \sum_{i=1}^{N_p} f_{U,i}(x,t) \cos(n\omega t) \Delta t \quad (38d)$$

where N_p is the number of time steps in one period of oscillation, and the subscripts L and U indicate the lower and upper periodic boundary.

The solutions at the overlapped nodes for the lower and upper periodic boundaries are then found by an N th order timewise Fourier series for the conservative variables, $f(x,t)$.

$$f_{L,i}(x,t) = f_{L,i}^0(x) + \sum_{n=1}^N [A_L^n(x) \sin(n(\omega t - \sigma)) + B_L^n(x) \cos(n(\omega t - \sigma))] \quad (39a)$$

$$f_{U,i}(x,t) = f_{U,i}^0(x) + \sum_{n=1}^N [A_U^n(x) \sin(n(\omega t + \sigma)) + B_U^n(x) \cos(n(\omega t + \sigma))] \quad (39b)$$

where f^0 is the time-averaged value of f .

The implementation procedure for Equations 38 and 39 is to first perform the timewise integration for the Fourier coefficients at one node interior to the periodic boundaries. This is an interior solution from the flow solver. The current solution at the expanded nodes is then calculated using the Fourier coefficients from the previous time period and Equation 39. After each period of integration, new values of the coefficients are obtained from Equation 38. Then the coefficients in Equation 39 are updated by the new values obtained. To accelerate convergence to a periodic solution, the coefficients and time-averaged values are updated 5 times per period of oscillation.

In this method, the Fourier coefficients of the response at the periodic boundaries are stored and continually updated. This is more efficient in computer memory usage than that of the direct store method which stores the entire time history at the periodic boundary.

To obtain coefficients for the first period of oscillation, a zero interblade phase angle configuration is analyzed with the coefficients calculated on the upper and lower boundaries and stored. For a non-zero interblade phase angle, the zero phase angle coefficients are used only for the first period with the appropriate nonzero interblade phase angle then applied. The analysis is then run until a periodic solution is achieved.

Results

In this paper, the unsteady periodic boundary conditions for unsteady Euler models are investigated. The two-dimensional unsteady Euler equations are solved for a cascade geometry, Figure 1, using a time-marching, flux-difference splitting scheme implemented on a C-grid which is allowed to deform with the airfoil motion, either torsional or translational. Predictions for both flat plate and loaded oscillating airfoil cascades are presented, with the oscillation amplitude, cascade geometry and interblade phase angles varied.

Flat Plate Results

To validate the Euler solutions, the unsteady flow past an oscillating flat plate cascade is analyzed and compared with linear theory predictions. The cascade consists of flat plates staggered at 45 degrees with a solidity of 1.0. The inlet Mach number is 0.7, the mean flow incidence angle is zero and the reduced frequency k is 0.75. A finite 1% thick, rounded nose airfoil is used to approximate the flat plate airfoils. A 145x28 C-grid is extended 0.95 chords upstream of the leading edge and 1.0 chords downstream of the trailing edge, Figure 3a. Initially, the flow variables are set equal to the previously determined steady-state values. Then the airfoils oscillate for a number of cycles sufficient to achieve a periodic unsteady solution. The airfoil surface unsteady pressures for the last cycle of oscillation are then Fourier decomposed to determine the first harmonic unsteady pressure distribution.

Figure 4 shows the magnitude and phase of the airfoil surface unsteady pressure response to a 1% chord translational motion at an interblade phase angle of 90 degrees. The predictions of the Euler solver using the stacked and Fourier periodic boundary conditions, four harmonics, are shown. There is no difference in the response for either of the two Euler periodic boundary conditions. Excellent agreement of the unsteady pressure magnitude between the Euler predictions and the linear theory analysis of Whitehead¹ is evident. The phase distributions are also in good agreement with the linear theory predictions. From 20% to 80% chord, the Euler solver predicts a slightly higher phase angle. The large jump in phase at the trailing edge is a result of the unsteady pressure difference magnitude approaching zero, thereby making any slight difference in the unsteady pressure appear large.

The computational time for the Fourier periodic boundary condition analysis, which required seven cycles of oscillation to converge, was 5 CPU hours versus 11 CPU hours on a HP-730 workstation for the stacked periodic boundary condition, which converged in four oscillations.

10th Standard Configuration

To demonstrate the Fourier periodic boundary conditions for subsonic flow, a loaded airfoil cascade was analyzed. The 10th standard configuration is a cascade of NACA 0006 airfoils at 45 degrees stagger, 10 degrees angle of attack, with a solidity of 1.0. The unsteady cascade flow generated by translational motion is analyzed.

A grid convergence study was conducted to verify grid

independent results. Figure 5 shows the unsteady magnitude and phase pressure response of the 10th standard configuration cascade oscillating with a 0.75 reduced frequency value, a freestream Mach number of 0.7 and a 0 degree interblade phase angle executing translational motion for two grid studies. The first study addresses the grid density independence. Both C-grids extend 0.92 chords upstream and 0.7 chords downstream, with 157x22 and 313x40 grid points respectively. As shown in Figure 5, there is no difference in the results. Thus the coarser grid, Figure 3b, is considered adequate.

The second study is performed to determine grid independence from effects at the inlet and exit plane. The C-grid was extended to 1.5 chords upstream of the leading edge plane and to 2.0 chords downstream of the trailing edge plane with 289x31 points in the grid. The same subsonic translational zero interblade phase angle configuration was analyzed. Note that this is a super-resonant cascade flow configuration, with propagating waves generated. For a super-resonant cascade, acoustic waves do not decay as they propagate away from the oscillating cascade. Therefore, a super resonance condition should be the most sensitive to the inlet and exit location. The results are also shown in Figure 5. No boundary reflection problem is evident. Thus the smaller grid is utilized.

The subsonic 10th standard configuration cascade airfoil surface unsteady pressure difference magnitude and phase response to a translational motion of 1% chord at an interblade phase angle of -45 degrees is shown in Figure 6. Both the Fourier and stacked periodic boundary conditions results are shown, along with the linear theory analysis of Whitehead¹. The two nonlinear analysis results are identical in both magnitude and phase. The magnitude of the Euler unsteady response is three times higher near the leading edge, with the difference decreasing until the Euler and linear solutions agree at the trailing edge. The phase results show that the Euler and linear solutions have the same trendwise behavior, but offset by 90 degrees.

The time history of the unsteady lift for the Fourier analysis is shown in Figure 7. This plot shows that the solution has reached a periodic state after 12 periods of oscillation. This takes 6.4 CPU hours on the HP-730, while the stacked analysis reached a periodic state in 4 periods taking 16.5 CPU hours.

The importance of the number of harmonics in the Fourier periodic boundary conditions is shown in Figure 8. The magnitude of the first eight harmonics of the conservative variable, pu , normalized by the first harmonic from the stacked analysis is shown for five different node locations along the periodic boundary. The Fourier periodic boundary conditions were used, with both the first and the first four harmonics used to determine the solution at the periodic boundary. The magnitude of the harmonics do not change whether the first or the first four terms are kept, i.e. the periodic boundary solution is dominated by the first harmonic.

Transonic Cascade

To demonstrate the Fourier periodic boundary conditions for transonic flow, a cascade configuration with a strong normal shock was analyzed. The 10th standard configuration geometry was used with a freestream Mach number of 0.8. The back pressure was reduced to 0.7, resulting in a strong shock wave completely across the flow passage. The number of grid points in the streamwise direction was increased to 223 to better resolve the shock wave, but no grid refining near the shock was done.

The flow field static pressure contours are presented in Figure 9, showing that the normal shock extends completely across the

blade passage. The steady pressure distribution on the suction and pressure surfaces of the cascade are given in Figure 10. The shock starts at 92% chord on the suction surface and intersects the pressure surface at 25% chord.

The cascade is then oscillated in a torsional mode about the mid-chord with a -90 degree interblade phase angle. The amplitude of the airfoil oscillation is varied from 0.1° to 3.5° . The magnitude of the unsteady moment coefficient from the 0.1° and 0.2° oscillations are extrapolated for the "linear" solution. The unsteady moment coefficient is then plotted versus the amplitude of oscillation, Figure 11. Nonlinear effects are evident for oscillation amplitudes greater than 1.0° . This result agrees with studies on nonlinear cascade effects reported in Reference 16.

Figure 12 shows the airfoil surface unsteady pressure magnitude and phase results for an oscillation amplitude of 3.5° for both the stacked and Fourier periodic boundary conditions, with the first six harmonics used for the Fourier method. The unsteady magnitude and phase pressure response are identical for both methods. The strong normal shock is seen in both the magnitude and phase plots at 25% and 92% chord, with this nonlinear behavior able to be calculated with the Fourier periodic method. The CPU time was 147.0 and 238.8 hours on the HP-730 for the Fourier and stacked periodic boundary conditions respectively, with 35 and 15 periods of oscillation required to reach a periodic solution.

To investigate the Fourier periodic boundary condition solution in more detail, the time history of the conservative variables, p and p_u , one node in from the periodic boundary at the shock wave location are plotted in Figure 13 for both the stacked periodic boundary condition and for the prediction with both the first and the first six harmonics of the Fourier periodic boundary condition method. Only the last four periods of oscillation are plotted to give better resolution. Although the first harmonic alone boundary condition does remarkably well, using the first six harmonics in the boundary condition yields a solution which is nearly identical to that with the stacked airfoils.

The magnitude of the first eight Fourier coefficients one node in from the periodic boundary for the conservative variable p_u at the normal shock location and for the two nodes upstream and downstream of the shock location are shown in Figure 14. Nearly exact agreement between the solution with the stacked and Fourier periodic boundary condition using the first six terms result. However it is evident that using only the first term in the boundary condition does not maintain the higher harmonic effect at the flow field periodic boundary. This figure also emphasizes the validity of only keeping the first six harmonics of the boundary condition, as the higher harmonics are quite small. These results validate that the Fourier periodic boundary conditions preserve the nonlinear behavior of the flow solver.

Computational Resources

The CPU time penalty due to the timewise integrations for the first six harmonics of the Fourier series along the periodic boundaries for a single passage was 2.7 minutes or 5.6% of the 48.5 minutes required for one period of oscillation of a transonic 10th standard configuration for a zero interblade phase angle analysis with overlapping of the grid. The number of oscillations needed to reach a periodic solution was usually double that needed for the stacked periodic boundary conditions. Therefore, depending on the interblade phase angle, the savings in CPU time can be enormous. Also any arbitrary interblade phase angle can easily be analyzed. The penalty in terms of memory requirements for a

particular cascade flow field analysis was approximately 3.0% of the stacked boundary condition. This should not pose any problem for most modern computers.

Summary and Conclusions

An investigation of the unsteady aerodynamics associated with an oscillating cascade of airfoils has been completed using a time-marching flux-difference splitting Euler code implemented on a deforming C-grid. The flow solver, which is second-order accurate in time and third-order accurate spatially, was first verified by analyzing a flat plate cascade and comparing the results with linear theory. This showed excellent agreement with the linear theory predictions, thus validating the flow solver. The 10th standard cascade configuration was then analyzed. As expected these predictions showed effects that the linear theory could not predict and showed the usefulness of applying the Fourier shape correction periodic boundary conditions in saving computer resources. To prove the nonlinear validity of the Fourier periodic boundary conditions, a transonic cascade configuration with a strong normal shock wave and high magnitudes of torsional blade oscillation was studied. These results proved the nonlinear behavior of the Fourier periodic boundary conditions.

The conclusion of this research into the nonlinear unsteady aerodynamics of a cascade of airfoils undergoing both translational and torsional oscillation is that applying a Fourier periodic boundary condition is valid. This periodic boundary condition has been demonstrated to model the nonlinear behavior of the flow field while greatly reducing the computer resources in both time and memory requirements over other methods.

Acknowledgments

Research sponsored by the Air Force Office of Scientific Research, Contract AFOSR-91-0251. The authors would like to acknowledge Major Dan Fant, program manager, for his support throughout the course of this investigation and Dennis Huff, NASA Lewis Research Center, for providing the basic flow algorithm. The United States Government is authorized to reproduce and distribute reprints for governmental purposes notwithstanding any copyright notation hereon.

References

- ¹Whitehead, D. S., "Classical Two-Dimensional Methods," AGARD Manual on Aeroelasticity in Axial-Flow Turbomachines, Vol. 1, Unsteady Turbomachinery Aerodynamics, 1987.
- ²Verdon, J. M., "Linearized Unsteady Aerodynamic Theory," AGARD Manual on Aeroelasticity in Axial-Flow Turbomachines, Vol. 1, Unsteady Turbomachinery Aerodynamics, 1987.
- ³Giles, M. B. and Haines, R., "Validation of a Numerical Method for Unsteady Flow Calculations," *ASME Paper 91-GT-271*, 1991.
- ⁴Gerolymos, G. A., "Numerical integration of the 3D unsteady Euler equations for flutter analysis of axial flow compressors," *ASME Paper 88-GT-255*, 1988.
- ⁵Huff, D. L., "Numerical Simulations of Unsteady, Viscous, Transonic Flow Over Isolated and Cascaded Airfoils Using a Deforming Grid," *AIAA Paper 87-1316*, 1987.
- ⁶Huff, D. L. and Reddy, T. S. R., "Numerical Analysis of Supersonic Flow through Oscillating Cascade Sections by Using a Deforming Grid," *AIAA Paper 89-2805*, 1989.
- ⁷Erdos, J. L., Alzner, E. and McNally, W., "Numerical

Solution of Periodic Transonic Flow Through a Fan Stage," *AAAA Journal*, Vol. 15, No. 11, 1977, pp. 1559-1568.

⁸Ha, L., "An Euler Solution for Unsteady Flows Around Oscillating Blades," *ASME Paper 89-GT-279*, 1989.

⁹Whitfield, D. L., Janus, J. M. and Simpson, L. B., "Implicit Finite Volume High Resolution Wave-Split Scheme for Solving the Unsteady Three-Dimensional Euler and Navier-Stokes Equations on Stationary or Dynamic Grids," Mississippi State Engineering and Industrial Research Station, Report # MSSU-EIRS-ASE-88-2, 1988.

¹⁰Janus, J. M., "Advanced 3-D CFD Algorithm for Turbomachinery," PhD Thesis, Mississippi State University, May 1989.

¹¹Sorenson, R. L., "A Computer Program to Generate Two-Dimensional Grids about Airfoils and Other Shapes by the Use of Poisson's Equation," *NASA TM 81198*, 1981.

¹²Chima, R. V., "Explicit Multi-Grid Algorithm for Quasi Three-Dimensional Viscous Flow in Turbomachinery," *Journal of Propulsion and Power*, Vol. 3, No. 5, Sept.-Oct. 1987, pp. 397-405.

¹³Huff, D. L., "Numerical Analysis of Flow Through Oscillating Cascade Sections," *AIAA Paper 89-0437*, 1989.

¹⁴Janus, J. M., "The Development of A Three-Dimensional Split Flux Vector Solver with Dynamic Grid Applications," MS Thesis, Mississippi State University, August 1984.

¹⁵Giles, M. B., "Non-Reflecting Boundary Conditions for Euler Equation Calculations," *AIAA Journal*, Vol. 28, No. 12, 1990, pp. 2050-2058.

¹⁶Huff, D. L., Swafford, T. W. and Reddy, T. S. R., "Euler Flow Predictions for an Oscillating Cascade Using A High Resolution Wave-Split Scheme," *NASA TM 104377*, 1991.

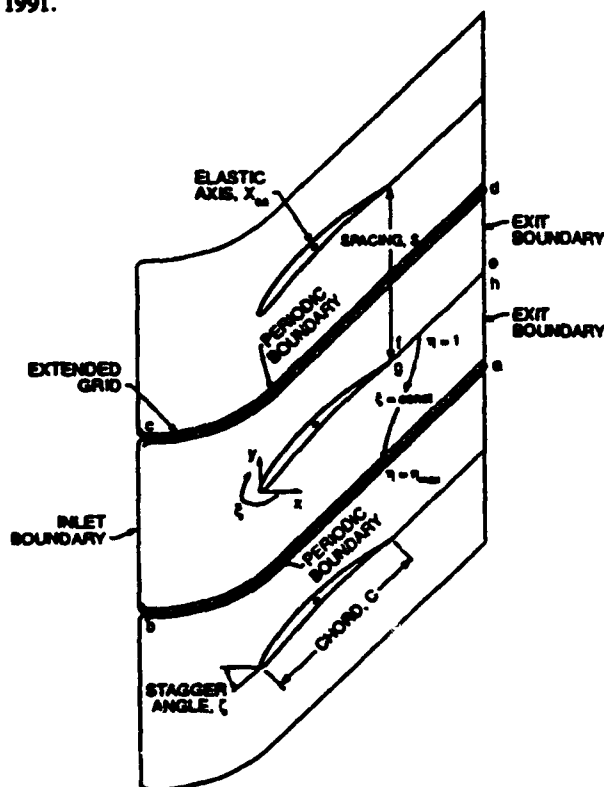
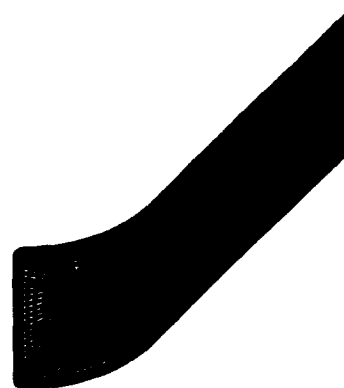


Figure 1. Computational and cascade geometry.



Figure 2. Deforming grid - $\sigma = 90^\circ$.



(a) Flat Plate



(b) 10th Standard Configuration
Figure 3. Computational grids.

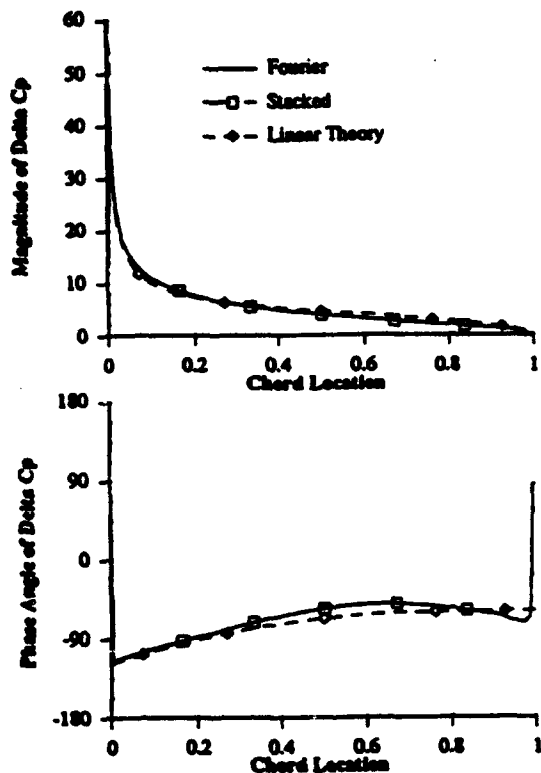


Figure 4. Flat plate cascade unsteady pressure difference: $M = 0.7, k = 0.75, \zeta = 45^\circ, \alpha = 0^\circ, p/P_0 = 0.721, h_1 = 0.01, C/S = 1.0, \sigma = 90^\circ$

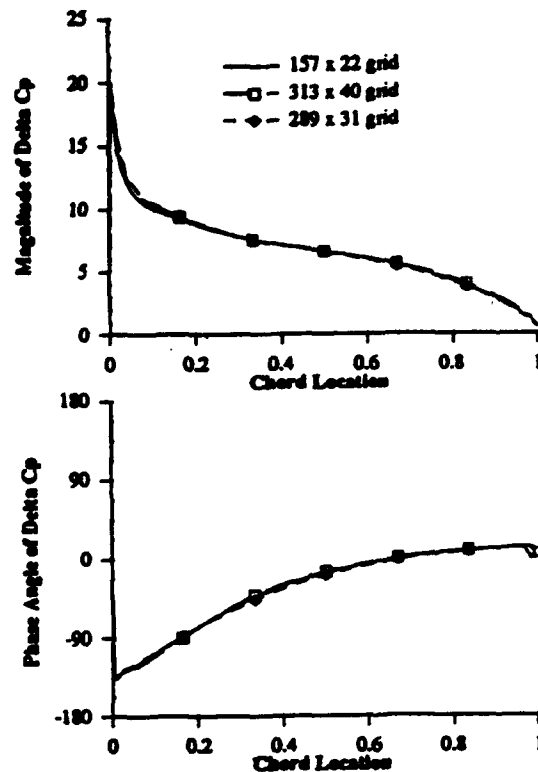


Figure 5. Grid effect on 10th standard configuration unsteady pressure difference: $M = 0.7, k = 0.75, \zeta = 45^\circ, \alpha = 10^\circ, p/P_0 = 0.87, h_1 = 0.01, C/S = 1.0, \sigma = 0^\circ$

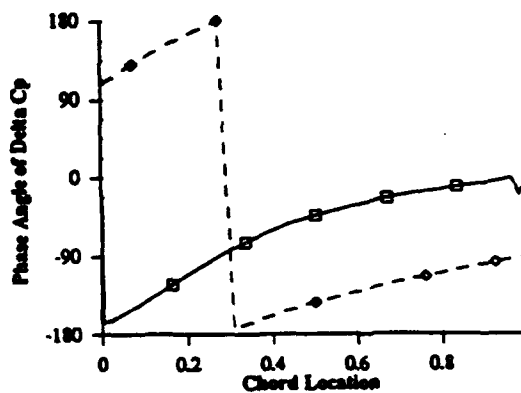
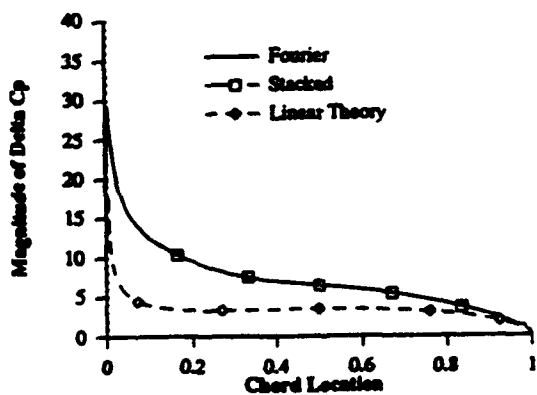


Figure 6. 10th standard configuration unsteady pressure difference: $M = 0.7, k = 0.75, \zeta = 45^\circ, \alpha = 10^\circ, p/P_0 = 0.87, h_1 = 0.01, C/S = 1.0, \sigma = -45^\circ$

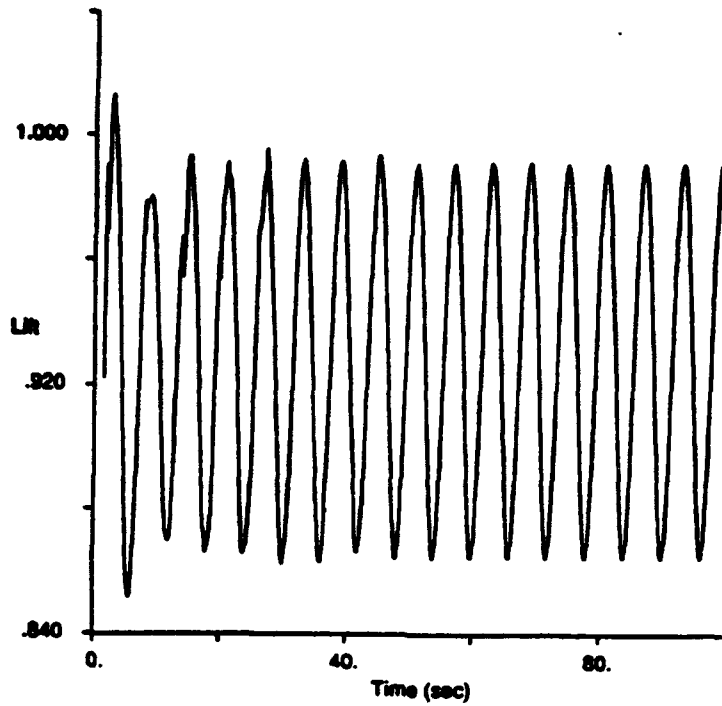


Figure 7. Lift time history.

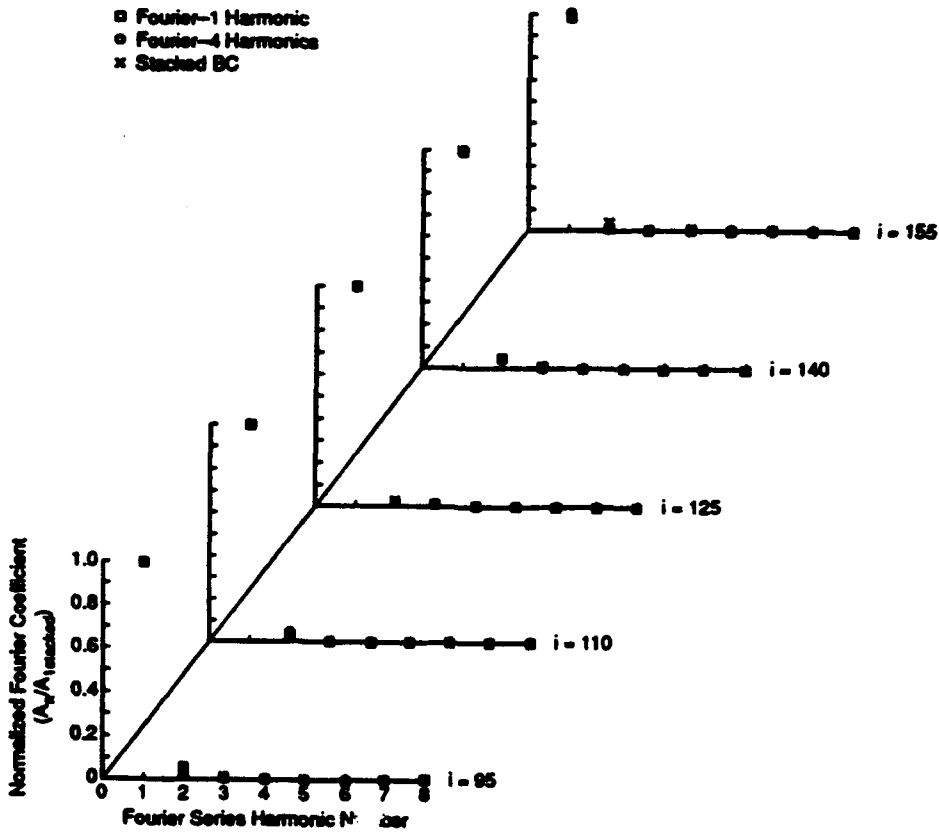


Figure 8. Normalized pu Fourier series harmonic amplitudes:
 $M = 0.7, k = 0.75, \zeta = 45^\circ, \alpha = 10^\circ, p/P_0 = 0.87, h_1 = 0.01, C/S = 1.0, \sigma = -45^\circ$

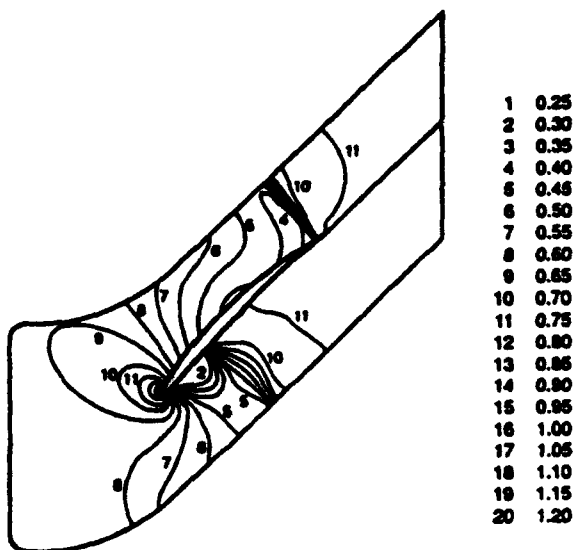


Figure 9. 10th standard configuration static pressure contours: $M = 0.8$, $\zeta = 45^\circ$, $\alpha = 10^\circ$, $C/S = 1.0$, $p/P_0 = 0.7$

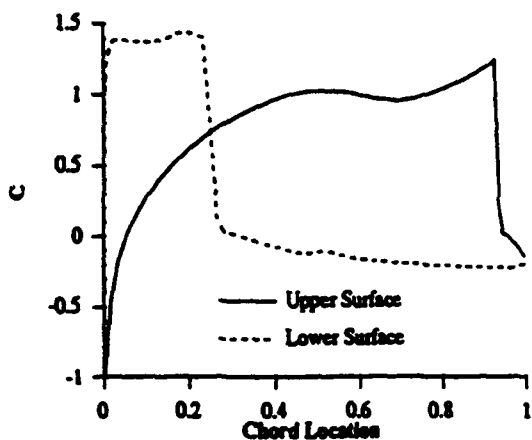


Figure 10. 10th standard configuration steady pressure distribution: $M = 0.8$, $\zeta = 45^\circ$, $\alpha = 10^\circ$, $C/S = 1.0$, $p/P_0 = 0.7$

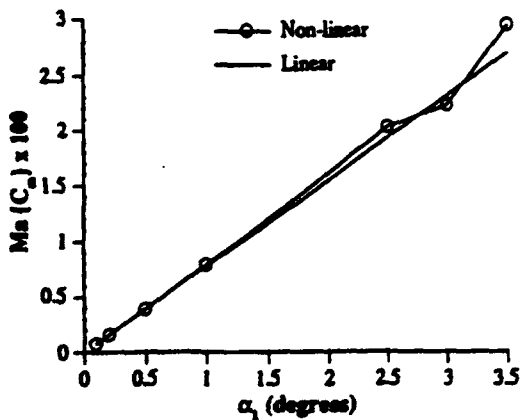


Figure 11. Unsteady moment coefficient vs amplitude of oscillation: $M = 0.8$, $k = 0.75$, $\zeta = 45^\circ$, $\alpha = 10^\circ$, $p/P_0 = 0.7$, $C/S = 1.0$, $\sigma = -90^\circ$

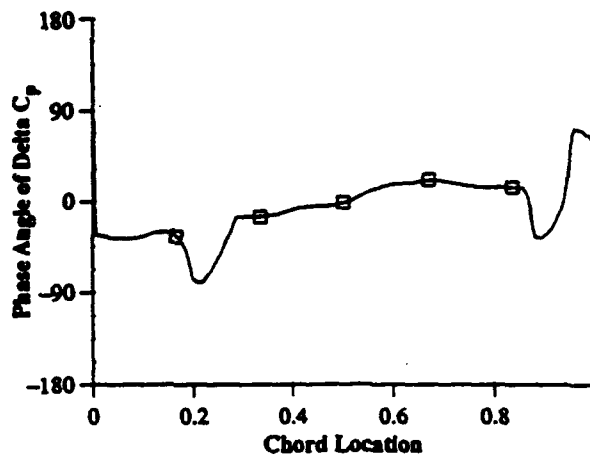
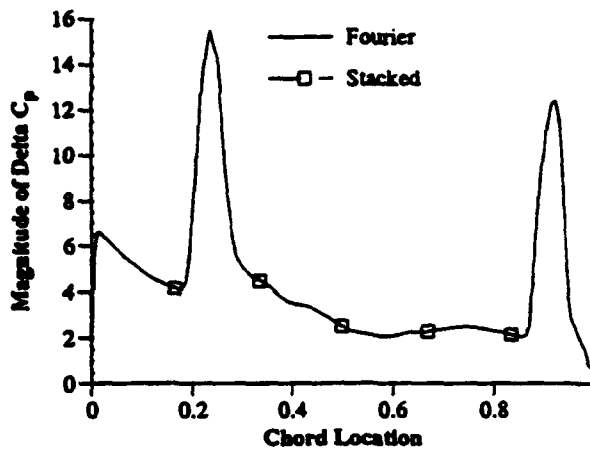


Figure 12. 10th standard configuration unsteady pressure difference: $M = 0.8$, $k = 0.75$, $\zeta = 45^\circ$, $\alpha = 10^\circ$, $p/P_0 = 0.7$, $\alpha_1 = 3.5^\circ$, $C/S = 1.0$, $\sigma = -90^\circ$

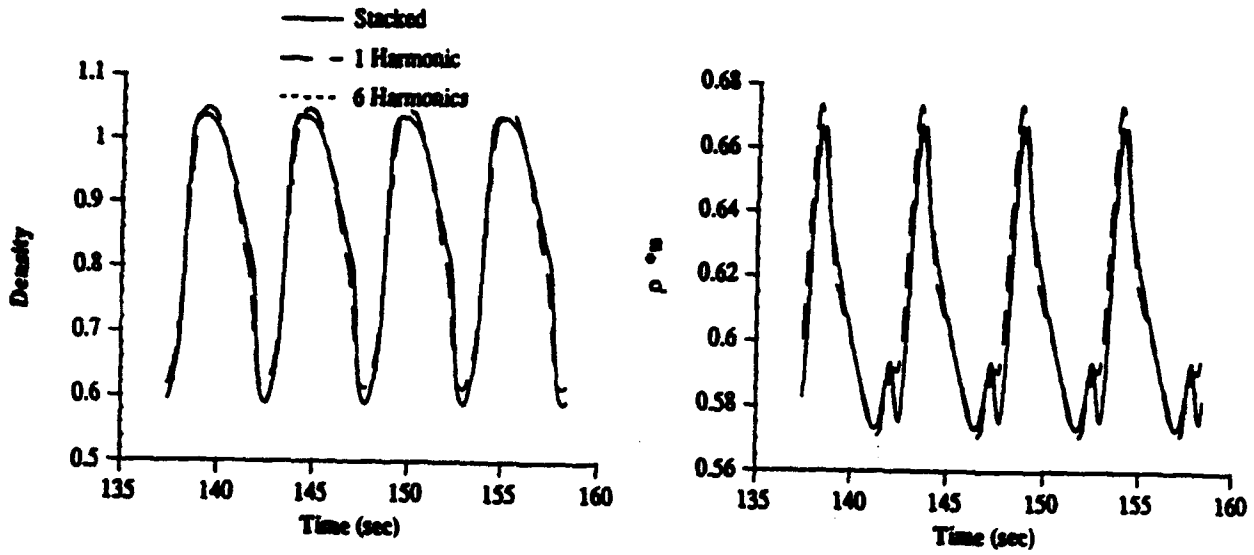


Figure 13. Time trace of conservative variables at periodic boundary:
 $M = 0.8, k = 0.75, \zeta = 45^\circ, \alpha = 10^\circ, p/P_0 = 0.7, \alpha_1 = 3.5^\circ, C/S = 1.0, \sigma = -90^\circ$

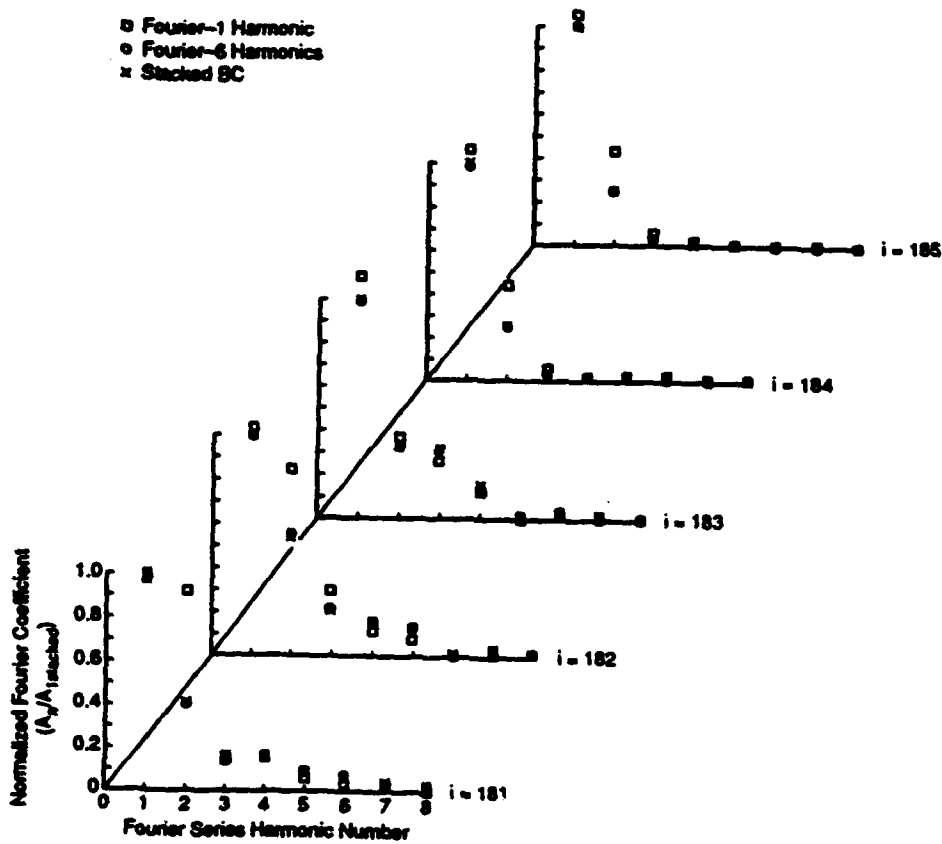


Figure 14. Normalized pu Fourier series harmonic amplitudes:
 $M = 0.8, k = 0.75, \zeta = 45^\circ, \alpha = 10^\circ, p/P_0 = 0.7, \alpha_1 = 3.5^\circ, C/S = 1.0, \sigma = -90^\circ$

APPENDIX VI**Acoustic Resonance Flow Conditions on Wake Generated Rotor Blade Gust Response***ASME Paper 93-187 , May 1993*



The Society shall not be responsible for statements or opinions advanced in papers or discussion at meetings of the Society or of its Divisions or Sections, or printed in its publications. Discussion is printed only if the paper is published in an ASME Journal. Papers are available from ASME for 15 months after the meeting.

Printed in U.S.A.

EFFECT OF ACOUSTIC RESONANCE CONDITION ON WAKE GENERATED ROTOR BLADE GUST RESPONSE

Steven R. Manwaring⁺ and Sanford Fleeter
Thermal Sciences and Propulsion Center
School of Mechanical Engineering
Purdue University
West Lafayette, Indiana

ABSTRACT

Unsteady aerodynamic blade row response is generally categorized as either subresonant or superresonant, with an acoustic resonance at the points where these regions meet. Although these far field acoustic responses are critical to obtaining correct predictions from linearized unsteady flow models, they are a subject of some controversy, both analytically and experimentally. In this paper, multistage axial flow compressor acoustic resonance conditions, including both subresonant and superresonant unsteady aerodynamic response in the immediate vicinity of an acoustic resonance, are experimentally investigated. This is accomplished by quantifying these acoustic resonance and subresonant and superresonant blade row interaction phenomena in terms of their effect on the rotor blade row periodic unsteady pressure response. The subresonant and superresonant acoustic environments are established by changing the number of vanes while maintaining the number of rotor blades, thereby altering the unsteady stator-rotor interactions and the interblade phase angle and by varying the Mach number without changing the blade row interactions. First the first stage rotor row periodic unsteady pressure response to a downstream stator-rotor interaction generated acoustic wave is studied. Then, the gust unsteady aerodynamic response of the first stage rotor row due to IGV wakes, with the IGV-instrumented first stage rotor itself configured to generate subresonant and superresonant conditions is considered. Appropriate data are correlated with predictions.

NOMENCLATURE

b	Rotor blade semichord
C_p	Rotor blade steady pressure coefficient
C_p	Rotor blade unsteady pressure coefficient
$C_{\Delta p}$	Rotor blade unsteady pressure difference coefficient
$C_{p\delta}$	Rotor blade acoustic wave unsteady pressure coefficient
i	Rotor blade mean incidence angle
k	Reduced frequency = $\omega b / \bar{V}_x$
p	Digitized ensemble averaged unsteady pressure
P_s	Rotor blade surface steady pressure
\bar{p}	First harmonic complex unsteady pressure
\bar{p}_0	Acoustic wave complex unsteady pressure
u_s	Streamwise gust first harmonic component
u_t	Streamwise periodic unsteady velocity
v_s	Transverse gust first harmonic component
v_t	Transverse periodic unsteady velocity
\bar{V}_x	Mean axial velocity
ΔV	Absolute velocity vector difference from mean value
	Total unsteady velocity
	Relative mean flow angle
$\Delta\beta$	Relative flow angle difference from mean value
ω	Forcing function frequency

INTRODUCTION

Turbomachine blade row aeroelastic and aeroacoustic response are driven by unsteady aerodynamic phenomena, currently analyzed by linearized unsteady aerodynamic models in which the unsteady flow is considered to be a small perturbation of a uniform, Whitehead [1987], Fleeter [1973], Adamczyk and Goldstein [1978], and Verdon and Usab [1990], or a nonuniform steady flow, Verdon and Hall [1990], Scott and Atassi [1990] and Fang [1991]. For these linearized models to yield mathematically valid predictions of the blade row unsteady aerodynamics, the far field solution characteristics are critical. Namely, the particular combination of unsteady flow conditions may result in these linearized unsteady aerodynamics models generating various wave propagation modes.

Unsteady aerodynamic blade row response is generally categorized based on the far field acoustic response. For a cascade in a subsonic flow, the unsteady flow is superresonant when pressure disturbances propagate away from the cascade unattenuated. When the pressure disturbances decay exponentially with distance, the cascade is subresonant. At an acoustic resonance, a point where subresonant and superresonant regions meet, the pressure disturbances propagate energy along the blade row, i.e., the energy is propagated in a purely tangential direction.

⁺ Currently Engineer, Aerodynamics Research Laboratory
General Electric, Aircraft Engines, Cincinnati, Ohio

Acoustic resonances exist for specific combinations of steady flow conditions, cascade geometries, and interblade phase angle β and reduced frequency k values. For a subsonic inlet Mach number, the unsteady flow and cascade geometry conditions which specify the acoustic resonant interblade phase angle value β_r^* is given in Equation 1. At positive and negative interblade phase angle values, acoustic resonances bracket the wave propagating superresonant region. When either $\beta > \beta_r^*$ or $\beta < \beta_r^*$, the cascade is subresonant and the waves decay [9].

$$\beta_r^* = \frac{2kM}{(C/S)(1 - M^2)} (M \sin(\alpha_0 + \gamma) \pm \sqrt{1 - M^2 \cos^2(\alpha_0 + \gamma)}) \quad (1)$$

where β_r^* is the acoustic resonant interblade phase angle, M denotes the Mach number, $k = \omega C/2U$, C/S is the cascade solidity, γ is the cascade stagger angle and α_0 is the mean flow incidence angle.

Although these acoustic resonances are critical to obtaining mathematically correct predictions from linearized unsteady flow models, they are a subject of some controversy. For example, Gerolymos, Blin, and Quiniou [1990] developed an Euler solver and obtained good correlation with vibrating transonic cascade data. However, this code did not exhibit any particular behavior at acoustic resonance conditions. Experimentally, superresonant flow wave propagation behavior has been shown by Buffum and Fletcher [1991a, 1991b] to have a significant effect on obtaining valid two-dimensional oscillating cascade data. The question has also been raised as to the significance of acoustic resonances in actual blade rows.

Of particular interest herein is a rotor blade operating in a multiblade row environment. The interaction of this rotor with distorted flow fields generated from vanes, struts, obstructions or inlet flow distortions, for example, generates propagating acoustic waves. These unsteady interactions are specified by the reduced frequency k and the relative number of upstream excitations $N_{excitations}$ and downstream rotor blades N_{blades} which specifies the interblade phase angle value β .

$$\beta = 2\pi \frac{N_{excitations}}{N_{blades}} \pm 2\pi m \quad (2)$$

where m is an integer.

These rotor interactions generate acoustic waves which propagate upstream and downstream. Depending on the interaction, i.e., the relative number of upstream excitations and downstream rotor blades, either a subresonant or a superresonant flow condition results. In the subresonant regime, the acoustic wave is attenuated whereas in the superresonant flow regime it propagates upstream and downstream.

In this paper, multistage axial flow compressor acoustic resonance conditions, including both subresonant and superresonant unsteady aerodynamic response in the immediate vicinity of an acoustic resonance, are experimentally investigated. This is accomplished by means of a series of experiments directed at quantifying these acoustic resonance and subresonant and superresonant blade row interaction phenomena in terms of their effect on the rotor blade row periodic unsteady pressure response. First the first stage rotor row periodic unsteady pressure response to a downstream stator-rotor interaction generated acoustic wave is studied. Then, the gust unsteady aerodynamic response of the first stage rotor row due to IGV wakes, with the IGV-instrumented first stage rotor itself configured to generate subresonant and superresonant conditions is considered.

RESEARCH COMPRESSOR

The Purdue Axial Flow Research Compressor models the fundamental turbomachinery unsteady aerodynamic multistage interaction phenomena which include the incidence angle, the velocity and pressure variations, the aerodynamic forcing function waveforms, the reduced frequency, and the unsteady blade row interactions. The compressor is driven by a 15 HP DC electric motor at a speed of 2,250 RPM. For the baseline configuration, each identical stage contains 43 rotor blades and 31 stator vanes having a British C4 airfoil profile, with the first stage rotor inlet flow field established by a variable setting inlet guide vane (IGV) row of 36 airfoils. The overall compressor and airfoil characteristics are defined in Table 1.

The first stage rotor row is instrumented, with the first stage stator row and second stage rotor row removed to assure that potential effects do not affect the instrumented blade row data. The propagating acoustic wave is generated by fixing the number of third stage rotor blades and varying the number of second stage stator vanes to obtain superresonant flow conditions from this downstream stator-rotor interaction. The IGV's and instrumented first stage rotor row combination is such that their interaction is far removed from the acoustic resonant condition.

To investigate the gust unsteady aerodynamic response of the first stage rotor row due to IGV wakes, with the IGV-instrumented rotor interaction generating subresonant and superresonant conditions, the number of first stage rotor blades is maintained constant and the number of IGV's is varied. Also, the downstream second stage stator and third stage rotor combinations are configured to operate far from an acoustic resonance.

INSTRUMENTATION

The compressor aerodynamic performance is determined utilizing a 48 port Scanivalve system, thermocouples, and a venturi orifice to measure the required pressures, temperatures and flow rate, respectively. The Scanivalve transducer is calibrated each time data are acquired, thus automatically compensating for zero and span shifts of the transducer output. A 95% confidence interval, root-mean-square error analysis of 20 samples is performed for each steady data measurement.

Both steady and unsteady rotor blade row data are required. The steady data quantify the rotor row mean inlet flowfield and the resulting rotor blade midspan steady loading distribution. The unsteady data define the periodic aerodynamic forcing function and the resulting midspan blade surface periodic unsteady pressure distributions.

The inlet flow field, both steady and unsteady, is measured with a rotating cross hot-wire probe. Disturbances in the stationary frame-of-reference, i.e., the IGV wakes, are the unsteady aerodynamic forcing functions to the first stage rotor row. The rotor periodic unsteady inlet flow field generated by these disturbances is measured with a cross hot-wire mounted in the rotor frame-of-reference. The probe is axially mounted 30% of rotor chord upstream of the rotor leading edge plane. A potential flow field analysis determined this axial location to be such that leading edge potential effects are negligible for all steady loading levels. The probe is angularly aligned to obtain rotor relative velocity and flow angle data. The cross hot-wire probe was calibrated and linearized for velocities from 18.3 m/sec to 53.4 m/sec and ± 35 degrees angular variation, with the accuracy of the velocity magnitude and flow angle were determined to be 4% and ± 1.0 degree, respectively. Centrifugal loading effects on the rotating hot-wire sensor resistances and, thus, the responses found to be negligible.

The detailed steady aerodynamic loading on the rotor blade surfaces is measured with a chordwise distribution of 20 midspan static pressure taps, 10 on each surface. The static pressure at the rotor exit plane, measured with a rotor drum static tap, is used as the blade surface static pressure reference. These static pressure measurements are made using a rotor based 48 port constant speed drive Scanivalve system located in the rotor drum.

The measurement of the midspan rotor blade surface unsteady pressures is accomplished with 20 ultra-miniature, high response transducers embedded in the rotor blades at the same chordwise locations as the static pressure taps. To minimize the possibility of flow disturbances associated with the inability of the transducer diaphragm to exactly maintain the surface curvature of the blade, a reverse mounting technique is utilized. The pressure surface of one blade and the suction surface of the adjacent blade are instrumented, with transducers embedded in the nonmeasurement surface and connected to the measurement surface by a static tap. The embedded dynamic transducers are both statically and dynamically calibrated. The static calibrations show good linearity and no discernible hysteresis. The dynamic calibrations demonstrate that the frequency response, in terms of gain attenuation and phase shift, are not affected by the reverse mounting technique. The accuracy of the unsteady pressure measurements, determined from the calibrations, is $\pm 4\%$.

The rotor-based static pressure Scanivalve transducer, rotating cross hot-wire probe and 20 blade surface dynamic pressure transducers are interfaced to the stationary frame-of-reference through a 40 channel slip ring assembly. On-board signal conditioning of the transducer output signals is performed to maintain a good signal-to-noise ratio through the slip rings. The remaining 17 channels of the slip-ring assembly are used to provide excitation to the transducers and on/off switching to the Scanivalve DC motor.

DATA ANALYSIS

Steady Data

The rotor blade surface static pressure data, measured with the rotor-based Scanivalve system, are defined by a root-mean-square error analysis of 20 samples with a 95% confidence interval. The reference for these midspan blade pressure measurements is the static pressure at the exit of the rotor measured on the rotor drum. Thus, the blade surface and the reference static pressures are measured at different radii. Hence, a correction for the resulting difference in the radial acceleration is applied in calculating the blade surface static pressure coefficient.

$$C_p = \frac{P_s - P_{exit}}{1/2 \rho U_1^2} \quad (3)$$

where U_1 is the rotor blade tip speed.

Periodic Data

The periodic data of interest are the first harmonic components of the aerodynamic forcing function to the first stage rotor blade row together with the resulting rotor blade surface unsteady pressures and unsteady pressure differences. These are determined by defining a digitized ensemble averaged periodic unsteady aerodynamic data set consisting of the rotating cross hot-wire probe and blade surface dynamic pressure transducer signals at each steady operating point. In particular, these time-variant signals are digitized with a high speed A-D system at a rate of 100 kHz and then ensemble averaged.

The key to this averaging technique is the ability to sample data at a preset time, accomplished by an optical encoder mounted on the rotor shaft. The microsecond range step voltage signal from the encoder is the data initiation time reference and triggers the high speed A-D multiplexer system. To significantly reduce the random fluctuations superimposed on the periodic signals of interest, 200 averages are used. A Fast Fourier Transform (FFT) algorithm is then applied to these ensemble averaged signals to determine the first harmonic component of the unsteady aerodynamic forcing function and the resulting rotor blade surface first harmonic unsteady pressures and pressure differences.

The unsteady inlet flow field to the rotor row is measured with the rotating cross hot-wire probe which quantifies the relative velocity and flow angle. The velocity triangle relations depicted in Figure 1 are then used to determine the unsteady inlet flow field to the rotor, in particular, the streamwise and transverse velocity components, u^+ and v^+ , respectively. These are then Fourier decomposed to determine the first harmonic of the streamwise and transverse gust components, \hat{u}^+ and \hat{v}^+ .

The various unsteady aerodynamic gust mathematical models reference the gust generated airfoil aerodynamic response to a transverse gust at the leading edge of the airfoil. However, in the experiments described herein, the time-variant data are referenced to the initiation of the data acquisition shaft trigger pulse. Thus, for consistency with the models, the periodic data are further analyzed and referenced to a transverse gust at the leading edge of the first stage rotor blade. This is accomplished by assuming that: (1) the aerodynamic forcing function remains fixed in the stationary reference frame; and (2) the forcing function does not decay from the rotating hot-wire probe axial location to the rotor row leading edge plane.

Two types of unsteady pressure data were measured and analyzed. The first type is the acoustic wave unsteady pressure generated by a downstream stator-rotor interaction and operation in the superresonant flow regime and measured by the instrumented first stage rotor row. These data are referenced to the second stage stator vane wake generated transverse first harmonic gust as defined by the following equation.

$$C_{pr} = \frac{\hat{p}_r}{\rho \hat{V}_1^2 \left(\frac{\hat{v}^+}{\bar{V}_1} \right)} \quad (4)$$

where C_{pr} is the acoustic wave unsteady pressure coefficient, \hat{p}_r is the acoustic wave unsteady pressure, \hat{v}^+ is the second stage stator vane wake generated transverse gust first harmonic and \bar{V}_1 is the mean axial velocity.

The second type is the unsteady pressure acting on the first stage rotor row due to the upstream IGV wakes while the IGV row and first stage rotor interaction operate in either a subresonant or a superresonant flow environment. The rotor blade surface unsteady pressure data, measured with the embedded high response pressure transducers, are analyzed to determine the first harmonic of the chordwise distribution of the unsteady pressure coefficient C_p and the unsteady pressure difference coefficient $C_{\Delta p}$. These are defined in Equation 5 and are specified from the Fourier coefficients of the digitized ensemble averaged dynamic pressure transducer signals.

$$C_p = \frac{\hat{p}}{\rho \hat{V}_1^2 \left(\frac{\hat{v}^+}{\bar{V}_1} \right) \beta} \quad (5)$$

$$C_{\Delta p} = C_{p, \text{pressure}} - C_{p, \text{suction}}$$

where \hat{v}^+ is the harmonic transverse gust component, \bar{V}_1 is the mean axial velocity and β is the relative mean flow angle. The normalization with β is used to correlate the effects of incidence angle changes on unsteady lift response per the work of Manwaring and Fletcher [1990].

The final form of the gust generated rotor blade row unsteady aerodynamic data define the chordwise distribution of the harmonic complex unsteady pressure and pressure difference coefficients. Also included as a reference where appropriate are predictions from the transverse gust analysis of Smith [1972]. This model analyzes the unsteady aerodynamics generated on a flat plate airfoil cascade at zero incidence by a transverse gust convected with an inviscid, subsonic, compressible flow.

RESULTS

To investigate multistage axial flow compressor acoustic resonance conditions, a series of experiments are directed at quantifying these acoustic resonance and subresonant and superresonant blade row interaction phenomena in terms of their effect on the rotor blade row periodic unsteady pressure response. First the first stage rotor row periodic unsteady pressure response to a downstream stator-rotor interaction generated acoustic wave is studied. Then, the gust unsteady aerodynamic response of the first stage rotor row due to IGV wakes, with the IGV-instrumented first stage rotor itself configured to generate subresonant and superresonant conditions is considered.

Acoustic Wave Generated Rotor Row Response

The first stage rotor blade row unsteady pressure response to upstream propagating acoustic waves generated by the superresonant interactions of a far downstream stator and rotor row is quantified. Varying the number of second stage stator row vanes while maintaining the number of third stage rotor blades enables subresonant and superresonant flow regimes to be established. In particular, superresonant flow regimes are established with a second stage stator row with 38, 39, 40 and 41 vanes and a third stage rotor row with 43 blades, while subresonant flow regimes are established with a second stage stator row with 36 and 37 vanes and a third stage rotor row of 43 blades. For these configurations, the corresponding reduced frequency values range from 4.76 to 5.42 while interblade phase angles range from -58.6° to -16.7° . The reduced frequency is minimally affected by this range in the number of vanes while the interblade phase angle is greatly affected and, thus the effects shown by variation in the number of vanes corresponds generally to interblade phase angle variations.

To demonstrate the generation of an upstream traveling acoustic wave, Figure 2 shows the Fourier decomposition of a typical first stage rotor blade surface unsteady pressure signal generated by the far downstream stator and rotor operating in a superresonant stator-rotor configuration consisting of 38 vanes and 43 blades, with a Mach number of 0.08 at an RPM of 2,250. This unsteady pressure measurement, located at 5% chord on the first stage rotor blade suction surface, clearly shows the strong frequency content due to the upstream traveling 38 per rev acoustic wave, with the amplitude being approximately one-third that of the 36 per rev IGV wake generated first harmonic amplitude.

Blade Surface Steady Pressures

A compressor operating condition corresponding to the lowest obtainable first stage rotor blade steady loading level is utilized, corresponding most closely to the flat plate cascade model. For this compressor configuration, this lowest loading condition is defined by a first stage rotor row mean incidence of approximately -3.5° . Figure 3 shows the chordwise distribution of the first stage rotor blade surface steady pressure coefficient with the downstream stator-rotor operating in a superresonant flow condition generated by a downstream configuration with 38 stator vanes and 43 rotor blades. The area between the pressure and suction surface steady pressure data is numerically integrated to determine the steady loading level. Figure 3 also shows the negligible variation of steady loading when the number of downstream stator vanes is varied to obtain subresonant and superresonant flow conditions. Therefore the blade steady loading and thus the surface steady pressure is unaffected by the upstream propagating acoustic wave generated by downstream superresonant stator-rotor interaction.

Rotor Row Periodic Unsteady Inlet Flow Field

Figure 4 shows the Fourier decomposition of the periodic unsteady inlet flow field entering the first stage rotor row and measured with the rotor-based cross hot-wire probe when the far downstream stator and rotor are in a superresonant condition with 38 vanes and 43 rotors. The periodic unsteady flow field, defined by the nondimensional streamwise and transverse gust components, shows the strong harmonic content due to the 36 IGV wakes upstream of the rotor row. However, frequency content due to the 38 per rev superresonant upstream propagating acoustic wave is not found. Three other downstream stator-rotor configurations, 39, 40 and 41 vanes, also give superresonant acoustic conditions. In all of these, however, the acoustic wave is not sensed. Thus, the upstream propagating acoustic wave does not affect the IGV wake generated periodic unsteady flow field entering the first stage rotor row.

Rotor Row Unsteady Pressure Response

Figures 5 and 6 show the first stage rotor blade row pressure and suction surface unsteady pressure response to the upstream propagating acoustic wave generated by the four superresonant stator-rotor configurations. For each configuration, both the pressure and suction surface show nearly constant unsteady pressure magnitude and linear phase chordwise distributions, with the magnitude decreasing as the number of vanes is increased from 38 to 41 and the linear phase distributions remaining relatively unaffected. The linear chordwise distribution of these phase data correspond to a convected wave speed of approximately 320 m/sec, which corresponds to the speed of an upstream traveling acoustic wave, i.e., the speed of sound minus the mean axial flow velocity. Since the pressure and suction surface unsteady pressure chordwise distributions are nearly identical in magnitude and phase, the magnitude of the unsteady pressure difference is nearly zero for each of the vane configurations. Thus, the unsteady lift due to upstream propagating acoustic waves is minimal.

The nondimensional acoustic wave unsteady pressure amplitude as a function of the number of vanes is compared to the flat plate cascade prediction in Figure 7. The acoustic wave amplitude is obtained from the blade surface unsteady pressure constant magnitude chordwise distributions. The prediction of the number of vanes at which resonance occurs is fair. The data show that resonance occurs at an interblade phase angle generated with between 37 and 38 vanes per stator row (s between -50.2° and -41.8°), while the flat plate cascade model predicts the resonance to occur at 38.4 vanes (s equal to -38.5°). However, there is very good trendwise agreement between the data and the prediction, with the magnitude of the superresonant acoustic wave increasing as resonance is approached and the acoustic wave greatly attenuated in the subresonant environment.

IGV Wake Generated Rotor Row Response

The gust unsteady aerodynamic response of a rotor row due to IGV wakes, with the IGV-instrumented rotor itself configured to generate subresonant and superresonant conditions is investigated. The acoustic conditions are achieved by varying the number of IGV's and maintaining the number of first stage rotor blades. In particular, subresonant and superresonant acoustic environments were established two ways: (1) by changing the number of vanes while maintaining the number of rotor blades, thereby altering the unsteady stator-rotor interactions and the interblade phase angle and (2) by varying the Mach number without changing the blade row interactions.

Subresonant flow regimes are established for an IGV row with 35, 36 and 37 vanes and a first stage rotor row with 43 blades, while superresonant flow regimes result with IGV rows with 38, 39 and 41 vanes and a first stage rotor row with 43 blades. For these configurations, the corresponding reduced frequencies range from 4.63 to 5.42 and the interblade phase angles range from -67.0° to -16.7° . The reduced frequency is minimally affected by this range in the number of vanes while the interblade phase angle is greatly affected and, thus, the effects shown by variation in the number of vanes corresponds generally to interblade phase angle variations.

Blade Surface Steady Pressures

Similar to the procedure described previously, the blade surface steady pressure coefficient data define the steady loading acting on the first stage rotor blade. Figure 8 shows the negligible effect on the blade steady loading as the number of IGV's is varied to achieve subresonant and superresonant flow conditions. This again demonstrates that the rotor blade steady loading and, thus the blade surface steady pressure distribution is unaffected by blade row operation near an acoustic resonant flow condition.

Rotor Row Unsteady Inlet Flow Field

The Fourier decomposition of the streamwise and transverse gust velocities measured by the rotor-based cross hot-wire probe and generated by the 38 IGV's upstream of the first stage rotor row shows a dominant 38 per-rev excitation fundamental harmonic with smaller higher harmonics. Figure 9 shows that the variation in the amplitudes of the transverse and streamwise harmonic gust components with the number of IGV's is minimal. However, as the number of IGV's is increased from 35 to 41, the rotor blade row goes through an acoustic resonance condition as will be shown. Thus, the periodic unsteady inlet flow field to a rotor row which is itself operating in either a subresonant or superresonant condition is not affected by the acoustic environment.

Unsteady Lift Response

The unsteady lift coefficient data are obtained by utilizing the trapezoidal rule to numerically integrate the chordwise distributions of the unsteady pressure difference data, with the unsteady pressure difference at the blade leading and trailing edge assumed to be zero, per inviscid models. Figure 10, shows the comparison between the data and the flat plate cascade prediction of the complex unsteady lift coefficient as a function of the number of vanes. As shown earlier, the flat plate model prediction of the resonance location is fairly good. The data indicate a resonance at an interblade phase value between -50.2° and -41.8° generated with between 37 and 38 vanes while the model predicts resonance at an interblade phase angle of -38.5° corresponding to 38.4 vanes. In the subresonant flow regime, the prediction of the unsteady lift magnitude is very good, with the data and the prediction both increasing in magnitude as the number of vanes is increased and the resonance is approached. Also, these magnitude data and the prediction would be nearly identical in value if the prediction of the number of vanes for resonance was in exact agreement with the data. In the superresonant flow regime, the magnitude prediction and data have comparable values. However, the prediction exhibits opposite trends with the number of vanes and interblade phase angle than does the data, with the magnitude prediction decreasing and the data increasing as number of vanes is decreased and the interblade phase angle approaches toward the resonance value.

The flat plate cascade unsteady lift coefficient phase prediction differs greatly from the data in both the subresonant and superresonant flow regimes. The predicted phase decreases slightly as the number of vanes is increased, with a sharp decrease near the resonant condition. However, the data show an increase in phase as the number of vanes is increased, with no sharp decrease near the resonance condition. Also, the predicted phase is generally 90° to 150° greater than the data.

Unsteady Pressure Difference

Figure 11 shows the complex unsteady pressure difference coefficient data for the three subresonant flow condition configurations generated with 35, 36, and 37 IGV's, while Figure 12 shows the analogous data for the three superresonant flow condition configurations with 38, 39 and 41 IGV's. The chordwise variations of the magnitude data for both near resonant flow conditions are almost identical, with the magnitude generally decreasing with increasing chord except in the quarter and aft chord. In the region about the quarter chord, the data show a large decreased magnitude whereas in the aft chord the data show an increased magnitude. In accordance with the previously presented unsteady lift magnitude trends, the magnitude data increase with an increasing number of vanes and an increasing interblade phase angle in the subresonant environment and decrease with an increasing number of vanes and interblade phase angle in the superresonant environment.

The complex unsteady pressure difference coefficient phase data also show nearly identical chordwise trends, with the data generally increasing with an increase in the number of vanes and the interblade phase angle. The exceptions are once again in the quarter chord and aft blade regions. At quarter chord, the large decrease in the phase data diminishes as the acoustic resonance condition is approached for both the subresonant and superresonant environments. In the aft blade, the phase data decrease, with the decrease becoming increasingly sharp as the number of vanes and interblade phase angle are increased.

Pressure Surface Unsteady Pressures

Figures 13 and 14 show the first stage rotor row pressure surface IGV wake generated first harmonic unsteady pressure response in the subresonant and superresonant flow regimes. The trends of the magnitude data with chordwise position are nearly identical for both flow environments, with a generally decreasing magnitude with increasing chord distribution except for a large decrease in magnitude at quarter chord. The pressure surface magnitude data exhibit the same variation with the number of vanes and interblade phase angle as did the unsteady lift and unsteady pressure difference magnitude data, i.e., the magnitude data increase in both the subresonant and superresonant environment as the number of vanes and interblade phase angle approach their resonant values.

The unsteady pressure phase data are relatively unaffected by the number of vanes and the interblade phase angle in the subresonant environment but show large effects in the superresonant environment. As the number of vanes increases from 35 to 37 in the subresonant region, the phase data decrease slightly with increasing chord except near the quarter chord where these data are increased in value. In the superresonant environment, while the chordwise trends still remain relatively unaffected by the number of vanes, the phase data generally increase with an increase in the number of vanes and interblade phase angle. The exception again is in the quarter chord region, where the decrease in phase becomes larger as the number of vanes and the interblade phase angle decreases in the subresonant environment and increases in the superresonant environment.

Suction Surface Unsteady Pressures

The first stage rotor blade suction surface IGV wake generated first harmonic unsteady pressure response is shown in Figures 15 and 16 for the subresonant and superresonant conditions. Once again, the

chordwise trends of the magnitude data are nearly identical, with these data decreasing in the front 20% of the chord, and generally increasing in the mid and aft chord regions, with the exception of a slight decrease at approximately 70% chord. Similar to the magnitude data trends on the pressure surface, the suction surface magnitude data increase in the subresonant environment and decrease in the superresonant environment as the number of vanes and interblade phase angle increases. Also, the decrease in the magnitude data from the subresonant to the superresonant conditions is much greater on the suction surface than on the pressure surface.

The suction surface phase data are affected by the number of vanes and interblade phase angle in the subresonant environment as well as in the superresonant environment, in contrast to the corresponding pressure surface data. The suction surface phase data chordwise trends are nearly identical for both the subresonant and superresonant conditions, with the phase data remaining generally constant along the chord except in the aft chord region where there is a decrease. As the number of vanes and interblade phase angle is increased, the phase data increase, with the decrease in the aft chord region becoming larger.

Mach Number Effects

In the previous section, the gust unsteady aerodynamic response of a rotor row due to IGV wakes, with the IGV-instrumented rotor itself configured to generate subresonant and superresonant conditions, was investigated. This was accomplished by varying the number of IGV's while maintaining a constant number of rotor blades and, thus, varying the reduced frequency and the interblade phase angle. In addition to the reduced frequency and interblade phase angle, the Mach number is also a key parameter for acoustic resonance, Equation 1. Therefore the effect of Mach number on the acoustic environment of the first stage rotor row periodic unsteady aerodynamic response is also experimentally investigated. This is accomplished by first configuring the compressor such that it operates in the subresonant flow regime nearest to the resonance, i.e., with 37 IGV's and 43 first stage rotor blades. The Mach number is then varied while maintaining the reduced frequency constant by changing the rotor speed and thus the flow through the compressor. Note that in these experiments the interblade phase angle is maintained constant at -50.2° as the number of IGV's and first stage rotor blades are fixed at 37 and 43 respectively. Four Mach numbers are considered, with three 0.072, 0.077 and 0.081, resulting in subresonant flow conditions and one, 0.085 resulting in a superresonant flow condition.

Figure 17 shows the comparison of the complex unsteady lift coefficient data and flat plate cascade prediction as a function of the Mach number. The prediction and data correlation results are similar to the previous results. Namely, the prediction of the Mach number where resonance occurs, 0.105, is only in fair agreement with the data, which shows the resonance between Mach number values of 0.081 and 0.085. Also, in the subresonant flow regime, the unsteady lift magnitude data and prediction are in good agreement, with both having approximately the same values and increasing with increasing Mach number. For the superresonant flow condition, the magnitude data and corresponding unsteady lift prediction show only fair agreement, with a large decrease in both as compared to the subresonant values. Once again, the phase prediction exhibits very poor correlation with the data. The prediction is relatively constant with Mach number except near the resonance condition. However, the phase data increase as the Mach number is increased, with no indication of the large phase variation near the resonance condition as shown by the prediction. Also, the predicted phase is greater than the data by approximately 90° .

Figure 18 shows the rotor blade unsteady pressure difference coefficient data chordwise distributions in the subresonant and superresonant flow regimes. Both the magnitude and phase data trends are unaffected by the acoustic environment, with these trends also corresponding to those previously found by varying the number of vanes and interblade phase angle. The magnitude data follow the near resonant trends of the unsteady lift data, i.e., the unsteady pressure difference magnitude data increase with increasing Mach number in the subresonant regime and are greatly reduced in the superresonant regime. Also, as the Mach number is increased, the phase data values are increased except in the quarter-chord region in the superresonant environment, where the decrease in phase becomes larger.

Figures 19 and 20 show the effect of subresonant and superresonant environments on the rotor blade pressure and suction surface IGV wake first harmonic unsteady pressure response. Once again, the trends of the data magnitude and phase are relatively unaffected by the acoustic environment. The exception is the unsteady pressure magnitude response in the front and aft suction surface in the superresonant environment with Mach number 0.085, where the magnitude is greatly decreased. The magnitude data follow the trends previously shown by the unsteady pressure difference data, with the magnitude increasing as the resonance is approached from the subresonant regime and reduced sharply in the superresonant regime. As the Mach number is increased, the phase data also increase in value, with the suction surface data increasing at a slightly greater rate than the pressure surface data.

SUMMARY AND CONCLUSIONS

A series of experiments have been performed to investigate multistage axial flow compressor acoustic resonance conditions, including both subresonant and superresonant unsteady aerodynamic response in the immediate vicinity of an acoustic resonance. In particular, these experiments quantified these acoustic resonance and subresonant and superresonant blade row interaction phenomena in terms of their effect on the rotor blade row periodic unsteady pressure response. Subresonant and superresonant acoustic environments were established by changing the number of vanes while maintaining the number of rotor blades, thereby altering the unsteady stator-rotor interactions and the interblade phase angle and by varying the Mach number without changing the blade row interactions. First the first stage rotor row periodic unsteady pressure response to a downstream stator-rotor interaction generated acoustic wave was studied. Then, the gust unsteady aerodynamic response of the first stage rotor row due to IGV wakes, with the IGV-instrumented first stage rotor itself configured to generate subresonant and superresonant conditions was considered. Results of these experiments are summarized in the following.

Acoustic Wave Unsteady Pressure Response

- The pressure and suction surfaces have the same constant magnitude and linear phase variation chordwise distributions.
- The prediction of the number of vanes and the interblade phase angle at which acoustic resonance occurs is fair, with the prediction and data differing by approximately one vane and 8.4° .
- There is very good trendwise agreement between the acoustic wave unsteady pressure prediction and data, with the superresonant environment magnitude increasing as resonance is approached and then sharply reduced to negligible values in the subresonant environment.

IGV Wake Generated Rotor Row Response Near Resonance

- The correlation of the unsteady lift coefficient data with the predictions was very good in the subresonant flow regime, with the correlation of these data in the superresonant flow regime only fair. In both acoustic environments, the correlation of the phase data were poor, both in value and trend.
- The subresonant and superresonant acoustic environments affect the rotor blade surface unsteady pressure difference magnitude and phase data, with the magnitude data increasing as the resonance condition is approached from either the subresonant or superresonant flow regimes.
- On the individual rotor blade suction and pressure surface, the IGV wake generated unsteady pressure magnitude data increase in value as the acoustic resonance condition is approached from either the subresonant or superresonant flow regimes, reflecting the unsteady lift and unsteady pressure difference results. Also, the corresponding phase data increase in value as the acoustic resonance is approached from the subresonant flow regime.

ACKNOWLEDGEMENTS

Research sponsored by the Air Force Office of Scientific Research (AFSC) under Contract F49620-88-C-0022. The United States Government is authorized to reproduce and distribute reprints for governmental purposes notwithstanding any copyright notation hereon.

REFERENCES

- Adamczyk, J.J. and Goldstein, M.E., "Unsteady Flow in a Supersonic Cascade with Subsonic Leading Edge Locus," *AIAA Journal*, Vol. 16, No. 12, 1978, pp. 1248-1254.
- Buffum, D.H. and Fleeter, S., "Wind Tunnel Wall Effects in a Linear Oscillating Cascade," *ASME Paper 91-GT-133*, June 1991.
- Buffum, D.H. and Fleeter, S., "Linear Oscillating Cascade Aerodynamic Experiments," *Sixth International Symposium on Unsteady Aerodynamics, Aeroelasticity and Aeroacoustics of Turbomachines and Propellers*, Notre Dame, September 1991.
- Fang, J., "Compressible Flows With Vortical Disturbances Around Cascades of Airfoils," *Ph.D. Thesis, University of Notre Dame*, April 1991.
- Fleeter, S., "The Fluctuation Lift and Moment Coefficients for Cascaded Airfoils in a Nonuniform Compressible Flow," *AIAA Journal of Aircraft*, Vol. 10, No. 2, February 1973, pp. 93-98.
- Gerolymos, G.A., Blin, E., and Quiniou, H., "Comparison of Inviscid Computations with Theory and Experiment in Vibrating Transonic Compressor Cascades," *ASME Paper 90-GT-373*, 1990.
- Manwaring, S.R. and Fleeter, S., "Inlet Distortion Generated Periodic Aerodynamic Rotor Response," *ASME Journal of Turbomachinery*, Vol. 112, No. 2, April 1990, pp.298-307.
- Scott, J.S. and Atassi, H.M., "Numerical Solutions of the Linearized Euler Equations for Unsteady Vortical Flows Around Lifting Airfoils," *AIAA Paper 90-*, 1990.
- Smith, S.N., "Discrete Frequency Sound Generation in Axial Flow Turbomachines," *Aeronautical Research Council R&M 3709*, Great Britain, March 1972.
- Verdon, J.M. and Usab, W.J., "Application of a Linearized Unsteady Aerodynamic Analysis to Standard Cascade Configurations," *ASME Paper 90-GT-11*, June 1990.

Verdon, J.M. and Hall, K.C., "Development of a Linearized Unsteady Aerodynamic Analysis for Cascade Gust Response Predictions," *NASA Report 4308*, July 1990.

Whitehead, D.S., "Classical Two-Dimensional Methods," *AGARDograph No. 298, AGARD Manual on Aeroelasticity in Axial Flow Turbomachines, Volume 1: Unsteady Turbomachinery Aerodynamics*, pp.3.1-3.30, 1987.

	MOTOR	STATOR	IGV
Airfoil type	C4	C4	C4
Number of Airfoils	43	11	16
Chord, C (mm)	30	30	30
Solidity, C/S	1.14	1.09	0.96
Camber, θ	28.0	27.7	16.4
Stagger Angle, γ	36.0	-16.0	21.0
Inlet Metal Angle, β_1	50.0	30.0	0.0
Aspect Ratio	2.0	2.0	2.0
Thickness/Chord (%)	10.0	10.0	10.0
Flow Rate (kg/s)		2.03	
Design Axial Velocity (m/s)		24.4	
Design Rotational Speed (RPM)		2250	
Number of Stages		3	
Design Stage Pressure Ratio		1.0	
Inlet Tip Diameter (mm)		420	
Hub/Tip Radius Ratio		0.714	
Stage Efficiency (%)		85	

Table 1. Overall airfoil and compressor characteristics

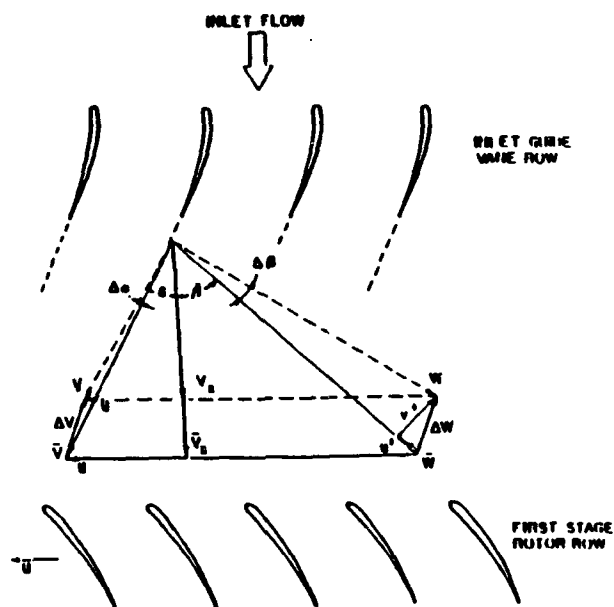


Figure 1. IGV wake generated rotor periodic unsteady velocity components

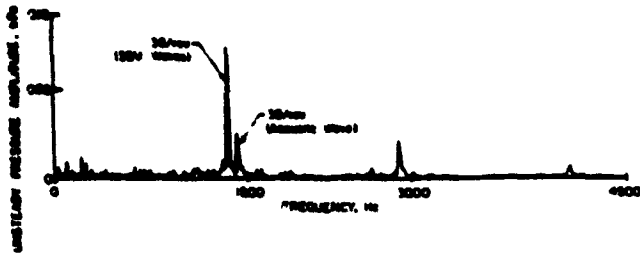


Figure 2. Fourier decomposition of 5% suction surface chord unsteady pressure signal

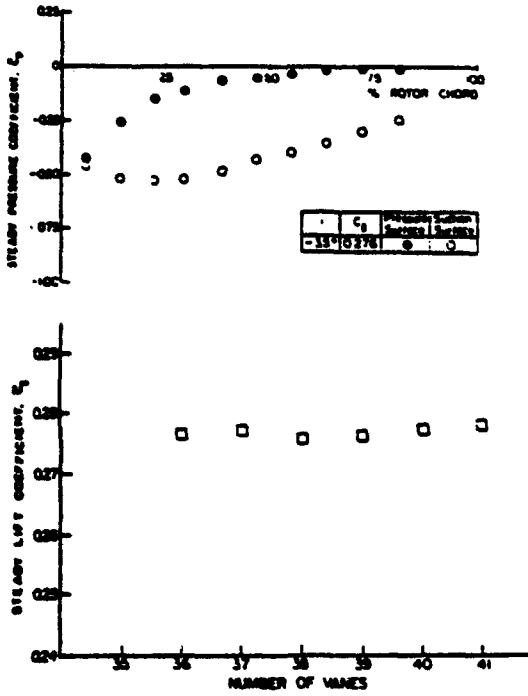


Figure 3. Blade surface steady pressures and downstream generated acoustic wave effect on rotor steady loading

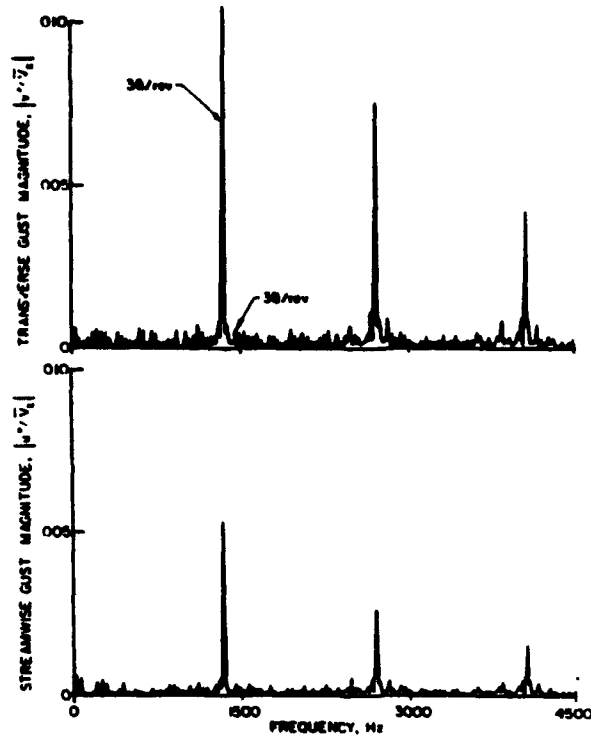


Figure 4. FFT of near acoustic resonance rotor periodic unsteady flow

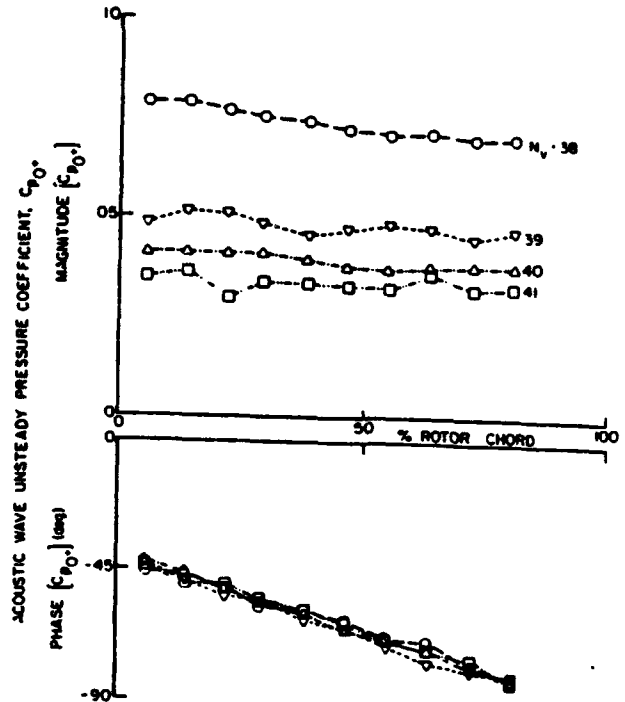


Figure 5. Pressure surface unsteady pressure response to an acoustic wave

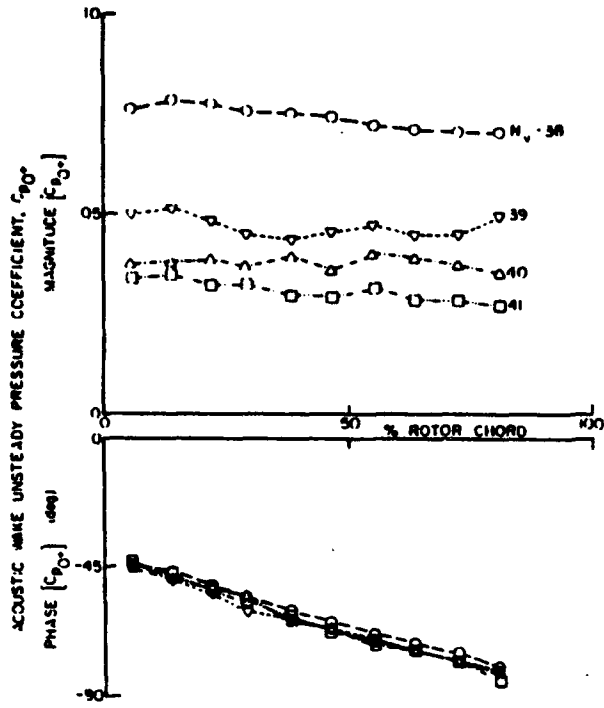


Figure 6. Suction surface unsteady pressure response to an acoustic wave

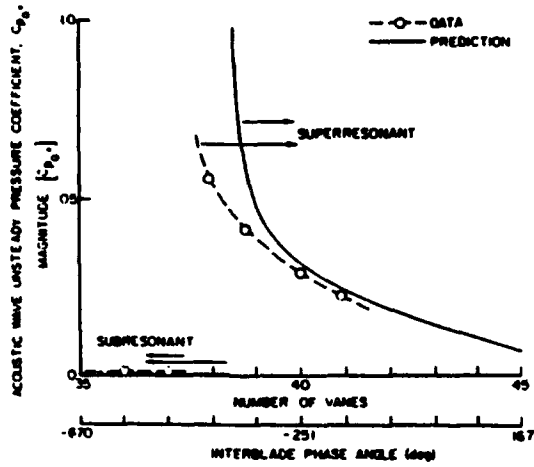


Figure 7. Data-prediction correlation of acoustic wave amplitude

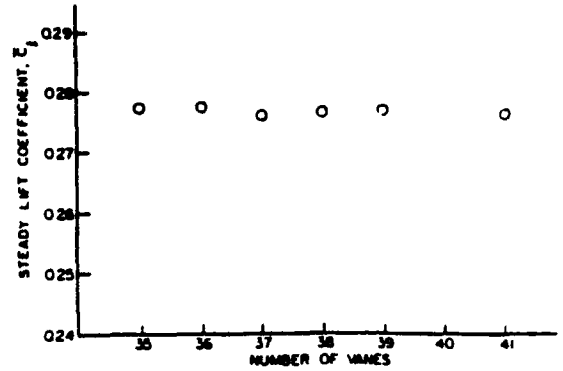


Figure 8. Near acoustic resonance operation effect on blade steady loading

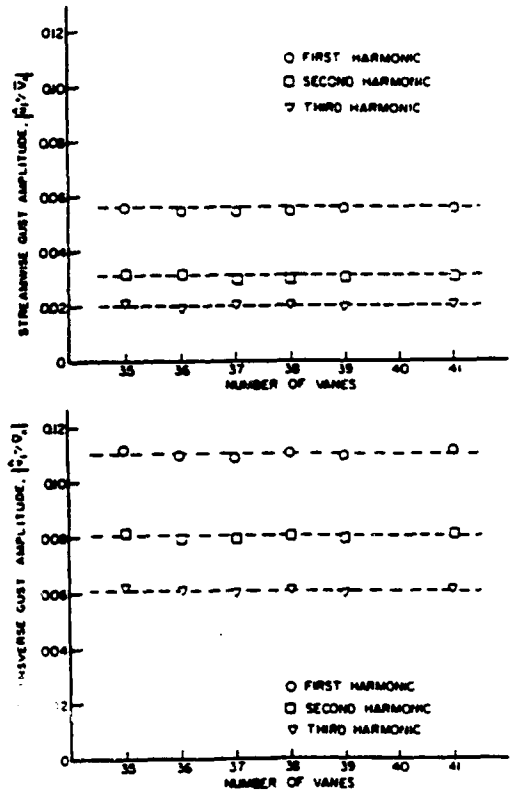


Figure 9. Variation of streamwise and transverse harmonic gusts with number of IGV's

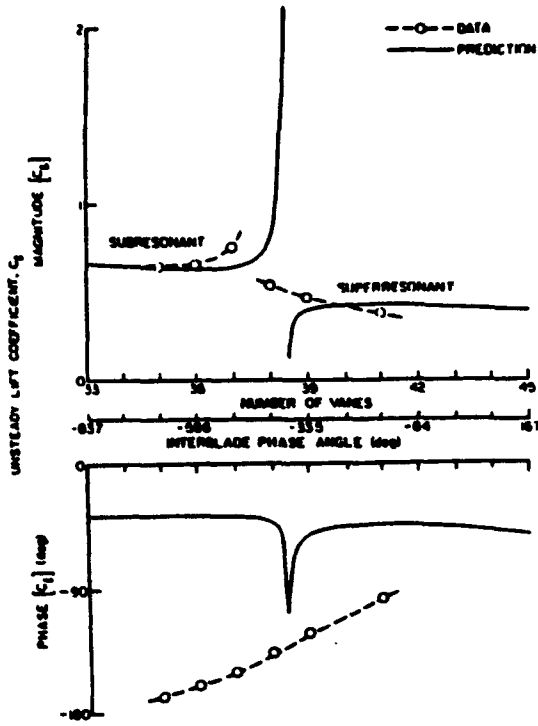


Figure 10. Correlation of the gust generated unsteady lift coefficient versus vane number

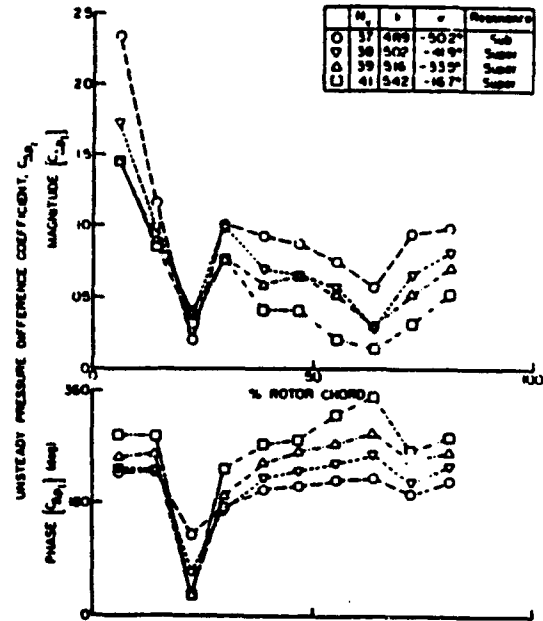


Figure 12. Superresonant flow vane number effect on blade unsteady pressure difference

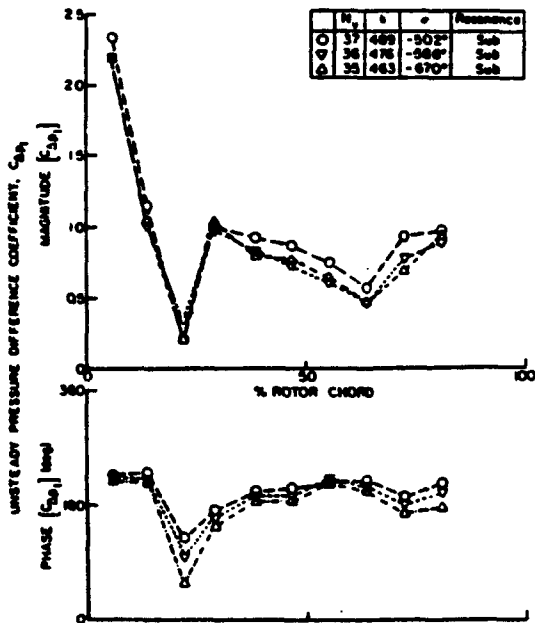


Figure 11. Subresonant flow vane number effect on blade unsteady pressure difference

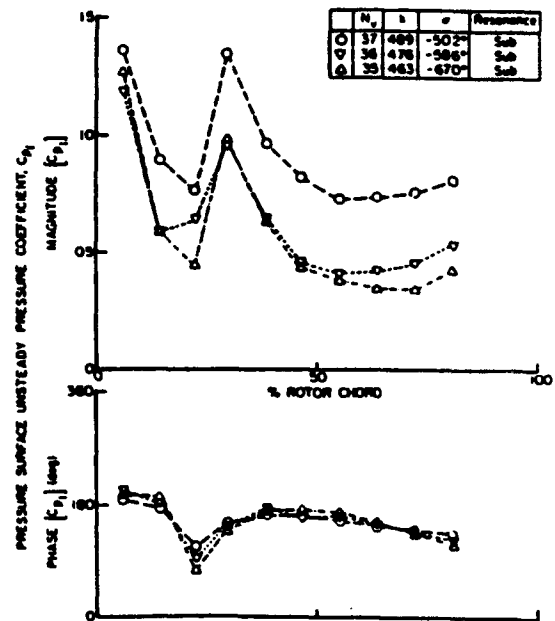


Figure 13. Subresonant flow vane number effect on blade pressure surface response

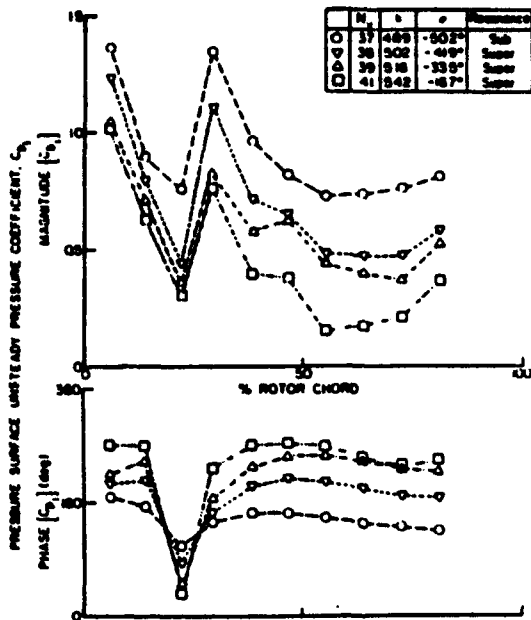


Figure 14. Superresonant flow vane number effect on blade pressure surface response

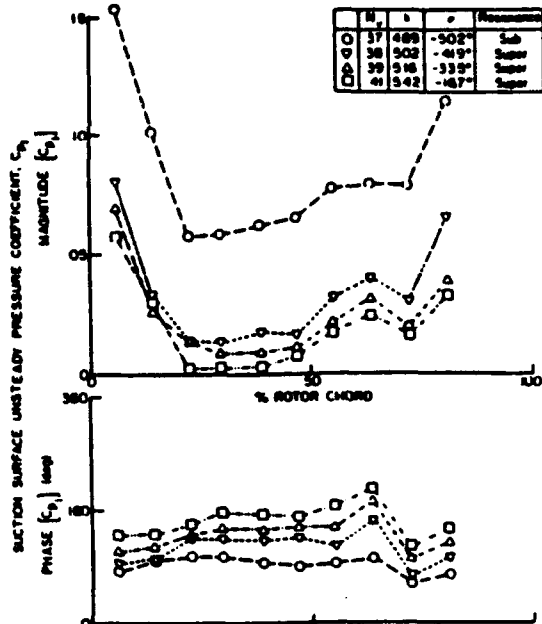


Figure 16. Superresonant flow vane number effect on blade suction surface response

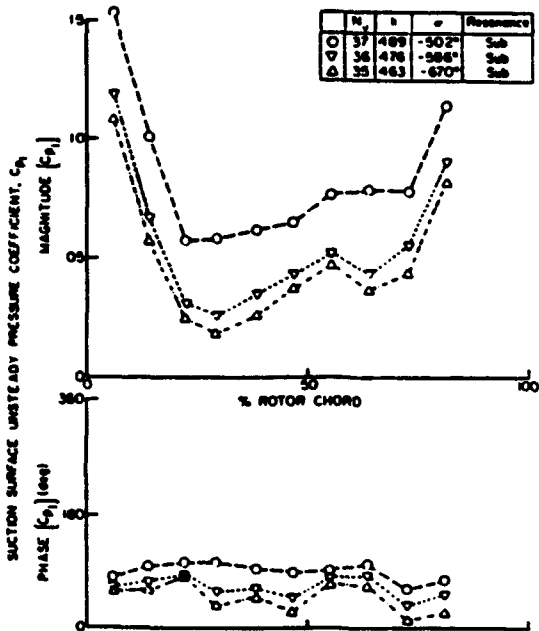


Figure 15. Subresonant flow vane number effect on blade suction surface response

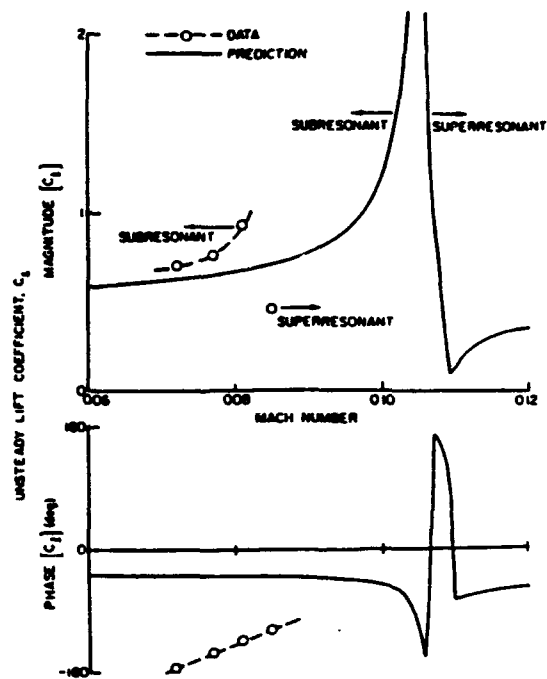


Figure 17. Correlation of gust generated unsteady lift coefficient versus Mach number

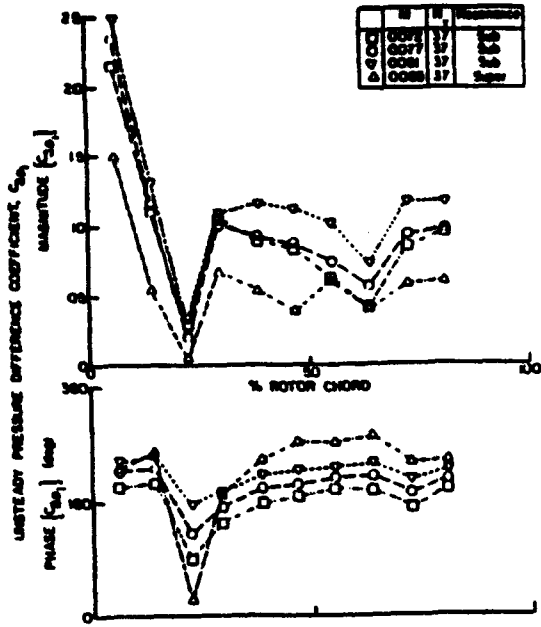


Figure 18 Near resonant Mach number effect on blade unsteady pressure difference

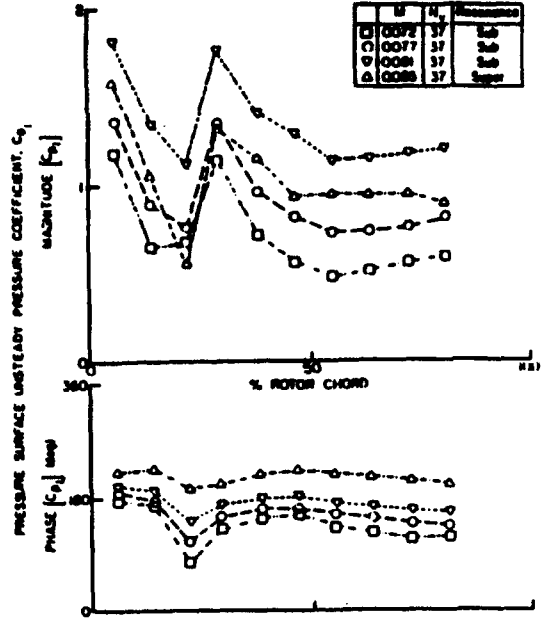


Figure 20. Near resonant Mach number effect on suction surface unsteady response

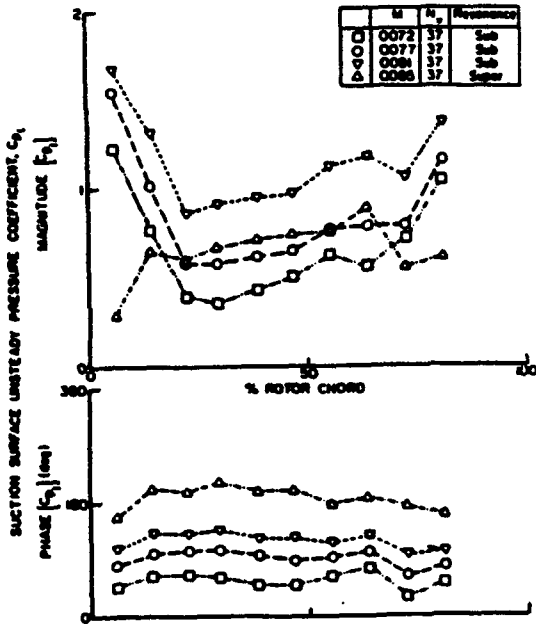


Figure 19. Near resonant Mach number effect on pressure surface unsteady response

APPENDIX VII**Compressor Unsteady Aerodynamic Response to Rotating Stall and Surge Excitations**

AIAA Paper 93-2087, June 1993
(also *AIAA Journal for Propulsion and Power*, in press)

Compressor Unsteady Aerodynamic Response to Rotating Stall and Surge Excitations

Kuk H. Kim and Sanford Fleeter

**School of Mechanical Engineering
Purdue University
West Lafayette, In 47907**

ABSTRACT

A series of experiments are performed in an extensively instrumented three stage axial flow research compressor to investigate the fundamental aeromechanics of compressor flow instabilities, including pure rotating stall, classic surge, and the unstable modified surge flow regimes between these two modes. In particular, the flow induced vibration forcing functions together with the resulting blade row unsteady aerodynamic response generated by these various compressor flow instabilities are measured with a rotating cross hot-wire, with the resulting blade row gust response measured with dynamic pressure transducers embedded in the 1st stage rotor blading. The forcing function data are analyzed in terms of the streamwise and transverse gust components and the mean rotor relative velocity, with the unsteady rotor blade row gust response specified by the unsteady lift response to each instability mode. The data show that rotating stall excites a relatively constant rotor blade response, approximately 27% of the steady loading. Surge excites an unsteady response proportional to the level of surge present in the instability mode, thereby increasing as the B parameter increases. However, the absolute level of the response resulting from surge is considerably less than the rotating stall generated response, approximately 37 - 67%. The quasi-steady AF vibrational response method predicts surge induced blade vibration levels approximately 20%-40% of rotating stall induced blade vibration levels. Both the unsteady response data and the AF predicted vibration levels suggest that the potential for forced response damage is greater from rotating stall than surge.

NOMENCLATURE

- a speed of sound
- A vibration amplitude
- A_c compressor equivalent flow area
- B compressor instability mode parameter
- f_c rotating stall cell frequency
- F frequency
- L_c compressor equivalent length
- T_c rotating stall cell period
- T_{sp} specified time period for one cycle of rotating stall propagation
- U midspan rotor speed
- u⁺ first harmonic streamwise gust velocity
- v⁺ first harmonic transverse gust velocity
- V_p compressor volume
- V_z axial velocity
- V_z⁺ first harmonic unsteady axial velocity
- W mean rotor relative velocity
- α mean absolute flow angle
- β mean rotor relative flow angle
- Δφ unsteady lift phase change between two successive rotating stall cell cycles

INTRODUCTION

Compressors encounter flow instabilities under certain operating conditions, demarcated on the compressor performance map by the surge line, a barrier which separates regions of stable and unstable operation. The surge line is of particular interest due to its close proximity to the region of compressor maximum pressure rise and efficiency. Current generation turbomachines must allow for a safety margin - the surge margin - which places the operating region far enough removed from the surge line so as to prevent the onset of instability. Unfortunately, this safety margin moves the compressor operating line away from its maximum efficiency.

The term surge line is somewhat misleading. Two possible phenomena can occur when this boundary is reached, generally categorized as rotating stall or surge. Surge refers to a global oscillation of the mass flow through the compression system, often with complete flow reversal. It is a phenomena of the entire compression system, consisting of the compressor and the system into which it discharges. Rotating stall, in contrast, is an instability local to the compressor itself, and is characterized by a circumferential non-uniform mass deficit which propagates around the compressor annulus at a fraction of rotor speed.

There are two disadvantages associated with a compressor encountering an instability marked by the surge line. First, compressor performance falls drastically when a surge line flow instability is encountered. On flight-rated turbine engines, such a performance degradation and resulting loss of thrust can be catastrophic. Second, the surge line flow instability may be a dangerous unsteady aerodynamic excitation resulting in blade vibrations, as discussed, for example, in regard to centrifugal compressors by Haupt et al. [1], and Jin et al. [2,3]. Thus, rotating stall and surge are flow instabilities that not only limit compressor performance but also affect their durability.

Blade vibration resulting from rotating stall, although violent, is of very short duration. However, modern high stage loading designs with low-to-moderate design weight and tip speeds can be life-limited in the number of stalls tolerable. Surge induced vibration is a self-excited limit-cycle instability. Excessive vibrational response far over the endurance limit can drastically restrict the number of stalls a compressor may experience without blade fatigue or serious reduction in its normal high cycle fatigue strength. Thus the surge instability forced response problem differs from the usual instability problem in that the interest is not the instability boundary but rather the level of response.

Research on rotating stall and surge has focused on determining their flow characteristics so as to improve the ability to predict them as well as on their impact on compressor performance. Only minimal fundamental research attention has been directed at the issues of rotating stall and surge flow induced vibrations. In fact, there have been no fundamental unsteady aerodynamic experiments directed at investigating the fundamental surge-line flow instability unsteady aerodynamics as applicable to blade row durability issues. Thus, there is a clear need for fundamental rotating stall and surge forcing function and resulting gust response unsteady aerodynamic data.

In this paper, fundamental experiments are performed which investigate surge, rotating stall and the modified surge instability regimes, including the flow induced vibration forcing functions generated during these various rotating stall and surge excitations together with the resulting blade row unsteady aerodynamic response. The various instability forcing functions are measured with a rotating cross hot-wire, with the resulting blade row gust response measured with dynamic pressure transducers embedded in the rotor blade. Specific technical objectives include: (1) identification of the compressor flow characteristics during the transition from pure rotating stall to the classic surge instability mode, i.e., with different levels of modified surge; (2) determination of the unsteady aerodynamic forcing function characteristics of rotating stall, surge, and the modified surge instabilities in between; (3) quantification of the unsteady aerodynamic response of the 1st stage rotor blade row to the various rotating stall and surge instability excitation unsteady aerodynamic forcing functions.

Rotating Stall & Surge Characteristics

The fundamental compressor flow instability is governed by the value of the B parameter defined in Equation 1. It is the ratio of the pressure or acceleration force to the fluid momentum or inertial force and characterizes whether the instability mode of a compressor is rotating stall or surge, Greitzer [4,5]. If B is smaller than $B_{critical}$, the instability mode of the compressor will be rotating stall, with a surge instability mode found for B values larger than $B_{critical}$. When the value of B is between those corresponding to rotating stall and classic surge or is near $B_{critical}$, the compressor encounters a modified surge instability. This has the basic characteristics of a surge cycle in that the entire annulus flow fluctuates in the axial direction but rotating stall persists throughout the surge cycle, during both the blowdown and the recovery phases. Until recently, this instability flow regime had not been recognized as a separate instability flow regime and, hence, had been neglected. The flow characteristics of this transitional flow regime were experimentally studied by Past [6], with the post-stall compressor performance computationally investigated by Jun et al. [7]. Still, information regarding this region is very limited.

$$B = \frac{\frac{1}{2} \rho U^2 A_c}{\rho \omega L_c A_c} = \frac{U}{2\alpha} \sqrt{\frac{V_p}{A_c}} \quad (1)$$

where α is the speed of sound, U denotes the midspan rotor speed, V_p is the compressor volume, L_c the equivalent compressor length and A_c is the equivalent compressor area.

RESEARCH COMPRESSOR

These experiments are performed in the Purdue Axial Flow Research Compressor which is extensively instrumented with cross hot-wire probes, steady and dynamic pressure transducers, and endwall microphones. The facility consists of a bellmouth inlet, the test section, a honeycomb flow straightener section, a venturi flow meter, a plenum, and a throttle plate. The axial velocity through this three stage low speed compressor is approximately 24.4 m/s (80.1 ft/s). Each compressor stage contains 43 rotor blades and 31 stator vanes having a British C4 airfoil profile, with the first stage rotor inlet flow field established by an inlet guide vane (IGV) row of 36 airfoils. The compressor plenum consists of two sections, first a small connecting section directly attached in line of flow and the main plenum section which contains a movable wall to generate different compressor volumes and thus compressor instability modes. The throttle plate is motorized with a variable speed control. The overall compressor, compressor volumes, and airfoil characteristics are defined in Table 1.

Experimental Techniques

The occurrence of rotating stall, surge or the transition flow regimes in between is determined by the compressor volume, thereby specifying the value of B, per Table 1. The flow instabilities are generated by operating the compressor at a constant speed of 2,250 RPM with the throttle completely open. The throttle is then very slowly closed until data acquisition is initiated by an analog trigger signal, with the trigger level set to capture the occurrence of rotating stall or surge. Unsteady data quantifying the flow field, the compressor end wall pressures, and the rotor blade surface unsteady pressures are acquired and digitized. Once data acquisition has been completed, the compressor is automatically shutdown by the computer, thereby minimizing the compressor operating time in the instability regions.

INSTRUMENTATION

Instability Flow Regime Characterization

The instability flow regimes are characterized by the time history of the instantaneous axial velocity as well as the transient rotating stall cell averaged flow coefficient, V_x/U and the nondimensional pressure rise coefficient $\Delta p/\rho U^2$, where Δp is the plenum pressure referenced to ambient.

Unsteady Aerodynamic Forcing Function

The compressor unsteady inlet flowfield generating the 1st stage rotor blade row unsteady aerodynamic response during rotating stall and surge initiation and development are measured using rotating cross hot-wire probes. Reverse flows, if they exist, are measured with two cross hot-wire probes, each oriented differently. The two probe orientations, shown in Figure 1 at their 0° incidence positions, provide flow measurement capability of -40° to 75° incidence to the rotor blade. The first cross hot-wire probe accurately measures flow angles varying from -40° to +40° of incidence, with the second accurately quantifying flow angles varying from -5° to +75° of incidence. These cross hot-wire probes are both located on the rotor drum 18.8% chord upstream and 65% blade spacing from a rotor blade. Both cross hot-wire probes are calibrated for velocities from 9.14 m/s (30 ft/s) to 51.8 m/s (170 ft/s) and angles ranging from +45° to -45°. The uncertainties in the velocity and the flow angle measurements were determined to be 5% and $\pm 1.0^\circ$. Centrifugal loading effects on the rotating hot-wire sensor resistance and thus the responses were found to be negligible.

Unsteady Aerodynamic Response

The 1st stage rotor blade midspan surface unsteady pressures are measured with 12 ultra-miniature, high response transducers embedded in the rotor blades. The chordwise locations of the unsteady pressure measurements are shown in Figure 1 together with the layout of these instrumented airfoils, along with the two hot-wires, on the compressor rotor drum. To minimize the possibility of flow disturbances associated with the inability of the transducer diaphragm to exactly maintain the surface curvature of the blade, a reverse mounting technique is utilized. The pressure surface of one blade and the suction surface of the adjacent blade are instrumented, with transducers embedded in the nonmeasurement surface and connected to the measurement surface by a static tap. The embedded dynamic transducers are both statically and dynamically calibrated. The static calibrations show good linearity and no discernible hysteresis. The dynamic calibrations demonstrate that the frequency response, in terms of gain attenuation and phase shift, are not affected by the reverse mounting technique. The maximum error in gain and phase angle were determined to be 0.60 dB and 1.5° respectively.

Rotating-Stationary Data Transfer

The two rotating cross hot-wire probes and the 12 blade surface mounted dynamic pressure transducers are interfaced to the stationary frame-of-reference through a 46 channel mercury wetted slip ring assembly. On-board signal conditioning of the transducer output signals is performed to maintain a good signal-to-noise ratio through the slip rings. The remaining channels of the slip-ring assembly provide excitation to the transducers and other miscellaneous data transfer.

Digital Data Acquisition

Digital data acquisition is initiated by an analog trigger signal from a single microphone upstream of the first rotor row, with the trigger level set to capture the occurrence of rotating stall or surge while the throttle is very slowly closed. The unsteady flowfield, the blade surface unsteady pressures, and the plenum pressure data are acquired with 2 cross hot-wire probes, 12 dynamic pressure transducers, and a Scanivalve pressure transducer respectively and then digitized. Fifty percent of a 5.5 second data burst is saved pre-trigger, with the remainder of the samples post-trigger. Once data acquisition has been completed, the compressor motor is automatically shutdown by the computer. A sampling rate of 5,000 Hz was chosen to avoid aliasing of the important machine frequencies, i.e., the rotor and IGV blade passing frequencies, 1.3 kHz and 1.6 kHz respectively.

Before analysis, all unsteady data are filtered to remove high frequency noise. The hot-wire data are low pass filtered to 100 Hz using a Butterworth filter of order 10, resulting in a response phase lag of approximately 0.5 revolutions. The unsteady pressure response data are bandpass filtered from 0.5 Hz to 100 Hz using a Butterworth band filter of order 2. Since the signals near the low frequency limit are of significant interest, minimal low frequency data distortion is desirable. Therefore, the low order filter is used for the band pass filtering of the pressure data because the higher order filter produces a longer numerical transient.

DATA ANALYSIS

Unsteady Aerodynamic Forcing Function

The unsteady velocity field quantifies the characteristics of the instability forcing functions generating the unsteady aerodynamic response of the rotor blade row. However, reverse flows can be a problem. Also, the annulus flow is both time and spatially variant. Greitzer and Day [5,8] avoided the reverse flow measurement problem by using an analytical technique to compute the flow coefficient, with the mass flow determined using a calibrated throttle and a continuity balance in the plenum.

In the experiments described herein, rotating cross hot-wire probes are utilized to measure the velocity, thereby avoiding the reverse flow measurement problem. Two rotating cross hot-wire probes, mounted with different orientations, enable flows with up to 160° in flow angle variation to be measured. Thus, the measured relative velocity is always positive, with reverse flow determined from the flow angle measurement alone. In these particular experiments, rotating cross hot-wire probes are set such that reverse flows to 40° can be measured.

The unsteady aerodynamic forcing function generating the rotor blade row unsteady aerodynamic response is characterized by the fluctuating velocity in the streamwise and the transverse directions. In particular, the first harmonic of the fluctuating velocity is analyzed, with the frequency of interest being the rotating stall frequency or the surge frequency. Since rotating stall and surge are transient phenomena, the mean flow is a localized mean, the average velocity during a single cycle of rotating stall or a single cycle of surge. In the presentation of the

localized mean rotor relative velocity time history for rotating stall forcing function data, successive rotating stall cycles are averaged. The surge excitation forcing function data acquisition period covers only 2-3 surge cycles. Hence, the averages on a single successive surge cycle is performed every few points. The hot-wire data provide the instantaneous rotor relative velocity W and the rotor relative flow angle β from which the mean and fluctuating flow fields are determined. The forcing function, defined by the first harmonics of the streamwise and transverse gust velocities, u^* and v^* , are determined from the u and v gust velocity components, where u and v are the streamwise and transverse gust components. \bar{W} denotes the localized mean rotor relative velocity and $\bar{\beta}$ denotes the localized mean rotor relative flow angle.

$$u = W - \bar{W} \cos(\beta - \bar{\beta}) \quad (2)$$

$$v = W \sin(\beta - \bar{\beta}) \quad (3)$$

Unsteady Pressure Data

Transient blade row unsteady pressure response data are necessary at the frequencies of interest. Hence, a Fourier analysis is performed to track the development of the transient event in the frequency domain and thereby determine the frequency content. However, when appropriate frequency resolution is achieved, time resolution becomes a problem, particularly if the sampling frequency is high. At a sampling speed of 5,000 Hz, chosen to avoid aliasing of the rotor blade pass frequency, the resulting surge and rotating stall frequencies are far from the sampling speed and time resolution is difficult.

To avoid these frequency-time resolution trade-off problems, an alternative method is used. First, the important frequencies in the transient history of stall and surge are identified by processing the data with the Gabor Spectrogram [9], a joint time-frequency analysis technique which avoids the limitations of the Short Time Fourier Transform (STFT) spectrogram by using two elemental techniques, the Gabor transform and the Pseudo Wigner-Ville Distribution (PWVD). Then, a Discrete Fourier Transform (DFT) is applied to successive cycles of data whose period corresponds to the frequency of interest, e.g. the rotating stall frequency, and the first harmonic analyzed. Since the number of points in a single cycle of data at the rotating stall frequency is smaller than that necessary for a Fast Fourier Transform (FFT), the time resolution is significantly improved with this method. One problem is that leakage error is introduced if the frequency of the transient phenomena changes, causing the period of data selected for the DFT to be incorrect for that frequency. A study of DFT leakage showed that for less than 20% variation in frequency, the resulting errors in magnitude and phase are less than 10% and 40° respectively. Fortunately, the maximum rotating stall frequency variation is 26% in these experiments, and therefore, the maximum errors in magnitude and phase are expected to be close to 10% and 40°. Although these errors are larger than desirable, it is considered to be a worthy trade-off for the improved time resolution, 20 times better with DFT as compared to FFT.

The unsteady aerodynamic response of the 1st stage rotor blade row to the various instabilities are quantified by the unsteady lift, the integral of the unsteady differential pressure across the rotor blade. To compute this, the voltages from the pressure and suction surface transducers are first band pass filtered from 0.5 Hz to 100 Hz to eliminate high frequency noise. Then the first harmonic of the unsteady pressures are analyzed by the DFT analysis. Note that since a dimensionless chordwise location is used as the variable of integration, the unsteady lift magnitude is per blade area and thus has dimensions of psi. The unsteady lift phase provides time

information. In particular, a coherent phase corresponds to a coherent wave, for example a rotating stall cell. Also, the phase value indicates whether the frequency selected for the harmonic analysis correctly matches the propagation speed of the physical wave. An incorrect frequency can be due to: (1) the characteristic frequency, i.e. rotating stall or surge frequency, changing with time, or (2) the specified frequency chosen for analysis is incorrect. If the frequency is correct, the phase should be constant. However, if the frequency is slightly incorrect, the magnitude data would be correct within the leakage error band and the phase would change by a constant value. Thus, the slope or the change in phase can be used to measure the propagation speed per the following.

$$T_c = \frac{T_{sp}}{\frac{\Delta\phi}{360} + 1} \quad (4)$$

$$\zeta = \frac{1}{T_c} \quad (5)$$

If the slope of the unsteady lift phase is negative, the correct frequency is less than the specified frequency. If the slope of the unsteady lift phase is positive, the correct frequency is greater than the specified frequency. Note that the correct speed can only be calculated if no data points are skipped or repeated at each DFT point because skipped or repeated data points will also cause a phase change. Thus, the actual surge frequency could not be calculated since the data did not cover enough surge cycles and thus data points were repeated. However, the magnitude data are still accurate within the leakage error bands.

Aeromechanical Impact Analysis

To assess the aeromechanical impact of the various instability forcing functions, the quasi-steady AF method is used to predict the vibrational response from the aerodynamic excitation. Pearson [10] and Pary and Pearson [11] related flow induced blade vibrations, described by the blade vibration amplitude A and frequency F , to the wake forcing function. The product AF is proportional to the blade stress level, with the proportionality constant dependent on the blade physical and material properties. Armstrong et al. [12,13] and Blackwell [14] experimentally established the AF method as an effective fatigue assessment technique.

The product AF given in Equation 6 is calculated from the energy transferred to the airfoil by the flow field during a single vibration cycle, i.e. the work done by the lift force in the direction of blade vibration. The primary assumptions inherent in this analysis include quasi-steady flow, no mechanical damping, harmonic unsteady aerodynamics and blade response, and small perturbations in flow angle and velocity. A detailed summary of the AF method is provided in reference 15.

$$af = \frac{\sin(\bar{\alpha} + \bar{\beta}) - 2(\bar{\beta} - \gamma)\cos(\bar{\alpha} + \bar{\beta})}{\cos(\gamma - \bar{\beta}) - 2(\bar{\beta} - \gamma)\sin(\gamma - \bar{\beta})} \frac{\sqrt{u^2 + v^2}}{2\pi} \quad (6)$$

where $\bar{\beta}$ is the mean rotor relative flow angle, $\bar{\alpha}$ is the mean absolute flow angle and γ denotes the rotor stagger angle.

RESULTS & DISCUSSION

The unsteady aerodynamic response of blade rows to rotating stall, surge and the transitional flow regime between pure rotating stall and classic surge are important with regard to engine durability. Specific technical issues of interest include the rotating stall and surge unsteady aerodynamic forcing functions and the resulting blade row response, i.e., the rotor blade surface unsteady pressure and unsteady lift harmonic magnitude and phase during instability inception and development, the level of the unsteady response, and the

differences in this response to rotating stall, surge and modified surge instability excitation.

STALL INSTABILITY MODES

Rotating Stall

With $B = 0.26$, the minimum plenum volume, the compressor enters into rotating stall when the flow to the compressor is very slowly throttled, Figure 2a. The axial velocity slowly decreases until about 98 rotor revolutions, where a small stall cell emerges and grows very rapidly to half the steady state size in less than 5 rotating stall cycles, less than 10 rotor revolutions. Initially, the stall cell size oscillates but it then grows to its constant size in about 30 rotor revolutions, with the magnitude of the stall cell depth being approximately 75 ft/s in axial velocity. The initial oscillation in the rotating stall cell size is indicative of the damped oscillatory motion which accompanies settlement into a stable equilibrium point. This behavior is exhibited by both the non-dimensional pressure rise coefficient and the average flow coefficient. However, since the throttle is continuously being closed, albeit very slowly, the compressor's stalled operating point changes with time.

Modified Surge Close to Pure Rotating Stall Mode

With $B = 0.40$, Figure 2b, the compressor exhibits behavior very different from that of rotating stall alone or surge alone. Analogous to the previous case, initially the axial velocity very slowly decreases as the compressor pressure rise increases toward the peak value, until approximately 103 revolutions, a small stall cell emerges and quickly grows into a full size stall cell depth of 80 ft/s in axial velocity in a little over 10 revolutions. This constitutes the "blowdown" phase of the surge cycle where the pressure in the plenum which had been building to the peak pressure rise point discharges and the flow in the entire annulus is significantly reduced from the non-stalled value. At approximately 115 rotor revolutions, where the axial velocity reaches its lowest value, the "charging" phase of the surge cycle begins where the plenum pressure starts to rise again. Thus so far, the compressor behavior exhibited is that of a classic surge cycle in which the entrance into the surge cycle is accompanied by rotating stall. However, the resemblance to the "classic" surge cycle ends here.

In contrast to the classic surge cycle in which the rotating stall quickly disappears during the recovery or the charging phase of the surge cycle, rotating stall persists throughout the recovery well into the beginning of the next surge cycle. The rotating stall cell merely gets smaller during the recovery phase and thus, the plenum is no longer able to recharge its pressure to the pre-surge value, recovering only 60% of the discharged pressure, Figure 2b. The compressor behavior during the entrance into the second surge cycle is much like the first: the plenum pressure discharges and the stall cell rapidly grows into the full size in approximately 15 rotor revolutions. However, during the recovery phase of the second surge cycle, rotating stall persists so strongly and without much reduction in size that the plenum pressure is only able to recover about 40% of the original discharged pressure. Also, due to the increased presence of rotating stall over the second surge cycle, the compressor starts to settle to an equilibrium value. After the entrance into the third surge cycle, the surge behavior disappears and the compressor is at a stalled, but stable operating point. Thus, the flow regime between rotating stall only and surge only is one of an equilibrating surge cycle, i.e. a surge cycle which decays to a stable equilibrium point.

Modified Surge Close to Surge Only Mode

A 15% increase in the value of B to $B = 0.46$, Figure 2c, results in very little change in the instability time history. A small stall cell emerges at about 96 revolutions and grows slowly until about 105 rotor revolutions. Over the next few rotor

revolutions, the stall cell rapidly grows into its full size depth of 80 ft/s in axial velocity, reaching its maximum size with the steady velocity at its lowest value at approximately 115 revolutions. However, with this increased volume, the overall compression system has more compliance and the plenum is able to recover about 85% of the discharged pressure, 25% more than with $B = 0.40$. This is still a rotating stall-surge transition zone because rotating stall again prevails throughout the pressure recovery phase. However, since the compression system is closer to classic surge, the stall cell size decreases to a smaller value than before, 15% of the maximum stall cell size is retained as compared to the 30% with a B value of 0.40. Starting from this stall cell size, the cell again grows quickly into its full size in less than 10 revolutions during the second surge cycle. Since the plenum pressure after the 1st surge cycle was lower, only 70% of the original discharged pressure is recovered and the rotating stall which persists throughout the recovery phase of the second surge cycle is even larger, with 25% of the maximum cell size being retained. Unlike the $B = 0.40$ case, the compressor at $B = 0.46$ undergoes one more surge cycle but the recovery is very weak, with only 40% of the discharged pressure recovered and 70% of the maximum stall cell size retained. Still, the compressor enters the 4th surge cycle but probably won't recover, rather settling into pure rotating stall.

Classic Surge Only

Further increasing the plenum volume to achieve $B = 0.76$, results in a classic surge instability. Figure 2d shows that steady flow exists up to 104 rotor revolutions, when a small stall cell emerges and rapidly grows into its full size in about 7 revolutions. For the next 11 rotor revolutions, the rotating stall cell stays relatively constant. At 134 revolutions, rotating stall quickly disappears and the compressor is unstalled until the plenum starts discharging again, with the cycle then repeating 1.5 more times. Note that unlike the rotating stall case or the two modified surge cases, the plenum pressure is able to charge up even higher than before the instability. The difference is that this process leads to a growing hysteresis loop on the performance map, i.e. the flow is not able to settle into a steady operating cycle. Also, there is no reverse flow, indicating that this is classic surge and not deep surge.

In summary, the compressor flow regime between rotating stall and classic surge is modified surge during which rotating stall persists throughout the surge cycle. At a B value of 0.26, rotating stall exists without any surge. At B values of 0.40 and 0.46, the instabilities are characteristically surge, but varying degrees of rotating stall is present throughout the entire time. At a B value of 0.76, surge cycle exists without rotating stall, hence the difference between classic surge and modified surge. Figure 3 illustrates the range of B parameters in which the behavior typical of modified surge exists. Greitzer's [5] modified surge cycle would exist over B parameter range of 0.65 to 1.0. Jun et. al [7] had modified surge cycles over a B range of 0.75 to 1.8. The broadness of B parameters through which modified surge occurs indicates the importance of this intermediate flow regime.

DET ANALYSIS FREQUENCIES

The importance of correctly identifying the rotating stall, the modified surge, or the surge frequency was previously discussed. Since the DFT analysis of the unsteady pressure response takes the first harmonic of one cycle of data of a known period or frequency, it is absolutely essential that the specified frequency for the DFT analysis be as accurate as possible to minimize leakage errors. The error in the specified rotating stall or surge excitation frequency must be less than 20% to keep the errors in the harmonic magnitude and phase to less than 10% and 40°.

The Gabor Transform is used to generate the Gabor spectrogram from which the characteristic rotating stall and

surge frequencies are identified for the four compressor instability configurations. Figure 4 shows the Gabor spectrogram for the 1st stage rotor blade row leading edge suction surface pressure transducer for the four instability modes. The vertical axis on these plots represents time and the horizontal axis is frequency. Thus, the rise and fall of important frequencies in the unsteady pressure response are shown by the intensity of the pressure magnitude. Since the pressure transducers are mounted on the rotor blading, the rotating stall cell speeds are relative to the rotor. However, since surge is not a circumferential flow phenomena, the surge frequencies identified by the Gabor spectrogram are the same in the rotating and absolute reference frames. The rotating stall speeds identified in all four instability mode configurations vary from 21.9 Hz to 25 Hz in the rotating reference frame, 15.6 Hz to 12.5 Hz in the absolute frame.

Figure 4 reveals that the relevant rotating stall frequencies emerge at approximately 100 rotor revolutions. The rotating stall frequencies undergo three changes: starting at 21.9 Hz (15.6 Hz absolute) and changing to 23.4 Hz (14.1 Hz) to 24.7 Hz (12.8 Hz) to 25 Hz (12.5 Hz). For $B = 0.4$, the modified surge close to pure rotating stall case, the relevant frequencies are the surge frequency, 1.17 Hz, and the rotating stall frequency of 25 Hz (12.5 Hz). Unlike the rotating stall case, the rotating stall cell speed during the modified surge cycle at $B=0.4$ does not undergo large changes. For the modified surge case of $B=0.46$, the pertinent frequencies are the surge frequency, 1.2 Hz, and the frequency of the rotating stall cell within the surge cycle. The rotating stall cell frequency changes in the first surge cycle from approximately 22 Hz (15.5 Hz) to 25 Hz (12.5 Hz) to 22 Hz, after which the core rotating stall frequency is 25 Hz (12.5 Hz). For the classic surge case, relevant frequencies are the surge frequency of 0.75 Hz and the rotating stall cell frequencies of 22 Hz (15.5 Hz) to 27.3 Hz (10.2 Hz). Note that the surge frequencies were approximately calculated from the time elapsed between each surge cycle rather than from the Gabor Spectrogram because of the poor frequency resolution of the spectrogram, 0.8 Hz.

The harmonic analysis is performed on the single frequency with the largest magnitude. The rotating stall and surge frequencies selected for this harmonic analysis together with the variation in the frequencies are presented in Table 2. The two values in the % spread column of this table represent the percentage of variation from the specified rotating stall frequency for the DFT analysis of the high and the low values of the rotating stall frequencies identified with the Gabor spectrogram. The negative % spread represents a frequency less than the specified frequency and the positive % spread represents a frequency greater than the specified frequency. Recall that frequencies in error by 20% would yield errors in magnitude and phase of 10% and 40° respectively.

UNSTEADY AERODYNAMIC FORCING FUNCTIONS

Rotating Stall Unsteady Aerodynamic Forcing Function

The transient forcing function resulting from the rotating stall excitation at the various compressor instability modes are presented in Figures 5 through 8. These forcing functions are the rotating stall frequency component of the total unsteady velocity. Each of these figures presents the streamwise and transverse gust velocities u^+ and v^+ , the mean rotor relative velocity \bar{W} , and the magnitude and phase of the streamwise-to-transverse gust ratio u^+/v^+ .

The rotating stall forcing function for $B=0.26$, the pure rotating stall instability mode, is shown in Figure 5. Until 100 rotor revolutions, the streamwise and transverse gust velocities are low, less than 5 ft/s, and the mean rotor relative velocity \bar{W} is constant at approximately 119 ft/s. Instability is encountered

at 100 rotor revolutions, with the transverse gust component v^+ increasing to approximately 20 ft/s in 1 rotor revolution and remaining at this level. In contrast, the streamwise gust u^+ increases linearly with time, while the mean rotor relative velocity local to the 24.2 Hz stall cell decreases linearly.

Before the onset of the instability, times less than 100 rotor revolutions, the magnitude and phase of u^+/v^+ undergo significant fluctuations. This is because no signal with the 24.2 Hz frequency is present, i.e. no rotating stall component. After the compressor encounters the rotating stall instability, the magnitude of u^+/v^+ initially fluctuates around a value of 0.6 for about 35 rotor revolutions and the phase of u^+/v^+ changes from about 60° to 150° . After 135 rotor revolutions, the magnitude of u^+/v^+ increases linearly while the phase becomes constant at approximately 150° . Note that the magnitude of u^+/v^+ has a value greater than 1 and is increasing. This is in contrast to typical forced response gust component ratios for compressors in which the streamwise gust component is small or of similar magnitude as compared to the transverse gust component. The rotating stall excitation generating large values of the u^+/v^+ magnitude is similar to the behavior observed by Kim and Fleeter [16,17] from separated flow forcing functions, i.e. rotating stall cell is a severely separated flow forcing function.

The rotating stall forcing function characteristic during the modified surge cycle close to pure rotating stall, $B=0.40$, is presented in Figure 6. Similar to the pure rotating stall case, the streamwise and transverse gust velocities are less than 5 ft/s for times less than 100 rotor revolutions. At 100 rotor revolutions, the modified surge instability is encountered, with both the streamwise and the transverse gust velocities corresponding to the 24.6 Hz increasing very rapidly in approximately 4 rotor revolutions to 45 ft/s and 25 ft/s respectively. The transverse gust then decreases to half amplitude during the recovery phase of the first surge cycle, but reaches the previous magnitude level during subsequent modified surge cycles. In contrast, the streamwise gust velocity and the localized mean rotor relative velocity track the blowdown and recovery phases of the modified surge cycle, increasing and decreasing in accord to the cyclic behavior of the modified surge cycle. Note that the streamwise gust component value during the middle of each modified surge cycle is approximately the same, with a maximum value of approximately 45 ft/s.

The magnitude of u^+/v^+ follows the behavior of the streamwise gust velocity since the transverse gust level is nearly constant except during the recovery phase of the first modified surge cycle. Values of u^+/v^+ are greater than 1.0, becoming 2.5 during the core of the modified surge cycle where the flow is most stalled. Similar to the previous case with $B=0.26$, the phase of u^+/v^+ is approximately constant at 150° when large rotating stall cells are prevalent, but change from/to 0° at the entrance and exit of the modified surge cycle where rotating stall is weak.

The rotating stall forcing function during the modified surge cycle close to classic surge case, $B=0.46$, is presented in Figure 7. The time histories of the streamwise and transverse gust velocities and the localized mean rotor relative velocity are similar to the previous case. The maximum streamwise gust velocity of approximately 45 ft/s is reached in the core region of each modified surge cycle. The transverse gust velocities are lower, between 20 and 25 ft/s in these regions. The increased value of the streamwise gust velocity as compared to the transverse gust velocity is reflected in the u^+/v^+ gust component ratio, with the magnitude of u^+/v^+ of approximately 2 in the core of each modified surge cycle. Compared to the two previous instability modes, the transverse gust velocity better tracks the modified surge behavior. This is because as the compressor volume increases or B increases, less rotating stall exists in the recovery phase of the modified surge cycle. The phase of u^+/v^+

is approximately 150° , as in the previous cases, when the extent of rotating stall is great.

During the classic surge instability mode, Figure 8, the temporal behavior of the streamwise and transverse gust velocities and the mean rotor relative velocity are the same because of the complete disappearance of rotating stall during the recovery phase of the surge cycle, i.e. u^+ , v^+ , and \bar{W} track the behavior of classic surges equally well. The maximum magnitude of gust velocities are relatively unchanged from other instability modes, being approximately 45 ft/s and 25 ft/s for u^+ and v^+ respectively. This results in a u^+/v^+ magnitude ranging from 1.5 to 3.0 within the surge cycle, with the phase of u^+/v^+ being nearly constant at 150° in regions where rotating stall exists.

In summary, the rotating stall forcing function during the various compressor instability modes has a large streamwise gust component that tracks the behavior of the compressor instability. However, the transverse gust velocity is relatively constant, though higher in magnitude than during unstalled flow, once the instability is encountered. The phase of the streamwise to transverse gust component ratio of the rotating stall excitation has a characteristic value of 150° .

Surge Excitation Unsteady Aerodynamic Forcing Function

The transient forcing functions resulting from the surge excitation during the various compressor instability modes are presented in Figures 9, 10 and 11. These forcing functions define the surge frequency component of the total unsteady velocity, with the streamwise and transverse gust velocities u^+ and v^+ , the mean rotor relative velocity \bar{W} , and the magnitude and phase of the streamwise-to-transverse gust ratio u^+/v^+ presented. Note that since the lowest B value, $B=0.26$, corresponds to pure rotating stall, this case is not analyzed for the surge excitation or response.

The unsteady aerodynamic forcing function characterizing the surge excitation during the modified surge cycle close to pure rotating stall, $B=0.40$, is shown in Figure 9. The streamwise and transverse gust velocities are small, less than 1 ft/s, before the start of the modified surge cycle at approximately 110 rotor revolutions. The streamwise and transverse gust velocities then undergo a sudden and rapid increase. The increase in u^+ is particularly large, approximately 15 ft/s or 12% of the pre-surge mean rotor relative velocity \bar{W} . The streamwise gust velocity remains at this value until approximately 150 rotor revolutions, when it decreases, first by 2 ft/s and then by 5 ft/s to reach a relative minimum at 170 rotor revolutions. At this time, the streamwise gust velocity rapidly decreases to less than 5 ft/s. The first decrease in the streamwise gust corresponds to the point at which the modified surge cycle exhibits increased rotating stall during the recovery phase of the second modified surge cycle. The magnitude of the streamwise gust continues to decrease as the rotating stall increases. In contrast, the transverse gust velocity increases to a peak value of 2.3 ft/s and remains at this value until 140 rotor revolutions. The transverse gust magnitude then decreases slowly to the pre-surge level of 1 ft/s.

The mean rotor relative velocity local to the surge cycle \bar{W} also responds to the modified surge instability. Prior to 110 rotor revolutions, \bar{W} is approximately constant at 121 ft/s. At the onset of the modified surge cycle, \bar{W} undergoes a sudden and rapid deceleration to 110 ft/s. This mean rotor relative velocity is then maintained during the core and exit of the modified surge cycle. During initiation into the second modified surge cycle, the mean rotor relative velocity again starts to decrease to 105 ft/s. The decrease in \bar{W} experienced during the second modified surge cycle is less because of the increasing

presence of rotating stall and hence the decrease in the surge component. Upon initiation into the third modified surge cycle, \bar{W} decreases further to approximately 97 ft/s.

The surge excitation forcing function is also presented as the ratio of the streamwise-to-transverse gust component ratio u^+/v^+ in Figure 9. Since both the streamwise and the transverse gust velocities are changing during the onset and development of the modified surge cycle, u^+/v^+ also changes with time. Approximately 20 rotor revolutions prior to the onset of the instability, there is a small peak, 2, in the magnitude of u^+/v^+ . At instability onset, the magnitude of u^+/v^+ increases rapidly to 10 in approximately 10 rotor revolutions and fluctuates between 4 and 11 during the development of the modified surge cycle. At the end of 200 rotor revolutions, the magnitude of u^+/v^+ is small because u^+ is at its low pre-surge levels.

The phase of u^+/v^+ provides information about the presence of surge. Prior to the start of the modified surge cycle, the phase is constantly changing. However, at instability onset, the phase changes by 180° from the pre-modified surge value and stays at a constant level of approximately 140° . Toward the end of the measurement period, near 190 rotor revolutions, the phase of u^+/v^+ undergoes a large change due to the disappearance of the surge cycle.

The surge unsteady aerodynamic forcing function for the modified surge cycle close to classic surge with $B=0.46$ is shown in Figure 10. The streamwise gust velocity u^+ behaves similar to the modified surge case of $B=0.4$, with u^+ less than 1 ft/s prior to surge initiation and then very rapidly increasing to the surge level of 15 ft/s in about 10 revolutions. However, since the B value is increased, there is less rotating stall in this case. Hence the streamwise gust velocity stays at this constant level for 40 revolutions longer than at $B=0.40$. At 180 revolutions, however, rotating stall lingers excessively during the recovery phase of the third modified surge cycle and, hence, the streamwise gust velocity decreases very rapidly.

The transverse gust velocity v^+ is less than 0.5 ft/s until 110 rotor revolutions when the modified surge instability is encountered. For 20 revolutions following the instability onset, the transient behavior of v^+ is similar to that at $B=0.40$, attaining a gust level of about 2 ft/s. However, instead of decreasing as in the case with $B=0.40$, the transverse gust velocity continues to increase to approximately 3.3 ft/s and stays at this value until the end of the second surge cycle, at 170 revolutions. Then rotating stall starts to dominate the modified surge cycle, with the transverse gust velocity due to surge decreasing in magnitude.

The transient behavior of the mean rotor relative velocity \bar{W} is similar to that during the previous instability case. However, the initial decrease in \bar{W} at the instability onset is lower by 2 ft/s, 108 ft/s. This indicates that the modified surge at $B=0.46$ involves a deeper surge cycle than at $B=0.4$. The second decrease in \bar{W} is less than 2 ft/s, resulting in a mean relative velocity of 103 ft/s. The final rapid decrease in \bar{W} starts just after 180 revolutions during the recovery phase of the third modified surge cycle, with the modified surge cycle becoming more like a pure rotating stall instability mode.

The forcing function is also presented in terms of the streamwise-to-transverse gust component ratio in Figure 10. Note the small peak in the magnitude of u^+/v^+ prior to the onset of the instability at 75 revolutions. A similar peak was noted in the $B=0.40$ case at 90 revolutions. Just before 110 rotor revolutions, modified surge is encountered and the magnitude of u^+/v^+ quickly increases to a value of 9 at about 120 revolutions. The u^+/v^+ magnitude then decreases since the magnitude of the transverse gust decreases while the streamwise gust remains constant. After reaching a local minimum of 4.5, the magnitude

of u^+/v^+ starts to increase again at 160 revolutions. The transient behavior during the next 20 revolutions is similar to that during the first modified surge cycle, increasing to a u^+/v^+ magnitude of 8. After 180 revolutions, during the recovery phase of the third modified surge cycle, u^+/v^+ fluctuates significantly. This is because of the decreased surge frequency content and the increased presence of rotating stall, i.e. the magnitude of the transverse gust is very small as is the streamwise gust magnitude. Hence the noisy gust component ratio. The phase of u^+/v^+ is very similar to that of the modified surge case, $B=0.40$, undergoing a 180° change at the onset of the stability before settling to constant value of approximately 160° .

In the classic surge mode, $B=0.76$, the temporal trends in the modified surge excitations are much more pronounced, Figure 11. The streamwise gust velocity increases rapidly to about 18 ft/s at instability onset. It remains at this value until the second surge cycle is encountered, with the streamwise gust velocity then further increasing to 20 ft/s. This second velocity increase is due to this classic surge cycle growing in size with time. Similarly, the transverse gust velocity is small until the onset of the instability. The transverse gust velocity then increases rapidly to a new value with each surge cycle. The transition to a new value occurs at the entrance and the exit of the surge cycle. Note the significant increase in the magnitude of the transverse gust velocity in comparison to the values during the modified surge cycles: 6 ft/s after the first cycle, 8 ft/s after the second cycle, a value more than twice that during the modified surge cycle at $B=0.46$. The mean rotor relative velocity experiences a trend opposite to the streamwise gust velocity, decreasing where u^+ increases and increasing where u^+ decreases.

The magnitude and phase of u^+/v^+ are also shown in Figure 11. Note the slight increase in the magnitude of u^+/v^+ before surge initiation, at approximately 90 revolutions. This pre-surge increase in the magnitude of u^+/v^+ is different from the two modified surge cases in that it does not exhibit a peak value. At surge initiation, the magnitude of u^+/v^+ increases almost instantaneously to 5.5. The magnitude of u^+/v^+ stays near 5.5 until approximately 130 rotor revolutions. The magnitude of u^+/v^+ then starts to decrease rapidly until about 140 revolutions, when the decrease slows and the magnitude of u^+/v^+ settles to about 2.6. The phase of u^+/v^+ undergoes a slight oscillation for about 20 revolutions during the time frame that the magnitude of u^+/v^+ rises and falls. At approximately 140 revolutions, the phase of u^+/v^+ settles to approximately 160° .

The surge forcing functions are similar to the rotating stall forcing function in several ways. The streamwise gust velocity and the mean rotor relative velocity follow the transient flow behavior of rotating stall, the modified surge and classic surge cycles. Also the level of the streamwise gust velocity is fairly constant regardless of the instability mode, being about 50 ft/s for rotating stall and 15-20 ft/s for surge. However, the transverse gust differs in magnitude between the rotating stall and the surge excitations. The rotating stall generated transverse gust is approximately constant regardless of the instability mode, being approximately 25 ft/s. The surge generated transverse gust changes with instability mode, being the lowest for $B=0.40$, having a peak value of about 2.3 ft/s, and the largest for $B=0.76$, having a peak value of about 8 ft/s. The gust component ratios for both the rotating stall and surge forcing functions are similar in that the transient behavior tracks the instability behavior in general, but differ in the magnitude of u^+/v^+ . The rotating stall excitation results in a lower magnitude of the gust components ratio, u^+/v^+ less than 3, while the surge excitation has a larger gust component ratio magnitude, u^+/v^+ ranging from 4 to 14.

UNSTEADY AERODYNAMIC RESPONSE

Unsteady Lift Due to Rotating Stall

The magnitude and phase of the unsteady lift on the 1st stage rotor blade for the four instability modes are shown in Figure 12. The unsteady lift magnitude specifies the rotor blade response to the rotating stall excitation since the frequencies selected for the DFT analysis described earlier are the rotating stall frequencies. The coherence of the phase of the unsteady lift indicates the presence of a physical wave, i.e. the rotating stall.

Figure 12a presents the unsteady lift magnitude and phase resulting from the rotating stall excitation. The unsteady lift is very low until just before 100 rotor revolutions when the rotor blade suddenly responds to the rotating stall, the unsteady lift magnitude very rapidly increasing from 0.0025 psi to 0.017 psi in approximately 10 rotor revolutions. Then the rotor responds to the growth in stall cell depth, with the unsteady lift magnitude increasing slowly from 0.017 psi to 0.0275 psi. These trends correspond to the time history of the transverse gust due to rotating stall excitation, Figure 5. At the same time that the unsteady lift magnitude sharply increases, the phase of the unsteady lift becomes coherent - indicating stall cell propagation. From about 100 rotor revolutions to 160 rotor revolutions, the phase decreases, showing that the actual rotating stall wave is slower than the specified frequency of 24.2 Hz (13.3 Hz). The actual speed at rotating stall inception is 21 Hz (17 Hz) per Equation 2. After 160 rotor revolutions, the actual stall speed is faster than the specified value of 24.7 Hz (12.8 Hz).

The rotor blade unsteady lift magnitude and phase response to rotating stall excitation during modified surge, $B = 0.40$, is shown in Figure 12b. The behavior of the modified surge which is characterized by approximately 1.5 cycles of surge becoming rotating stall is reflected in the development of the unsteady lift. Until approximately 100 rotor revolutions, the unsteady lift magnitude is low, approximately 0.002 psi. Then, the blade row responds to the rotating stall cell excitation in the first surge cycle and the unsteady lift increases very rapidly to its peak value during the next 15 rotor revolutions. After the maximum unsteady pressure is reached, the unsteady lift magnitude decreases during the compressor recovery period of the first surge cycle and reaches the local minimum unsteady lift of 0.015 psi at about 125 rotor revolutions. The unsteady lift then undergoes two more small fluctuations, settling to an unsteady lift magnitude of 0.0275 psi. These fluctuations correspond to the fluctuations in the rotating stall transverse gust velocity of Figure 6. The rotating stall wave is seen by the coherence of the unsteady lift phase. At approximately 100 rotor revolutions, the phase starts to become coherent, with the phase slope being negative corresponding to a speed of 23 Hz (14 Hz). At approximately 115 rotor revolutions, the phase becomes flat, indicating that the stall speed is 24.6 Hz (12.9 Hz). During the recovery period of the first modified surge cycle, the stall speed is approximately 22.9 Hz (14.6 Hz). During the peak of the second modified surge cycle, at 140 rotor revolutions, the stall speed is again 24.6 Hz. From the recovery period of the second surge cycle and the settling into a steady stalled operating loop, the stall speed changes from 24.2 Hz (13.3 Hz) to 24.7 Hz (12.8 Hz).

Figure 12c shows the unsteady lift due to the rotating stall excitation during the modified surge cycle, $B=0.46$. The peaks in the unsteady lift correspond to the peaks in the strength of the rotating stall. At approximately 100 rotor revolutions, rotating stall emerges and rapidly grows, with the resulting unsteady lift magnitude reaching its maximum of 0.03 psi during the middle of the first surge cycle at 110 rotor revolutions. Then the unsteady lift decreases during the recovery period of the first modified surge cycle but increases and decreases again, corresponding to the second and third modified surge cycles. Again, this behavior reflects the changes in the rotating stall

transverse gust magnitude which occur during the initiation and development of the modified surge cycle. Note that in each modified surge cycle, the maximum unsteady lift magnitude due to the rotating stall excitation is constant, approximately 0.03 psi. It is apparent from the constant unsteady lift magnitude during the various instability modes that the blade surface responds to the transverse gust component, which are relatively constant for all the instability modes. At the same time that the magnitude of the unsteady lift undergoes the sudden increase, the unsteady lift phase becomes coherent, indicating the presence of the physical wave propagation, in this case a rotating stall cell. Within the first surge cycle, the rotating stall cell undergoes propagation speed changes, from 23 Hz (14.5 Hz) to 25 Hz (12.5 Hz) to 23 Hz (14.5 Hz). Note that in the two modified surge cycles, Figures 12b and 12c, the unsteady lift phase stays coherent during the recovery zone of each modified surge cycle. This is because rotating stall is always present during the surge in the modified surge cycle.

The rotor blade unsteady lift and phase resulting from the rotating stall excitation during the classic surge cycle is presented in Figure 12d. Analogous to the rotating stall generated transverse gust magnitude of Figure 8, the time history of the unsteady lift magnitude clearly shows the nature of the classic surge cycle. The unsteady lift magnitude increases very rapidly and suddenly at 100 rotor revolutions, reaching its peak value of 0.032 psi, and then decreases just as rapidly to its pre-surge level. This is in contrast to the blade row response to the rotating stall-modified surge cycle excitation where the transverse gust component and the blade unsteady lift magnitude did not fall to pre-surge levels because of the continued presence of rotating stall throughout the surge cycle. This difference between the modified and classic surge cycles is also evident in the unsteady lift phase data. The phase coherence during the rise and fall of rotating stall within the surge cycle is no longer present during the surge recovery periods. Within the surge cycle, the rotating stall speed changes from 23.5 Hz (14 Hz) to 26.8 Hz (10.7 Hz) to 23.5 Hz.

In summary, the 1st stage rotor row responds to the transverse gust component of the rotating stall excitation. From the four compressor instability mode configurations, it is evident that whenever rotating stall is present, the resulting maximum unsteady lift is approximately constant, in these experiments being 0.03 psi, and not strongly affected by how the rotating stall was generated. This is because the excitation transverse gust magnitude is approximately constant at 25 ft/s. The 0.03 psi value of the unsteady lift represents approximately 27% of the steady lift just before the onset of instability, estimated to be approximately 0.11 psi at 9° incidence. This steady lift is estimated from previous steady loading data. Also, the coherence of the unsteady lift phase is a clear indicator of the presence of a rotating stall wave.

Unsteady Lift Due to Surge

Figure 13 presents the magnitude of the unsteady lift on the 1st stage rotor blade generated by a surge excitation for three different compressor instability modes. These are the modified surge close to pure rotating stall at 17 Hz, the modified surge close to classic surge at 1.17 Hz, and classic surge at 0.75 Hz. Note that the unsteady lift phase data are not presented because of the phase data distortion resulting from the repetition of data points for the DFT analysis of the unsteady pressures.

The modified surge close to pure rotating stall cycle is initiated at approximately 100 rotor revolutions, with the unsteady lift magnitude increasing very sharply to 0.007 psi where there is a slight lull in the growth of the unsteady lift. The unsteady lift magnitude then continues to rapidly increase until a maximum unsteady lift of 0.011 psi is achieved at the end of the first modified surge cycle. The increase in the unsteady lift magnitude and the time of maximum lift correspond to the transient behavior of the transverse gust. The decrease in the

surge generated unsteady lift occurs because after the first modified surge cycle, the presence of rotating stall increases significantly with each modified surge cycle. Therefore, after 130 rotor revolutions, the unsteady lift magnitude decreases fairly rapidly until 140 rotor revolutions, when the decrease in the unsteady lift magnitude is considerably slower. This slow decay tracks the merging of surge characteristics with rotating stall.

The development of the rotor blade unsteady lift during the modified surge cycle with $B = 0.46$ is similar to the previous case, with the unsteady lift magnitude increasing very abruptly at approximately 100 rotor revolutions in response to the modified surge cycle initiation. At approximately 120 rotor revolutions, the lowest compressor flow rate is reached and the unsteady lift undergoes a period of slow increase. During the recovery zone of the first surge cycle, the unsteady lift continues to increase and peaks at entry into the second modified surge cycle. The peak unsteady lift magnitude reached during this cycle is 0.013 psi, slightly higher than that with the $B = 0.40$ modified surge cycle. Then the unsteady lift magnitude decreases fairly slowly, in contrast to the previous case where the unsteady lift magnitude decreased to a value of 0.004 psi in 15 rotor revolutions, versus 50 rotor revolutions in this case. The increased unsteady lift due to surge is due to the decreased rotating stall with increased surge strength and corresponds to the increased value of the transverse gust velocity.

For the classic surge cycle, the unsteady lift magnitude starts to increase at approximately 105 rotor revolutions, with the rate of increase initially similar to the two modified surge cases. However, in contrast to these modified surge cases, the unsteady lift does not decrease. Instead, the unsteady lift continues to increase throughout the entire surge development period for which the data are acquired. This is also in correspondence with the transverse gust component time history.

In summary, the rotor blade unsteady lift generated by the surge excitation is dependent on the instability mode because the transverse gust component of the forcing function depended on the instability mode. The unsteady lift magnitude tends to be larger with the classic surge cycle than with the modified surge cycles. This is due to the increased presence of rotating stall in the modified surge cycles. Also, since the modified surge cycles transform into rotating stall with time, the unsteady lift magnitude reaches a maximum and then decreases with time whereas the classic surge excitation does not attain a maximum unsteady lift.

Surge & Rotating Stall Response Amplitudes

A direct comparison of the unsteady lift magnitude is not sufficient to determine whether rotating stall or surge is more likely to cause forced response damage since frequency effects are not incorporated. Rather the AF method is utilized. Note that for these rotating stall and surge forcing functions, the assumptions inherent in the AF method are appropriate, with the exception of small perturbations. The rotating stall and surge forcing functions are quasi-steady as their frequencies are fractions of the rotor fundamental frequency, with reduced frequencies of 0.0033 and 0.12, below the 0.20 limiting value suggested by Pearson (10).

The AF analysis results are presented in terms of predicted blade vibration levels nondimensionalized by the maximum level. Equation 6 shows that the product AF is proportional to the gust magnitude, with the proportionality constant based on steady flow parameters. For these experiments, the steady flow coefficient is of unit order. Hence, the vibration levels generally follow the gust trends. Furthermore, since the rotating stall u^+ magnitude is at least twice the v^+ magnitude, Figures 6,7 and 8, and the surge u^+ magnitude 2.5 to 7 times the v^+ magnitude, Figures 9, 10 and

11, AF has the character of the streamwise gust component v^+ . This is reflected in the data, Figure 14.

With $B=0.4$, the surge induced vibration level is relatively constant for 40 rotor revolutions after the instability is initiated. Since the rotating stall then dominates over the surge, the surge induced vibrational level is predicted to decrease until approximately 195 rotor revolutions where the surge character completely disappears. In contrast, the rotating stall induced vibration level increases and decreases while the surge component is strong, i.e., during the first 70 rotor revolutions. The rotating stall generated vibration then remains high. The maximum surge generated vibration is approximately 25% of that for rotating stall because the rotating stall gust magnitude is much larger than that of surge.

The vibrational response trends are similar when B is increased to $B=0.46$. However the vibration level due to surge remains at the high level almost 40 rotor revolutions longer. Rotating stall induced vibration follows the cyclic behavior of surge, with the vibration level at the end of each surge cycle becoming higher due to the increased presence of rotating stall over surge with time.

A further increase of B to $B=0.76$, the surge generated vibration is higher than the previous two cases, 30-35% of the maximum rotating stall value. This is because rotating stall disappears completely during the recovery period of the classic surge cycle. Hence the increased surge component.

In each instability mode, the predicted maximum surge induced vibration is considerably smaller than that due to rotating stall. The rotating stall unsteady lift magnitude is larger than that due to surge in each instability mode as well. Thus, with regard to blade vibration and, hence, stress, rotating stall forcing functions are of greater concern than those due to surge. Exceptions to this conclusion might result from the transient nature of the rotating stall.

SUMMARY AND CONCLUSIONS

The compressor unsteady aerodynamic forcing function and resulting unsteady aerodynamic response to rotating stall and surge excitation during the various compressor instability modes was experimentally investigated in a 3-stage axial flow research compressor. The forcing function was measured with a rotating cross-hot-wire probe, with the resulting 1st stage rotor blade response measured with blade surface mounted dynamic pressure transducers. Different compressor instability modes were generated by varying the compressor volume with the compressor operating at a constant rotational speed.

The rotating stall forcing function is characterized by a large streamwise gust velocity component which tracks the behavior of the compressor instability mode, increasing continuously during the pure rotating stall instability mode and increasing and decreasing accordingly during the modified surge and classic surge instability modes. The transverse gust, in contrast, increases very abruptly at instability onset, with the gust velocity remaining nearly constant except where the level of rotating stall is very low. In addition, the magnitude of the streamwise-to-transverse gust ratio is large, 2 - 3, similar to the finding by Kim and Fleeter [16,17] where increased values of the gust component ratio were observed with separated flow forcing functions, i.e. rotating stall represents a severely separated flow forcing function to a blade row. The streamwise to transverse gust component ratio also has a characteristic phase of approximately 150°.

The surge forcing function is characterized by a large streamwise gust velocity component which tracks the compressor instability behavior. It increases at surge initiation and then either decreases due to the decreased surge content and increased rotating stall content, or increases in the classic surge

case since the surge cycle becomes deeper with time in this instability mode. The surge generated transverse gust component is dependent on the particular instability mode, increasing in magnitude with increasing B value or decreased rotating stall component. The surge generated streamwise-to-transverse gust component ratios are an order of magnitude larger than those due to rotating stalls, indicating that surge also represents a severely separated flow forcing function to the blade row.

The unsteady aerodynamic response as quantified by the unsteady lift reflects the basic behavior of rotating stall, increasing continuously during the pure rotating stall instability mode and increasing and decreasing accordingly during the modified surge and classic surge instability modes. The maximum unsteady lift due to the rotating stall excitation during the different instability modes were approximately constant in value, being independent of the instability mode. This unsteady lift is approximately 27% of the steady lift achieved by the rotor blade just before the onset of the compressor instability. The unsteady lift due to the surge excitation, in contrast, showed strong dependence on the instability mode.

Corresponding to the magnitude of the unsteady lift, the predicted blade vibration and hence the stress levels from the quasi-steady AF analysis also indicate that rotating stall is potentially more damaging than surge to blade life, being approximately 3 to 4 times the surge induced vibration levels.

ACKNOWLEDGMENTS

Research sponsored by the Air Force Office of Scientific Research (AFSC) under Grant 91-0251. The United States Government is authorized to reproduce and distribute reprints for governmental purposes notwithstanding any copyright notation hereon.

REFERENCES

1. Haupt, U., A.N. Abdel-Hamid, N. Kaemmer, and M. Rautenberg, "Excitation of Blade Vibration by Flow Instability in Centrifugal Compressor", *ASME Paper 86-GT-283*, 1986.
2. Jin, D. U. Haupt, H. Hasemann, and M. Rautenberg, "Excitation of Blade Vibration Due to Surge of Centrifugal Compressor", *ASME Paper 92-GT-149*, 1992.
3. Jin, D., U. Haupt, H. Hasemann, and M. Rautenberg, "Blade Excitation by Circumferentially Asymmetric Rotating Stall in Centrifugal Compressors", *ASME Paper 92-GT-148*, 1992.
4. Greitzer, E. M., "Surge and Rotating Stall in Axial Flow Compressors, Part I: Theoretical Compression System Model", *Transactions of the ASME*, April 1976, pp 190-198.
5. Greitzer, E. M., "Surge and Rotating Stall in Axial Flow Compressors, Part II: Experimental Results and Comparison With Theory", *Journal of Engineering for Power*, April 1976, pp. 199-217.
6. Pust, Libor, "Modified Surge in an Axial Flow Compressor", *ASME Paper No. 92-GT-59*, 1992.
7. Jun, Hu, Tang Guo Cai and Zhang Hui Min, "An Investigation of Post Stall Transients and Recoverability of Axial Compression Systems: Part I - A Simplified Method," *ASME Paper No. 92-GT- 55*, 1992.
8. Day, I. J., "Axial Compressor Performance During Surge", *AIAA Paper 91-7098*, 1991.

9. Almgren, Ray., "Gabor Spectrogram: A revolution in Joint Time-Frequency Analysis", *National Instruments Product Information Sheet No. 360175-01*, Summer 1992.
10. Pearson, H. "The Aerodynamics of Compressor Blade Vibration", *4th Anglo-American Aeronautical Conference*, London, September 16-17 1953, pp. 127-162.
11. Parry, J.F.W. and Pearson, H. "Cascade Flutter & Wake Excitation", *Journal of Royal Aeronautical Society*, July 1954, pp. 505-508.
12. Armstrong, "Recent Blade vibration Technique", *Transactions of ASME, Journal of Engineering for Power*, Volume 89, Series A, No. 3, July 1967, pp. 437-444.
13. Armstrong, Crowcroft, and Hunt, "Fatigue Life of Compressor Blading", *Paper 14, Applied Mechanics Convention 1966, Proceedings Institution of Mechanical Engineers*, Volume 180,1965-1966.
14. Blackwell, B. D., "Some Investigations in the Field of Blade Engineering", *Journal of Royal Aeronautical Society*, Vol. 62, pp. 633-646.
15. Armstrong, E. K., "Fatigue and Assessment Methods of Blade Vibration", *AGARDograph No. 298, AGARD Manual on Aeroelasticity in Axial-Flow Turbomachines, Volume 2: Structural Dynamics and Aeroelasticity*, pp. 16-13 - 16-15.
16. Kim, K. H. and Fleeter, S., "Compressor Blade Row Unsteady Aerodynamic Response to Attached and Separated Flow Forcing Functions," *AIAA Paper 92-0147*, January 1992.
17. Kim, K. H. and Fleeter, S., "Forcing Function Generator Fluid Dynamic Effects on Compressor Blade Gust Response," *AIAA Paper 93-0157*, January 1993.

Airfoil Type	IPV	ROTOR	STATOR
Number of Airfoils	26	43	31
Chord, C (mm)	50	30	30
Stiffly	.96	1.14	1.09
Center, C (mm)	34.9	28.0	27.7
Stagger Angle, γ (deg)	21.0	34.0	-36.0
Aspect Ratio	2.0	2.0	2.0
Thickness/Chord (%)	10	10	10
Design Flow Rate (g/s)		2.83	
Design Axial Velocity (m/s)		24.38	
Design Rotational Speed (RPM)		2250	
Number of Stages		3	
Design Stage Pressure Ratio		1.0	
Inlet Tip Diameter (mm)		430	
Hub/Tip Radius Ratio		0.714	
Stage Efficiency (%)		83	

B-VALUE	VOLUME (m ³)
0.26	3.4
0.40	8.5
0.46	11.0
0.76	30.04
L ₀ (m)	2.93
a (m/s)	343.2
U (m/s)	42.5

Table 1. Airfoil and Compressor Characteristics

	Surge (Hz)	Leading stall (Hz)	% Speed
Rotating Stall		24.2	-11/3.2
Modified Surge Class to Rotating Stall	1.17	24.6	1.6
Modified Surge Class to Classic Surge	1.17	25.0	-12/12
Classic Surge	6.75	25.8	-13%

Table 2. DFT Analysis Surge and Rotating Stall Frequencies

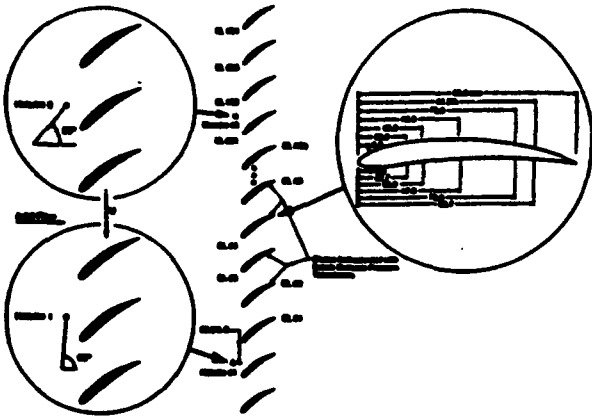


Figure 1. Rotor Instrumentation

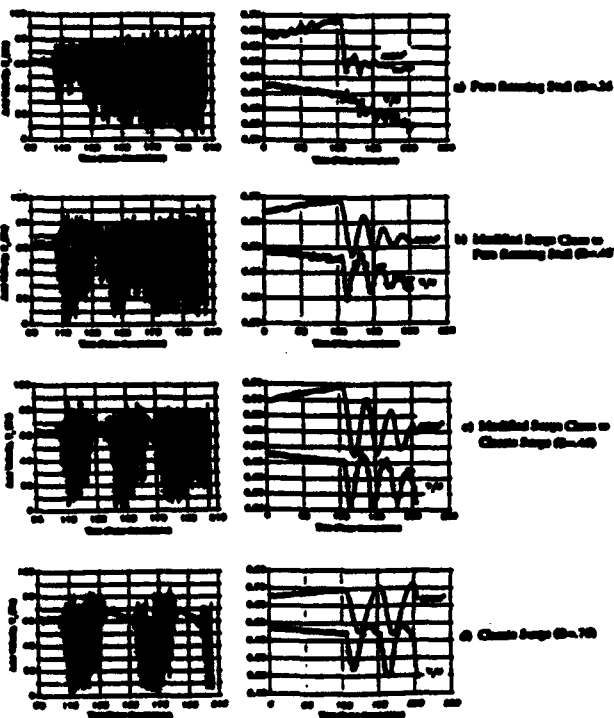


Figure 2. Instability Flow Regime Characterization

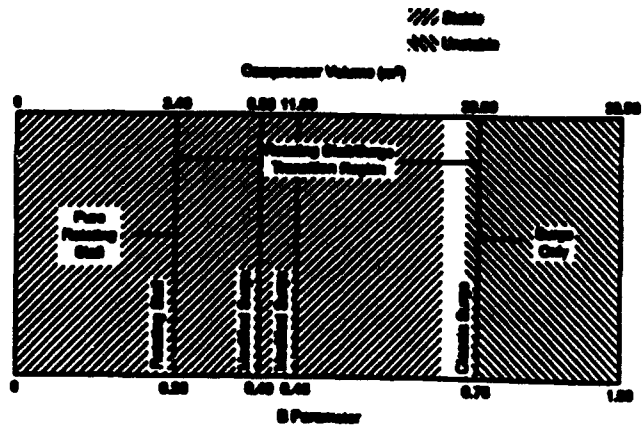


Figure 3. Compressor Instability Modes

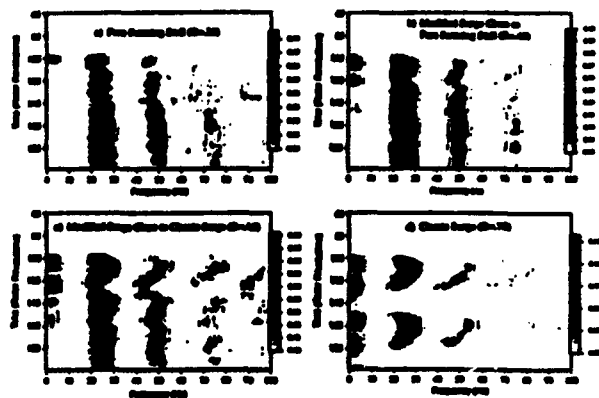


Figure 4. Gabor Spectrogram of Suction Surface Leading Edge Pressure Response at Various Instability Modes

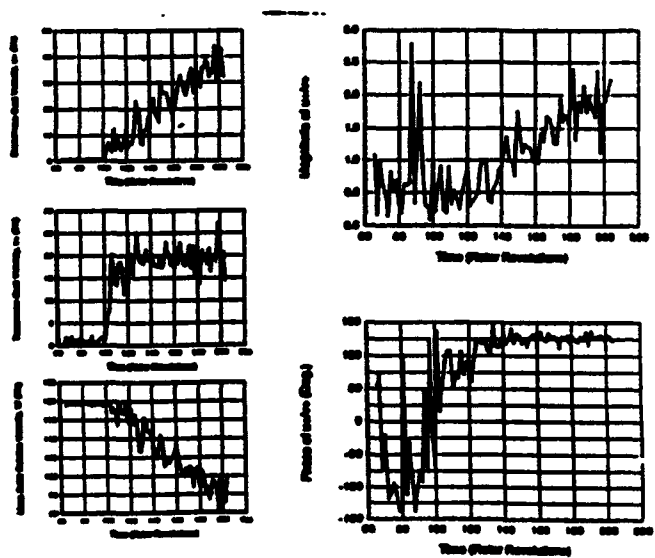


Figure 5. Rotating Stall Unsteady Aerodynamic Forcing Function During Pure Aerodynamic Stall Instability Mode (13.3 Hz or 24.2 Hz Rotating Frame)

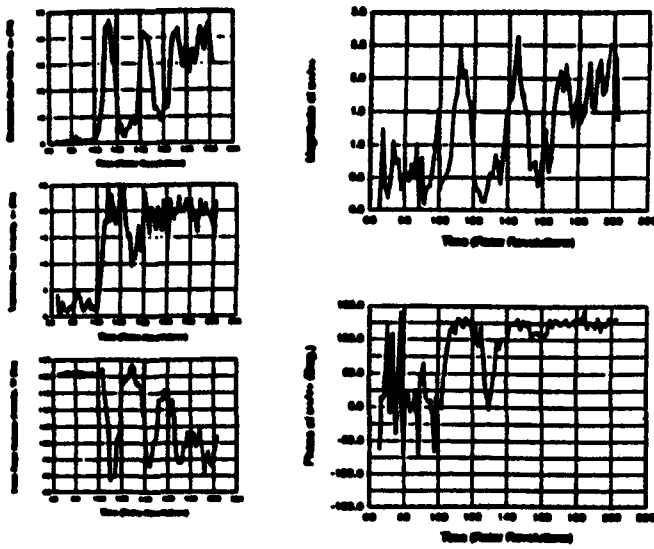


Figure 6. Rotating Stall Unsteady Aerodynamic Forcing Function During Modified Surge Close to Pure Rotating Stall Instability Mode (12.9 Hz or 24.6 Hz Rotating Frame)

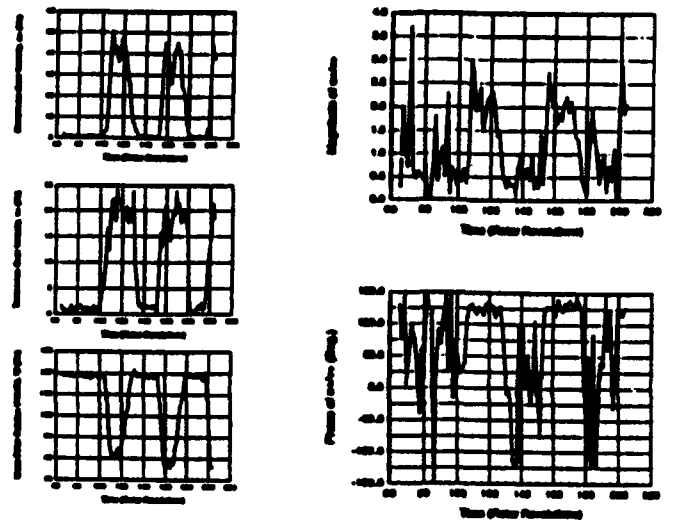


Figure 8. Rotating Stall Unsteady Aerodynamic Forcing Function During Classic Surge Instability Mode (11.7 Hz or 25.8 Hz Rotating Frame)

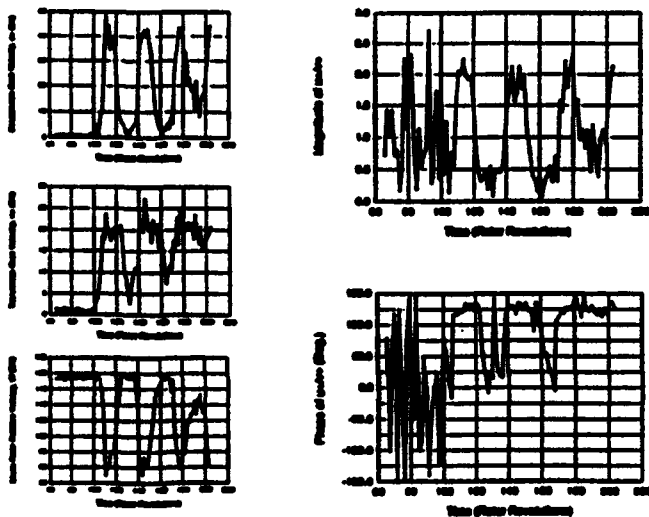


Figure 7. Rotating Stall Unsteady Aerodynamic Forcing Function During Modified Surge Close to Classic Surge Instability Mode (12.5 Hz or 25.0 Hz Rotating Frame)

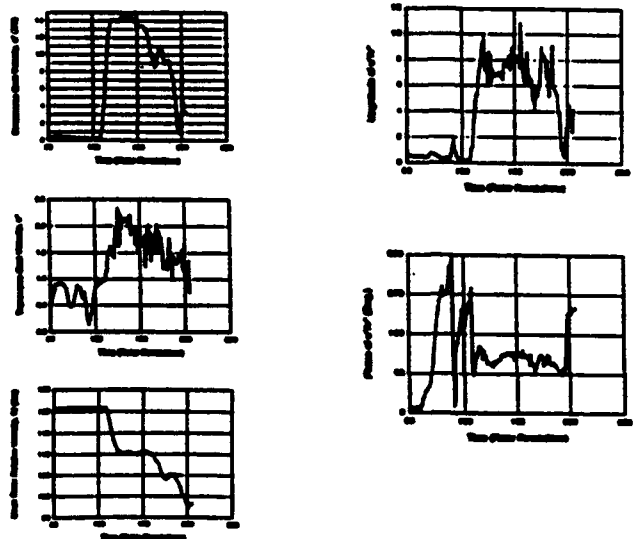


Figure 9. Surge Unsteady Aerodynamic Forcing Function During Modified Surge Close to Pure Rotating Stall Instability Mode (1.17 Hz)

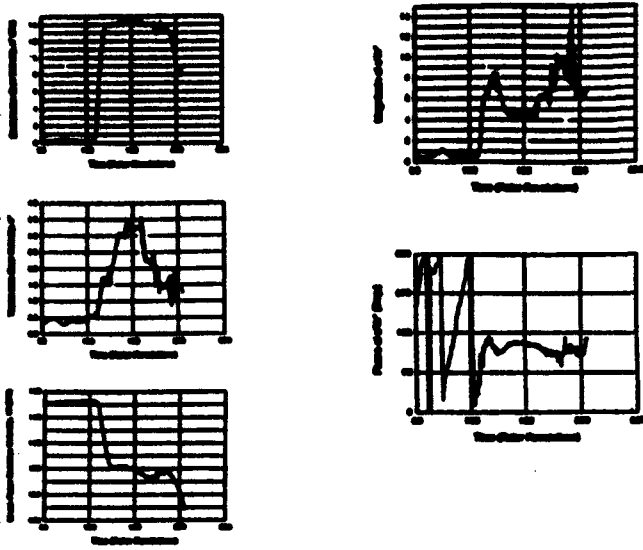


Figure 10. Surge Unsteady Aerodynamic Forcing Function During Modified Surge Close to Classic Surge Instability Mode (1.17 Hz)

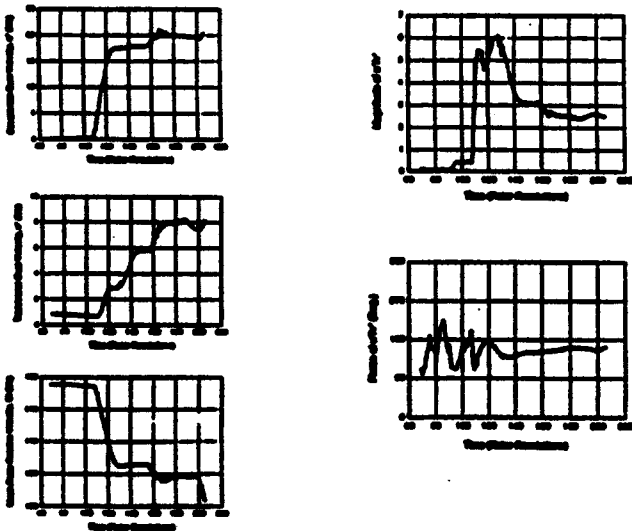


Figure 11. Surge Unsteady Aerodynamic Forcing Function During Classic Surge Instability Mode (0.75 Hz)

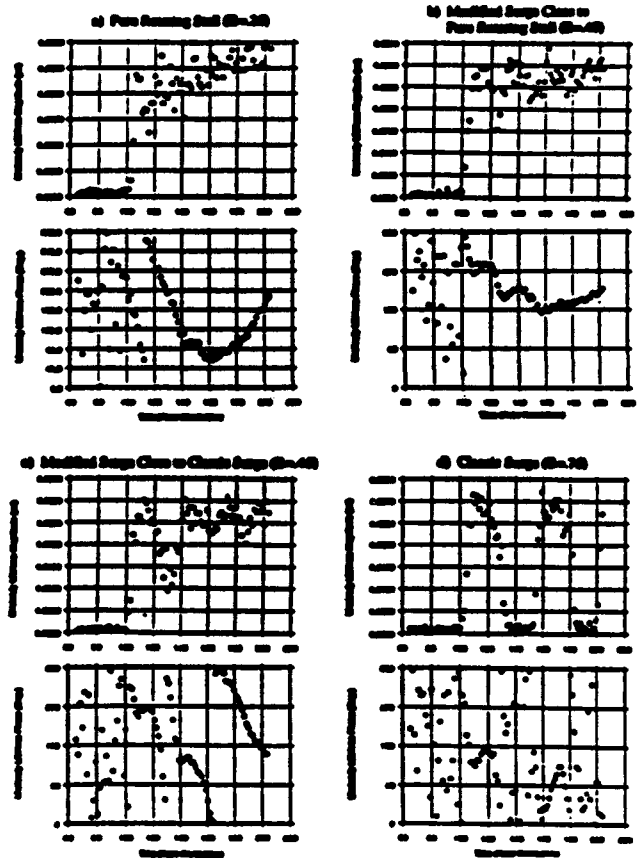


Figure 12. Unsteady Lift Due to Rotating Stall Excitation

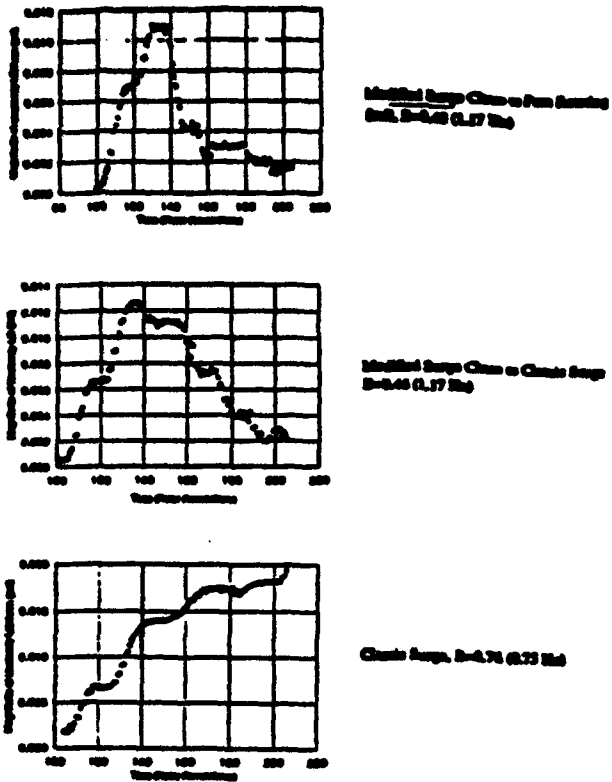


Figure 13. Unsteady Lift Due to Surge Excitation

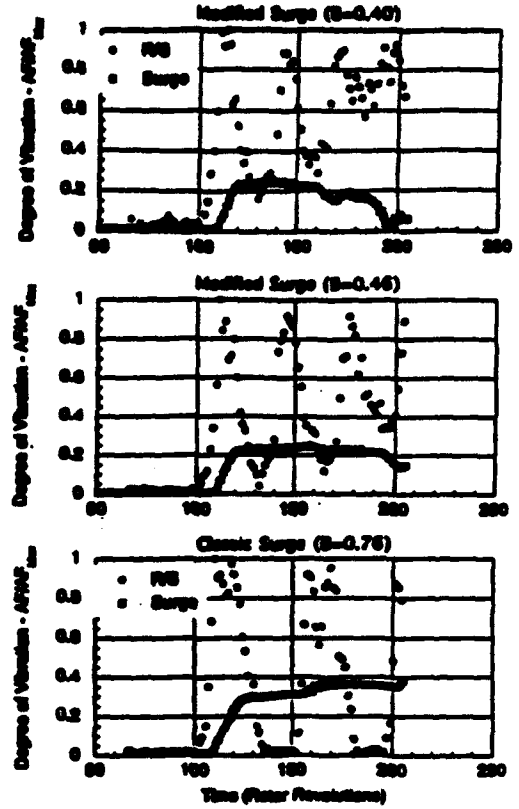


Figure 14. AF Method: Comparison of the Predicted Blade Vibration Levels from Rotation Stall and Surge Excitation